Quantum simulation of strongly-correlated two-dimensional fermions in optical lattices

Dissertation
zur
Erlangung des Doktorgrades (Dr. rer. nat.)
der
Mathematisch-Naturwissenschaftlichen Fakultät
der
Rheinischen Friedrich-Wilhelms-Universität Bonn

von
Chun Fai Chan
aus
Hong Kong

Bonn, 2019

Dieser Forschungsbericht wurde als Dissertation von der Mathematisch-Naturwissenschaftlichen Fakultät der Universität Bonn angenommen und ist auf dem Hochschulschriftenserver der ULB Bonn https://nbn-resolving.org/urn:nbn:de:hbz:5-57923 elektronisch publiziert.

1. Gutachter:	Prof. Dr. Michael Köhl
2. Gutachter:	Prof. Dr. Martin Weitz
Tag der Promotion:	04.03.2020
Erscheinungsjahr:	2020

To my parents and Phyllis.

Abstract

In this thesis, I present the experimental realisation of the two-dimensional Hubbard model with ultracold fermionic ^{40}K atoms in optical lattices. By tuning the dimensionality, kinetic and interaction in the optical lattices, we perform an analogue quantum simulation to explore the phase diagram of the Hubbard model.

The first key result is the experimental observation of particle-hole symmetry, namely a phase mapping between repulsive and attractive interactions. We compare a density-ordered, Mott-insulating phase with repulsive interaction to a spin-ordered, preformed pair phase and found excellent agreement with the theoretical prediction. The precise control and excellent detection capability of our quantum gas apparatus allow us to validate the particle-hole symmetry, and utilise it to explore quantum phases with a novel approach.

Next, we investigate the spin-ordering on the repulsive side. By implementing a novel scheme based on coherent manipulation of spin correlations, we probe the anti-ferromagnetic ordering in the low-temperature phase diagram. The momentum-resolved spin correlations permit the reconstruction of spatial correlators without site-resolved imaging fidelity.

Finally, we probe the attractive side of the phase diagram with a focus in pairing phenomenon, in which we draw a close analogy with BCS-BEC crossovers present in high-temperature superconducting cuprates and trapped ultracold Fermi gases. From the pair correlation function derived from thermodynamics observables, we observe the competition between the effective Pauli repulsion in fermionic systems and the on-site attraction we implemented.

Acknowledgements

Firstly, I would like to thank my supervisor Prof. Michael Köhl, for his continued guidance. His enthusiasm in physics continues to inspire me. I am in debt to his guidance, not only from the technical skills and critical thinking I learnt from him but from the way he teaches and how he breaks down complicated ideas in digestible size.

When I first started my internship here in Bonn, I was uncertain about my future career paths. What the internship showed me is an entirely new way of performing researches in contrast to my Master study in theoretical physics. I want to thank the leading postdoc of the Fermi team, Ferdinand Brennecke, who encouraged me to take on the leap. I am deeply grateful for my decision to take on the switch from theoretical physics to hand-on experimental works. After I started my PhD in Bonn, Ferdinand continued to be my go-to person for assistance. His vast knowledge in a variety of areas never fails to amaze me. Besides, I also learnt an enormous amount of experience from the previous generation of PhD students. I have always been a fan of Luke Miller's critical way of thinking during discussions. Eugenio Cocchi and Jan Drewes were always available, either in the lab or office, to explain the minutest details of the experiment to me patiently. The technical dictionary postdoc, Daniel Pertot, whose skill ranges from building electronics to giving the out-of-the-box idea in physics, was a dream to work with and the perpetual final resort.

Of course, I am most grateful to have been able to work alongside with Marcell Gall, whose technical instinct I admire so much, and Nicola Wurz, who never fails to challenge me on concepts I am uncertain of in a discussion. I feel truly fortunate to have met you two, sharing almost countless scary moments in labs (such as those related to fire and water), enjoying the great moment of sending an impeccable over-weekend run and brainstorming crazy ideas in the office. My doctoral life would have been so bored without you two. I also feel confident that the next generation PhD and Master students: Jens Samland, Nick Klemmer and Janek Fleper, would be able to continue pushing the experiments in ways I could never have imagined. I also want to thank all members of the Fermi team for rigorously reviewing the draft of this thesis.

Aside from people in the Fermi team, I am grateful to have known the fantastic people in the lab. I want to thank the two Tims (Tim Harrison and Tim Ballance) for inviting me to the first beer night in Bonn. Massive shout out to Martin Link for referring me to rent his old apartment. I have also enjoyed the time spent and learnt a great deal of, during working as tutors with Kuiyi Gao and Hendrik Meyer. I would also like to the many other members of the lab: Alexandra Behrle, Ashwin Boddeti, Jonathan Silver, Robert Maiwald, Jonas Schmitz, Andreas Kell, Vidhya Nair, Thorsten Langerfeld, Pascal Kobel and Tobias Kree. Last but certainly not least, I would like to thank our group secretary, Tina Naggert, for always taking care of all the administrative works.

Finally, I would like to thank the most important people in my life: to my parents for tolerating their stubborn son, to my sister and brother, for your patience about my winding, to Phyllis, in spite of

the distance we now part, for your support throughout the year ad I will be forever grateful for the companion, and to dear friend for life, Pang, for countless night of phone calls.

To all my friends in Hong Kong, I am proud to be a Hong Konger, more than ever.

Contents

CHAPTER 1

Introduction

Nature isn't classical, dammit, and if you want to make a simulation of nature, you'd better make it quantum mechanical, and golly it's a wonderful problem because it doesn't look so easy.

RICHARD P. FEYNMAN [1]

Simulating a complicated quantum system using another more controllable one is the core idea delivered by Richard Feynman in his seminal lecture "Simulating Physics with Computers" [1]. At first, the notion was a nice idea yet relatively impractical due to the lack of available quantum systems back in the days. With the technical and experimental breakthroughs in the last few decades, the engineering of quantum systems had changed from novel thought experiments to a reality happening in many laboratories across inter-disciplinary fields of physics. Implementation of quantum systems had been realised in an ever-increasing number of systems including, but not limited to, dilute ultracold atomic or molecular gases [2], trapped ions [3], superconducting qubits [4] and semiconductors quantum dot arrays [5]. These systems represent the state-of-the-art platforms ideal for carrying out quantum simulations originally put forth by Feynman. In particular, ultracold atomic gases are extremely suited for simulating problems in solid-state physics. The high degree of controllability allows the simulation of extreme parameter regimes previously not accessible in conventional solid materials. By creating the so-called "artificial solids", ultracold quantum gases significantly complement the study of natural condensed matter systems.

The simplest problem in condensed matter physics, yet still computationally too demanding for classical computers to solve, is the famous ***Hubbard model***. First introduced by J. Hubbard in 1963 in a series of papers, discussing electronic correlations in narrow-band materials [6–10], the Hubbard model had been the "hydrogen atom" analogue to atomic physics as in condensed matter physics. Based on the tight-binding approximation, the Hubbard model encapsulates the simple but subtle interplay of kinetic and interaction energy of electrons which are fermionic. The model, however, can be extended to describe interacting bosons in a periodic potential, in which case, is known as the Bose Hubbard model. Hereafter, we refer the fermionic version simply as the Hubbard model, in the spirit of Hubbard's original work.

The tremendous advances in cooling and trapping of atomic gases have led to the first realisation of Bose-Einstein condensate and degenerate Fermi gas [11–13]. Exceptional control of these quantum systems has since been extensively implemented and tested for the last decades such as coherent transfer between quantum states, controllable interaction via Feshbach resonance [14] and high-resolution (even site-resolved) imaging techniques [15]. The combinations of all such incredible techniques enable the various experimental investigations such as observing novel quantum phase transition of the superfluid to Mott-insulating phase in the Bose Hubbard model [16, 17], the realisation of the unitary regime of interacting Fermi gases [18], and realisation of artificial solids with novel geometries such as graphene-like structure [19]. These experiments demonstrate the versatility of ultracold quantum gases as a platform to investigate quantum mechanical problems that are hard to tackle otherwise.

In our experiment, we specifically investigate the two-dimensional Hubbard model using ultracold potassium ^{40}K atoms. The atomic vapours are brought down to quantum degeneracy temperature by a series of laser cooling and evaporative cooling. Using three dimensional, anisotropic optical lattices, we realised the spin-$1/2$ Hubbard model in two-dimensions using the lowest two hyperfine states as pseudospins. The first two following chapters outline the backbone of this thesis, namely the theoretical background and our experimental implementation of the two-dimensional Hubbard model.

- Chapter 2 presents an introduction of the Hubbard model, including several limiting pedagogical cases. The resulting phase diagrams are discussed. A brief introduction of engineering the Hubbard model with optical lattices and Feshbach resonances are presented as well. At last, the relevant numerical simulations utilised in this thesis are given for completeness.

- Chapter 3 details the experimental apparatus used in this thesis. Various cooling procedures are discussed, followed by the loading into optical lattices. The last section discusses the relevant detection techniques used.

For chapters which include the major experimental results, each chapter is written in the spirit of a stand-alone discussion involving the motivation, experimental techniques and measurement, and data analysis. An occasional back reference to the first two chapters are kept at minimal and only done so regarding the physical principles or specific experimental setup, in order to avoid frequent jumping while reading the thesis.

- Chapter 4 is dedicated to exploring the particle-hole symmetry of the Hubbard model. In particular, we experimentally verify the phase diagram mapping between repulsive and

attractive Hubbard systems.

- Chapter 5 details a novel scheme in coherently manipulating spin-spin correlations in the repulsive Hubbard model.
- Chapter 6 explores the pairing behaviour of the normal (non-superconducting) phase in the attractive Hubbard model.
- Chapter 7 includes a summary of the main scientific achievement in this thesis. An outlook for the future planned experimental endeavour is provided as well.

In chronological order, the following articles were published during the course of the thesis work, and will be covered in this thesis

- N. Wurz, **C. F. Chan**, M. Gall, J. H. Drewes, E. Cocchi, L. A. Miller, D. Pertot, F. Brennecke and M. Köhl, "Coherent manipulation of spin correlations in the Hubbard model", Physical Review A 97 (5), 051602 (2018)
- M. Gall, **C. F. Chan**, N. Wurz and M. Köhl, "Simulating a Mott insulator using attractive interaction", Phys. Rev. Lett. 124 (1) 010403 (2020)
- **C. F. Chan**, M. Gall, N. Wurz and M. Köhl, "Pair correlations in the attractive Hubbard model", accepted for publication in Phys. Rev. Research. (2020)

Furthermore, the author also contributed to the following articles, which are related to the work presented in this thesis but not included as significant portions of the thesis.

- E. Cocchi, L. A. Miller, J. H. Drewes, **C. F. Chan**, D. Pertot, F. Brennecke and M. Köhl, "Measuring entropy and short-range correlations in the two-dimensional Hubbard model", Physical Review X 7 (3), 031025, (2017)
- J. H. Drewes, L. A. Miller, E. Cocchi, **C. F. Chan**, D. Pertot, F. Brennecke, and M. Köhl, "Antiferromagnetic correlations in two-dimensional fermionic Mott-insulating and metallic phases", Physical review letters, 118 (17) 170401 (2017)
- J. H. Drewes, E. Cocchi, L. A. Miller, **C. F. Chan**, D. Pertot, F. Brennecke and M. Köhl, "Thermodynamics vs. local density fluctuations in the metal/Mott-insulator crossover", Physical review letters 117 (13), 135301, (2016)

CHAPTER 2

Introduction to the Hubbard Model

The simplicity of the Hubbard model, when written down, is deceptive.

"THE HUBBARD MODEL AT HALF A CENTURY" [20]

In pursuit of a quantum simulator to model complex problems in solid-state physics, we motivate the study of the Hubbard model, which captures the essential interplay between kinetic energy and interaction. A brief overview of the Hubbard model in connection to solid-state physics is given. Then, we introduce several exactly solvable cases of the model under certain limiting conditions. We then proceed to discuss the rich phase diagrams encapsulated in the Hubbard model. We also discuss the implementation of the Hubbard model with ultracold atomic gases in optical lattices. Finally, we outline several numerical approach in solving the Hubbard model, which we used to benchmark with experimental data throughout this thesis.

2.1 The Hubbard model

This section is dedicated to an introduction to the Hubbard model. We begin with an outline of the many-body Hamiltonian of interacting fermions in a periodic lattice potential. We then show that by motivating the second quantisation, and allowing only ***nearest-neighbour hopping*** and ***on-site interaction***, the many-body Hamiltonian can be cast into a compact form.

From single-particle to many-body The behaviour of a single, non-relativistic particle can be studied by the ***time-independent*** Schrödinger equation as follow

$$\hat{H}\psi = E\psi, \tag{2.1}$$

where $\hat{H}$ is the Hamiltonian operator and ψ is the wavefunction describing the particle. For a single particle, $\hat{H}$ can be written as the sum of kinetic and the potential energy,

$$\hat{H} = -\frac{\hbar^2}{2m}\nabla^2 + V(\boldsymbol{r}), \tag{2.2}$$

where $\hbar$ is the Plank's constant, m is the particle mass and $V(\boldsymbol{r})$ is the potential energy. In essence, Eq. (2.2) can be cast into an eigenvalue problem in linear algebra where the matrix is the Hamiltonian projected by the basis states. The solution (eigenfunctions) describes travelling wave-packet in certain potential (In the similar way a water wave travelling in a pond with spatially varying depths), whereas the eigenvalue E is related to the the ***phase velocity*** of the wave-packet.

For a general N-particle ***many-body*** problems, however, the Hamiltonian becomes increasingly hard to solve due to the exponential scaling of the Hilbert space. To further complicate the problem, quantum statistics arising from the inherent indistinguishability of particles affect the symmetry of the wavefunctions. Particles with an even symmetry under exchange of identical particle are called ***bosons***. On the other hand, particles that are anti-symmetric are known as ***fermions***. Electrons, with its fermionic nature, carry an intrinsic angular momentum know as *spin*. In solid materials, the typical external potential is periodic, *i.e.* $V(r) = V(r + a)$ where a is periodicity of the lattice. A many-body Hamiltonian for electrons in solids can be written as in general as

$$\hat{H} = \underbrace{\sum_i^N \left(-\frac{\hbar^2}{2m}\nabla_i^2 + V_i\right)}_{=\hat{T}} + \underbrace{\frac{1}{2}\sum_{i\neq j}^N U_{ij}}_{=\hat{U}}. \tag{2.3}$$

Here, $\hat{T}$ contains the same single particle energy in Eq.(2.2) and $\hat{U}$ describes the inter-particle interaction energy. The first term in $\hat{T}$ describes the kinetic energy of individual particles. The second term is a result of the potential landscape in which particles are subjected to. For interacting electrons in solid, the potential is given by the electron-nucleus attractive potential as shown in Fig. 2.1 **a**. In the context of this thesis, we consider ultracold fermionic atoms trapped in an optical lattice, and this potential energy term corresponds to sinusoidal optical potential, as shown Fig. 2.1 **b**.

The "elephant in the room", however, is the interaction term U_{ij}. In solid, this is dominantly caused by the electron-electron Coulombic repulsion since the electron-nuclei interaction can be separated

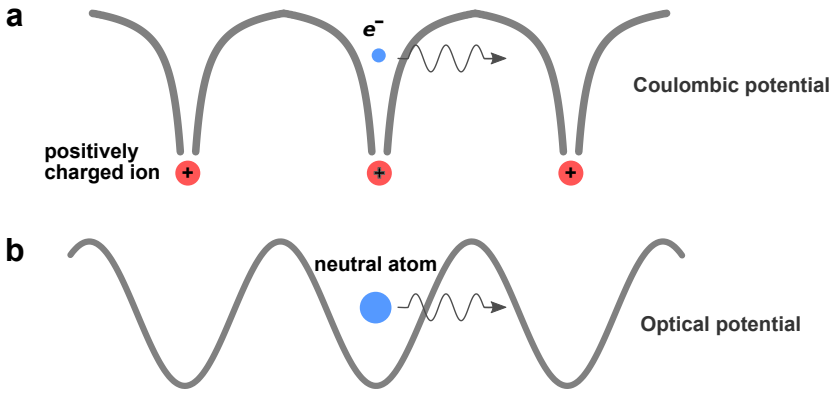

Figure 2.1: **Electrons in solid and atoms in optical lattice. a.** For electrons in solid, the periodic potential is provided by the Coulombic electron-nucleus attraction. **b** For neutral atoms trapped in an optical lattice, the constructive interference of far-off resonant laser light creates a sinusoidal standing wave pattern. This then induces a intensity-dependent energy shift, resulting in an optical trapping potential.

due to the large difference in mass scales.[1] Due to the two-particle nature of U_{ij}, the motion of one particle affects that of another one. In other words, the behaviours of particles are *correlated*. The presence of correlations in quantum systems often forbids a simple solution (*i.e.* separable solution), and approximate solutions typically work only in the weakly-correlated regime.

Second quantisation Using the framework of ***second quantisation***, we deploy a set of localised *Wannier states* as basis. As will be shown in later section, by exact digonalisation, the energy dispersion in a periodic potential can be solved as energy bands (see Sec. 2.4.1). And the Wannier basis can be constructed as a superposition of the eigenfunctions (Bloch waves). Thus we construct the fermionic field operator

$$\hat{\psi}_i^\dagger = w(\mathbf{r} - \mathbf{r}_i)\hat{c}_i^\dagger, \tag{2.4}$$

and its Hermitian conjugate. Here we have,

$$\psi_i(\mathbf{r}) = \langle \mathbf{r}|\psi_i\rangle = \langle \mathbf{r}|\hat{\psi}_i^\dagger|vac\rangle = w(\mathbf{r} - \mathbf{r}_i). \tag{2.5}$$

In the following derivation, we assume the only the lowest energy band is occupied, which allow us to exclude the possibility of having two distinct localised states in a single site. With the notations set, we can rewrite Eq.(2.3) into its second quantised form.

Tunnelling matrix element The single-particle term $\hat{T}$ can be written as the following

$$\hat{T} = \sum_{i,j}\langle\psi_j|\hat{T}|\psi_i\rangle\hat{c}_i^\dagger\hat{c}_j = \sum_{i,j} T_{ij}\hat{c}_i^\dagger\hat{c}_j, \tag{2.6}$$

where the matrix element T_{ij} is given by

$$T_{ij} = \int d^3\boldsymbol{r}\psi_j^*(\boldsymbol{r})\left(-\frac{\hbar^2}{2m}\nabla_i^2 + V_i(\boldsymbol{r})\right)\psi_i(\boldsymbol{r}) = \begin{cases} E_i, & \text{if } i = j \\ -t_{ij}, & \text{otherwise.} \end{cases} \tag{2.7}$$

[1] This is known as the ***Born-Oppenheimer approximation*** [21].

The integral in Eq.(2.7) can be solved in two cases. For $i = j$, and T_{ii} gives the on-site energy E_i, which describes the energy of a single particle at site i arisen from the single-particle potential $V(\boldsymbol{r})$. Since both the ∇^2 operator and $V(\boldsymbol{r})$ are translational invariant, E_i results in an offset energy for a homogeneous system. In optical lattices the potential landscape V_i is spatially-dependent due to intensity variation. The on-site energy E_i thus varies accordingly and constitutes an harmonic confinement. The difference in E_i between two thermally-equilibrated spatial regions are compensated by the local chemical potential.

For $i \neq j$, the matrix element corresponds to a ***tunnelling*** event, where a finite value of T_{ij} means there is finite probability that a state localised in site i can be coupled to another state localised at site j.[2] Fig. 2.2 **a** depicts the overlap of two Wannier functions localised at a neighbouring site. It is apparent that for wavefunction separated with larger distance, the overlap matrix element decreases. In addition, the tunnelling amplitude reduces as the potential well of individual site deepens and the wavefunction becomes more localised.

Interaction Next, we turn to the interaction term. Following a similar procedure, we arrive at

$$\hat{U} = \sum_{i,i',j,j'} U_{ij}^{i'j'} \hat{c}_i^\dagger \hat{c}_{i'}^\dagger \hat{c}_j \hat{c}_{j'}, \tag{2.8}$$

where the matrix elements reads

$$U_{ij}^{i'j'} = \langle \psi_j, \psi_{j'} | \hat{U} | \psi_i, \psi_{i'} \rangle = \int d^3\mathbf{r} d^3\mathbf{r}' \psi_j^*(\mathbf{r}) \psi_{j'}^*(\mathbf{r}') \left(\frac{1}{2} U_{ii'} \right) \psi_i(\mathbf{r}) \psi_{i'}(\mathbf{r}'). \tag{2.9}$$

Here, $U_{ij}^{i'j'}$ describes the interaction between particles with spin σ and σ'. We note that for particles with the same spin, the interaction is effectively zero due to the Pauli exclusion principle (See Sec. 2.4.2). In Fig. 2.2 **b**, we depict the overlap of two particle's wavefunction which results in interaction energy U between two particles. Here we assume a short-range interaction such that the dominant effect happens for particles at the same lattice site.

Hubbard Hamiltonian So far Eq. (2.7) and Eq.(2.9) are general description that include various kinds of tunnellings and two-body interactions. The Hubbard model significantly simplies these relations by introducing two approximations. The first approximation the *tight-binding approximation* is to only near-neighbour tunnelling, therefore

$$t_{ij} \rightarrow t_{i,j} \delta_{i,i+1}. \tag{2.10}$$

It is straight-forward to observe that the Wannier functions, as shown in Fig. 2.2 **a**, when separated at larger distance, the tunnelling matrix element t_{ij} decreases in magnitude. In Sec. 2.4.1, we will see that the tunnelling can be restricted to near-neighbour term by ramping the lattice depth.

The second approximation is to restrict interaction to local sites, such that

$$U_{i,j}^{i',j'} \rightarrow U_i. \tag{2.11}$$

[2] For convenience, we explicitly put a minus sign in front of t_{ij} in Eq. (2.7) since the tunnelling delocalises the particle wavefunctions and lower the energy.

Interaction localised at a single-lattice site is called the ***on-site*** interaction. Similar to the tight-binding approximation, this is justified by the decreasing overlap of the wavefunctions at a larger distance. In addition, in cold atomic gases, the scattering of particles is characterised by a short-range contact potential $U \propto \delta(\boldsymbol{r})$, which makes the longer-range interaction negligible.[3]

By invoking the above approximations, we now formally state the single-band ***Hubbard Hamiltonian*** as

$$\hat{H} = -t \sum_{\langle i,j\rangle,\sigma} \left(\hat{c}^{\dagger}_{i,\sigma}\hat{c}_{j,\sigma} + h.c.\right) + U \sum_{i} \left(\hat{n}_{i,\uparrow} - \frac{1}{2}\right)\left(\hat{n}_{i,\downarrow} - \frac{1}{2}\right) - \mu \sum_{i,\sigma} \hat{n}_{i,\sigma}\,, \tag{2.12}$$

where t is the tunnelling amplitude an $h.c.$ refers to the Hermitian conjugate, U is the on-site interaction energy between spin-up and spin-down fermions and μ is the chemical potential. For now, the chemical potential μ is understood by re-writing the on-site energy $E_i = \mu$ in Eq. (2.7).

Analogous to the role of the hydrogen atom in atomic physics, the Hubbard model is the simplest model which describe the interplay of kinetic energy (hopping term) and interaction in a lattice. In Fig. 2.2 **c**, we show the interplay of kinetic and interaction energy of the two-dimensional Hubbard model in a square lattice. As we will see, this is a minimal model of a strongly-correlated many-body system with density- and spin-ordering. Despite its theoretical simplicity, the Hubbard model has only been solved with exact solution in one-dimension [22–24]. The Hilbert space grows exponentially with particle numbers, implying that numerically approach to the problem is NP-hard [25]. This offers a perfect opportunity for analogue quantum simulation experiments to investigate these theoretically intractable problems.

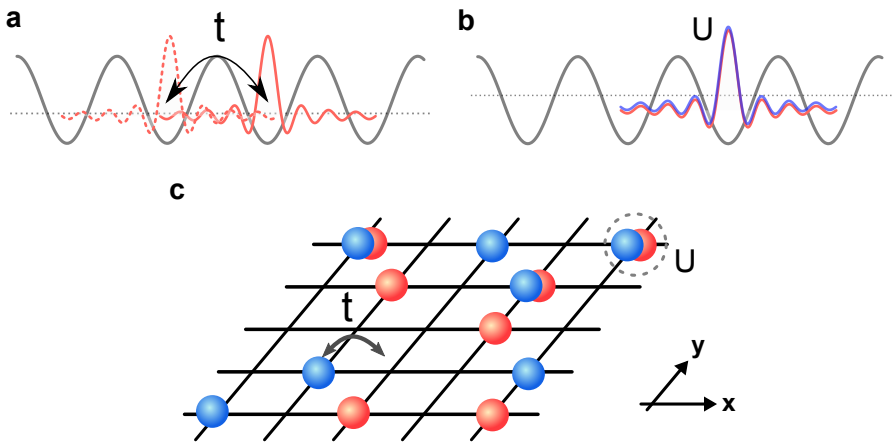

Figure 2.2: **Recipe of the Hubbard model.** **a** Tunnelling. Due to finite overlap between wavefunctions localised at neighbouring sites, fermion can hop between from one site to another. This hopping event encapsulates the single-particle kinetic energy and potential energy, as shown in Eq. (2.7). **b** On-site interaction. For two fermions with opposite spins at the same lattice site, the scattering between them leads to an energy shift U. If U is positive (negative), the interaction is repulsive (attractive). **c** Schematic representation of the two-dimensional Hubbard model. The combination of quantum mechanical tunnelling and on-site interaction constitutes the Hubbard model. Throughout this thesis, the core investigation centres at the two-dimensional lattice. Two types of coloured spheres represent the two fermionic spins.

[3] For neutral atoms such as erbium and dysprosium, the large magnetic dipole moments allow long-range dipole-dipole interaction.

2.2 Limiting cases

We introduce the exact solutions of the Hubbard model under several limiting conditions. By combining the non-interacting limit and the atomic limit, we qualitatively show that the important phases in the Hubbard model with dominated kinetic or interaction terms. For simplicity, we first focus on repulsive interaction and later generalise to attractive interaction. In addition, in the two-site limit, the Hubbard model constitutes a double-well problem and offers the minimal toy model for spin ordering state. This will prepare the reader for the many-body phase diagrams of the Hubbard model in the following section.

2.2.1 Non-interacting

The simplest case for the Hubbard model is the ***non-interacting*** limit, at which $U = 0$ in Eq.(2.12). This reduces the Hamiltonian to

$$\hat{H} = -t \sum_{\langle i,j\rangle,\sigma} \left(\hat{c}^{\dagger}_{i,\sigma} \hat{c}_{j\sigma} + h.c. \right) - \mu \sum_{i,\sigma} \hat{n}_{i,\sigma}. \tag{2.13}$$

This is known as the ***tight-binding model***, at which particles are only allowed to delocalise via nearest-neighbour tunnelling. In this section, we focus on the one-dimensional case, and we note that the two- and three-dimension follow a similar derivation procedure. The tight-binding Hamiltonian can be easily solved via Fourier transform from discrete position space to the discrete momentum space. We note that the Fourier transform of the fermionic operators read

$$\begin{aligned} \hat{c}_{k,\sigma} &= \frac{1}{\sqrt{L}} \sum_{i=1}^{L} \hat{c}_{i,\sigma} e^{ikx_i} \\ \hat{c}^{\dagger}_{k,\sigma} &= \frac{1}{\sqrt{L}} \sum_{i=1}^{L} \hat{c}^{\dagger}_{i,\sigma} e^{-ikx_i}, \end{aligned} \tag{2.14}$$

where we can choose a discrete set of $k = m\frac{2\pi}{La}$ and m is an integer. We note that k is confined in the reciprocal lattice space due to the discrete nature of the basis. One convenient choice of the reciprocal lattice space is the so called 1$^{\text{st}}$ ***Brillouin zone***, *i.e.* $k \in [-\pi/a, \pi/a)$. The leads to $-L/2 \leq m < L/2$ in order to have L discrete momentum states. It can be easily shown that $c_{i,\sigma} = \frac{1}{\sqrt{L}} \sum_k c_{k,\sigma} e^{-ikx_i}$ (same for the Hermitian conjugate). Substituting this into the Hamiltonian, the tunnelling term transforms as

$$\begin{aligned} -t \sum_{i,\sigma} \hat{c}^{\dagger}_{i,\sigma} \hat{c}_{i+1,\sigma} + h.c. &= -t \sum_{kk',\sigma} \hat{c}^{\dagger}_{k,\sigma} \hat{c}_{k',\sigma} e^{-ik'a} \underbrace{\frac{1}{L} \sum_{i} e^{i(k-k')x_i}}_{=\delta_{kk'}} \\ &= -t \sum_{k,\sigma} \left(e^{ika} + e^{-ika} \right) \hat{c}^{\dagger}_{k,\sigma} \hat{c}_{k,\sigma} = \sum_{k,\sigma} -2t \cos(ka)\, \hat{c}^{\dagger}_{k,\sigma} \hat{c}_{k,\sigma}, \end{aligned} \tag{2.15}$$

where a is the lattice spacing. It is straight-forward to show that the chemical potential term is diagonal in both position and momentum space. To this end, we obtain

$$\hat{H} = \sum_{k,\sigma} (\varepsilon_k - \mu)\, c^{\dagger}_{k,\sigma} c_{k,\sigma}. \tag{2.16}$$

Here, $\varepsilon_k = -2t\cos(ka)$ is the tight-binding dispersion relation. One immediate observation about Eq.(2.16) is that it is diagonal, therefore the eigenstates are well-defined momentum states k with energy ε_k. From Eq. (2.15), we can define the ***bandwidth*** W of the energy dispersion as the maximum spread in energy, *i.e.* $W = 4t$ as shown in the left plot of Fig. 2.3. In a general N-dimensional hypercubic lattice, the bandwidth is given by $W = 4Nt$.[4] To understand the ground state and the excited state, we deploy the ***Fermi-Dirac*** distribution, which is given by

$$f_{\mathrm{FD}}(\varepsilon, T) = \frac{1}{e^{\frac{\varepsilon - \varepsilon_F}{k_B T}} + 1}. \tag{2.17}$$

Here, ε_F is the Fermi energy, k_B is the Boltzmann constant and T is the temperature of the system. At $T = 0$, the Fermi-Dirac distribution is step-function around $\varepsilon = \varepsilon_F$, *i.e.*

$$f_{\mathrm{FD}}(\varepsilon, T = 0) = \Theta(\varepsilon - \varepsilon_F), \tag{2.18}$$

where $\Theta(\varepsilon - \varepsilon_F)$ is a Heaviside function. For $\varepsilon < \varepsilon_F$ the probability of occupying the energy state is unity, whereas for $\varepsilon > \varepsilon_F$ the probability of occupying the energy state is zero. The Fermi-Dirac distribution is depicted for zero temperature and finite temperature in Fig. 2.3 **a** and **b** respectively. The ground state of the N-particle system in a lattice is a fully-filled ***Fermi sea*** and can be written as

$$|GS\rangle = \prod_{k,\sigma}^{|\varepsilon(k)|<\varepsilon_F} c^{\dagger}_{k,\sigma} |0\rangle. \tag{2.19}$$

The Fermi energy $\varepsilon_F = \hbar^2 k_F^2 / 2m$ is normalised with respect to the total particle number N ,

$$\int_{-\infty}^{\infty} f_{\mathrm{FD}}(\varepsilon, T) d\varepsilon = N. \tag{2.20}$$

Therefore, the corresponding Fermi wavevector k_F sets the end-points in the dispersion, as shown in Fig. 2.3 **a**. The two endpoints enclosing the Fermi sea is know as the ***Fermi-points*** and can be generalised to a ***Fermi surface*** in higher dimensions. At finite temperature $T > 0$, the Fermi-Dirac distribution "melts down", such that there is a finite probability of occupying the energy states with energy above ε and the probability of occupying state below ε reduces accordingly. The thermally excited state, as a result, can be treated as a particle-hole excitation with respect to the Fermi sea.

Metal and band insulator In a lattice configuration, a natural constraint to the many-body state is the total particle number N due to the limited number of sites. For a lattice with L sites, the maximum number of fermions allowed is $N = 2L$ due to the two spin components.[5] By varying the particle numbers, the system exhibits three different physical phases. The first is when $N = 0$ and the

[4] A hypercubic lattice with $N = 2$ is a square lattice; with $N = 3$ is a simple-cubic lattice.

[5] We recall that we work in the single-band limit and thus this constraint changes when the multi-band effect is considered.

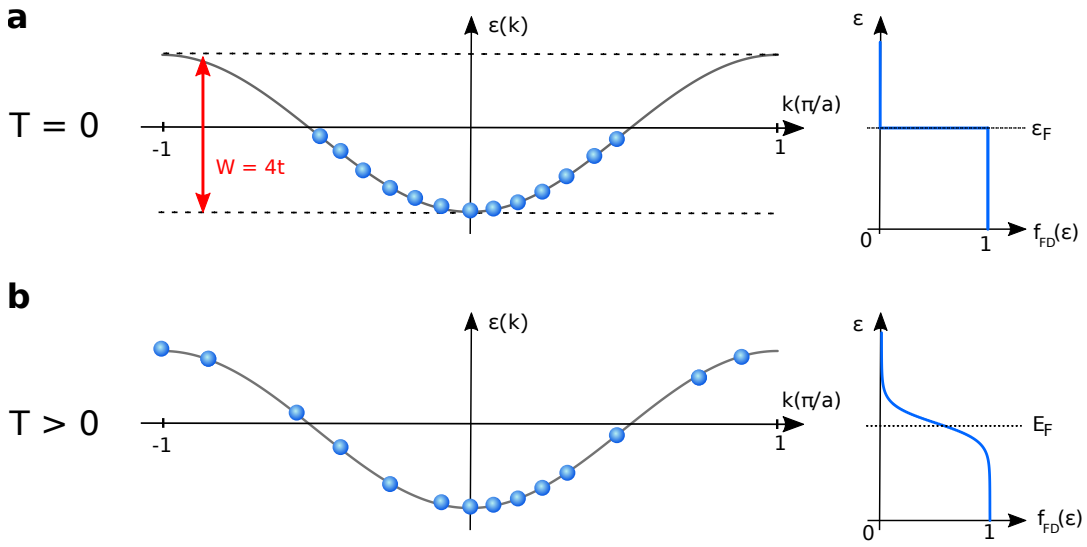

Figure 2.3: **Non-interacting lattice : ground state and excited state.** In one dimension, the energy dispersion follows a sinusoidal form as in Eq. (2.15) with bandwidth $W = 4t$. **a** At $T = 0$, energy states below the Fermi energy ε_F is fully filled and the energy state above ε_F is empty. The left column shows the energy dispersion and momentum occupation. The right column display the Fermi-Dirac distribution at ground state and excited state. **b** At $T > 0$, the Fermi-Dirac distribution "melts down", indicating that energy states within the Fermi sea have finite probability to be excited above the Fermi sea due to thermal effect.

system is a trivial vacuum state. For $0 < N < 2L$, the system is in the so-called ***metallic*** phase. In the absence of the interaction, momentum states are allowed to traverse within the energy band under an external force [6], therefore coined by the term "metal" with respect to metallic conductors. We note that the conducting nature of such metallic phase is more complicated than simple vacancies in the dispersion relation. This conducting feature is a transport phenomenon and can be linked to the non-zero isothermal compressibility and related density-density correlations, which we study in Chapter 4 and 6 respectively. Even for non-interacting fermions in a lattice, the compressibility is subjected to the Pauli exclusion principle and exhibits a non-trivial density dependence.

Finally, for $N = 2L$, the entire energy band are fully-filled, and the system enters the ***band-insulating*** phase due to the absence of mobile energy states. In addition, we note that temperature effect becomes irrelevant in this case since the Fermi energy lies above the entire energy dispersion. In the full multi-band treatment, the band insulator is caused by the large inter-band energy gap, hence the name band insulator. In contrast to the metallic phase, the band insulator exhibits a suppression in the isothermal compressibility. Another important feature of the band insulator is that it exhibits in principle zero entropy. This can be readily understood by considering the Gibbs entropy,

$$S = -k_B \sum_i p_i \log p_i. \tag{2.21}$$

Here, the summation is over all possible microstates i and p_i is the probability of occupying the microstate. In a band insulator, only one microstate of fully-filled lattice is allowed, therefore $S = -k_B \cdot 1 \cdot \log 1 = 0$. In Chapter 7, we discuss potential aspects of utilising this ultralow entropy

[6] An applied force leads to Bloch oscillation within the 1st Brillouin zone. For solid-state metallic material, thermal effects quickly dephase the oscillation. In ultracold atomic system, however, long-lifetime coherent Bloch oscillation has been observed in both momentum and position spaces [26, 27].

feature to implement novel cooling scheme of squeezing entropy out of the atomic ensembles to metallic particle reservoirs.

2.2.2 The atomic limit

Switching to the opposite side of the non-interacting limit, one arrives at the so-called ***atomic limit***, also known as the strong coupling regime, where the interaction is much greater than the kinetic term, *i.e.* $|U| \gg W \propto t$. In this case, the tight-binding dispersion can be separated into two bands, one of which corresponds to singly-occupied site band where only on particle stay in a well, anther one with doubly-occupied site thereby with additional interaction shift in energy. For repulsive interactions, the doubly-occupied is energetically unfavourable and is shifted up in energy by U. The energy gap between the singly and doubly-occupied states is an example of ***density ordering***.

Mott insulator Since U is the dominant energy scale in the atomic limit, we deploy the so-called Hubbard band picture. To demonstrate, we start by considering two Hubbard bands with varying particles number N at the ground state. The lower Hubbard band (LHB) corresponds to states at which only one particle sits in the lattice site, also known the singly-occupied state. On the other hand, the upper Hubbard band corresponds to two particles with opposite spin sit in the same site, also known as the doubly-occupied state. Here, we defined the ***filling*** of the system as $n = N/L$, where L is the number of lattice sites. As shown in Fig. 2.4 **a** and **b**, $n = 0$ is the typical and $n < 1$ we have the trivial vacuum state and metallic phase respectively. One crucial case to study is the half-filled case, where on average there is one particle per lattice site, *i.e.* $n = 1$. In this case, the system enters the ***Mott insulating*** phase. One distinction between a Mott insulator and a band insulator is that the former is caused by interaction effect, whereas the latter is induced by the large energy gap to the next available energy band. Therefore, the energy gap induced by the interaction U is also known as the ***Mott*** gap. Similar to the band insulator, the insulating feature of a Mott insulator can be observed from the suppression in compressibility. The Mott insulator supports a much richer phase diagram compared to the band insulator where all correlations are suppressed despite its ultralow entropy profile. For instance, there exists additional ***spin ordering*** in a Mott insulating phase, which supports a long-range ordered phase in the ground state. In Sec. 2.2.3 , we discuss the origin of such magnetic nature. And in chapter 5, we discuss the full experimental measurement of spin correlations in our quantum gases experiment.

The single-site limit One can show that the atomic limit in a single lattice site ($t = 0$) is consistent with the Hubbard band picture. In Fig. 2.5 **a**, we show the four possible Fock states in a single lattice site, namely the empty state $|0\rangle$, singly-occupied state for both spins $|\uparrow\rangle$ and $|\downarrow\rangle$, and the doubly-occupied state $|\uparrow\downarrow\rangle$. Each of them, in the single-site limit, is an eigenstate of the Hubbard Hamiltonian $\hat{H}$ with energy $U/4$, $-U/t - \mu$, $-U/t - \mu$ and $U/4 - 2\mu$ respectively. Therefore, we can write down the partition function[7] Z

$$Z = \mathrm{Tr}\left[e^{-\beta\hat{H}}\right] = e^{-\beta U/4} + 2e^{-\beta(-U/4-\mu)} + e^{-\beta(U/4-2\mu)}. \tag{2.22}$$

[7] Here, a canonical ensemble is assumed and thus the chemical potential is a fixed parameter. The use of grand-canonical ensemble would result in the same partition function in which μ is the result of thermal equilibrium between two particle reservoirs.

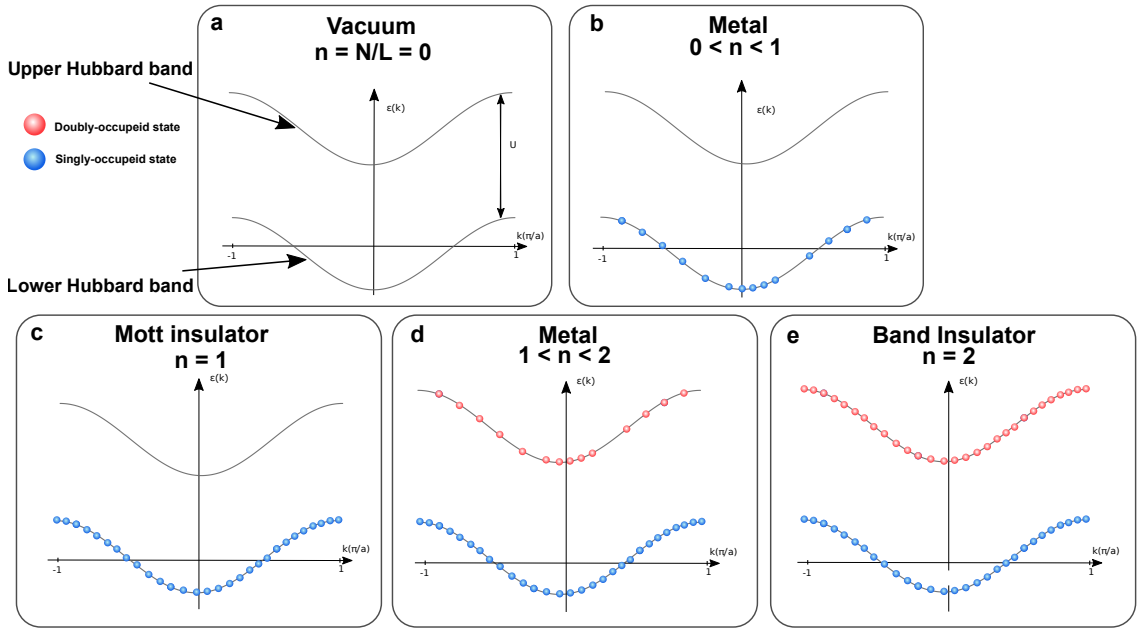

Figure 2.4: **Hubbard band picture in the atomic limit. a** For $n = 0$, no energy state is filled, which represents a vacuum state. **b** For $0 < n < 1$, only the lower Hubbard band (LHB) is filled, and particles can traverse within the band under external force, resulting in a metallic phase. **c** For $n = 1$, the LHB is completely filled, and the next available energy state is gapped by the interaction U. This results insulating behaviour and the phase is known as the Mott insulator. **d** Above half-filling $n > 1$, the upper Hubbard band (UHB) starts to be occupied, and the energy cost to excite the system to higher energy state is no longer gapped. The system therefore returns to the metal phase. **e.** For $n = 2$, both the LHB and UHB are fully filled. Particles are no longer mobile and the system is a band insulator.

Here $\beta = k_B T$ is the inverse temperature. Then, one can compute the average particle occupation $\langle \hat{n} \rangle$ as

$$\langle \hat{n} \rangle = \left\langle \hat{n}_\uparrow + \hat{n}_\downarrow \right\rangle = \frac{1}{Z} \mathrm{Tr} \left[\left(\hat{n}_\uparrow + \hat{n}_\downarrow \right) e^{-\beta \hat{H}} \right] = \frac{1}{Z} \left(2e^{-\beta(-U/4-\mu)} + 2e^{-\beta(U/4-2\mu)} \right) . \tag{2.23}$$

In Fig. 2.5, we plot the occupation $\langle \hat{n} \rangle$ of a single site Hubbard model as a function of chemical potential μ and for different temperatures. Here, we note that the chemical potential μ takes the role of adjusting particle number. To this end, varying μ is equivalent to shifting the overall energy dispersion with respect to the Fermi-Dirac distribution, thereby changing the particle numbers N.[8] Throughout this thesis, we use the notation at which $\mu = 0$ corresponds to the half-filled case, where the average site occupation is one particle per site. In general, for $\mu \ll 0$, the occupation is close to zero, indicating the vacuum state. As μ increases, the occupation also increases accordingly and enters the metallic phase.

Near $\mu = 0$, $\langle \hat{n} \rangle \sim 1$ and the occupation shows a ***Mott plateau***. Upon lowering temperature T, the Mott plateau becomes more significant due to reduced thermal fluctuations. The energy spacing indicated by the red arrow is the Mott gap. When μ increases further beyond the half-filling point,

[8] The reverse statement about N fixes the chemical potential is equivalently true since both of them stems from the normalisation condition in Eq. (2.20).

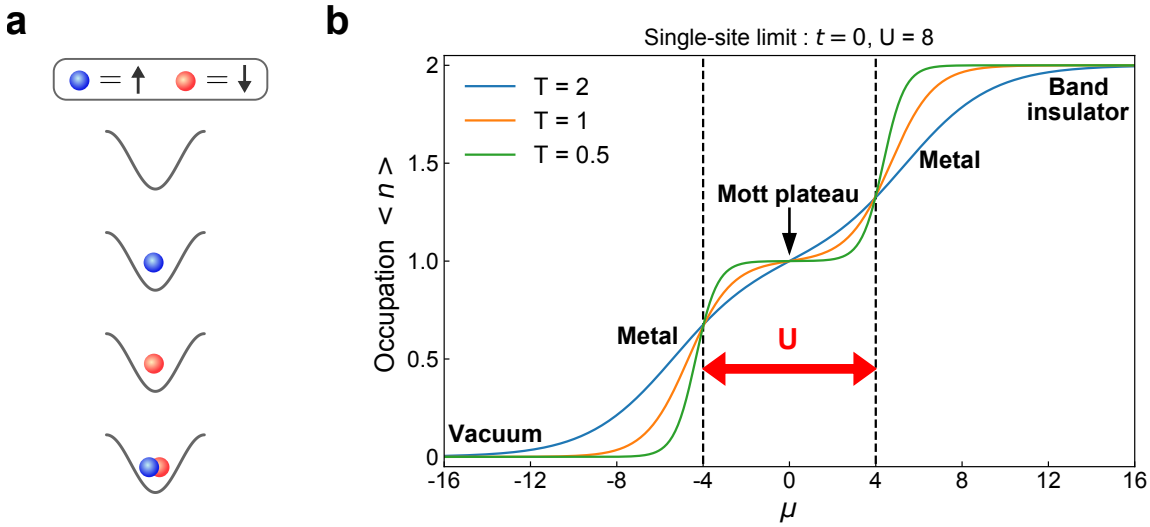

Figure 2.5: **Repulsive Hubbard model in a single site.** **a** Four possible states in the single-site Hubbard model : empty site, spin-up occupied, spin-down occupied and doubly-occupied state. **b** Occupation $\langle n \rangle$ as a function of chemical potential μ and T. Near $\mu = 0$, the Mott insulating phase with repulsive interaction opens up an energy gap against density excitation and is signalled by the appearance of a Mott plateau.

the system re-enters into a metallic phase and finally reaches the band insulator state when $\mu \gg 0$, at which the average occupations is two (fully-filled). The behaviour of the Hubbard system to traverse from a metallic phase to Mott insulator is called the ***metal/Mott-insulator crossover*** [28]. It should be noted that this is a distinct feature of the Hubbard model with fermions. For the Bose Hubbard model, the system instead exhibits a Mott-insulator-to-superfluid quantum phase transition, where the superfluid coherence is the order parameter [16, 29].

2.2.3 Two site Hubbard model : toy model for quantum magnetism

The Hubbard double well at half-filling After discussing the two limiting cases at which either the kinetic term or the interaction term dominates the physical behaviours, we now move onto investigating the competition between two terms. One common pedagogical example is the two-site Hubbard model, where the Hilbert space is still small enough to handle analytically. The maximum atom number in a Hubbard double-well is limited to 4. More importantly, the Hilbert space can be further subdivided into subspaces according to total atom number. We restrict the discussion to the half-filled case in which there is exactly one spin-up and spin-down component, *i.e.* $N_\uparrow = N_\downarrow = 1$. We can then project the Hamiltonian in the basis of $|\uparrow,\downarrow\rangle$,$|\downarrow,\uparrow\rangle$,$|\uparrow\downarrow,0\rangle$ and $|0,\uparrow\downarrow\rangle$, where the first (second) quantum number represents the occupations in the left (right) site. We note that the Fock states with well defined particle number are in general not eigenstates. We write the Hubbard Hamiltonian in Eq. (2.12) as

$$H = \begin{pmatrix} -U/2 & 0 & -t & -t \\ 0 & -U/2 & t & t \\ -t & t & U/2 & 0 \\ -t & t & 0 & U/2 \end{pmatrix} - 2\mu\, \mathbb{1}_{4\times4}. \tag{2.24}$$

Again, we set $\mu = 0$ for simplicity. The Hamiltonian can be diagonalised and the explicit eigenenergies, in ascending order, are given by

$$\begin{aligned} \varepsilon_a &= -\frac{1}{2}\left(\sqrt{16t^2 + U^2}\right), \\ \varepsilon_b &= -\frac{U}{2}\ ,\ \varepsilon_c = \frac{U}{2} \\ \text{and}\quad \varepsilon_d &= \frac{1}{2}\left(\sqrt{16t^2 + U^2}\right). \end{aligned} \tag{2.25}$$

And the corresponding eigenstates are given by

$$\begin{aligned} \phi_a &= \frac{1}{\sqrt{2}} \frac{(|\uparrow,\downarrow\rangle - |\downarrow,\uparrow\rangle) - \frac{U+2\varepsilon_a}{4t}(|\uparrow\downarrow,0\rangle + |0,\uparrow\downarrow\rangle)}{\sqrt{1 + \left(\frac{U+2\varepsilon_a}{4t}\right)^2}}, \\ \phi_b &= \frac{1}{\sqrt{2}}(|\uparrow,\downarrow\rangle + |\downarrow,\uparrow\rangle),\ \phi_c = \frac{1}{\sqrt{2}}(|\uparrow\downarrow,0\rangle - |0,\uparrow\downarrow\rangle), \\ \text{and}\quad \phi_d &= \frac{1}{\sqrt{2}} \frac{(|\uparrow,\downarrow\rangle - |\downarrow,\uparrow\rangle) - \frac{U+2\varepsilon_d}{4t}(|\uparrow\downarrow,0\rangle + |0,\uparrow\downarrow\rangle)}{\sqrt{1 + \left(\frac{U+2\varepsilon_d}{4t}\right)^2}}. \end{aligned} \tag{2.26}$$

The eigenenergies are plotted as a function of interaction U in Fig. 2.6. One immediate observation from Eq. (2.26) is that ϕ_b and ϕ_c are independent of interaction. This is because both of them contains no admixing between singly- and doubly-occupied state. As a result their eigenenergies follow a simple linear dependence to U. For ϕ_a and ϕ_d, the eigenstate contains a superposition of singly- and doubly-occupied states, weighted by interaction-dependent coefficients. This implies that in the ground state of double-well with finite repulsive interaction U, there is always a finite double occupancy. This is in stark contrast to the atomic limit at which the double occupancy is zero at half-filling $n = 1$ (see Fig. 2.4 **c**).

Next, we focus on the strongly repulsive case $U \gg t$. One can immediately observe that the eigenstates can be classified into two classes, one with large negative energies and one with large positive energies. This coincides with Hubbard band picture previously discussed. To obtain further insight into properties of the low-energy states, we treat the energy states in the lower Hubbard band as isolated two-level system (see dotted black circle in Fig. 2.6 **b**), and write down eigenstates and eigenenergies

$$\begin{aligned} \phi_a &\approx \frac{1}{\sqrt{2}}(|\uparrow,\downarrow\rangle - |\downarrow,\uparrow\rangle) \ \text{ and } \ \phi_b = \frac{1}{\sqrt{2}}(|\uparrow,\downarrow\rangle + |\downarrow,\uparrow\rangle). \\ \varepsilon_a &\approx -U - \frac{4t^2}{U} \ \text{ and } \ \varepsilon_b = -U. \end{aligned} \tag{2.27}$$

We can see that the ground state ϕ_a reduces to an anti-symmetric superposition of $|\uparrow,\downarrow\rangle$ and $|\downarrow,\uparrow\rangle$. This is also known as a ***spin-singlet*** state because the total spin angular momentum $\langle S\rangle = 0$. On the other hand, the higher energy state ϕ_b is a symmetric superposition of $|\uparrow,\downarrow\rangle$ and $|\downarrow,\uparrow\rangle$. And it is called the ***spin-triplet*** state since $\langle S\rangle = 1$.[9] The energy difference between the singlet and triplet

[9] We note that the other two higher energy states are also spin-triplets.

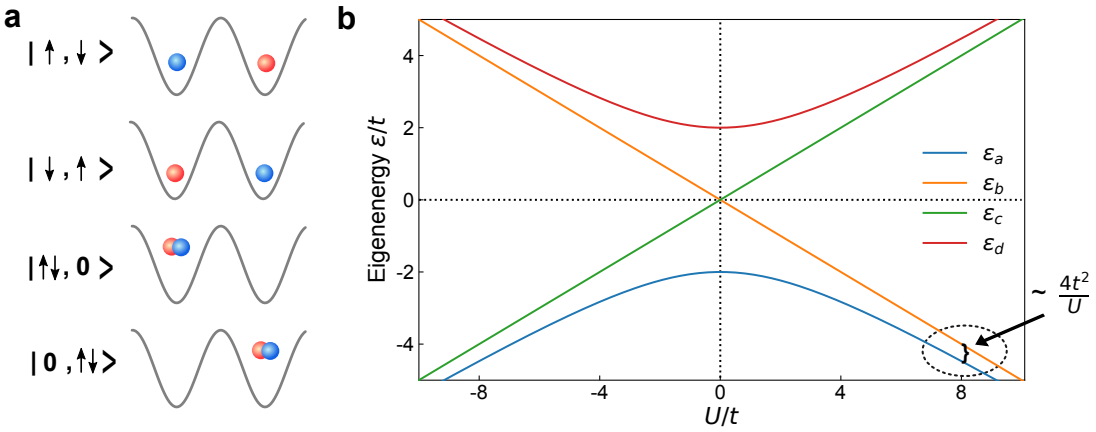

Figure 2.6: **Eigenenergies of the Hubbard double well at half-filling. a** The four possible Fock states in a Hubbard double well with half-filling $n = N/L = 2/2 = 1$. The doubly-occupied state has an energy shift of U with respect to the singly-occupied state. **b** Eigenenergy spectrum of the double well as a function of interaction U. For large $|U|$, the eigenenergies show two separated energy domains, spaced by the interaction energy U. For the lower Hubbard band (gray dotted circle), the two eigenstates can be considered an effective two-level system, with a coupling interaction $J \approx \frac{4t^2}{U}$. For the repulsive side, this two-level system contains of the spin-singlet ground state and a spin triplet state. A superposition state of the singlet and triplet give rise to magnetic property.

state is given by

$$J = \frac{4t^2}{U}. \tag{2.28}$$

This is the energy required to excite a spin-singlet to the nearest triplet state and is called the ***super-exchange***. When naively extending the ground state result to the infinite lattice sites, one can obtain a many-body state at which total magnetisation is zero (similar to how the total spin angular momentum of a singlet state is zero), yet with spin-up and spin-down aligned between neighbouring lattice sites. This would result in an alternating spin orientation, also known as an anti-ferromagnet. Even in this simple toy model, we can observe that quantum magnetism (spin-ordering) can arise without any magnetic interaction (*e.g.* bias field to spin component). Indeed, more sophisticated calculation reveals that anti-ferromagnetism emerges when temperature are close to the super-exchange energy scale. In Chapter 5, we describe the experimental detection of such anti-ferromagnetic phase in our Hubbard simulator.

2.3 Phase diagram of the Hubbard model

With knowledge from previous sections, we are now able to discuss the rich phase diagram of the Hubbard model. While the exact solution to the Hubbard model is unknown, except in one-dimension [30, 31], the physical properties of certain phases are relatively well-established. This section serves as an overview of the physics arisen in the Hubbard model due to the interplay of quantum tunnelling, interaction, Pauli principle, and density and spin degrees of freedom. Examples are the aforementioned Mott insulator and anti-ferromagnet. On the other hand, we point out that a substantial aspect of the Hubbard model remains debated, especially for parameters regime at which advanced numerical techniques fail to converge. Such phases range from a d-wave superconducting

state upon hole doping to the strange metal phase with peculiar properties. A brief mention of these unsolved problems is also provided for completeness.

2.3.1 Phase diagram at half-filling

To begin with, we restrict our discussion of the phase diagram near half-filling. We start with strongly-repulsive interaction, then move onto weakly-interacting regime and finally discuss the case with attractive interaction. In the strong-coupling regime, the separation of the density and spin degree of freedom allows an intuitive physical picture. In the weakly interacting case, the two degrees of freedom can no longer be separated and thus results in coupled dynamics between density and spin excitations.

Strong repulsion: density ordering As seen from the discussion in the atomic limit, for infinitely strong repulsion, the Hubbard model at half-filling turns into a Mott insulator driven by interaction effect. In this regime, the tunnelling is negligible and fermions are strongly localised. This is due to the fact that it is energetically unfavourable to redistribute particles within the system. A change in density is likely to incur a particle-hole excitation (also know as density excitations). For example, such excitation can happen when a fermion, say of spin-up, is destroyed at site i, and then being re-created in another site already occupied by a spin-down fermion. This results in the formation of doubly-occupied state and the energy cost in this process is the density (Mott) gap

$$\Delta_{\text{Mott}} \approx U. \tag{2.29}$$

A characteristic Mott temperature scale can be defined similarly, *i.e.* $k_B T_{\text{Mott}} = \Delta_{\text{Mott}}$. At finite temperature, thermal fluctuations lead to density excitation. For $T \gg \Delta_{\text{Mott}}$, the thermal fluctuation result in an enhanced population of the doubly-occupied state. However, when $T \ll \Delta_{Mott}$, the thermal effect becomes insignificant and the density degree is said to be frozen and attains ***density ordering***. Therefore, the Mott insulator can be signalled by the reduction of doubly-occupied states. In addition, density-density correlation is suppressed in the Mott insulator, which results in the corresponding reduction in thermodynamic observable such as isothermal compressibility. Early days quantum gases experiments utilise these properties to detect the emergence of Mott insulating phase, such as spectroscopic measurement of *global* double-occupancy and *global* compressibility based on renormalised cloud size [32, 33]. In Chapter 4, we outline our experimental procedures in measuring the ***local*** compressibility in our quantum gases ensembles.

Strong repulsion : spin ordering In addition to density ordering, the repulsive Hubbard model supports the emergence of ***spin ordering***. From the two-site Hubbard double well in previous section, we learn that a local spin-singlet state is coupled to a spin-triplet state via the super-exchange energy. This exchange energy arises from a second-order virtual hopping process, with the doubly-occupied as an intermediary state. Due to the Pauli exclusion principle, this virtual hopping process is only allowed between different spin components (otherwise the virtual state would contain two spin-up or spin-down fermions forbidden by the Pauli principle). A full second-order perturbation theory treatment reveals that the super-exchange process is indeed characterised by the energy $J = 4t^2/U$. At half-filling, the Hubbard model with strong repulsion can be effectively mapped to a Heisenberg

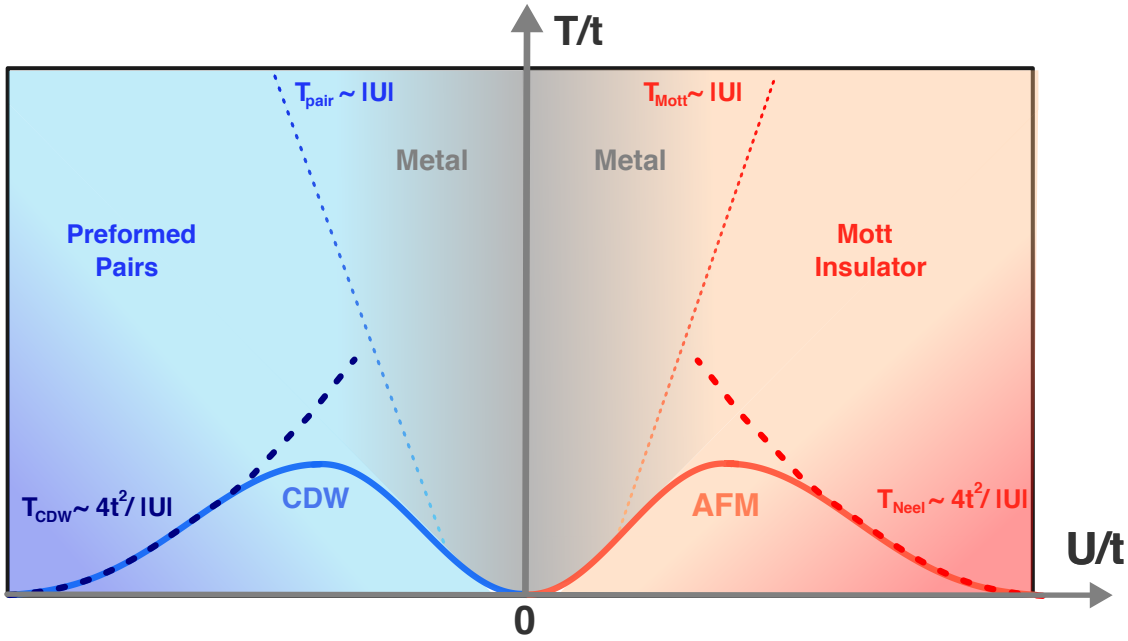

Figure 2.7: **Schematic phase diagram of the Hubbard model at half-filling.** For strong repulsive interaction $U \gg t$, the system attains density ordering for temperature is below the Mott gap $T < T_{\text{Mott}} \approx U$. Upon further lowering of temperature near the Neel's temperature T_N, spin ordering emerges and result in the anti-ferromagnetic (AFM) phase. For strong attractive interaction, a preformed pair phase emerges when temperature is below the interaction energy scale $T < T_{\text{pair}} \approx |U|$. Analogous to the repulsive side, a doublon-hole patterns are mediated by a super-exchange process, resulting in a charge-density-wave (CDW) ordering.

spin model

$$\hat{H}_{\text{Heisenberg}} = J \sum_{\langle i,j \rangle} \boldsymbol{S}_i \cdot \boldsymbol{S}_j. \tag{2.30}$$

This sets up an addition energy scale at which spin-ordering emerges. This so-called Neel's temperature is given by,

$$k_B T_N \approx \frac{4t^2}{U}. \tag{2.31}$$

Similar to the density ordering, for $T \gg T_N$, thermal excitations is dominant compared to the spin-exchange term. The spin patterns in the system are therefore randomised and uncorrelated. Typically $U \gg k_B T_N$ for strong interaction U, thus for temperature below the Mott temperature scale but above the super-exchange energy, the system is said to be a paramagnetic Mott insulator. For low temperature, $T \ll T_N$, the super-exchange term dominates and results in anti-ferromagnetic ordering. One iconic feature of the anti-ferromagnetic phase is the existence of a chequerboard structure in spin-spin correlations. In three dimension, there exists a finite temperature phase transition at which the anti-ferromagnetic spin ordering is long-range. In two-dimensions, enhanced quantum fluctuations destroy any true long-range ordering at finite temperature. However, in a two dimensional Hubbard model, which is the main focus of this thesis, only short-range spin-ordering can be observed above $T = 0$. In Chapter 5, we introduce the experimental observation of anti-ferromagnetic ordering via a novel momentum-resolved manipulation scheme.

Weak repulsion and attraction The physics becomes subtle in the weak-coupling regime $U \ll t$, because the density and spin degrees of freedom are no longer separated. For weak repulsive interaction, this regime is called the Slater regime. In this regime, the Mott temperature is similar to the Neel's temperature, *i.e.* $T_{\text{Mott}} \approx T_N$, indicating that the density and spin dynamics take place at roughly the same energy scales. In other words, the emergence of density ordering and anti-ferromagnetic ordering happens simultaneously at similar temperatures. A simple energy argument no longer works nicely in this regime. More advanced theoretically approaches [34–36], such as self-consistent Hartree-Fock calculation and spin-density wave theory predicts a characteristic temperature scale of

$$T \approx \frac{6t}{k_{\text{B}}} \exp(-7t/U). \tag{2.32}$$

Eq. (2.32) indicates that in the weakly repulsive regime, the characteristic energy scale for the emergence of both spin and density ordering vanishes exponentially with decreasing U.

For weak attractive interaction, a similar approach based on the Bardeen-Cooper-Schrieffer (BCS) superconducting theory predicts the onset of fermionic pairing on the same energy scale in Eq. (2.32) [37–40]. Below the critical temperature, the system enters an s-wave superfluid phase. As a result, the weakly attractive regime is often coined as the BCS regime.

Strong attraction Similar to the strongly-repulsive case, the strong, attractive on-site interaction allows the separation of density and spin degrees of freedom. The attractive interaction favours the formations of doubly-occupied (local pairs) states below the pair temperature $T_{\text{pair}} \approx |U|$. In contrast to density ordering, the pair temperature signals a spin-ordering as the high-energy excitation incurs pair breaking. Since a doubly-occupied site carries no net moment, this excitation leads to accumulation of net spins. In the same spirit as the Mott insulator with reduced compressibility, this so-called ***preformed pair*** phase is signalled by the suppression of spin-susceptibility. In Chapter 4, we experimentally explore both the Mott-insulating and preformed pairs phases, validating a particle-hole symmetry which connects the attractive and repulsive Hubbard model. Upon further lowering in temperature, the super-exchange energy scales again take over. However, unlike the repulsive side, the super-exchange energy scale acts between particle with opposite spin. The attractive analogue of $J = 4t^2/|U|$ describe the super-exchange between a doublon (doubly-occupied state) and hole. This results in a doublon-hole ordering know as the charge-density-wave phase.

2.3.2 Phase diagram away from half-filling

Away from half-filling, the doped Hubbard model exhibits an extremely rich phase diagram. In particular, one immense interest within the condensed matter community is the physics of superconductivity in the repulsive Hubbard model. As shown in Fig. 2.8, a superconducting phase with $d_{x^2-y^2}$ pairing symmetry is predicted to exist a finite doping. Such superconductivity is believed to be closely connected to high-temperature superconductivity in cuprates materials [41], of which the origin and mechanism of this superconducting behaviour cannot be described by conventional Bardeen-Cooper-Schrieffer (BCS) theory and remains unclear to this date [42]. In the BCS theory, superconductivity arises from the s-wave Copper pairing. Based on results from various numerical simulations, the superconducting phase predicted in the doped, repulsive Hubbard model would be

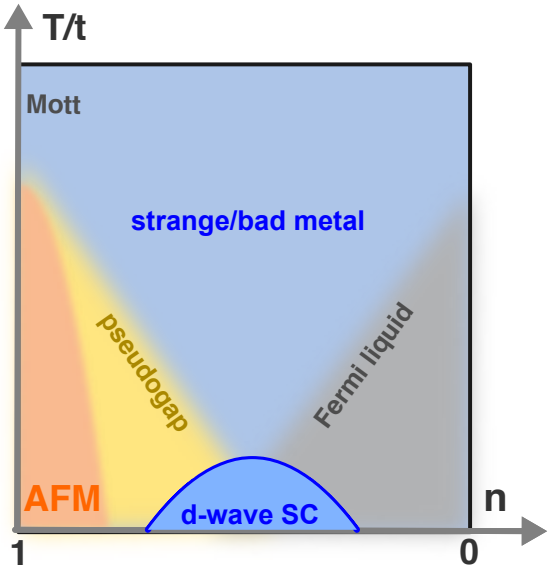

Figure 2.8: **Phase diagram of the doped repulsive Hubbard model.** Starting from the anti-ferromagnetic phase (AFM), increasing the doping eventually leads to loss of spin-ordering. At temperature below the critical temperature, the predicted yet undetected d-wave superconducting phase emerges. Above which near the underdoped side is a pseudogap phase where pairing signature begins to show up. The strange or bad metallic phase is characterised by a linear temperature dependence in resistivity.

signalled by an unconventional d-wave pairing order parameter

$$\tilde{\Delta}^{\dagger}_{d_{x^2-y^2}} = \sum_{k} \Delta_{d_{x^2-y^2}}(k)\, \hat{c}^{\dagger}_{k\uparrow} \hat{c}^{\dagger}_{-k\downarrow}, \tag{2.33}$$

where the operator is given by

$$\begin{aligned} \tilde{\Delta}^{\dagger}_{d_{x^2-y^2}} = \frac{\Delta_0}{2} \sum_{l} \Big[&\left(\hat{c}^{\dagger}_{l+x\uparrow} \hat{c}^{\dagger}_{l\downarrow} - \hat{c}^{\dagger}_{l+x\downarrow} \hat{c}^{\dagger}_{l\uparrow} \right) - \left(\hat{c}^{\dagger}_{l+y\uparrow} \hat{c}^{\dagger}_{l\downarrow} - \hat{c}^{\dagger}_{l+y\downarrow} \hat{c}^{\dagger}_{l\uparrow} \right) \\ &+ \left(\hat{c}^{\dagger}_{l-x\uparrow} \hat{c}^{\dagger}_{l\downarrow} - \hat{c}^{\dagger}_{l-x\downarrow} \hat{c}^{\dagger}_{l\uparrow} \right) - \left(\hat{c}^{\dagger}_{l-y\uparrow} \hat{c}^{\dagger}_{l\downarrow} - \hat{c}^{\dagger}_{l-y\downarrow} \hat{c}^{\dagger}_{l\uparrow} \right) \Big] . \end{aligned} \tag{2.34}$$

One "Holy Grail" in quantum simulation of the Hubbard model is to show whether or not, such minimal model supports the existence of a superconducting state in this minimal model. If quantum simulation experiments do observe a superconducting phase reminiscent to those observed in cuprates, it offers a tremendous simplification and thus formulating an analytical theory for high-temperature superconductivity. For instance, several immediate questions a quantum simulator could provide insight are how anti-ferromagnetism is lost with increasing doping? And do anti-ferromagnetic fluctuations induce the d-wave pairing or compete with the superconductivity? At temperature higher than the superconducting critical temperature, how is the pseudogap related to the pairing behaviour?

Even if a quantum simulator could not observe the signature of a superconducting phase, it still provides clear insight to the community that addition mechanism beyond the interplay of nearest-neighbour hopping and on-site interaction are required to capture the mechanism of the superconducting phase. Either way, accessing the low-temperature phase diagram of the model would provide valuable

information to the study of high-temperature superconducting materials.

Another intriguing effect of doping can be found on the attractive side of the phase diagram. Near the ground state, the Hubbard model supports an s-wave pairing phase. Since the on-site interaction term depends on both U and the product of density $n_{i,\uparrow}n_{i,\downarrow}$, doping can drive the system from weakly-coupled to the strongly-correlated regime. On the attractive side, the ground state behaviour can be interpreted as a BCS-BEC type crossover. In Chapter 6, we present the experimental measurement of pair correlation in the normal phase and observe a resemblance to the ground state behaviour.

2.4 Realisation of the Hubbard with ultracold atoms

In this section, we introduce the experimental implementation of a quantum simulator, which emulates the Hubbard Hamiltonian. First, we outline the mechanism of optical trapping where the optical light shift of far-off-resonant laser light as external, highly-controllable and conservative trapping potential. The superposition of laser light fields results in a defect-free periodic lattice structure, allowing us to realise a two-dimensional lattice. The full energy band structure of a one-dimensional optical lattice is reviewed, in which we draw particular focus to how this emulates the kinetic term in the Hubbard Hamiltonian. This is followed by an introduction of scattering properties of cold atoms in an optical lattice and the magnetic Feshbach resonance which allows the adjustment of scattering lengths. An on-site interaction naturally emerges from the contact potential, thereby completing the realisation of the Hubbard model.

2.4.1 Optical lattice

Atom-light interaction The interaction of a neutral atom under an external electric field $\boldsymbol{E}(\boldsymbol{r},t) = \boldsymbol{E}_0(\boldsymbol{r})e^{i\omega t+\boldsymbol{k}\cdot\boldsymbol{r}}$ is described by the Hamiltonian

$$\hat{H}_{\text{dip}} = -\mathbf{p}\cdot\mathbf{E}(\mathbf{r},t), \tag{2.35}$$

where $\boldsymbol{p} = \alpha(\omega)\mathbf{E}(\mathbf{r},t)$ is the induced electric dipole moment and $\alpha(\omega)$ is the complex polarisability which depends on the driving frequency ω. The problem can be treated as a driven oscillator under the electric field. Two major terms result from this electric-dipole interaction [43]. The first is an absorptive term which describe the absorption and re-emission of photons and is characterised by the power

$$P_{\text{abs}}(\boldsymbol{r}) = \langle\frac{d\boldsymbol{p}}{dt}\boldsymbol{E}\rangle_t = 2\omega\,\text{Im}(\alpha)I(\boldsymbol{r}). \tag{2.36}$$

Here the bracket $\langle\cdots\rangle_t$ is the time-averaged over the rapid oscillating electric field, and $I(\boldsymbol{r}) = \frac{1}{2}\epsilon_0 c|E_0(\boldsymbol{r})|^2$ is the spatial profile of the electric field intensity. The scattering rate is given by

$$\Gamma_{\text{sc}}(\boldsymbol{r}) = \frac{P_{\text{abs}}(\boldsymbol{r})}{\hbar\omega}. \tag{2.37}$$

As reflected in Eq. (2.36), such scattering is caused by the imaginary part of the polarisability. On the other hand, a dispersive term arisen from the real part of the polarisability α leads to a conservative

potential

$$V_{\text{dip}}(\mathbf{r}) = -\frac{1}{2}\langle \mathbf{p}\cdot\mathbf{E}\rangle_t = -\frac{1}{2\epsilon_0 c}\,\text{Re}[\alpha]I(\mathbf{r}). \tag{2.38}$$

The explicit form of the atomic polarisability α is given by

$$\alpha(\omega) = \sum_e |\langle e|\mathbf{p}\cdot\boldsymbol{\epsilon}|g\rangle|^2 \left(\frac{1}{\hbar\omega_e - i\hbar\Gamma_e/2 - \hbar\omega_g - \hbar\omega} + \frac{1}{\hbar\omega_e - i\hbar\Gamma_e/2 - \hbar\omega_g + \hbar\omega}\right). \tag{2.39}$$

Here, g (e) denotes the ground (excited) states, and the matrix element $\langle e|\mathbf{p}\cdot\boldsymbol{\epsilon}|g\rangle$ gives the strengths of the electric-dipole transition. Substituting Eq. (2.39) into Eq. (2.37) and Eq. (2.38) and assuming the frequency detuning $\Delta \equiv$ satisfy $|\Delta| \ll \omega_e - \omega_g$, we can obtain the expressions

$$\begin{aligned}\Gamma_{\text{sc}}(\mathbf{r}) &= \frac{3\pi c^2}{2\hbar\omega_0^3}\left(\frac{\Gamma}{\Delta}\right)^2 I(\mathbf{r}) \\ V_{\text{dip}}(\mathbf{r}) &= \frac{3\pi c^2}{2\omega_0^3}\frac{\Gamma}{\Delta}I(\mathbf{r}).\end{aligned} \tag{2.40}$$

Eq. (2.40) demonstrates the two essential points for optical trapping. First, the trapping potential $V(\boldsymbol{r})$ depends on the sign of the detuning Δ. For optical frequency below the atomic resonant frequency, also known as ***red-detuning***, the dipole potential is negative and thus the atom-light interaction attracts atoms to the light field. On the other hand, for frequency above the resonant frequency, also known as ***blue-detuning***, atoms are repelled by the atom-light interaction. Secondly, the dipole potential scales as $1/\Delta$ while the scattering rate scales as $1/\Delta^2$. Typical optical trapping therefore is implemented with large detuning and high intensity such that the trapping potential is strong while keeping the scattering rate low to prevent atom loss. In our experiment, we utilise red-detuned light primarily for optical trapping and for subsequent evaporative cooling. As for creation of optical lattice potentials, we make use of a balance between red-tuned and blue-detuned laser light in order to achieve minimal heating and optimal thermalisation performance at the final stage of the experiment.

Optical lattice potential With the knowledge of the conservative potential in Eq. (2.40), we are in the position to outline the creation of optical lattice potential by superposition of laser light. The simplest configuration of an optical lattice is a pair of ***counter-propagating*** beams, which results in a standing-wave intensity pattern, as shown in Fig. 2.9 **a**. The one-dimensional lattice potential can be expressed in simple form

$$V_x(x) \simeq V_{\text{latt}}\,\cos^2\left(\frac{\pi x}{a}\right), \tag{2.41}$$

where $a = \lambda/2$ is the lattice spacing and V_{latt} is the ***lattice depth***. One common energy scale used to characterise the lattice depth is the ***recoil energy*** of the laser light $E_R = \frac{\hbar^2}{8ma^2}$. In our experiment, twp in-plane (horizontal) optical lattices are formed by this approach using infra-red wavelength $\lambda = 1064\,\text{nm}$, leading to a lattice spacing of $a_{x/y} = \lambda/2 = 532\,\text{nm}$

Another type of configuration is the so-called ***accordion lattice*** [44], which we also use in our experiment. In Fig. 2.9 **b**, we show the configuration in which two laser beams propagating with an offset angle of 2θ. The y-component of two laser beams are co-propagating, thus do not contribute to a standing wave pattern. Instead, the optical light potential along the y-direction is the simple sum of two trapping potential. However, along the z-direction, the wave-vector projection of two beams point

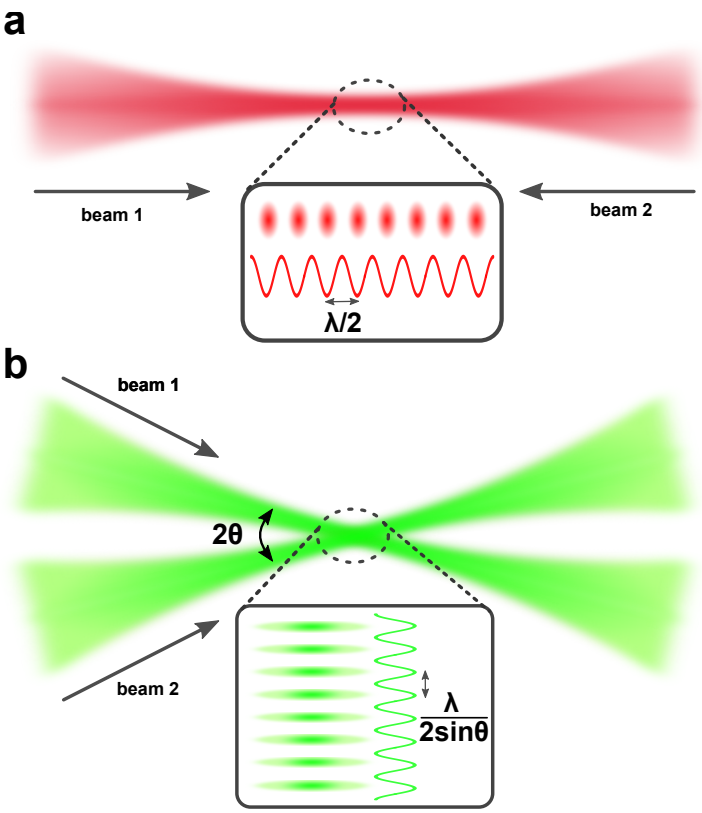

Figure 2.9: **Schematic diagram for optical lattice potential implemented in this thesis.** **a** Counter-propagating configuration. Beam 1 is superimposed with the retro-reflected beam 2 to form a stationary wave pattern with a periodicity of $\lambda/2$. **b** Accordion configuration. Beam 1 and beam 2 are sent in from the same yz-plane, intersecting at an angle of 2θ. The wavevectors in y-direction are co-propagating while those along z-direction are counter-propagating. This results in an stationary wave along the z-direction with periodicity $\lambda/2\sin\theta$.

in opposite direction. This results in a standing wave pattern with the wavevector $k_z = (2\pi/\lambda)\sin\theta$, with a lattice spacing

$$a_{\text{accordion}} = \frac{\lambda}{2\sin\theta}. \tag{2.42}$$

As shown in Eq. (2.42), the lattice spacing of an accordion-type lattice can be adjusted by varying the angle θ. In our experimental set, we implement the vertical accordion optical lattice using visible green wavelength $\lambda = 532\,\text{nm}$ with a $\theta \approx 15°$, resulting in a lattice spacing $a_z \approx 532\,\text{nm}/2\sin(15°) = 1064\,\text{nm}$.

Energy band theory Next, we show that the tunnelling matrix elements as shown in Eq. (2.7) arise naturally in solving the single-particle Hamiltonian in a periodic potential. Using the one-dimensional lattice potential in Eq. (2.41), we write down the Schrödinger equation as follow

$$\hat{H}\phi_q^n(x) = \left[-\frac{\hbar^2\nabla^2}{2m} + V(x)\right]\phi_q^n(x) = E_q^n\phi_q^n(x). \tag{2.43}$$

Here, the n is the band index and q is the crystal momentum q in the Bloch wavefucntions ansatz [45]

$$\phi_q^n(x) = \frac{1}{\sqrt{L}} u_q^n(x) e^{iqx}. \tag{2.44}$$

This follows from the ***Bloch's theorem*** which state that the eigenstates can be expressed a plane wave modified by the coefficient $u_q^n(x)$ with same periodicity of the crystal structure, *i.e.* $u_q^n(r+a) = u_q^n(x)$ [46]. By expanding both the lattice potential $V(x)$ and $u_q^n(x)$ in Fourier series, we have

$$\begin{aligned} V(x) &= \sum_l \tilde{V}_l e^{i\frac{2\pi l x}{a}}, \\ u_q^n(x) &= \sum_l \tilde{u}_{q,l}^n e^{i\frac{2\pi l x}{a}}. \end{aligned} \tag{2.45}$$

Here, the index l is the summation over all allowed discrete momentum states. It can be easily shown that for a simple sinusoidal potential as shown in Eq. (2.41), the non-zero Fourier components are given by $\tilde{V}_0 = V_x/2$ and $\tilde{V}_1 = \tilde{V}_{-1} = V_x/4$. Eq. (2.45) can then be recast in the block-diagonal matrix as follow

$$\sum_{l,m} H_{l,m} \tilde{u}_{q,l}^n = E_q^n \tilde{u}_{q,l}^n, \tag{2.46}$$

where

$$H_{l,m} = \begin{cases} \frac{\hbar^2}{2m}(2kl+q)^2 + \frac{V_x}{2} & \text{for } |l-m| = 0 \\ \frac{V_x}{4} & \text{for } |l-m| = 1 \\ 0 & \text{for } |l-m| > 1 \end{cases} \tag{2.47}$$

This matrix equation can be solved by diagonalisation. The eigenfunctions $\{\tilde{u}_{q,l}^n\}$ gives the Fourier spectrum of the Bloch wavefunctions, and the eigenenergies is the energy of the corresponding Bloch waves E_q^n. In Fig. 2.10 **a**-**c**, we plot the energy band structures for ascending lattice depths. For high lattice depths, we note that the first three energy bands become flat (with respect to the inter-band energy gap) and equally-spaced. In this limit, the solution of the wavefunction can be approximated by a local harmonic oscillator. We later utilise this observation as an intermediate step to compute the interaction energy parameter U (see Sec 2.4.2).

Deriving tunnelling t from the band structure With the Bloch wavefunctions, we can defined a different orthogonal set of maximally-localised wavefunctions [47], which for the lowest energy band, is given by

$$w_0\left(x - x_i\right) = \frac{1}{\sqrt{N}} \sum_q e^{-iqx_i} \phi_q^0(x). \tag{2.48}$$

This is know as the ***Wannier*** basis. The use of only the lowest energy band can be justified when only the lowest Bloch band is occupied. Substituting this into Eq. (2.7), we can obtain

$$\begin{aligned} t_{i,j} &= \int dx w_0^*(x - x_i) \left(-\frac{\hbar^2}{2m} \frac{\partial^2}{\partial^2 x} + V(x) \right) w_0(x - x_j) \\ &= \frac{1}{N} \sum_{q,q'} E_q^0 e^{-i(qx_j - q'x_i)/\hbar} \int dx \phi_{q'}^{*0}(x) \phi_q^0(x) \\ &= \frac{1}{N} \sum_q E_q^0 e^{-iq(x_j - x_i)/\hbar} \end{aligned} \tag{2.49}$$

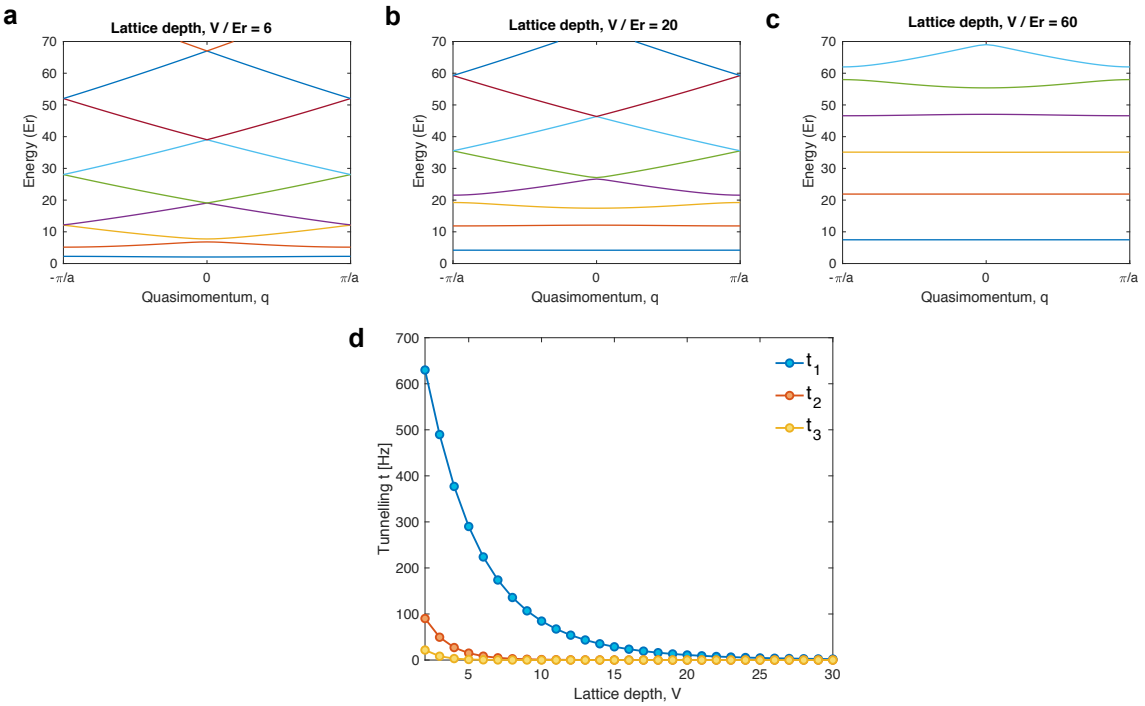

Figure 2.10: **Energy band structure and extracted tunnelling matrix elements. a-c** Energy band structures for lattice depths $V_{\text{latt}} = 6$, 20 and 60 E_R respectively. The left column is the schematic representation of the energy levels with respect to the lattice potential (black). The right column is the energy band structure in the 1$^{\text{st}}$ Brillouin zone. **d** By expanding the lowest energy band in Fourier series, the Fourier coefficients give the tunnelling amplitudes. In general, the tunnelling amplitudes decreases as lattice depths increases due to localisation of the wavefunctions. For lattice depths $V_{\text{latt}} > 5$, the NNN tunnelling t_2 starts to become negligible as compared to to the NN term t_1, therefore signalling the tight-binding regime.

Therefore, the tunnelling matrix element is given by the Fourier series of the energy band. One important observation is that Eq. (2.49) provide a powerful tool to evaluate the tunnelling matrix elements and is not limited to nearest-neighbour tunnelling. In Fig. 2.10 **c**, we plot the first three tunnelling matrix elements including the nearest-neighbour (NN) tunnelling t_1 and next-nearest-neighbour (NNN) tunnelling t_2 as a function of lattice depths. One can observe that, for moderate lattice depth, say $V_{\text{latt}} \approx 5$, the NNN tunnelling is negligible compared to the NN one. In other words, for regime where t_1 is dominant, the lowest energy band indeed obtains the sinusoidal energy dispersion as shown in Eq. (2.15).

2.4.2 Tuning on-site interaction U

Another important element in the quantum simulation of any strongly-correlated system is the interaction. A brief review of scattering theory in the low energy limit is given in this section. The on-site interaction of two fermions in a single lattice site can be approximated by the ground state wavefunction of a quantum harmonic oscillator. Finally, we introduce the magnetic Feshbach resonance, which allows the adjustment of scattering lengths (thereby interaction).

Scattering theory The scattering between two particles can be formally stated as a single-particle with reduced mass $m = \frac{m_1 m_2}{m_1+m_2}$ in a spherically symmetric interacting potential $V(r)$, where the Schrödinger equation is given by [48, 49],

$$\left(-\frac{\hbar^2}{2m}\left(\frac{\partial^2}{\partial^2 r}+\frac{\boldsymbol{L}^2}{r^2}\right)+V(\boldsymbol{r})\right)\psi = E\psi, \tag{2.50}$$

where $\boldsymbol{L}^2$ is the orbital angular momentum operator in spherical coordinates,

$$\mathbf{L}^2 = -\hbar^2\left[\frac{1}{\sin^2\theta}\frac{\partial^2}{\partial\phi^2}+\frac{1}{\sin\theta}\frac{\partial}{\partial\theta}\sin\theta\frac{\partial}{\partial\theta}\right]. \tag{2.51}$$

For two-body collision, the resulting wavefunction can be written as the sum of an incoming plane wave and a scattered wave weighted by the strengths of the scattering process,

$$\psi_{\mathbf{k}}(\mathbf{r}) = \left(e^{i\mathbf{k}\mathbf{r}} + f\left(\mathbf{k},\mathbf{k}'\right)\frac{e^{ik'r}}{r}\right). \tag{2.52}$$

Here, $f(\boldsymbol{k},\boldsymbol{k}')$ is the ***scattering amplitude***. In particular the radial part of Eq. (2.50) can be separated,

$$\left[-\frac{\hbar^2}{2m}\left(\frac{\mathrm{d}^2}{\mathrm{d}r^2}+\frac{2}{r}\frac{\mathrm{d}}{\mathrm{d}r}\right)+V_{\text{eff}}(r)\right]R_l(r) = ER_l(r). \tag{2.53}$$

The orbital angular momentum term is absorbed into the effective potential $V_{\text{eff}}(r)$ as a repulsive potential, also known as the ***centrifugal barrier***,

$$V_{\text{eff}}(r) = V(r) + \frac{\hbar^2 l(l+1)}{2mr^2}, \tag{2.54}$$

where $l = 0, 1, 2, \cdots$ is the orbital quantum number. The centrifugal barrier represents the rotational energy of the particle pairs at a given distance r and for the rotational quantum number l. For $l = 0$, the effective potential is spherically symmetric and the corresponding scattering process is known as ***s-wave*** scattering, as shown in Fig. 2.11.

Low-energy scattering For low energy scattering, the thermal de Broglie wavelength λ_{th} is much larger than the effective range of the interaction potential. By associating the typical wave-number of the particle pair $k \sim 1/\lambda_{\text{th}}$, the condition for low-energy scattering can be stated as

$$kr_0 \ll 1\,. \tag{2.55}$$

For the case with $l > 0$, there exists a distance r_{cl}, the so-called classical turning point, below which the particle is classically forbidden. While quantum mechanically, the wavefunction would also decay exponentially as particle traverse towards the center. As r decreases below r_{cl}, the rotational energy exceeds the total energy $\varepsilon = \hbar^2 k^2/2m$, which results in the following equality

$$k^2 = \frac{l(l+1)}{r_{cl}^2}. \tag{2.56}$$

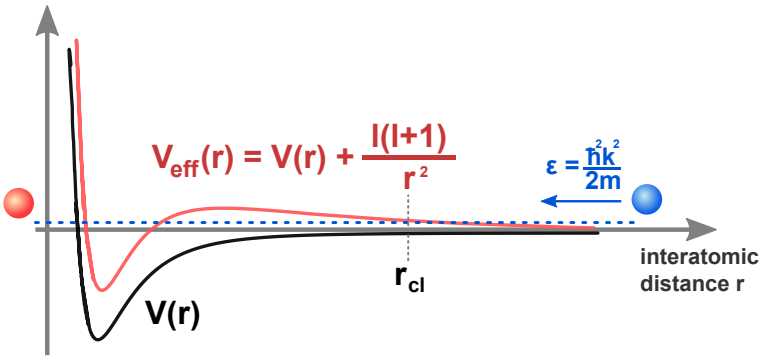

Figure 2.11: **Effective scattering potential.** The presence of the centrifugal barrier $l(l+1)/r^2$ results in exponential suppression of the wavefunction in the classically-forbidden zone $r < r_{cl}$. For low energy scattering, the energy of the particle pair $\varepsilon = \hbar^2 k^2/2m$ is not sufficient to overcome this repulsive potential, therefore r_{cl} is much larger than the effective range of the interacting potential. As a result, higher partial waves scattering are significantly suppressed in the low energy limit.

Combining this with the condition for low-energy scattering in Eq. (2.55), we have the inequality

$$kr_0 = \sqrt{l(l+1)}\frac{r_0}{r_{cl}} \ll 1\,. \tag{2.57}$$

As a result, for $l > 0$, the classical turning point is at a much larger distance than the interaction range, and therefore the collisions with non-zero partial waves ($l > 0$) are strongly suppressed [50]. In other words, scattering can only take place from collision with zero angular momentum in the low energy domain. This regime is also called the s-wave regime for this reason. The scattering process induces a scattering phase shift $\delta(k)$ which is linked to the scattering amplitude by

$$f_s(k) = \frac{1}{k\cot\delta_0(k) - ik} = \frac{1}{-1/a_s + r_e k^2/2 - ik}\,, \tag{2.58}$$

here a_s is the s-wave scattering length. For fermions with the same spin, s-wave scattering is forbbiden due to the symmetric property of the wavefunctions [14]. Therefore, one convenient way to realise non-interacting gases in ultracold temperature is to implement a spin-polarised atomic cloud. For instance, in Chapter 5, we make use of a spin-polarised cloud for calibrating the spin-wave pattern we imprinted. However, working with a single spin component results in difficulty in thermalisation due to the non-scattering nature. The study of equilibrium physics in a many-body fermionic states, therefore, requires the use of a spin-mixtures atomic cloud.

Scattering potential in lattice In the s-wave regime, it is customary to approximate the inter-particle potential by the regularised pseudopotential [51, 52],

$$V(r) = \frac{4\pi h^2 a_s}{m}\delta(r)\frac{d}{dr}r. \tag{2.59}$$

This is a contact potential and is empirically proven that to accurately reproduce the scattering properties of system [14, 53]. Next, we are in the position to discuss the on-site interaction arises from this contact potential. Using the Wannier basis as shown in Eq. (2.48), the on-site interaction U

is given by

$$U = \frac{4\pi h^2 a_s}{m} \int d^3\mathbf{r} \left| W_{0,0}(\mathbf{r}) \right|^4 . \tag{2.60}$$

From Eq. (2.60), it is apparent that interaction parameter is completely characterised by the shape of the Wannier functions. One convenient approximation in the deep lattice limit, *i.e.* $V_{latt} > 5E_R$, is to approximate the ground band wavefunction as the ground state of a quantum harmonic oscillator. In this way, the Wannier function in Eq. (2.60) can be replaced with a Gaussian wavefunction. For a local harmonic oscillator well in a single lattice site, the on-site trapping frequency can be obtained by

$$\omega_{\text{on-site}} = \left(\frac{\pi}{a}\right) \sqrt{\frac{2V_0}{m}}. \tag{2.61}$$

Therefore, by invoking the analytical solution of two interacting fermions in a harmonic oscillator [54], the harmonic approximation of the on-site U_{harmonic} can be obtained. The final interaction parameters U used in the experimental analysis are inferred by multiplying a correction factor that takes into account of the anharmonicity of the Wannier wavefunction [55].

Feshbach resonance One key advantage of quantum gases experiment is the ability to vary the interaction strength. This can be achieved by utilising the resonance between two scattering channels with different magnetic moment. For a given energy E of a particle pair, a channel is called ***open*** when ε is higher the potential energy at $r \to \infty$, otherwise it is called a ***closed*** channel. When the energy of the open channel is tuned near the bound state energy level of the closed channel, the scattering properties can be significantly modified. Below we use potassium ^{40}K as an example, our experiment typically work with the two lowest hyperfine states in the $4S_{1/2}$, $F = 9/2$ manifold. The $|a\rangle = |F = 9/2, m_F = -9/2\rangle$ and $|b\rangle = |F = 9/2, m_F = -7/2\rangle$ constitute the open channel. The closed channel is formed by $|a\rangle = |F = 9/2, m_F = -9/2\rangle$ and $|c\rangle = |F = 7/2, m_F = -7/2\rangle$. Due

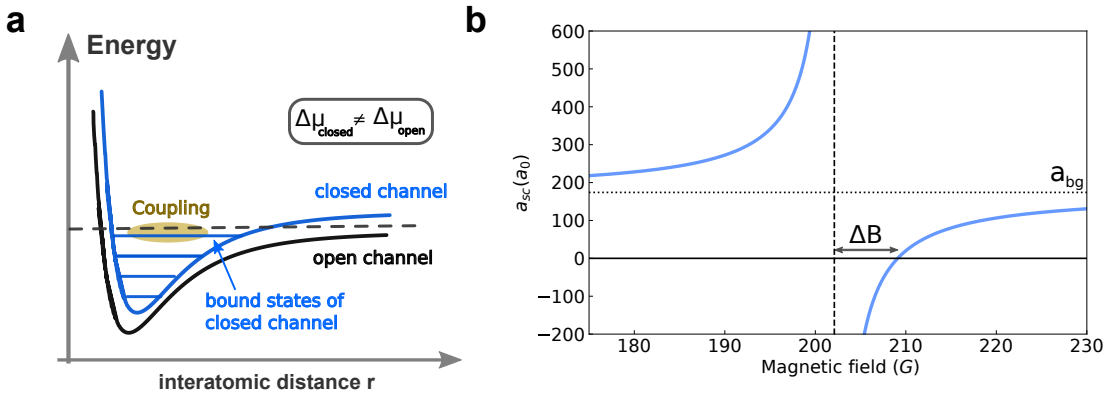

Figure 2.12: **Feshbach resonance. a** Schematic diagram of two-channel model of the Feshbach resonance. The closed channel contains a number of bound states, which can be magnetically tuned with respect to the open channel (due to the difference in magnetic moments in two channels). The scattering length is resonantly enhanced when the bound state energy coupled with the energy of the open channel. **b** s-wave Feshbach resonance of the open channel involving $|a\rangle = |F = 9/2, m_F = -9/2\rangle$ and $|b\rangle = |F = 9/2, m_F = -7/2\rangle$, where $B_0 = 202.1(7)\,\text{G}$ and $\Delta B = 7.0(2)\,\text{G}$ [13, 56]. A non-interacting two-component Fermi gases is realised at $B = B_0 + \Delta B \approx 209\,\text{G}$. For $a_s > 0$, the Hubbard on-site interaction $U > 0$ is repulsive, whereas for $a_s < 0$, it is attractive.

to their difference in magnetic moment of two channels, the relative energy between them can be adjusted by a magnetic field. This results in the magnetic-field dependent scattering length [14]

$$a_s(B) = a_{\mathrm{bg}}\left(1 - \frac{\Delta B}{B - B_0}\right). \tag{2.62}$$

In Fig. (2.12) **b**, we show the scattering lengths between $|a\rangle$ and $|b\rangle$ as a function of magnetic field. This in turns allows us to vary the interaction parameter U in the Hubbard model according to Eq. (2.60).

2.5 Advanced numerical methods

In the quantum simulation of the Hubbard model, one important goal is to benchmark existing theoretical to experimental measurements. Throughout this thesis, we utilise several methods to compare with our experimental outcomes. We start by an analytical series expansion in the inverse temperature β, which offers nice converging result at the high-temperature regime. Next, we introduce two state-of-the-art numerical approaches to the Hubbard model, namely the numerical linked cluster expansion (NLCE) and determinant quantum Monte Carlo (DQMC) method. The numerics of the former is provided by M. Rigol et al. [57, 58], and we perform the numerical computation for the latter one. The discussion presented here is, by no mean, complete picture of the theoretical study of the Hubbard model, yet it offers the reader a glimpse of the fundamental capability in numerical methods. In later chapters, we will see how we deploy the numerics obtained by these methods for data analysis such as thermometry and extraction local variables.

High-temperature series expansion (HTSE) The high temperature series expansion solves the atomic-limit Hubbard model ($t = 0$) with the tunnelling term as perturbation, *i.e.*

$$V = -t \sum_{<i,j>,\sigma} \left(\hat{c}_{i,\sigma}\hat{c}_{j,\sigma} + h.c.\right). \tag{2.63}$$

As its name suggests, we start by writing down series expansion of the grand canonical partition function

$$Z = Z_0 \left\{1 + \sum_{n=1}(-1)^n \int_0^\beta \int_0^{\tau_1} \int_0^{\tau_{n-1}} \langle \tilde{V}(\tau_1)\tilde{V}(\tau_2)\cdots\tilde{V}(\tau_n)\rangle_0 d\tau_1 d\tau_2 \cdots d\tau_n\right\}, \tag{2.64}$$

where $\beta = 1/k_B T$ is the inverse temperature and $\tilde{V}(\tau)$ is the perturbation in the interaction picture,

$$\tilde{V}(\tau) = e^{\tau H_0} V e^{-\tau H_0}. \tag{2.65}$$

The unperturbed partition function Z_0 can be shown to be separable, *i.e.* $Z_0 = z_0^N$,

$$z_0 = 1 + 2z + z^2 u, \tag{2.66}$$

where $z = \exp(\beta\mu)$ is the fugacity, and $u = \exp(-\beta U)$. Same as any approximation scheme, the HTSE assumes high temperature, thus $\beta \ll 1$, which allows the analytical expansion of the partition function Z. From the partition function, in theory, all system properties can be obtained. For instance,

we can calculate the grand canonical potential,

$$\Omega = -\frac{\ln Z}{\beta}. \tag{2.67}$$

By expanding up to 2-nd order in β in Eq. (2.64), one can derive the following relation for a two-dimensional system,

$$\Omega_2 = -\frac{\ln Z_2}{\beta} = -\frac{1}{\beta}\ln z_0 - \frac{1}{\beta}(\frac{\beta}{z_0})^2(4t_{xy}^2)\left(z + z^3u + 2z^2\frac{1-u}{\beta U}\right) \tag{2.68}$$

From the analytical form of Ω, one can obtain the expectation values various thermodynamic observables such as total particle number, entropy and double occupancy,

$$\langle N\rangle = -\frac{\partial\Omega}{\partial\mu}\ , \langle S\rangle = -\frac{\partial\Omega}{\partial T} \text{ and } \langle D\rangle = \frac{\partial\Omega}{\partial U}, \tag{2.69}$$

respectively. In this thesis, the HTSE no longer converges at the final temperatures reached in the experiments ($T \approx 0.6t$). However, it offers a guiding theory for initial optimisation of the cooling. In addition, a similar series expansion approach plays a critical role in the more advanced numerical methods discussed later.

Numerical Linked Cluster Expansion (NLCE) Numerical Linked Cluster Expansion (NLCE) shares a similar idea with the HTSE and is in essence, also a series expansion in the thermodynamic limit [59]. Rather than grouping terms based on different orders of tunnelling, the NLCE groups different contributions by the ***cluster geometries***. To this end, for some extensive property P of an infinite lattice $\mathcal{L}$, the following relation can be written down

$$P(\mathcal{L})/N = \sum_c L(c)W_P(c). \tag{2.70}$$

Here $L(c)$ is the number of embeddings of the cluster c per lattice site and $W_P(c)$ is the weight of the cluster c for property P. $W_P(c)$ can be understood as the part of the property that *cannot* be accounted by a smaller sub-cluster s. One can use the recursive notation

$$W_P(c) = P(c) - \sum_{s\subset c} W_P(s), \tag{2.71}$$

where $P(c)$ is the property P calculated for a finite cluster by ***exact diagonalisation***. In HTSE, essentially every cluster is expanded in powers of the inverse temperature β and only a finite number of terms are kept. On the other hand, NLCE expands up to finite-size clusters using Eq. (2.71). Therefore, the cluster expansion is able to capture correlations on the order of the cluster size and thus converges at lower temperatures than HTSE (close to $T \sim 0.1t$ near half-filling). With proper extrapolation techniques (also known as re-summing), the calculation can be accelerated. In principle, under the NLCE formalism, only extensive quantities can be directly computed. Local correlators, such as the nearest-neighbour spin-spin correlators, are computed as summed quantity over the entire lattice (therefore extensive). In this thesis, we utilise NLCE numeric data, provided by authors from [57], based on a calculation up to a 9-site cluster.[10] The theoretical numerics are then interpolated on a fine grid of chemical potential, interaction and temperatures. We primarily use the NLCE data for

[10] The cluster of size 9 refers to the number of sites in various configuration, *e.g.* a 1×9 chain or a 3×3 plaquette.

comparing spin-correlations measurement, which will be discussed in Chapter 4.

Determinant Quantum Monte Carlo (DQMC) The quantum Monte Carlo (QMC) method has been the powerhouse for simulating many-body systems in two and higher dimensions. In particular, QMC simulations utilise stochastic sampling to map out a small yet representative subspace in the Hilbert space, which offers a tremendous advantage over a brute-force approach. In addition, unlike variational methods, QMC is intrinsically unbiased due to its stochastic nature.

The first step to perform QMC simulation is generally noticing that a n-dimensional quantum system can be mapped to a $n+1$-dimensional classical system, in which for a set of classical configurations, the partition function can be easily computed. In determinant quantum Monte Carlo (DQMC) simulation of the Hubbard model, this mapping is achieved via the Trotter decomposition, which discretises the partition function into L imaginary time slices, *i.e.* $\beta/L = \Delta\tau$,

$$\begin{aligned} Z &= \mathrm{Tr}\left(e^{-\beta(H_K+H_U)}\right) = \mathrm{Tr}\left(e^{-L\Delta\tau(H_K+H_U)}\right) \\ &= \mathrm{Tr}\left(\prod_{l=1}^{L} e^{-\Delta\tau(H_K+H_U)}\right) = \mathrm{Tr}\left(\prod_{l=1}^{L} e^{-\Delta\tau H_K} e^{-\Delta\tau H_U}\right) + O(\Delta\tau^2). \end{aligned} \tag{2.72}$$

Here, $H = H_K + H_U$ is written as the sum of kinetic energy term (absorbing the chemical potential term) and the interacting term. And the trace is over the entire Hilbert space, that is, all possible quantum states. For two-component fermions in a $N \times N$ square lattice, the size of the Hilbert space is 2^{N^2}. Therefore, the partition function is expressed as a $N \times N \times L$ space-time lattice. By implementing a Monte Carlo sampling algorithm, the partition function can be computed and physical measurments can be expressed as products of the determinants. In this thesis, we compare our experimental data with DQMC simulations on a square lattice, using the Quantum Electron Simulation Toolbox (QUEST) Fortran package [60]. Details of the DQMC simulation can be found in Appendix A.

CHAPTER 3

Experimental Setup

I might be suffering from a permanent head damage (PHD) syndrome.

MYSELF DREAMING ABOUT THE EXPERIMENT

This chapter discusses the experimental implementation of the two-dimensional Hubbard model. After a brief historical review of the experimental apparatus, we give an overview of the experimental timeline. We explain the production of our quantum degenerate, ultracold fermionic gases by various stages of cooling, from a magneto-optical trap to an optical dipole trap. Next, we elaborate on the realisation of the two-dimensional lattices and related characterisation measurements. Finally, we move on to the relevant experimental techniques for coherent control and detection of the atomic ensembles.

3.1 Pathway to ultracold Fermi gases

Our main experimental apparatus witnessed its construction since 2006 in Cambridge, the United Kingdom. Since then, the machine has been moved to Bonn in 2013 and refined to suit various experimental requirements for studying of fermions in optical lattices. Past experiments include studying pseudogap physics in two-dimensional Fermi gases [61, 62], the observation of Fermi polarons in spin-imbalanced Fermi gases [63], spin-diffusion of one-dimensional Fermi gases [64] and recently the characterisation of the thermodynamic equation of state of the repulsive Hubbard model, [65, 66] and the observation of density and spin correlations [67, 68]. Details on these experiments can be found in the theses of the past generation members of the Fermi team [55, 69–73].

In Fig. 3.1, we outline the experimental cycle in a simple "Monopoly" style board. In this chapter, we will explain the full experimental cycle, with a particular focus on brevity and specific experimental details that are necessary for the context of this thesis.

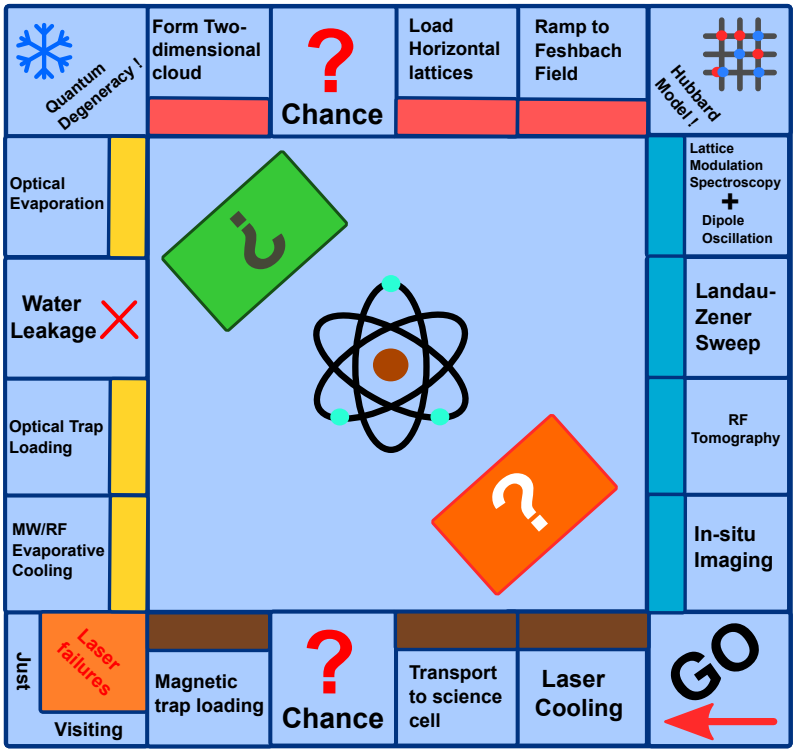

Figure 3.1: **The Quantum Gases "Monopoly".** Each experimental cycle (one loop around the board) takes 60 s, with the occasional unexpected chance for failures. Similar to most quantum gases experiment, the duty cycle begins with laser cooling of ^{40}K down to the Doppler temperature. This is followed by transportation to a magnetic trap and subsequent evaporative cooling. Quantum degeneracy is reached upon further evaporation in an optical dipole trap. A two-dimensional Hubbard model is realised by the juxtaposition of three individual optical lattices. Combining coherent control and high-resolution imaging, we probe the two-dimensional Fermi gases in optical lattices. Inspiration courtesy of E. Cocchi.

3.1.1 Laser cooling

Magneto-optical trap The first step of our experiment is based on laser cooling, which utilises the radiation pressure of laser light (photons) to simultaneously cool and confine the atomic gases [74, 75]. A standard three-dimensional magneto-optical trap (MOT) is deployed. A schematic diagram of the MOT chamber is shown in Fig. 3.2 **a**. The magnetic field is produced by a pair of magnetic field coils in anti-Helmholtz configuration outside the main chamber.[1] This generates a linear magnetic quadrupole field. This results in a position-dependent Zeeman splitting for the trapped atoms,

$$E_{\text{Zeeman}}(\boldsymbol{r}) = g_F m_F \mu_B |\boldsymbol{B}(\boldsymbol{r})|. \tag{3.1}$$

The main chamber is kept at vacuum with a pressure of 10^{-9} mbar by an ion pump. It is connected to a small oven with a potassium source. The potassium source used contains a high concentration of ^{40}K, about 10% as compared to its natural abundance of 0.0117(1)% [76]. For potassium, the oven only needs to operate at relatively low temperature of 350 K for sufficiently high vapour pressure for cooling.

At the beginning of the experimental cycle, six circularly polarised laser beams are sent into the MOT chamber and intersect at the centre of the magnetic quadrupole field. In order to achieve cooling, we make use of the D_2 transition ($|F = 9/2\rangle \rightarrow |F' = 11/2\rangle$), as shown in Fig. 3.2 **b**. We drive this transition with a laser (hereafter referred to as the ***cooling*** laser) that is slightly red-detuned. This cooling transition is not fully closed, a ***repumper*** laser is thus required to pump the atoms back to relevant ground states. The cooling laser is a single-frequency Ti:Sapphire laser (*Coherent MBR-110*), along with a high-power pump laser (*Verdi V18*). The repumping laser is a seed laser (*Toptica DL Pro*) fed towards a tapered amplifier (TA). The repumping laser is stabilised to a ^{39}K spectroscopy cell using frequency modulation spectroscopy [77]. The cooler laser is then stabilised to the repumper with an offset lock [78]. A detailed description of the laser locking schemes in our experimental apparatus can be found in [69, 70]. Relevant properties of ^{40}K, laser parameters and

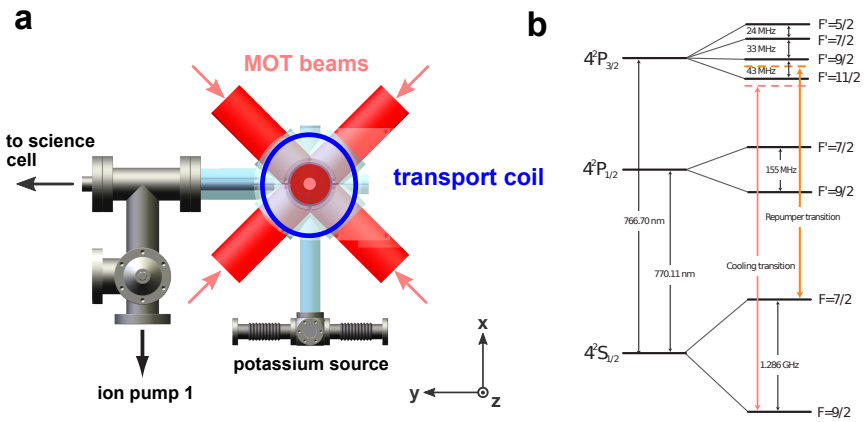

Figure 3.2: **Magneto-optical trap and levels scheme of ^{40}K. a** Top-down view of the MOT chamber. MOT beams containing both the cooling and repumping frequencies are sent in through six axes (pink). After atoms are loaded into the MOT for around 4 s, the transport coils (blue) mounted on a movable translation stage move over 70 cm to the science cell. Figure adapted and modified from [55].

[1] We note that MOT coils are named the transport coils since they double as magnetic trap used to transport the cooled atoms later on.

typical cooling results are summarised in Table 3.1.

natural abundance of ^{40}K	0.0117(1)%
atomic mass m	39.9639985 u
nuclear spin I	4
D_2 transition wavelength	766.700674872(173) nm
D_1 transition wavelength	770.108136807(144) nm
saturation intensity of D_2 transition I^0_{sat}	17.5 W/m^2
resonant absorption cross-section σ_0	0.2807 μm^2
natural linewidth of D_2 line	$2\pi \times 6.035(11)$ MHz
background scattering lengths a_{bg}	174 a_0
cooler power at atoms	$\sim$ 1 W
repumper power at atoms	$\sim$ 0.3 W
MOT loading time	$\sim$ 4 s
Doppler temperature T_D	$\sim$ 145 μK

Table 3.1: **Properties of ^{40}K and laser cooling parameters.** Properties of ^{40}K are from [76, 79]. The resulting performance of the MOT is subjected to daily variations of laser beams alignment, power drift and degradation of vacuum.

3.1.2 Transport and magnetic trapping

The following step of the experiment involves transporting the atomic sample to a second chamber (the science cell) with an ultrahigh vacuum. A lower pressure of 10^{-11} mbar in the science chamber (as compared to the MOT chamber) is maintained via differential pumping with a second ion pump. At the end of the MOT stage, atoms are optically pumped to states in the $|4^2S_{1/2} = 9/2\rangle$ manifold with positive magnetic moment ($g_F m_F \mu_B > 0$), which are ***low-field seeking*** states. Therefore, these atoms can be trapped in the magnetic field minimum of a magnetic quadrupole trap. The transport of atoms is achieved by a two steps process: first the current of the transport coils is increased up to 100 A to produce a strong enough confinement, and followed by physically moving the MOT coils (also referred to as the transport coils in Fig. 3.2 **a**) using a motorised translation stage over a distance of 70 cm [69, 70]. After moving to the science cell, the atoms in the quadrupole trap are transferred to an Ioffe-Pritchard trap [80]. This is achieved by ramping down the current of the transport coils while ramping up that of the Ioffe trap. The two long Ioffe bars produce a two-dimensional quadrupole field in the axial direction. The pinch and offset coils create an offset magnetic field to prevent ***Majorana losses*** at the magnetic field zero [81, 82]. The magnetic field coils, including those used later in the experimental stages, are shown in Fig. 3.3.

Evaporative cooling in magnetic trap Next, a microwave pulse is sent to the atoms via an antenna, and its frequency is swept. The aim is to perform a spin-flip of magnetically-trappable states in the $|4^2S_{1/2} = 9/2\rangle$ manifold to the non-trappable state in the $|4^2S_{1/2} = 7/2\rangle$ manifold (where the magnetic moment is negative $g_F m_F \mu_B < 0$). Due to the position-dependent magnetic field of the quadrupole trap, atoms at the outside of the trap experience the largest Zeeman energy shift. We adjust the microwave sweep such that it only resonates with atoms farthest away from the trap centre. These atoms, once transferred to the non-trappable states, leave the trap and remove thermal energy from the ensemble. This process is known as ***evaporative cooling***. A radio-frequency knife is used

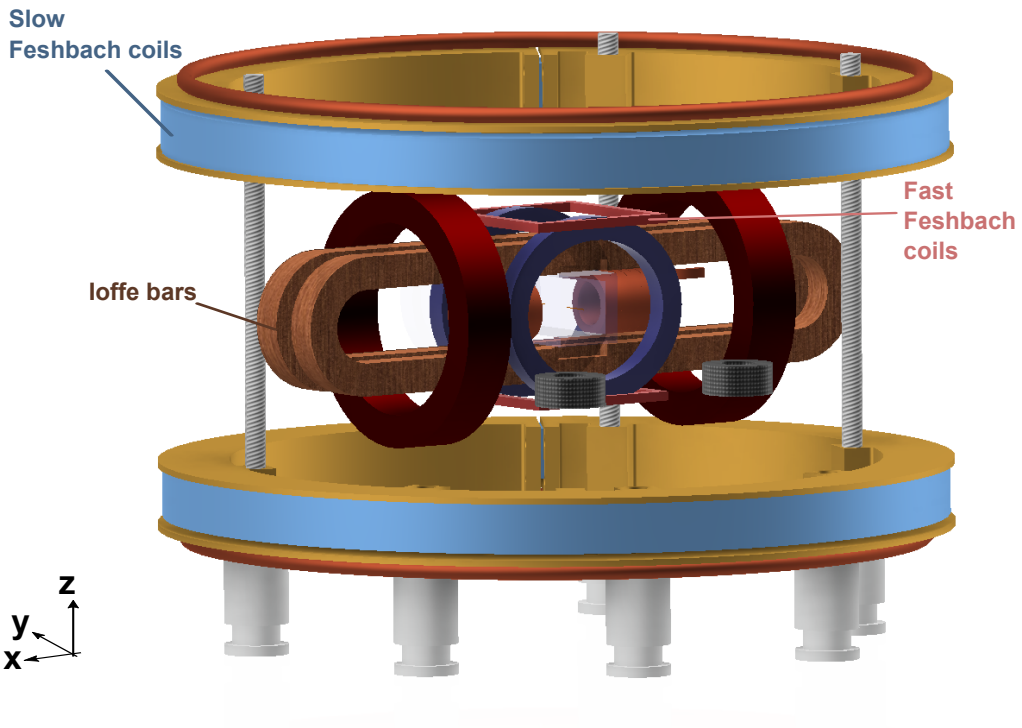

Figure 3.3: **Magnetic field coils setup.** Shown in the centre is the science cell (transparent blue). The long Ioffe bars (brown) provide an axially-symmetric two-dimensional quadrupole field. The pinch and offset coils (deep brown and deep red) are a set of coils to provide a magnetic field offset. The large circular coil pairs (light blue) is called the slow Feshbach coil, which is used to set a homogeneous magnetic field in later stages of the experiment. The rectangular coils above and below the science cell are the fast Feshbach coils which enable a quick change of the magnetic field over a smaller range as compared to the slow Feshbach coils. Finally, shown in grey are two small coils used to fine-tune the in-plane magnetic field gradient in the experimental xy-plane. These so-called gradient compensation coils can also be used to imprint phase patterns onto the atomic clouds (see Chapter 5). Figure adapted and modified from [72].

at the final stage of the microwave evaporation to complement the effect near the trap bottom and select the resulting hyperfine states [69, 70]. At the end of this evaporative process, a typical atom number of approximately $10(1) \times 10^6$ at a temperature of $2.6(2)\,\mu$K is achieved.

3.1.3 Optical trapping

While magnetic trapping provides a strong trapping potential for the atom cloud in a sizeable region, realising the Hubbard model with it is impractical. As discussed in Sec. 2.4.2, the magnetic field affects the scattering properties between atoms via the Feshbach resonance, and a position-dependent magnetic field is in general undesirable for further manipulation. To circumvent this drawback, we load the atomic cloud from the magnetic trap to a crossed-beam optical dipole trap. The optical dipole trap is based on the AC Stark effect described in Sec. 2.4.1. To this end, the magnetic field is adjusted by a large pair of Feshbach coils, providing a homogeneous magnetic field over the entire atomic cloud. Due to the conservative nature of the optical potential, the dipole trap does not transfer energy directly to the atomic cloud and hence is ideal for trapping and further cooling down the sample.

Evaporative cooling in optical dipole traps In Fig. 3.4 **a**, we show the schematic plot of our crossed-beam dipole trap setup. A highly asymmetric laser beam is sent through the science cell along the x-direction and is conveniently named as the horizontal dipole trap (DTh). The purpose of this asymmetric beam profile is two-fold; first, it squeezes the atomic cloud with its much shorter waist ($\sim 14.5\,\mu$m) along the vertical direction (z-direction), preparing for subsequent formation of a quasi two-dimensional cloud. Secondly, it provides a relatively shallow potential along the x-direction that is favourable for further evaporation down to quantum degeneracy.

A second "dimple" laser beam (conveniently named DTd) is sent in along the yz-plane, intersecting with the DTh. The main role of the DTd, as its name suggests, is to "poke" a hole in the trapping potential as shown in Fig. 3.4 **b**, which draws atoms into a small region and increases the local phase space density [83]. This so-called "dimple trick" offers a powerful tool in cooling atomic gases in all-optical configurations [84, 85]. The flexibility of optical light fields facilitates the realisation of quantum degenerate gases in various trapping geometries or optical evaporation involving multiple species ensembles [86, 87].

With two optical dipole traps in place, the experiment is in the position to perform the critical evaporative cooling down to quantum degeneracy, where $T < T_F$. This evaporative process is slightly different than the one previously introduced. Instead of relying on a microwave or radio-frequency pulses to select the atoms to be removed, the optical evaporation makes use of the inter-particle scattering process in which the more energetically atoms leave the trap earlier. Then the atomic cloud thermalises to lower temperatures after removal of the "hot" atoms. This process repeats when slowly ramping down the power of the DTh, which reduces the confinement for the outermost atoms, forcing them to leave the trap. In the final stage of our experiment, we mainly work with the lowest two hyperfine states $|F = 9/2, m_F = -9/2\rangle$ and $|F = 9/2, m_F = -7/2\rangle$. The optical evaporation is therefore adjusted based on the final atom number and temperature of the atomic cloud. Depending on whether we work at a magnetic field above or below the relevant s-wave Feshbach resonance around 202 G, we deploy slightly different evaporation schemes. This prevents the need for ramping

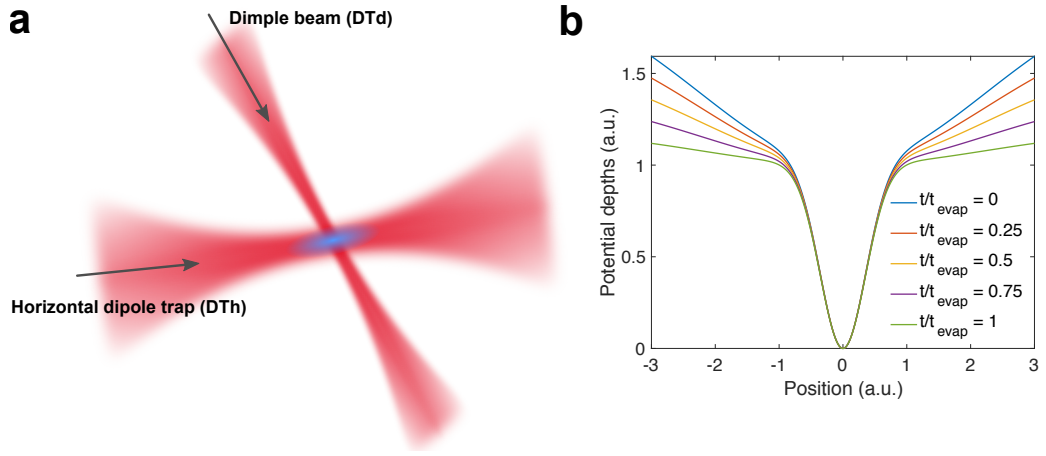

Figure 3.4: **Optical dipole traps and evaporative cooling. a** Schematic diagram for the cross-beam dipole trap. A highly asymmetric horizontal dipole trap (DTh) compresses the atomic clouds to a thin sheet, while the dimple trap (DTd) squeezes atoms within a small region for higher local phase space density. **b** Trap potential of the cross-beam trap in x-direction. The large Gaussian profile is provided by DTh, whereas the sharp potential well in the centre is provided by DTd. By ramping the down the DTh and keeping the DTd power fixed, atoms on the edge are forced evaporated out of the trap.

the magnetic field across unitarity in a lattice configuration.

3.1.4 Thermometry of trapped Fermi gases

At the end of the optical evaporation, we benchmark the temperature achieved by measuring the momentum distribution profile of the Fermi gases. We deploy a time-of-flight (TOF) measurement by switching off the optical trap suddenly and allowing the atomic cloud to undergo ballistic expansion while falling down with gravity (see Fig. 3.5 **a**). The atomic distribution is taken via absorption imaging along the y-direction. By fitting the recorded atomic cloud profile with the following fitting function [88],

$$n_{2\mathrm{D}}(x,y) = n_{2\mathrm{D},0}\frac{\mathrm{Li}_2\left(\pm\exp\left[q-\left(\frac{x^2}{R_x^2}+\frac{y^2}{R_y^2}\right)f\left(e^q\right)\right]\right)}{\mathrm{Li}_2\left(\pm e^q\right)}, \tag{3.2}$$

one can extract the logarithm of the ***fugacity*** $q = \mu\beta$. For small fugacity (large, negative q), the fitting function reduces to a Gaussian distribution of a thermal cloud. For high fugacity (large, positive q),

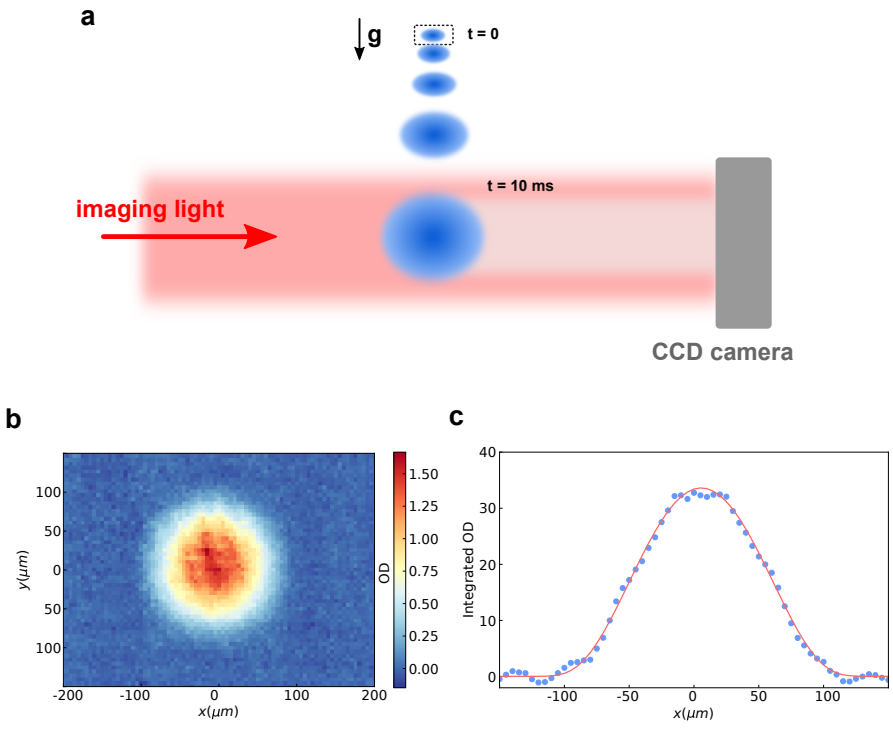

Figure 3.5: **Time-of-flight (TOF) thermometry after evaporation in optical dipole traps. a** After a ballistic expansion of $t_{\mathrm{TOF}} = 10\,\mathrm{ms}$, the atomic profile is captured by absorption imaging. **b** Typical absorption images after TOF, averaged over 5 experimental realisations. **c** Data points shown are integrated optical density along the y-direction. Deploying the fit function (solid line) in Eq. (3.2) results in a normalised temperature of $T/T_F = 0.09(1)$ with $2.03(9)\times10^5$ atoms.

the fitting function approaches the ***Thomas-Fermi*** profile

$$n_{2D}(x,y) = n_{2D,0}\left(1 - \frac{x^2}{R_{Fx}^2} - \frac{y^2}{R_{Fy}^2}\right). \tag{3.3}$$

Fig. 3.5 **b** shows a typical absorption image used for thermometry and Fig. 3.5 **c** shows a fit to the density profile using Eq. (3.2). At this point, we obtain a quantum degenerate Fermi gas with a degeneracy parameter $T/T_F = 0.11(1)$ with $1.75(3) \times 10^5$ atoms when the optical evaporation takes place at a magnetic field of 189 G.

3.2 Experimental setup of optical lattices

In this section, we describe the experimental setup to realise a two-dimensional optical lattice. First, we discuss the vertical optical superlattice, which produces multiple two-dimensional atomic clouds. Next, we lay out the setup for the in-plane optical lattices. Finally, we outline the experimental calibration of the lattice depths and trapping frequencies, which ultimately opens access to the overall optical potential landscape.

3.2.1 Two-dimensional Fermi gases via vertical superlattices

Optical superlattice To realise a two-dimensional quantum system, we first make use of a vertical ***superlattice*** in accordion configuration as shown in Fig. 2.9 **b**. In our experiment, we implement the optical superlattice with laser light of two distinct wavelengths λ_1 and λ_2. The purpose of the optical superlattice will be apparent in Sec. 3.3.2. Here, we consider two independent optical lattice potentials of different wavelengths with mutually-orthogonal polarisations. Thus, there is no interference between the two lattice potentials due to the mismatched polarisations. The lattice depths of two potentials, V_1 and V_2 can be tuned independently. In our particular usage, the lattice spacings are chosen to be $a_1 = \frac{\lambda_1}{2}$ and $a_2 = 2a_1$, respectively. Henceforth, we name the former as the *short-wavelength* lattice and the latter as the *long-wavelength* lattice. In this case, the one-dimensional potential, ignoring effects from Gaussian, inhomogeneous beam profiles, can be locally written as

$$V_{\text{superlattice}}(z) = V_1 \sin^2\left(\frac{\pi}{a_1}z\right) + V_2 \sin^2\left(\frac{\pi}{2a_1}z + \phi\right). \tag{3.4}$$

Here ϕ is the relative phase between the two optical lattices. The phase difference can be adjusted by introducing an optical path length difference between the two laser beams forming the lattice structure, *i.e.* $\phi = nkd$, where n is the refractive index of the propagating medium, $k = 2\pi/\lambda$ is the optical wavevector and d is the path difference. For simplicity, we first focus on the case $V_1 = V_2$. In Fig. 3.6, we schematically depict the idea of an optical superlattice. By varying ϕ, the structure of the superlattice changes. When ϕ is an *even* multiple of $\pi/4$, *i.e.*

$$\phi = m\frac{\pi}{4} \text{ and } m = 0, 2, 4, \cdots. \tag{3.5}$$

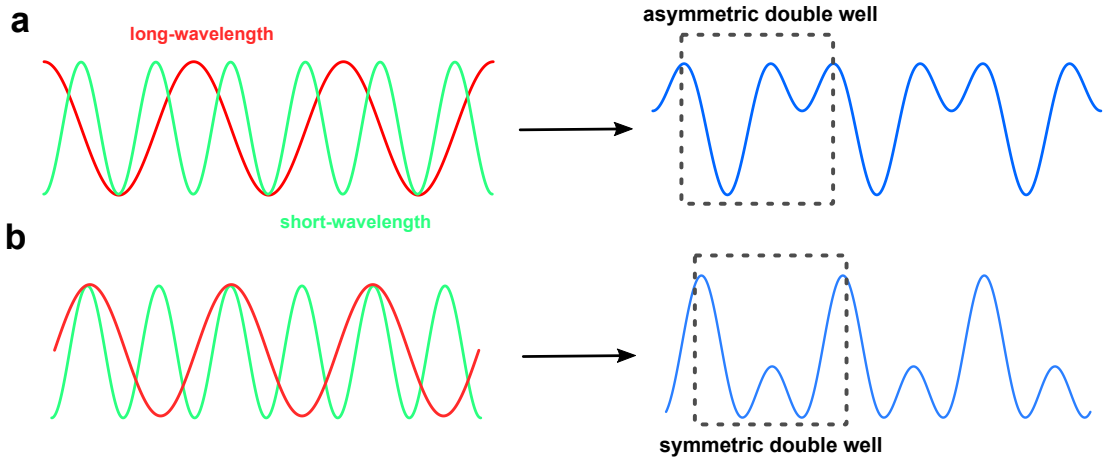

Figure 3.6: **Optical superlattice. a** Asymmetric configuration of superlattice. **b** Symmetric configuration of superlattice.

The potential minimum of the long-wavelength lattice coincides with that of the short-wavelength lattice. This results in a series of lattice sites with alternating deep and shallow depths. A series of these alternating deep and shallow wells can be considered as a periodic lattice containing two sub-lattices. On the other hand, when ϕ is an *odd* multiple of $\pi/4$, *i.e.*

$$\phi = m\,\frac{\pi}{4} \text{ and } m = 1, 3, 5, \cdots . \tag{3.6}$$

The potential minimum of the long-wavelength lattice is located in the middle of two adjacent sites of the short-wavelength lattice. This results in an equal magnitude pull-down of each site of the short-wavelength lattice. As shown in Fig. 3.6 **d**, the superlattice, in this case, consists of a periodic assembly of symmetric double-well potentials. For deep lattice depths and sufficiently low temperature T, the atoms trapped in a single lattice site become *quasi* two-dimensional as the thermal energy $k_B T$ is much smaller than the longitudinal trap frequency ω_z, *i.e.* $k_B T \ll \hbar\omega_z$.

Optical setup The optical setup for the vertical superlattice is shown in Fig. 3.7. For the short-wavelength lattice, we deploy a 532 nm laser (*Coherent Verdi V10*). It is sent in a direction parallel to the yz-plane and split into 50:50 ratio by a polarising beam splitter (PBS). On the lower beam path, a half-wave plate rotates the polarisation about 90° such that it can form an interference pattern with the upper beam path. For the long-wavelength lattice, we use a single-frequency, high power laser with wavelength twice that of the green laser, *i.e.* 1064 nm (*Mephisto MOPA*). After beam shaping optics, the infrared beam is sent into the other port of the PBS. We note that the PBS used here is only polarisation-splitting around 532 nm wavelength, therefore, for the infrared beam the polarisation emerging from the cube is not perfectly p- and s-polarised and it results in a finite imbalance of beam powers. A small glass-plate is placed on the upper beam path to introduce a sufficient path difference between the upper and lower beams in order to achieve the required phase tunability.

Superlattice as a tool for sublattice evaporation Finally, we outline the motivation for implementing an optical superlattice along the vertical direction. As will be shown in Sec. 3.3.2, we employ a radio-frequency (RF) tomography procedure for the detection of a single two-dimensional layer. Without this tomography procedure, imaging the atomic ensemble along the z-direction would

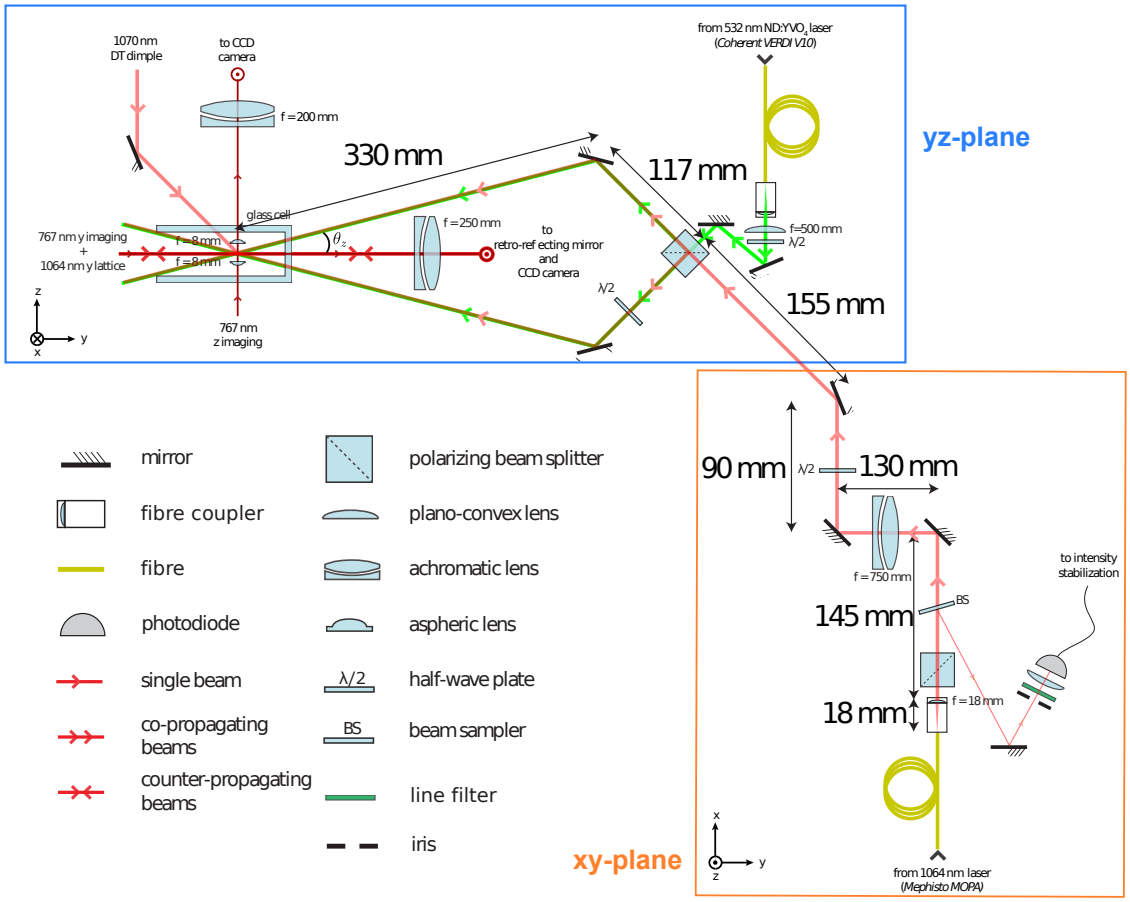

Figure 3.7: **Optical setup for vertical superlattice.** Figure adapted and modified from [72].

result in column-integrated density profile. The critical procedure in the tomography sequence is to use a vertical magnetic field gradient (generated by the fast Feshbach coils in anti-Helmholtz configuration) to discriminate individual planes. Our ability to address one single plane depends significantly on the magnetic field stability of the system.

In addition, the optical superlattice provides a controllable way to evaporate individual two-dimensional atomic gases further. As shown in Fig. 3.8, by utilising the asymmetric configuration with a careful adjustment of the laser intensities, the potential of one sublattice A deepens while that of sublattice B becomes shallower. The end result is that, in the middle of the loading process, the B sublattice can no longer trap the atoms. The atoms in these sites then leave the sublattice along with gravity as the longitudinal confinement loosens. Although by the time of evaporation, the tunnelling between deep and shallow sites is already strongly suppressed, and thus no significant cooling effect is observed. This approach effectively doubles our lattice spacing along the vertical direction at the end of the evaporation by only loading atoms into the A sublattice. As a result, this allows a much more stable tomography process in the extraction of two-dimensional samples. Comparison of tomography performance with and without the superlattice can be found in Sec. 3.3.2 and Fig. 3.12.

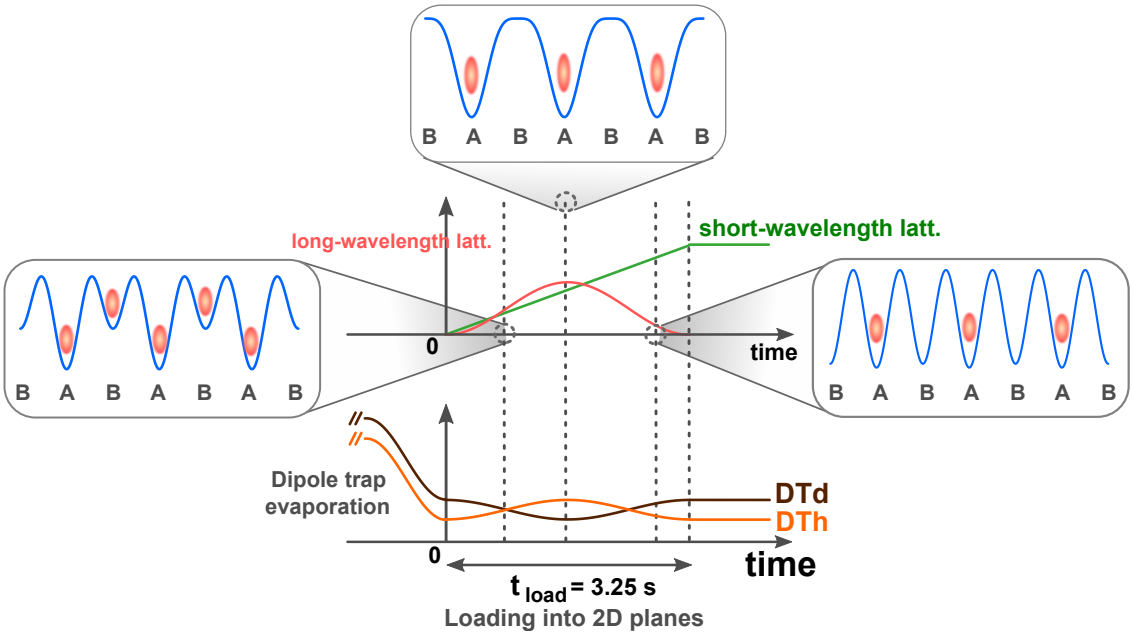

Figure 3.8: **Removal of atoms in sublattices.** Shown is the experimental sequence for eliminating atoms in one of the sublattices (labelled B here) along the vertical direction. After the optical evaporation in the dipole trap, we load the atom clouds into the superlattice in an asymmetric configuration. The short-wavelength lattice depth increases linearly with time, whereas the long-wavelength lattice ramps up to an intermediary peak and then ramps down to zero. We pin-point three particular scenes during the loading process. At the beginning (instance 1), the lattice depths of both short and long-wavelength lattices are similar, forming a superlattice where two sublattices A and B have a small offset. Next, the long-wavelength lattice outweighs the short one (instance 2). Therefore the on-site trap frequency of the sublattice B reduces and atoms can no longer be trapped. This allows atoms to leave the system via gravity or tunnelling to the sublattice A. Finally, at the end of the loading process (instance 3), the long-wavelength lattice depths become zero, and only sublattice A is filled with two-dimensional samples. The overall process takes 3.25 s in order to avoid non-adiabaticity and is optimised based on the final temperature reached in the experiment. We note that during the loading process, the laser powers of the dipole traps are also adjusted in order to maintain similar in-plane trapping frequencies to avoid excessive loss of atoms in sublattice A.

3.2.2 Horizontal lattice

After the loading into the vertical lattice, two horizontal lattices within the xy-plane are turned on. We deploy the counter-propagating configuration discussed in Fig. 2.9 **a**. Similar to the vertical lattice, we utilise orthogonal polarisation between the lattices along the x- and y-direction (henceforth, they are referred to as the x-lattice and y-lattice, respectively).

Fig. 3.9 depicts the optical setup for the x- and y-lattices. Both lattices have a wavelength of 1064 nm and originate from the same single-frequency, narrow-linewidth laser source (*Innolight Mephisto MOPA 15W*). In order to avoid internal reflection from the glass cell back onto the atom clouds, the lattice beams enter the glass-cell at a slight angle. The two-dimensional lattice realised here is not a perfect square lattice. Instead x-lattice and y-lattice intersect at an angles of $\theta_{xy} = 85.5°$. The beam waists of both the x-lattice and y-lattice are intentionally shaped such that they are of similar size ($\sim 170\,\mu$m). We note that, throughout our experimental measurement, we do not observe a significant dependence of this small angle deviation from a perfectly square lattice. Therefore, as

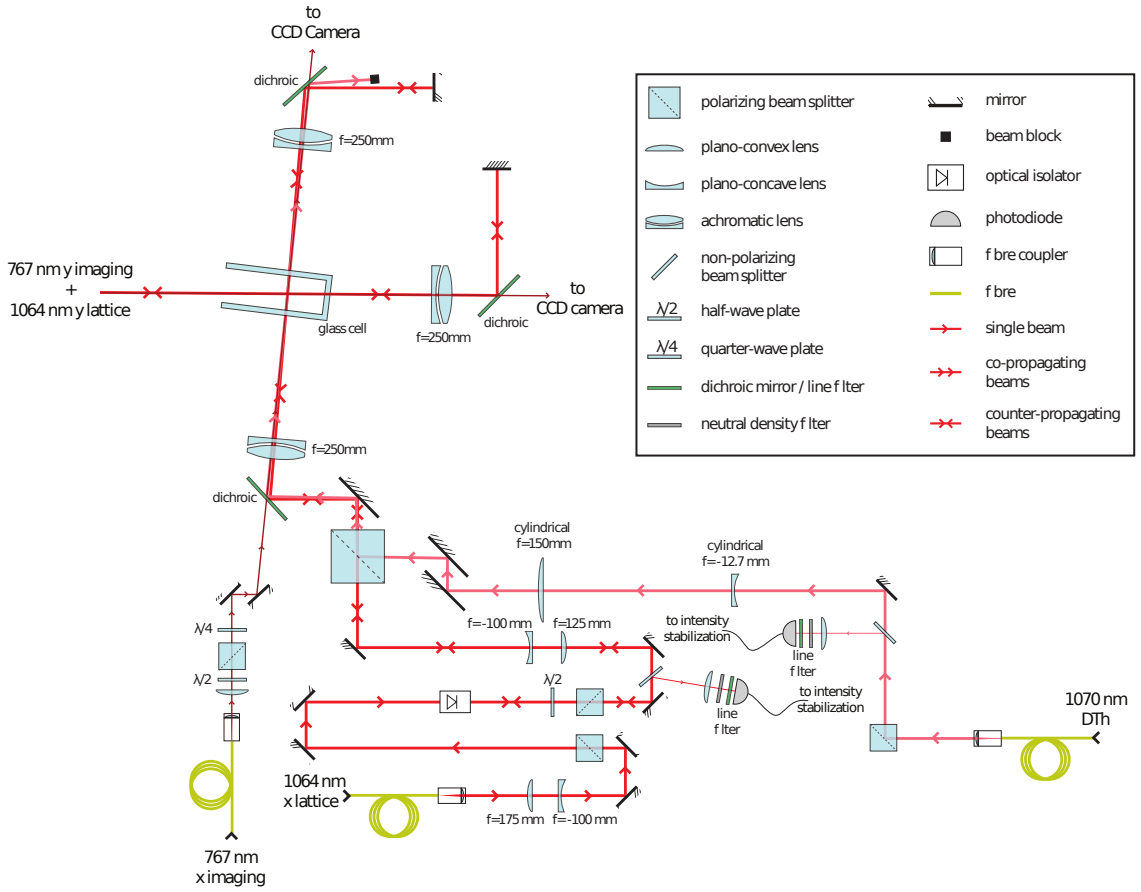

Figure 3.9: **Optical setup for in-plane lattices.** Figure adapted and modified from [72].

will be shown in later chapters, we still compare our experimental measurement with theoretical calculations results based on a square lattice.

Typically, during in-plane lattice loading, we deploy a sine-squared ramp shape in intensity. One primary reason for this is to prevent higher band occupations at the final lattice depths of $V_{x/y} = 6\,\mathrm{E_R}$. We note that in two-dimension, the ground band and the first excited band are not gapped until a small but non-zero lattice depths ($V_{\mathrm{latt}} \sim 2\,\mathrm{E_R}$). This explains the slow intensity ramp during the initial stage in order to ensure maximal adiabaticity during loading and avoid higher band excitation. In Chapter 5, we make use of correlation thermometry to investigate the problem of local and global thermalisation during lattice loading.

3.2.3 Characterisation of the lattice potential

To calibrate the Hubbard parameters, it is imperative to accurately characterise the lattice potentials formed by the juxtaposition of laser beams. Below, we describe two major measurements required for characterising the overall optical potential. First, we start with lattice modulation spectroscopy which determines the individual lattice depths by driving band transitions. Second, we measure the trap frequency of optical lattice potential by exciting dipole modes near the trap centre, where the

confinement is harmonic. Finally, combining the knowledge of lattice depths and trap frequencies, one can infer the relevant lattice beam waists at the position of the atoms. This allows us to reconstruct the underlying confinement beyond harmonic approximation and thus enables the use of local density approximation in later chapters.

Lattice modulation spectroscopy: calibration of lattice depth Introducing low-amplitude, periodic modulation to the Hamiltonian is a common way to "inject" energy into a many-body quantum system. This can be readily understood from a perturbation perspective, where the transition probability per unit time from the initial state $|\psi_i\rangle$ to the final state $|\psi_f\rangle$, to first order, is given by

$$\Gamma_{i\to f} = \frac{2\pi}{\hbar} \left|\langle \psi_f \left| H' \right| \psi_i \rangle\right|^2 g(E_f). \tag{3.7}$$

Here, $g(E_f)$ is the ***density of states*** at energy of the final state. Eq. (3.7) is know as the ***Fermi's golden rule*** [49]. In a lattice system, we can consider a time-periodic perturbation in the lattice depth (shown in Fig. 3.10 **a**), *i.e.*

$$V(t) = V_0 + \underbrace{\delta V \sin(2\pi\nu t)}_{=H'} . \tag{3.8}$$

The perturbation limit is satisfied for $\delta V \ll V_0$. In addition, for sufficiently large lattice depths, we note that the first few energy bands approach the so-called ***narrow band*** regime (see Sec. 2.4.1). In this limit, one can effectively treat the energy levels as a quantum harmonic oscillator. One immediate

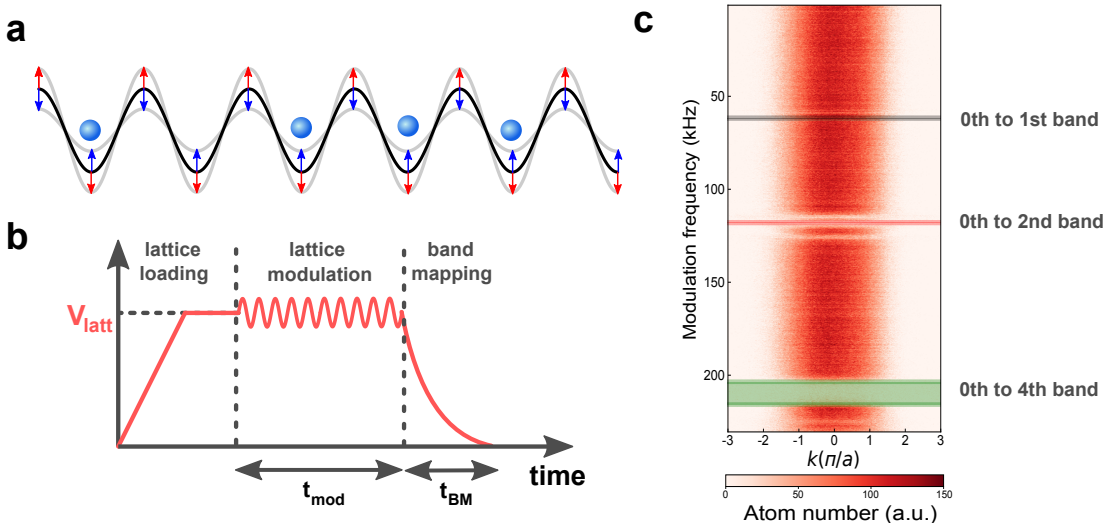

Figure 3.10: **Lattice modulation spectroscopy. a** Periodic modulation of lattice depth. Modulation scheme according to Eq. (3.8). We note that this is an intensity modulation, and not a phase modulation of the optical lattice, which would shift the absolute position of lattice sites. **b** Experimental sequences of lattice modulation. After loading the atomic cloud into the lattice potential, the lattice modulation is turned on for $t_{\mathrm{mod}} = 100\,\mathrm{ms}$ to drive the interband transition. Afterwards, the lattice beams power are ramped down adiabatically within a time $t_{\mathrm{BM}} = 4\,\mathrm{ms}$ for band mapping. **c** Excitation spectrum of lattice modulation at lattice depth $V_0 = 60$. The sharp decrease in atom number upon modulation signals the interband transitions. The 0 to 2^{nd} band transition is the narrowest due to the deep lattice limit, whereas the 0 to 4^{th} one is much broader.

observation regarding the transition probability is that any even wavefunction can only transition to another state with even symmetry, otherwise the integral $\langle\psi_f|H'|\psi_i\rangle \approx 0$.

By driving the inter-band transitions, the occupations of the lowest band decrease, giving a clear signal to the transition frequency. In Fig. 3.10 **b**, we show the schematic sequence for lattice modulation spectroscopy. The lattice intensity is first ramped up to the desired level of V_0. Subsequently, a simple sinusoidal modulation of frequency ν is applied. Finally, we adiabatically ramp down the laser intensity for the lattice, such that the quasi-momentum is mapped to real momentum. This is known as ***band mapping***. By measuring the reduced occupation in the first Brillouin zone, we obtain the transition energy of the relevant inter-band transition. From this, we can infer the lattice depth V_0 by comparing the spectrum to band structure calculations, as shown in Fig. 3.10 **c**.

Dipole oscillation : calibration of trap frequencies In optical lattices, the Gaussian laser beams result in an underlying spatial profile of the laser intensity, thereby inducing spatial inhomogeneity. This can be considered as a lattice structure with an underlying slow-varying potential. Near the trap centre, such confinement can be approximated by a quadratic term, *i.e.*

$$V_{\text{trap}}(x,y,z) = \frac{1}{2}\left(\omega_x x^2 + \omega_z z^2 + \omega_z z^2\right) + O(\boldsymbol{r}^4). \tag{3.9}$$

For our two-dimensional quantum gases, the trap frequency along the vertical direction is much larger than that in the transverse direction, *i.e.* $\omega_z \gg \omega_x, \omega_y$ and we are within the quasi two-dimensional regime ($k_B T \ll \omega_z$). Therefore, we are only interested in the trap frequencies within our two-dimensional lattice plane. One straight forward way to obtain the trap frequency is by the excitation of a dipole mode oscillation.

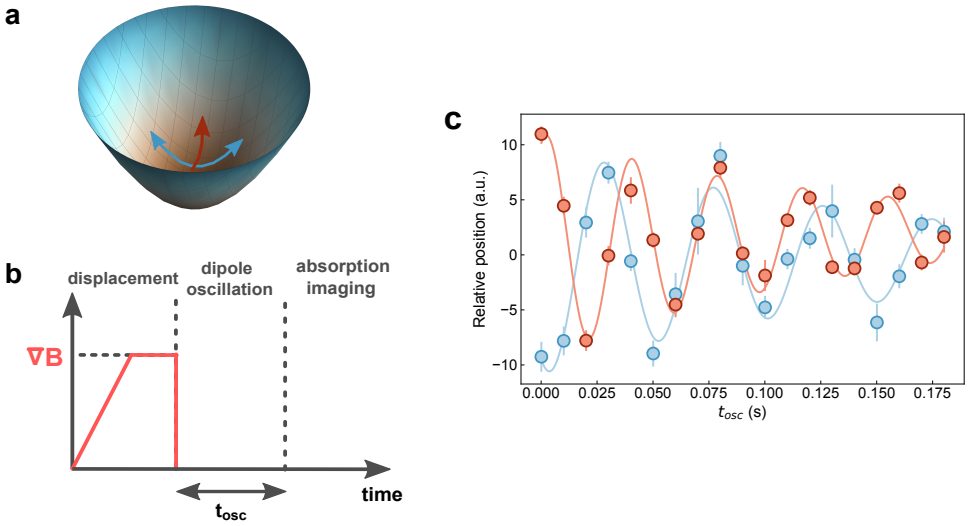

Figure 3.11: **Dipole Oscillations. a** Dipole oscillation. A magnetic field gradient displaces the atomic cloud away from it equilibrium position at the trap centre, thus inducing a collective oscillation about the x-axis (blue bi-arrows) and y-axis (red). **b** Experimental sequence for exciting the dipole mode. A magnetic field gradient is ramped up to a constant value to induce the displacement. A sudden turn off of this gradient results in the oscillation. **c** Dipole oscillations. Experimental data of dipole modes along the x-(blue) and y-direction (red), with oscillating frequencies of 20.7(2) Hz and 26.2(3) Hz, respectively. Solid lines are the fits using Eq. (3.10).

In Fig. 3.11 **a** and **b**, we outline the trap frequency measurement sequence deployed. A magnetic field gradient creates a displacement in the position of the atomic cloud. The magnetic field gradient is then abruptly switched off, inducing the so-called ***sloshing*** motion. We then allow a variable oscillating time t_{osc} and finally image the atomic cloud profile using the imaging setup along the z-direction (see Sec. 3.3.3). From the center-of-mass motion of the atomic cloud, we can fit the solution of a damped harmonic oscillator,

$$x(t) = A\mathrm{e}^{-\zeta\omega_0 t}\sin\left(\sqrt{1-\zeta^2}\omega_0 t + \varphi\right). \tag{3.10}$$

3.2.4 Potential landscape

Combining the experimental measurement of the lattice depths and trap frequencies, we can deduce the potential landscape within the xy-plane. We note that there are two contributions to the external confinement. First, the spatial intensity variations of laser beams lead to a potential offset between individual lattice sites. This term is directly proportional to the intensity distribution of the laser beam. Second, we point out that atoms are not simply residing at the potential minimum and taking up its value as energy. Instead, atoms conform to the quantum mechanical states. By Taylor expansion of the lattice potential, we can approximate the potential near its minimum as

$$\gamma V_{\text{latt}}\cos^2(kx) \simeq \gamma V_{\text{latt}}\left(1-k^2x^2\right). \tag{3.11}$$

And the harmonic oscillator frequency is given by

$$\omega_{\text{on-site}}^2 = \frac{2k^2}{m}\gamma|V_{\text{latt}}|. \tag{3.12}$$

Here, $\omega_{\text{on-site}}$ is the harmonic oscillator frequency in a single lattice well and γ is the intensity imbalance due to power loss in the retro-reflected beam.[2] We note that quantum mechanically, each site contains a zero-point energy $\varepsilon = \frac{\hbar\omega_{\text{on-site}}}{2}$. Therefore a spatially-varying lattice depths result in a spatially-varying zero-point energy. Using Eq. (3.12), we can conclude that the zero point energy profile is proportional to the square of lattice depths $\sqrt{V_{\text{latt}}}$. Taking both effects into account, we can write down the overall confinement potential as follow

$$\begin{aligned}
U_{z\,\text{latt}}(x,y) &\simeq E_{\text{R},z}\left[\frac{(1-\sqrt{\gamma_z})^2}{4\sqrt{\gamma_z}}\frac{V_z}{E_{\text{R},z}}e^{-2\left[\left(\frac{x}{w_z}\right)^2+\left(\frac{y\sin\theta_z}{w_z}\right)^2\right]}+\sqrt{\frac{V_z}{E_{\text{R},z}}}e^{-\left[\left(\frac{x}{w_z}\right)^2+\left(\frac{y\sin\theta_z}{w_z}\right)^2\right]}\right],\\
U_{x\,\text{latt}}(x,y) &\simeq E_{\text{R},x}\left[-\frac{(1+\sqrt{\gamma_x})^2}{4\sqrt{\gamma_x}}\frac{V_{xy}}{E_{\text{R},x}}e^{-2\left(\frac{x\sin\theta_x+y\cos\theta_x}{w_x}\right)^2}+\sqrt{\frac{V_{xy}}{E_{\text{R},x}}}e^{-\left(\frac{x\sin\theta_x+y\cos\theta_x}{w_x}\right)^2}\right],\\
U_{y\,\text{latt}}(x,y) &\simeq E_{\text{R},y}\left[-\frac{(1+\sqrt{\gamma_y})^2}{4\sqrt{\gamma_y}}\frac{V_{xy}}{E_{\text{R},y}}e^{-2\left(\frac{x\cos\theta_y-y\sin\theta_y}{w_y}\right)^2}+\sqrt{\frac{V_{xy}}{E_{\text{R},y}}}e^{-\left(\frac{x\cos\theta_y-y\sin\theta_y}{w_y}\right)^2}\right].
\end{aligned} \tag{3.13}$$

Here $U_{x/y/z}$ is the confinement resulting from the $x/y/z$-lattices. $\theta_{x/y/z}$ are the angles between the lattice propagation directions and the principle axes ($x/y/z$-direction), respectively. The knowledge of this confinement potential enables us to map local the spatial coordinates to *iso-potential* regions.

[2] For the three lattices, we have $\gamma_z = 1$ due to the accordion configuration, $\gamma_x \approx 0.84$ and $\gamma_y \approx 0.77$.

3.3 Detection techniques

Throughout this thesis, we investigate the equilibrium physics of the Hubbard model. After loading the atomic cloud into the optical lattices. We allow for a variable equilibration time before increasing the lattice depths of all three optical lattices within a time τ much faster than the characteristic tunnelling time, *i.e.* $\tau \ll h/t$. In this way, the atomic density distribution is said to be ***frozen***, meaning that the tunnelling dynamics happens at a much slower time, which can be neglected in our subsequent detection phase. In this final section, we introduce the necessary experimental protocols for coherent control and manipulation of the atomic ensemble during the detection.

3.3.1 State manipulation

Fundamentals of a two-level system We first consider a single atom under a coherent electric field $\boldsymbol{E}(t) = \boldsymbol{E}_0 \cos(\omega t)$. Given an appropriately chosen driving frequency ω, the atomic energy levels can be considered as a two-level system involving only the relevant energy states. The full time-evolution of such a two-level system can be written as a state-vector

$$|\psi\rangle = a_g(t)\,|g\rangle + a_e(t)\,|e\rangle\,. \tag{3.14}$$

Here $|g\rangle$ and $|e\rangle$ are the ground and excited state of the atom, with $a_g(t)$ and $a_e(t)$ being complex and time-dependent coefficients. The Schrödinger equation for this two-level system in the rotating frame can be written as

$$\frac{\mathrm{d}}{\mathrm{d}t}\begin{pmatrix} a_g(t) \\ a_e(t) \end{pmatrix} = \begin{pmatrix} 0 & \frac{1}{2}\Omega_0(t) \\ \frac{1}{2}\Omega_0(t) & \Delta(t) \end{pmatrix}\begin{pmatrix} a_g(t) \\ a_e(t) \end{pmatrix}. \tag{3.15}$$

The off-diagonal terms contain the so-called **Rabi frequency** $\Omega_0 \propto |\boldsymbol{E}_0|^2$, which describes the light-matter interaction between the two energy levels. Here, we defined $\Delta(t) = \omega_0 - \omega(t)$ as the detuning of the electric field with respect to the two-level transition energy ω_0. The populations of ground and excited state are given by $|a_g(t)|^2$ and $|a_e(t)|^2$, respectively.

Rabi oscillation The solution of Eq. (3.15) results in a coherent oscillation between the ground state and excited state population. For two-level systems initially fully populated in the ground state, i.e. $|a_g(t=0)| = 1$, the time evolution of the ground and excited state populations are given by

$$\begin{aligned} P_g(t) &= |a_g(t)|^2 = \cos^2\left(\frac{1}{2}\int_0^t \Omega(t')dt'\right), \\ P_e(t) &= |a_e(t)|^2 = \sin^2\left(\frac{1}{2}\int_0^t \Omega(t')dt'\right). \end{aligned} \tag{3.16}$$

The integral in Eq. (3.16) is the pulse area and $\Omega(t) = \sqrt{\Omega_0^2(t) + \Delta(t)}$. For $\int_0^t \Omega(t')dt' = \pi$, the driving field is said to realise a ***π-pulse***, at which the probability of occupying the excited state is unity. And for $\int_{t=0}^t \Omega(t')dt' = \pi/2$, we have a ***π/2-pulse*** at which the state is in a equal superposition of the ground and excited states.

Landau-Zener sweep Another way to transfer an atomic state coherently from one to another is to use a frequency sweep of the driving field $\boldsymbol{E}(t)$. When the rate of the frequency sweep is slow with respect to the energy gap between two states, the population can be transferred between the two dressed states with high fidelity. The driving induces an avoided crossing to make the adiabatic transfer possible. In the limit of infinitely-slow sweep, *i.e.* $|d\Delta/dt| \to 0$, known as the Landau-Zener (LZ) limit, the following transfer probability from state $|a\rangle$ to $|b\rangle$ is given by

$$P_{a\to b} = 1 - \exp\left(-\frac{\pi^2\Omega_0^2}{2|d\Delta(t)/dt|}\right). \tag{3.17}$$

One example of a common LZ sweep used in the detection phase is the coherent transfer between magnetic hyperfine states. We take the energy states of ^{40}K in the $F = 9/2$ manifold as an example. At a magnetic field of $189(G)$, typical energy difference between hyperfine states ranges from $\Delta E/h = 45\,\mathrm{MHz}$ to $\Delta E/h = 52\,\mathrm{MHz}$. The LZ sweep can thus be achieved using a radio-frequency (RF) pulse. We linearly sweep the detuning of the RF pulse across the resonant frequency, with a window of 175 kHz in a duration of 2 ms. Here, the amplitude of the RF pulse follows a smoothed box envelope to prevent non-adiabatic projection. Further details of pulse shaping and coherent manipulation can be found in [55, 72].

3.3.2 Single-plane tomography

One critical aspect in investigating a system with multiple two-dimensional layers is to ensure that the system being probed only contains information from one single two-dimensional layer. This is in particular important in local measurements such as density and correlations. Simultaneously probing more than one uncorrelated two-dimensional planes would result in the undesirable, uncorrelated background, which is hard to remove in the analysis.

We deploy a tomographic approach in resolving a single layer of our entire atomic ensemble. The basic idea is to utilise a vertical magnetic field gradient, such that the resonant transition frequencies are shifted due to the Zeeman effect. Then, a specifically shaped RF pulse is shone onto the system to address one single layer. In order to achieve this addressing, the RF pulse needs to fulfil a more stringent requirement compared to a global LZ sweep discussed before. For one thing, we require the frequency spread of the RF pulse being sufficiently narrow with respect to the transition energy difference between neighbouring two-dimensional layers. At the maximum gradient strength that the fast Feshbach coils can reliably produce without overheating ($dB/dz \approx 33.3\,\mathrm{G/cm}$), the frequency shift is approximately $641(14)\,\mathrm{Hz}$ per plane for the transition between $|F = 9/2, m_F = -5/2\rangle$ and $|F = 9/2, m_F = -3/2\rangle$.

However, it is also beneficial to address the single layer with the highest fidelity as well as stability. Therefore, this motivates the use of RF pulse with a flat-top frequency feature. We deploy the so-called hyperbolic-secant (HS1) pulse, which can be generated with a combination of amplitude and frequency modulation,

$$\begin{aligned} E_{\mathrm{HS1}}(t) &= E_0\,\mathrm{sech}\left(\left[C_{\mathrm{trunc}}\left(\frac{2t}{T_{\mathrm{pulse}}-1}\right)\right]\right), \\ \Delta_{\mathrm{HS1}}(t) &= \frac{\Delta_0}{2}\tanh\left(\left[C_{\mathrm{trunc}}\left(\frac{2t}{T_{\mathrm{pulse}}-1}\right)\right]\right). \end{aligned} \tag{3.18}$$

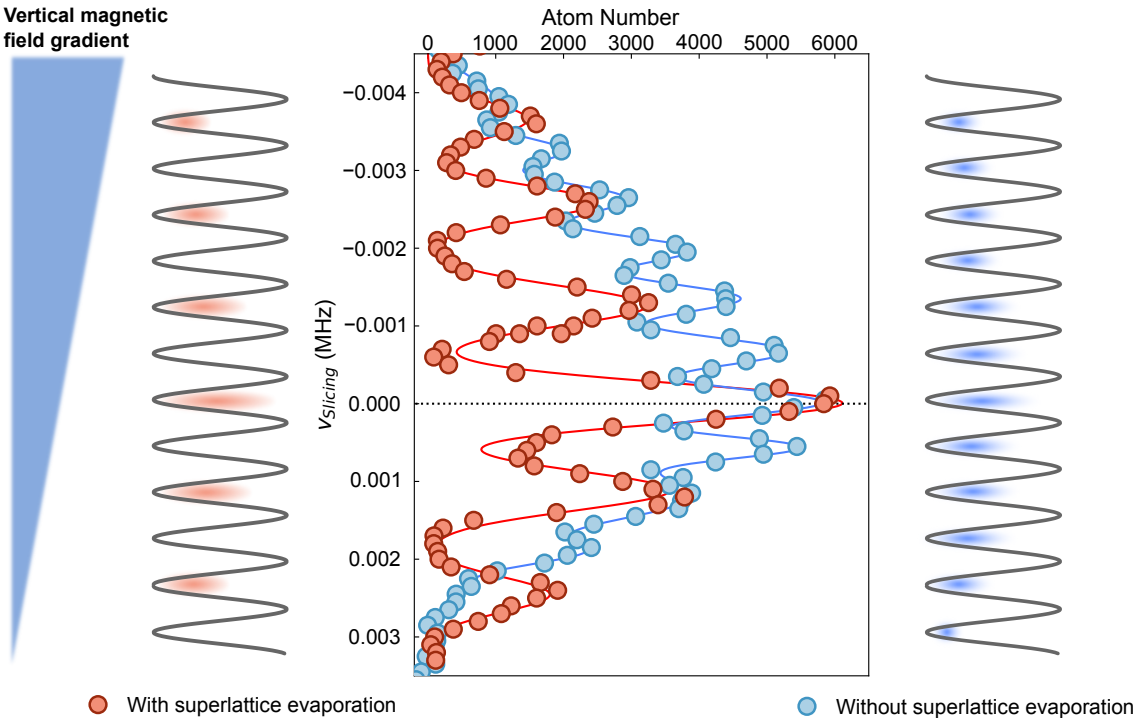

Figure 3.12: **Single-plane tomography.** Tomography spectra with and without the superlattice evaporation described in Sec. 3.8. A magnetic field gradient $dB/dz = 33.3\,\mathrm{G/cm}$ provides the relative Zeeman shifts in transition frequency between hyperfine states. Solid lines are fit with multiple Gaussian peaks overlapped, from which we extract a frequency spacing between neighbouring planes of $\Delta\nu = 641(14)\,\mathrm{Hz}$.

We optimise the final shape of the frequency profile of the HS1 pulse using a truncation parameter $C_{\mathrm{trunc}} = 4.5$ and a pulse window $T_{\mathrm{pulse}} = 7\,\mathrm{ms}$.[3] In Fig. 3.12, we show the tomography spectra of our two-dimensional gases. With the requirement of addressing a two-dimensional layer, one powerful utility of the vertical superlattice can be fully justified. Without emptying one of the sublattices as shown in Fig. 3.8, the slicing spectra typically consist of overlapping resonance peaks. To ensure data quality, only data points at the peak are selected for post-analysis in all of the experiments. With the additional evaporation in the optical superlattice, the "effective" plane separation is doubled, therefore, allowing the use of RF pulse with wider windows for improved data quality and data acquisition rate.

3.3.3 High resolution in-situ imaging

At last, we are in the position to discuss the final stage of the experiment, namely the *in-situ* imaging of the atomic distribution. We deploy conventional absorption imaging technique. We first outline the modified Beer-Lambert law used to deduce the optical density of the sample.

[3] With an upgraded arbitrary waveform generator, we can now generate flat-top pulse in larger time window of $T_{\mathrm{pulse}} = 14\,\mathrm{ms}$ for sharper frequency response.

The modified Beer-Lambert law To image the atoms, we make use of the D_2 transition of with σ^--polarised light (see Fig. 3.2 **b**). The Beer-Lambert law describes the degradation of light intensity when propagating through a dilute medium of density $n(x, y, z)$ is given by [89],

$$\frac{\mathrm{d}I(x, y, z)}{\mathrm{d}z} = -\sigma_0 n(x, y, z) I(x, y, z). \tag{3.19}$$

Here, σ_0 is the scattering cross section of two-level atoms in the vicinity of the D_2 transition and z is the along the light propagating direction. Integrating Eq. (3.19) along the z direction results in an optical density based on logarithm of fraction of absorbed light intensity, *i.e.*

$$\sigma_0 n(x, y) = -\ln\left(\frac{I_f(x, y)}{I_i(x, y)}\right). \tag{3.20}$$

However, due to saturation effects in Eq. (3.21), the photon scattering cannot take place efficiently in the case of high imaging intensity, resulting in the intensity-dependent scattering cross section

$$\sigma(I) = \frac{\sigma_0}{1 + (\frac{2\Delta}{\Gamma})^2 + s}. \tag{3.21}$$

Similar to the notations used in Sec. 3.3.1, $\Delta = \omega - \omega_0$ is the detuning of imaging light with respect to the transition frequency ω_0. Γ is the natural linewidth of the D_2 line and the saturation parameter $s = I/I_{\mathrm{sat}}$ is the ratio of the imaging intensity to the saturation intensity. The relevant properties of the D_2 transition are provided in Table. 3.1. Eq. (3.19), therefore, needs to be modified with intensity-dependent scattering cross section which takes into account the effect of saturation. With this in mind, the modified Beer-Lambert law reads [90]

$$\sigma_0 n(x, y) = -\alpha \ln\left(\frac{I_f(x, y)}{I_i(x, y)}\right) + \frac{I_i(x, y) - I_f(x, y)}{I^0_{\mathrm{sat}}}. \tag{3.22}$$

The calibration procedure for obtaining effective camera counts corresponding to I^0_{sat} can be found in [73]. To this end, we deploy an imaging pulse of 10 μs, with intensity $I \approx 1.5 I_{\mathrm{sat}}$. The imaging setup along the vertical direction is shown in Fig. 3.13.

Frame transfer scheme To record multiple images in a single experimental run within a short period of time, we deploy the fast kinetics mode of the Andor iXon888 camera. The camera contains a CCD sensor with resolution of 1024 pixel × 2048 pixel. Only an area of 1024 pixel × 512 pixel is illuminated, where the rest of the chip serves as storage area as shown in Fig. 3.13 **b**. Upon triggering, the CCD is exposed to imaging light for a time T_{exp}. After this, the image acquisition pauses, and the recorded charges are shifted vertically by 512 pixels such that a new image can be recorded. This process repeats twice, giving access to two additional images. To this end, three consecutive exposures are taken.

Before recording the images, we have the to-be-recorded atomic cloud typically residing in the two lowest hyperfine states $|F = 9/2, m_F = -9/2\rangle$ and $|F = 9/2, m_F = -7/2\rangle$. A microwave pulse is first shone onto the cloud to transfer the atoms in the $|F = 9/2, m_F = -9/2\rangle$ state to the $F = 7/2$ manifold, which is insensitive to the imaging light used later. Next, the atoms in the $|F = 9/2, m_F = -7/2\rangle$ state is transferred to the $|F = 9/2, m_F = -9/2\rangle$ via a LZ sweep. Subsequently, the first exposure records the atomic ensemble in the $|F = 9/2, m_F = -9/2\rangle$ with an imaging pulse duration of $\tau_{\mathrm{img}} = 10\,\mu$s.

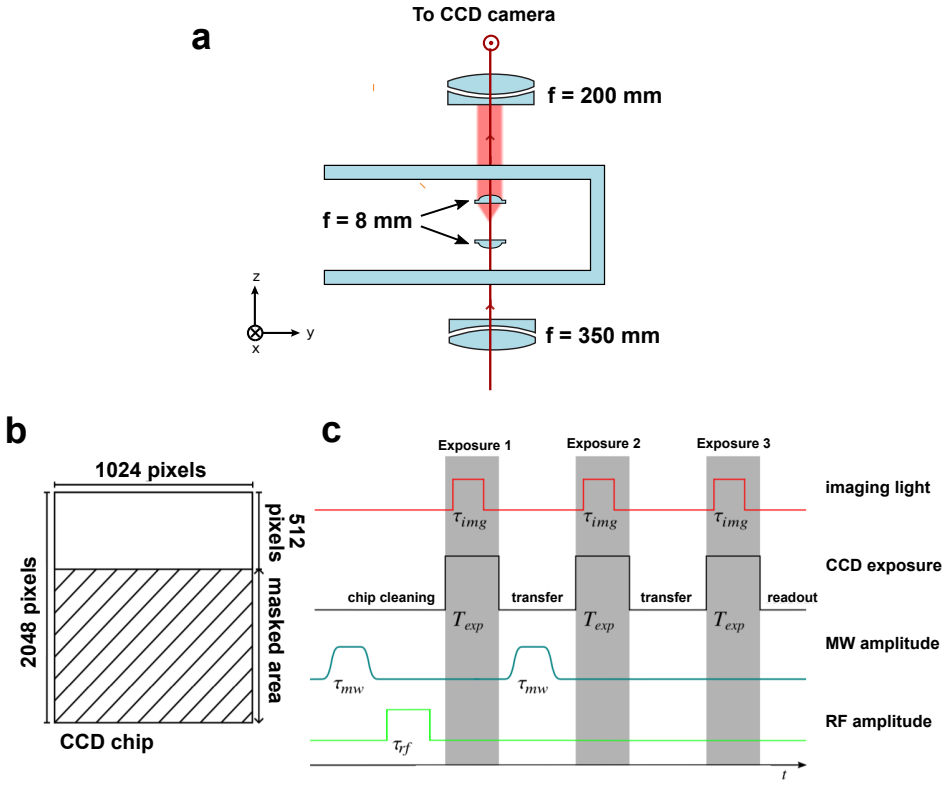

Figure 3.13: **Vertical imaging setup and fast kinetics scheme. a** Main imaging setup along the z-direction. **b** Outline of the CCD chip of the Andor iXon888 camera. **c** Details on the fast kinetics scheme. After each exposure, the charges accumulated are shifted vertically down in 6.5 μs into the masked region for storage. **b** and **c** are adapted from [73].

After that, atoms in the $F = 7/2$ manifold are transferred back to a $|F = 9/2, m_F = -9/2\rangle$, followed by the second exposure. Finally, a third image is taken with no atoms remained in the system. This serves a "bright" image for computing the optical density using Eq. (3.22).[4]

[4] In addition the bright image, we typically record a series of images (up to $\sim$ 1000 reproductions) at which no light is shone onto the camera. This so-called dark image is then used in the post-analysis to eliminate the effect of stray charges accumulated during the image acquisition.

CHAPTER 4

Simulating the Metal/Mott-insulator crossover using attractive interaction

So our problem is to explain where symmetry comes from. Why is nature so nearly symmetrical?

Richard P. Feynman

In this chapter, we investigate the symmetry of the two-dimensional Hubbard model under a particle-hole transformation using the quantum simulator apparatus in our experiment. We first begin with a pedagogical discussion on various symmetries in the Hubbard model and its consequences. In particular, we focus on the particle-hole symmetry and the resulting correspondence in phase diagrams of the repulsive and attractive interaction. In order to discuss the physical behaviour of a strongly correlated Hubbard system, we introduce the concept of the equation of state in the Hubbard model and its experimental measurement. In particular, we experimentally observe a "spin-incompressible" phase with attractive interaction, equivalent to a Mott insulator under repulsive interaction. The results presented here validate a novel pathway towards simulating the Hubbard Hamiltonian.

The experimental results discussed in this chapter was published in *Phys. Rev. Lett.* 124 (1), 010403 (2020).

4.1 Symmetries in the Hubbard model

In simple terms, a physical system is said to possess a symmetry when it remains unchanged under a specific transformation. The celebrated Noether's theorem states that every *continuous*, *differentiable* symmetry of a physical system corresponds to a *conservation law* [91]. One example is a uniform, rotating sphere which possesses global rotational symmetry. This implies that there is no bias in any direction. As a result, the rotation possesses the same angular momentum, regardless of any global rotated observing frame. Such *Indistinguishability* in direction leads naturally to the inability to describe the system differently along differently-rotated coordinates. Table 4.1 displays several common symmetries and their corresponding conversation laws and indistinguishabilities.

For a quantum system, the symmetry operations can be identified via a transformation of the Hamiltonian. For a Hamiltonian to fulfil a given symmetry, characterised by the operator $\hat{R}$, it needs to be invariant under the operation,

$$\hat{H} \rightarrow \hat{R}^{\dagger}\hat{H}\hat{R}. \tag{4.1}$$

It is not difficult to see that, when a physical system is invariant under certain symmetry operation, it can be significantly simplified. Most notably, the measurements (expectation values) would also be invariant under the transformation.[1] In this section, we discuss the role of symmetry in the Hubbard model and state explicitly the symmetry operation and their corresponding consequences in our quantum simulator.

Symmetry	**Operation**	**Conservation law**	**Indistinguishability**
Translation	$\boldsymbol{r} \rightarrow \boldsymbol{r} + \delta\boldsymbol{r}$	momentum	absolute space
Time-translation	$t \rightarrow t + \delta t$	energy	absolute time
Rotation	$\boldsymbol{r} \rightarrow \boldsymbol{r}'$	angular momentum	absolute direction
Space inversion	$\boldsymbol{r} \rightarrow -\boldsymbol{r}$	parity	absolute left/right
Time-reversal	$t \rightarrow -t$	Kramers degeneracy	absolute sign of time
Charge inversion	$e \rightarrow -e$	particle/anti-particles	charge conjugation
Particle exchange	$\psi(i,\cdots,j) \rightarrow \psi(j,\cdots,i)$	Bose/Fermi Statistics	identical particles

Table 4.1: **List of symmetries in physical systems.** Common continuous transformations including global translation, rotation and time-translation lead to the conservation of momentum, angular momentum and energy. Discrete symmetries such as parity, time-reversal and charge inversion form the combined CPT-symmetry which is observed in all physical laws so far. Under exchange of identical particles, the Bose-Einstein or Fermi-Dirac statistics arise depending on whether a symmetry or anti-symmetry is fulfilled.

4.1.1 Internal symmetries

Spin SU(2) symmetry In addition to transformations in space and time, one can consider a transformation regarding the internal degrees of freedom of a system, *e.g.* the electronic spin. In the context of ultracold atoms, the magnetic hyperfine states are taken as pseudo-spins. In the absence of a Zeeman field and anisotropic exchange interaction, the dispersion relation of the particle is independent of the spin. More generally speaking, this corresponds to a spin rotation symmetry

[1] In the Schrödinger (Heisenberg) picture of quantum mechanics, the eigenstates (observables) are invariant under symmetry transformation.

analogous to the classical rotational symmetry. To demonstrate this, we state the spin rotational operator $\hat{R}$ as

$$\hat{R}(\theta, \hat{\boldsymbol{r}}) = \exp\left(-\frac{i}{\hbar}\theta \hat{\boldsymbol{r}} \cdot \hat{\boldsymbol{S}}\right). \tag{4.2}$$

Here, θ is the rotation angle and $\hat{\boldsymbol{S}} = (\hat{S}^x, \hat{S}^y, \hat{S}^z)$ are the global spin operators. Since an SU(2) algebra can be constructed by,

$$\begin{aligned}
\hat{S}^z &= \sum_i \frac{1}{2}\left(\hat{n}_{i,\uparrow} - \hat{n}_{i,\downarrow}\right), \\
\hat{S}^+ &= \sum_i \hat{c}^\dagger_{i,\uparrow}\hat{c}_{i,\downarrow}, \\
\hat{S}^- &= \sum_i \hat{c}^\dagger_{i,\downarrow}\hat{c}_{i,\uparrow} = \left(\hat{S}^+\right)^\dagger .
\end{aligned} \tag{4.3}$$

A symmetry upon this rotation is typically referred to as the ***spin SU(2) symmetry*** [92]. In the Hubbard model, the spin SU(2) symmetry is naturally fulfilled when the population of spin-up and spin-down particles are equal, *i.e.* $\langle S^z \rangle = 0$. This results in the equivalence of spin-spin correlation in all spin directions, *i.e.* $\langle S^z_i S^z_j \rangle = \langle S^x_i S^x_j \rangle = \langle S^y_i S^y_j \rangle$. In Chapter 5, we make use of this property of the Hubbard Hamiltonian to construct a Ramsey-type scheme to observe coherent evolution of spin correlations.

Charge SU(2) symmetry Analogous to the spin SU(2) symmetry, one can construct another set of SU(2) operators, which read

$$\begin{aligned}
\hat{C}^z &= \sum_i \frac{1}{2}\left(\hat{n}_{i,\uparrow} + \hat{n}_{i,\downarrow} - 1\right), \\
\hat{C}^+ &= \sum_i (-1)^i \hat{c}^\dagger_{i,\uparrow}\hat{c}^\dagger_{i,\downarrow}, \\
\hat{C}^- &= \sum_i (-1)^i \hat{c}_{i,\downarrow}\hat{c}_{i,\uparrow} = \left(\hat{C}^+\right)^\dagger .
\end{aligned} \tag{4.4}$$

The rotational symmetry generated using this set of SU(2) algebra, similar to Eq. (4.2), is known as the ***charge SU(2) symmetry***. We use the naming convention such that $\hat{C}^z$ measures the charge carrier doping of the system. It should be noted that in cold atom systems, particles are neutral in charge and the name *charge* is simply a borrowed term from solid state physics where electrons are charge carriers. The Hubbard model is charge SU(2) symmetric at half-filling, where $\langle C^z \rangle = 0$. Altogether with both SU(2) symmetries, the Hubbard model is SO(4) = SU(2) × SU(2)/$\mathbb{Z}_2$ invariant at half-filling and spin-balanced. The notation $\mathbb{Z}_2$ refers to the fact that $\langle S^z \rangle = 0$ and $\langle C^z = 0 \rangle$ are both integers [93].

4.1.2 Discrete symmetries

Another important kind of symmetry is the so-called discrete symmetry. For example, crystals with periodic lattice structure exhibit a discrete translation symmetry. A single particle problem in such a system can be solved using the Bloch's theorem, as discussed in (see Sec. 2.4.1). In this chapter,

we focus on the particle-hole symmetry based on interchange of particle with hole in the lattice system, which is analogous to the charge conjugation symmetry in the field of elementary particles [93, 94].

Charge conjugation in physics Particles can be transformed into their anti-particles by a charge conjugation. For example, charge conjugation transforms a negatively charged electron to a positively charged positron, given by the following operation

$$C : q \rightarrow -q, \tag{4.5}$$

where C is a unitary operator, *i.e.* $CC^{\dagger} = 1$. All fundamental forces, except weak interaction, are symmetric under charge conjugation [94]. For example, the Maxwell equations are invariant under C, meaning the electromagnetic behaviour of a positron is governed by the same Maxwell equations. The idea of such discrete symmetry is more than mere theoretical abstraction, as it provides a unified framework to understand various physical systems. Charge conjugation (C) symmetry is one of the three fundamental discrete symmetries in nature, together with parity transformation (P) and time-reversal (T) symmetries. While violation of an individual discrete symmetry is possible, the combined CPT symmetry is believed to be a fundamental property in physics [95]. Historically, the particle-antiparticle symmetry was mainly studied in the context of elementary particles [96, 97], the concept can be extended to describe a wide range of problems. Even in the low-energy domain of condensed matter physics, the symmetry results in the emergence of novel effects and provides stability to exotic quantum states [98, 99]. For instance, particle-hole symmetry in a BCS superconductor takes the role of Lorentz invariance and leads to the emergence of the well known Higgs mode [100].

Particle-hole symmetries: an analogue of charge conjugation in lattice systems In condensed matter systems, the natural anti-particle for an electron is a positively charged hole (absence of an electron). Electrons and holes share similar physical properties including, but not limited to, effective masses, dispersion relation, transport coefficients and interaction. The interplay of electron-doped and hole-doped semiconductors exhibit rich physical application ranging from a simple p-n junction in photoelectric devices to transistors in modern computing silicon. In this section, we introduce two distinct kinds of particle-hole transformation in a lattice model. Then, we discuss its consequences in the Hubbard model.

Particle-hole transformation $\mathcal{P}_1$ In a general lattice system, one possible particle-hole transformation is given by

$$\mathcal{P}_1 : c_{i,\sigma} \rightarrow c^{\dagger}_{i,\sigma}, \tag{4.6}$$

where i is the site index and σ is the spin. The creation and annihilation operators exchange their role, independent of their spin component under $\mathcal{P}_1$. It is clear that both particle and hole follow the same quantum statistics. The transformation essentially maps occupied sites into empty sites and vice versa, *i.e.*

$$n_{i,\sigma} = c^{\dagger}_{i,\sigma} c_{i,\sigma} \xrightarrow{\mathcal{P}_1} c_{i,\sigma} c^{\dagger}_{i,\sigma} = 1 - n_{i,\sigma}, \tag{4.7}$$

as depicted in Fig. (4.1) **a**. It is straight-forward to notice that the upper bound of 1 in Eq. (4.7) stems from the single-band limit where the maximum filling allowed (for either particle or hole) is kept at unity.

We now look at how the Hubbard model transforms under $\mathcal{P}_1$. To highlight the effect of the transformation, we deploy a slightly different form, of which the Hubbard Hamiltonian in a Zeeman shift between spin-up and spin-down states. In cold atom systems, authentic magnetic effects can not be implemented due to the electrically neutral atoms. We note that synthetical gauge fields can be realised via novel schemes such as Raman coupling in trapped quantum gases [101–103] or engineering spatially-dependent couplings in optical lattices [104, 105]. On the other hand, an effective Zeeman shift h mimicking the magnetic energy shift can be easily realised via population imbalance, as will be discussed later in this chapter. To this end we write down the Hubbard Hamiltonian

$$H = -t \sum_{<i,j>,\sigma} c^{\dagger}_{i,\sigma} c_{j,\sigma} + U \sum_{i} \left(n_{i\uparrow} - 1/2\right)\left(n_{i,\downarrow} - 1/2\right) - \mu \sum_{i} \left(n_{i\uparrow} + n_{i\downarrow} - 1\right) - h \sum_{i} \left(n_{i\uparrow} - n_{i\downarrow}\right) . \tag{4.8}$$

Here $\mu = (\mu_\uparrow + \mu_\downarrow)/2$ and $h = (\mu_\uparrow - \mu_\downarrow)/2$. Under the transformation $\mathcal{P}_1$ in Eq. (4.6), we note the following consequences in the Hubbard Hamiltonian in Eq. (4.8).

1. The kinetic energy remains unchanged.
2. Interaction term remains unchanged.
3. The chemical potential and Zeeman term changes as $\mu \rightarrow -\mu$ and $h \rightarrow -h$.

When using the Hamiltonian in the form of Eq. (4.8), $\mu = 0$ corresponds to half-filling and $h = 0$ indicates spin-balance. Hence, the sign inversion in μ implies that it is sufficient to study either particle-doped ($\mu > 0$) or hole-doped ($\mu < 0$) systems. Similarly, the sign inversion in h draws equivalence between the spin-up dominated ($h > 0$) and a spin-down dominated ($h < 0$) case. This offers a tremendous simplification, as studying phases on either side automatically provides information on the other half.

Partial particle-hole transformation $\mathcal{P}_2$ Another particle-hole transformation can be constructed if only one of the spin components is conjugated [93, 106]. Such partial transformation is given by

$$\mathcal{P}_2 : c_{i,\uparrow} \rightarrow c_{i,\uparrow} \;\; ; \;\; c_{i,\downarrow} \rightarrow (-1)^{i_x + i_y} c^{\dagger}_{i,\downarrow}, \tag{4.9}$$

here $i = (i_x, i_y)$ denotes the two-dimensional lattice site index. The choice to conjugate only one of the spin components is arbitrary from first glance. It turns out that this transformation results in;

To understand this intricacy, we can take one step back and consider the electron gas in a solid state material as an example (see Eq. (2.3)), where the on-site interaction is caused by the electron-electron (e-e) Coulombic ***repulsion***. Partially conjugating one of the electron component would naturally result in an electron-hole (e-h) ***attraction*** instead (since holes are positively charged). This offers us the first clue to the distinction between $\mathcal{P}_1$ and $\mathcal{P}_2$. Applying $\mathcal{P}_2$ term by term in Eq. (4.8), the partial transform has the following consequences

1. Same as $\mathcal{P}_1$, the transformation $\mathcal{P}_2$ leaves the kinetic term invariant.
2. The interaction term transforms as $U \rightarrow -U$.

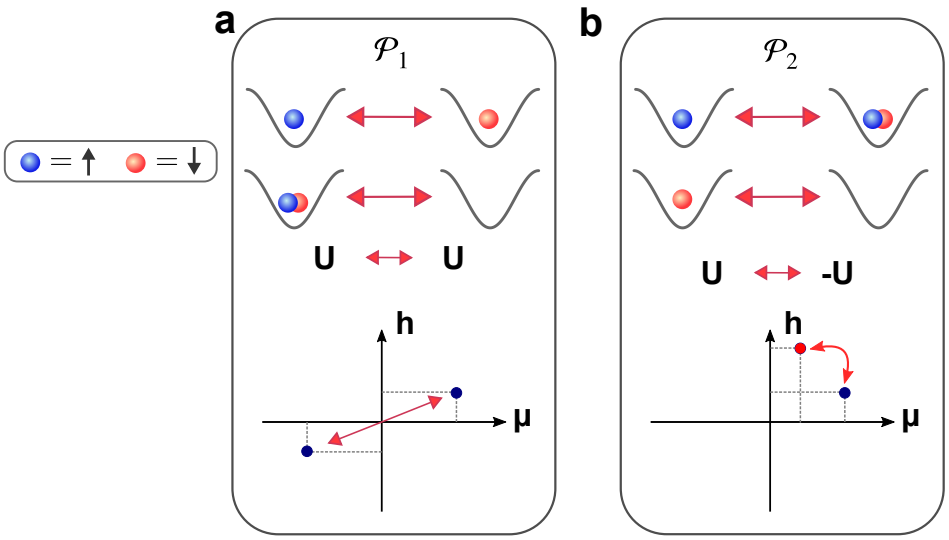

Figure 4.1: **Two particle-hole transformations in the Hubbard model. a**. Particle-hole transformation $\mathcal{P}_1$. The consequence on local density is the interchange of filled and empty sites. The parameters space maps to another Hubbard system with opposite μ and h, with the same kinetic and interaction terms. **b** Particle-hole transformation $\mathcal{P}_2$. Only the spin-down component is conjugated, while the spin-up occupation remains unchanged. The on-site particle-particle interaction hence maps to a particle-hole interaction, leading to a change of sign in interaction. The parameter space transforms to that of another Hubbard system with interchanged μ and h.

3. The generalised forces μ and h interchange their role under $\mathcal{P}_2$ as $\mu \leftrightarrow h$.

4. Conserved quantity $n_\uparrow + n_\downarrow - 1$ (total density) transforms to another conserved quantity $n_\uparrow - n_\downarrow$ (total magnetisation).[2]

From point (2), $\mathcal{P}_2$ inverts the sign of the interaction term, meaning a repulsively-interacting system is mapped onto an attractively-interacting one. Next, points (3) and (4) imply that $\mathcal{P}_2$ essentially interchanges the density and local moment. In other words, a repulsive model with finite density doping is equivalent to that of the attractive interaction with corresponding spin doping. Unlike the previous particle-hole transformation, $\mathcal{P}_2$ transforms site occupation as the following,

- singly-occupied site of spin-up state to doubly-occupied site, and *vice versa*.
- singly-occupied site of spin-down state to an empty site (hole), and *vice versa*.

As shown in Fig. 4.1 **b**, $\mathcal{P}_2$ transforms the singly-occupied spin-up and spin-down states (singles) to doubly-occupied (doubles) and empty sites (holes), respectively. Hence, $\mathcal{P}_2$ maps a spin-imbalance into an imbalance of doubles and holes, and vice versa. This gives us a first glimpse into the interchange of density and spin degrees of freedom. Furthermore, when applying $\mathcal{P}_2$ on a many-body state, the Mott insulator near half-filling, for example, would transform into the occurrence of local pairs near spin-balance. Similarly, an anti-ferromagnetically ordered state maps to a density-ordered wave pattern, as depicted in Fig. 4.2.[3]

[2] Here, we refer to conserved quantity in a close system. Among AMO and condensed matter literatures, the term moment is sometimes referred interchangeably with magnetic moment or polarisation.

[3] In the language of condensed matter physics, the density ordering corresponds to a charge density wave (CDW) state.

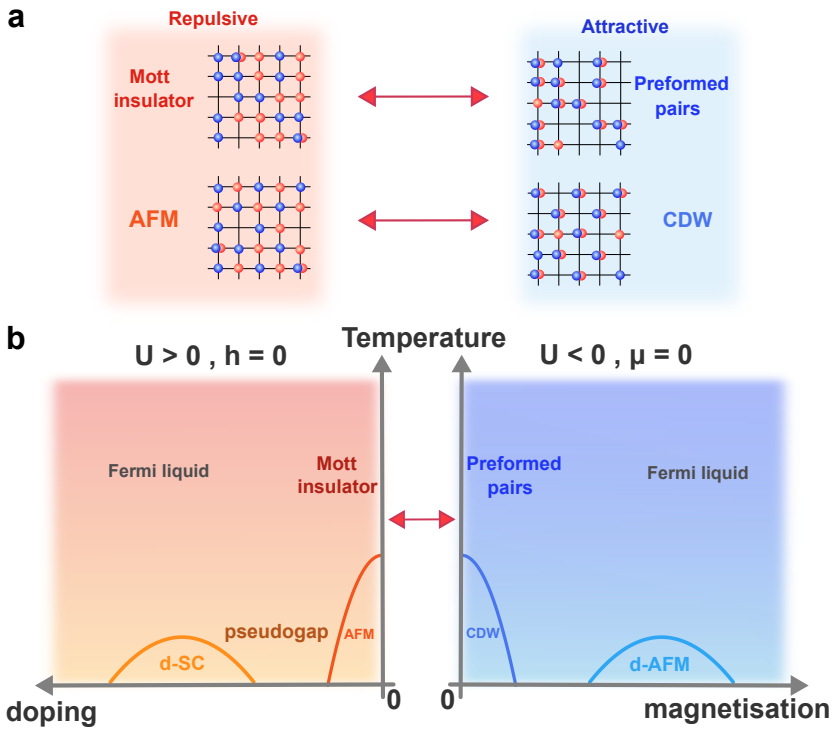

Figure 4.2: **Phase mapping under $\mathcal{P}_2$. a** Mapping many-body states. A Mott insulator with density ordering, induced by the repulsive on-site interaction, transforms into the local preformed pairs, where attractive interaction favours the formation of uncorrelated pairs and suppresses local moment. Similarly, the spin ordering in the anti-ferromagnet (AFM) transforms into a density ordering of the charge density wave (CDW). **b** Particle-hole mapping of the schematic phase diagrams. For the repulsive case (left), a paramagnetic Mott insulator becomes anti-ferromagnetically ordered upon cooling due to the rising dominance of the super-exchange energy. This corresponds to the preformed pairs forming order with doublons and holes (right). In addition, a conjectured d-wave superconducting phase lies upon doping the AFM phase, which is separated by a pseudogap phase, would transform to a d-wave anti-ferromagnetic state.

4.2 Measuring the equations of state of the Hubbard model

After discussing the role of the particle-hole symmetries in the Hubbard model, we are in the position to elaborate our experimental venture to observe its consequence, namely a mapping between the density and spin degrees of freedom. Throughout this chapter, we will draw a close analogy between the repulsive and attractive Hubbard model. Although the fundamental concept of density and spin ordering in the Hubbard model has already been presented in Chapter 2, a formal definition of the density and spin sectors will be given in the next section. We also outline the experimental detection sequence used for probing the two sectors with repulsive and attractive interactions.

4.2.1 Density and spin sectors

After loading the atomic clouds into the two-dimensional optical lattices, the atomic ensemble is in thermal equilibrium (details on the preparations of our ultracold atomic gases can be found in Chapter 3). The detection begins with spatially locking the equilibrium atomic density profile

via rapid lattice ramps. The detection typically takes place at high lattice depths of $(V_x, V_y, Vz) = (60E_{R,x}, 60E_{R,y}, 120E_{R,z})$, at which the characteristic tunnelling times are on the order of seconds. Therefore, the dynamics occur at such during the entire detection process (~ 300 ms) is negligible. In general, we probe either the density or the spin degrees of freedom, which corresponds to two distinct experimental sequences (see Fig. 4.3 and 4.4).

Density sector In a closed, homogeneous system, the total particle number is a conversed quantity. The density sector is conventionally known as the charge sector in condensed matter physics as charged particles are of interest. It concerns with the dynamics involved in the change of density $n = n_\uparrow + n_\downarrow$ within the system, *e.g.* induced via compression of trapping potential. As suggested by its name, a high-lying energy excitation in the density sector is accompanied with a change in density.

For instance, with repulsive on-site interaction $U > 0$, the particles at half-filling tend to order by avoiding the accumulation of double occupancies. This, in terms of the energy spectrum, opens a gap between singly- and doubly-occupied states. When interaction strength becomes sufficiently strong and larger than the bandwidth W, *i.e.* $U > W$, the system becomes insulating. This energy gap is often referred to as the density gap, or more conveniently, the Mott gap. Exciting a high energy state in this picture requires a change in local density. Attractive interaction, on the other hand, does not prohibit the accumulation of doubly-occupied sites. Instead, the formation of pairs is energetically favourable for increasing attraction. Such local pairing, despite its s-wave symmetric nature, is a key to understanding the pairing phenomenon in materials such as BCS-type superconductors. In Chapter 6, we experimentally characterise the pair correlation lengths in an attractive Hubbard system.

From the particle-hole symmetry $\mathcal{P}_1$ discussed in Sec. 4.1.2, half-filling (one particle per site) is the symmetric point, away from which the physics maps to each other. Here, we formally define density doping as the following

$$\tilde{n} = n_\uparrow + n_\downarrow - 1, \tag{4.10}$$

where $\tilde{n} = 0$ indicates half-filling, $\tilde{n} > 0$ is overdoped and $\tilde{n} < 0$ is underdoped. In a spin-balanced Hubbard model, where the number of spin-up and spin-down state is the same, *i.e.* $\langle n_\uparrow \rangle = \langle n_\downarrow \rangle$, the total density n is given by

$$\langle n \rangle = 2\langle n_\uparrow \rangle = 2\left(\langle n_\uparrow \rangle - \langle n_\uparrow n_\downarrow \rangle\right) + 2\langle n_\uparrow n_\downarrow \rangle = 2(S_\uparrow + D). \tag{4.11}$$

Here we define the probability of singly-occupied spin-up(down) state, henceforth we refer to as "***Singles***", as

$$S_{\uparrow/\downarrow} = \langle n_{\uparrow/\downarrow} \rangle - \langle n_\uparrow n_\downarrow \rangle, \tag{4.12}$$

and that of doubly-occupied sites, hereafter we refer to as "***Doubles***", as

$$D = \langle n_\uparrow n_\downarrow \rangle. \tag{4.13}$$

From Eq. (4.11), we know that it is sufficient to measure the density profiles $S_\uparrow$ and D to complete characterise the total density n. In Fig. 4.3, we depict the experimental detection sequence to resolve the density sector. The detection sequence is separated into the following parts,

- (1) – (3) : We started with the two lowest hyperfine levels $|F = 9/2, m_F = -7/2\rangle$

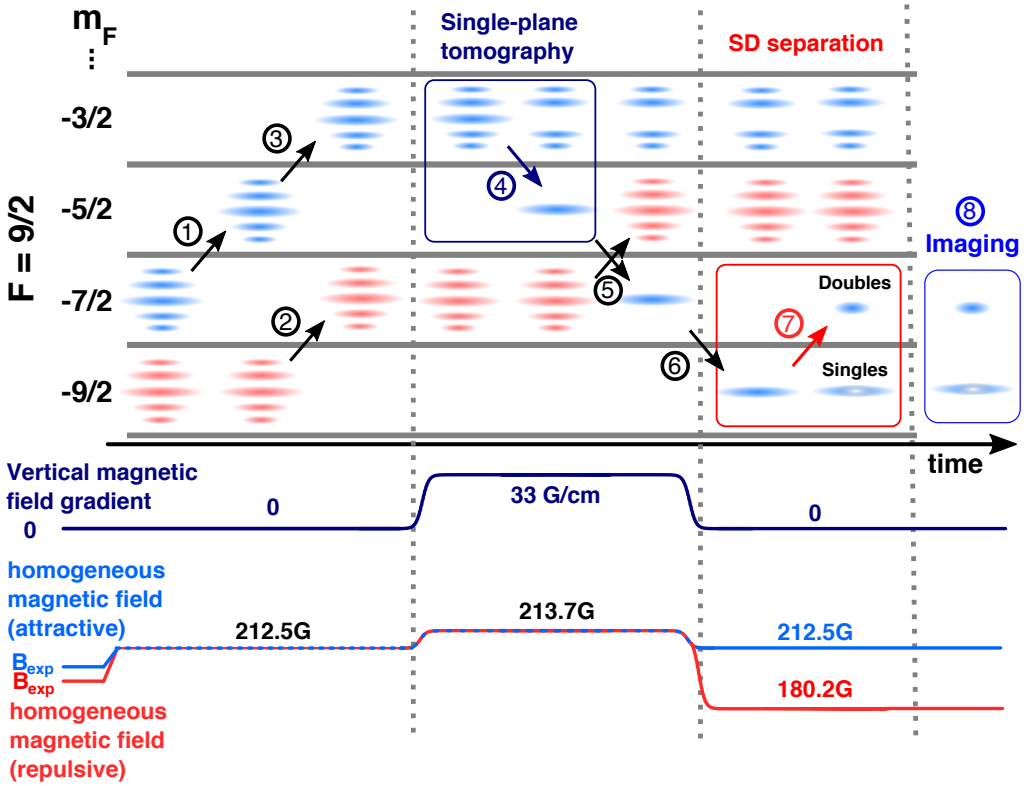

Figure 4.3: **Experimental detection sequence for the density sector.**

and $|F = 9/2, m_F = -9/2\rangle$. The former is first transferred to $|F = 9/2, m_F = -5/2\rangle$ and the latter is then transferred to $|F = 9/2, m_F = -7/2\rangle$ via a Landau-Zener RF sweep (see Sec. 3.3.1). Subsequently, the $|F = 9/2, m_F = -5/2\rangle$ is transferred to $|F = 9/2, m_F = -3/2\rangle$. We note that the order of the sweep is critical since a coexistence of the $|F = 9/2, m_F = -9/2\rangle$ and$|F = 9/2, m_F = -3/2\rangle$ results in a spin changing collision, that would eliminate all doubly-occupied sites due to its highly exothermic nature.

- (4) : **Single-plane tomography.** The vertical magnetic field gradient is ramped up to 33 G/cm, giving each two-dimensional layer a frequency spacing of 1.28 kHz. A hyperbolic secant (HS1) RF pulse is deployed to resonantly drive only one single layer back to the $|F = 9/2, m_F = -5/2\rangle$. We note that this so-called slicing operation needs to take place at a magnetic field near 213.7 G, where the interaction energy shift between the initial states and final states are identical.

- (5) – (6) : Two Landau-Zener sweeps to transfer the "sliced" cloud back to the lowest hyperfine state $|F = 9/2, m_F = -9/2\rangle$ to prepare for separation of singly- and doubly-occupied states in the sample.

- (7) : **Singles-doubles (SD) separation.** For the repulsive interaction sequence, we ramp the magnetic field to 180.2 G, at which the interaction shift between singly- and doubly-occupied states are large ($\sim$ 6.6 kHz) and thus could be spectroscopically addressed. The doubly-occupied states are then transferred to the $|F = 9/2, m_F = -7/2\rangle$ state. As

for the attractive interaction sequence, this SD separation is performed at a same magnetic field to the RF tomography, where the interaction shift is limited to 1.8 kHz. However, the improvement in arbitrary pulse shaping gives us access to narrower frequency range as compared to the repulsive data acquisition.

- (8) : ***In-situ* imaging.** Finally, atoms in the lowest two hyperfine states are imaged, resulting to the *in-situ* distribution profiles as shown in Fig. 4.6. Details in simultaneous imaging of the two lowest hyperfine states can be found in Chapter 3.

Spin sector Analogous to the density sector, the spin sector centres around the formation of magnetic moment (magnetisation) in a system. In a closed, homogeneous system, the global magnetisation is another conserved quantity and is set by the difference in particle numbers between spin states, as measured along the quantisation axis. Dynamics in the spin sector involves change of magnetisation and is accompanied with a corresponding spin excitation energy. For repulsive interaction, the relevant spin gap between non-spin-ordered state and spin-ordered state is on the energy scale of super-exchange amplitude $J \sim 4t^2/U$. A more detailed discussion of anti-ferromagnetic ordering can be found in Chapter. 5.

As discussed earlier this chapter, authentic magnetic interaction in neutral atoms are impossible. Instead, an offset of particle reservoirs (difference of chemical potential between two spin states) plays the role of pseudo-magnetic field, as shown in the Zeeman field in Eq. 4.8. We define the magnetisation as

$$m^z = n_\uparrow - n_\downarrow, \tag{4.14}$$

where the superscript z refers the spin in the σ_z basis. Here $m^z = 0$ denotes spin-balanced case, whereas $m \neq 0$ refers to spin-imbalanced case. This leads to the main observable of the spin sector

$$\langle m^z \rangle = \langle n_\uparrow \rangle - \langle n_\uparrow \rangle = S_\uparrow - S_\downarrow. \tag{4.15}$$

To connect with the density sector, magnetisation plays the similar role of density doping. From Eq. (4.15), we know that it is sufficient to measure the singly-occupied sites of both spin components, since doubly-occupied sites or holes possess zero local moment. In Fig. 4.4, we outline the detection sequence for measuring the magnetisation (spin sector). The detection sequence consists of the following steps,

- (1)–(3): **Removal of doubles via spin-changing collisions.** Utilising the spin-changing collision between the $|F = 9/2, m_F = -3/2\rangle$ and $|F = 9/2, m_F = -9/2\rangle$ hyperfine states, we remove the doubly-occupied states in the entire atomic cloud.

- (4) : **Single-plane tomography.** Similar to the density detection sequence, a single two-dimensional layer needs to be extracted. However, for the spin sector, this involves two spin states instead of one in the density sector. A dual-frequency RF pulse with resonant frequencies of both the $m_F - 7/2 \rightarrow m_F = -9/2$ and $m_F - 3/2 \rightarrow m_F = -5/2$ transitions is used. This enables simultaneous addressing of both spin components in the same layer.

- (5) : A single Landau-Zener sweep to shift the target layer back to the lowest two hyperfine states.

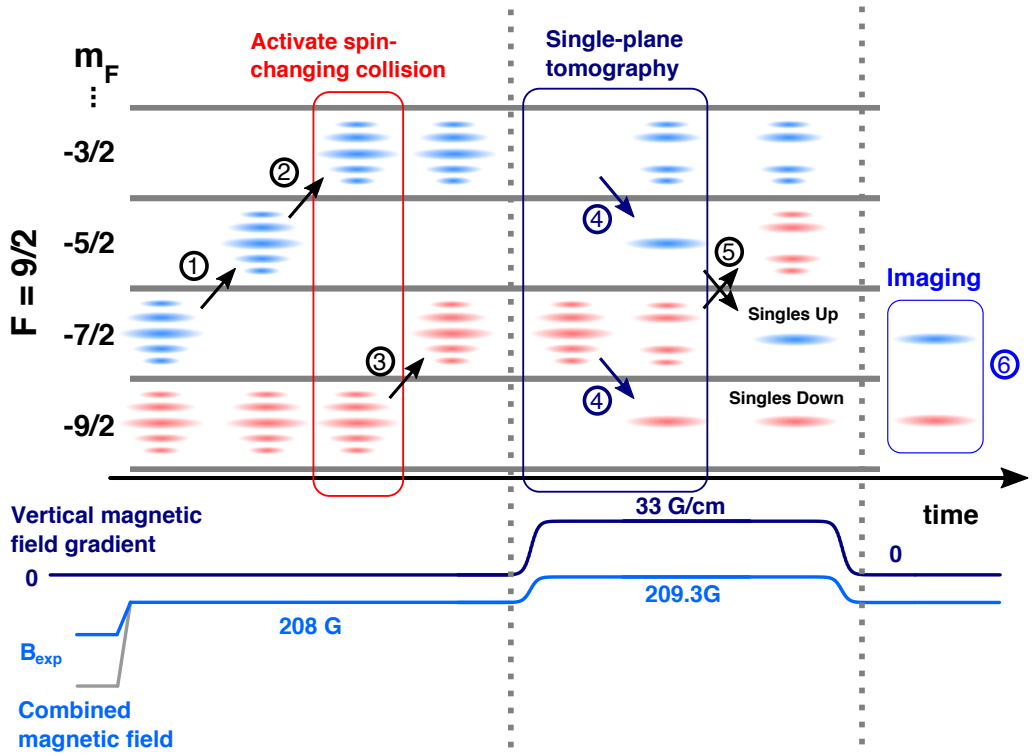

Figure 4.4: **Experimental detection sequence for the spin sector.**

- (6) : ***In-situ* imaging.** Successive imaging, using the fast kinetics scheme, of the two spin states results in two *in-situ* occupation profiles of $S_\uparrow$ and $S_\downarrow$, as shown in Fig. 4.6.

4.2.2 Data analysis

After acquiring *in-situ* images from the detection sequence, depending on which degrees of freedom to probe, we have access to either the density or spin degrees of freedom, *i.e* $n(x, y)$ or $m(x, y)$ respectively. Under the framework of local density approximation (LDA), the spatial coordinates can be mapped to local chemical potential, therefore giving direct access to the thermodynamical equation of state $n(\mu)$ and $m(\mu)$. State-of-the-art numerical simulation is used to extract the temperature of the atomic clouds via chi-square fitting. Using the Gibbs-Duhem relations, various thermodynamical quantities such as compressibility and pressure can then be derived.

Grand canonical ensembles Consider a system of fermions under thermal equilibrium, the Gibbs-Duhem relations describe the change of chemical potential with respect to other thermodynamical variables such as temperature, pressure and external field. It can be written into the following form [107],

$$N d\mu = S dT + V dP - M dH, \tag{4.16}$$

here N is the particle number, μ is the chemical potential, S is entropy, T is temperature, V is volume, P is pressure, M is magnetisation and H is external field which induces M. We note that in the above form, all variables are capitalised to indicate the total quantity in a homogeneous system. Recasting

Eq. (4.16) for averaged quantities in a two-dimensional lattice, we have

$$nd\mu = sdT + a^2 dP - mdh, \tag{4.17}$$

where the quantities n, s and m are the corresponding particles, entropy, and magnetisation ***per lattice site*** respectively, and a^2 is the area of lattice unit cell.

Local density approximation Since Eq. (4.16) is constructed under the grand canonical ensemble, it describes a system in equilibrium with external reservoirs, *i.e.* a particle bath characterised by the chemical potential μ. This motivates the use of local density approximation (LDA) in analysing our quantum gases sample. Under thermal equilibrium, the LDA asserts that an inhomogeneous system can be partitioned into homogeneous subsystems that are in equilibrium with each other. Obviously, this assumes that the Hubbard parameters are sufficiently stationary with respect to the spatial change of thermodynamical variables.

In optical lattices, the inhomogeneity arises mainly from the spatially-varying potential landscape. The inter-site tunnelling and interaction terms can be treated as constant throughout the whole lattice. As shown in Fig. 4.5 **a**, the LDA allows the partition of the whole inhomogeneous system (the trap shown as the grey solid line) into multiple, spatially-connected homogeneous subsystems (approximated by red solid steps). In thermal equilibrium, the subsystems have the ***same*** thermodynamic potentials (μ_0, T, P, h). However, the potential landscape $V_{\text{trap}}(x, y)$ offsets part of the global chemical potential and thus leads to a local chemical potential μ_{local} given by

$$\mu(x, y) = \mu_0 - V_{\text{trap}}(x, y). \tag{4.18}$$

For the region closer to the trap centre, the local chemical potential is higher, and thus the atom number increases accordingly. This leads to the coexistence of phases within the different position in the systems, as depicted for repulsive interaction in Fig. 4.5 **b** The low-filling region corresponds to a low local chemical potential μ and hence realises the compressible metallic phase. Upon increasing density, the interaction contribution rises and is maximum at half-filling, thus leading to the interaction induced Mott-insulating phase.

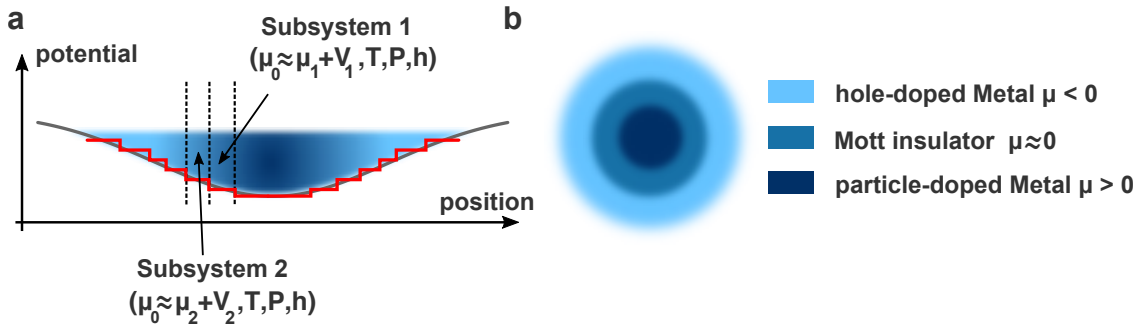

Figure 4.5: **Principle of local density approximation (LDA) . a** Sketch of trapping potential landscape. The LDA approximates region with same trapping depths as a homogeneous system. The deeper the trap (closer to centre), the higher the local chemical potential μ and total density n. Within a single experimental realisation, the entire system can be separated into coupled subsystems. **b** Coexistence of phases. The harmonic confinement provides a natural knob to adjust the chemical potential μ and hence supports the coexistence of phases within the optical trap.

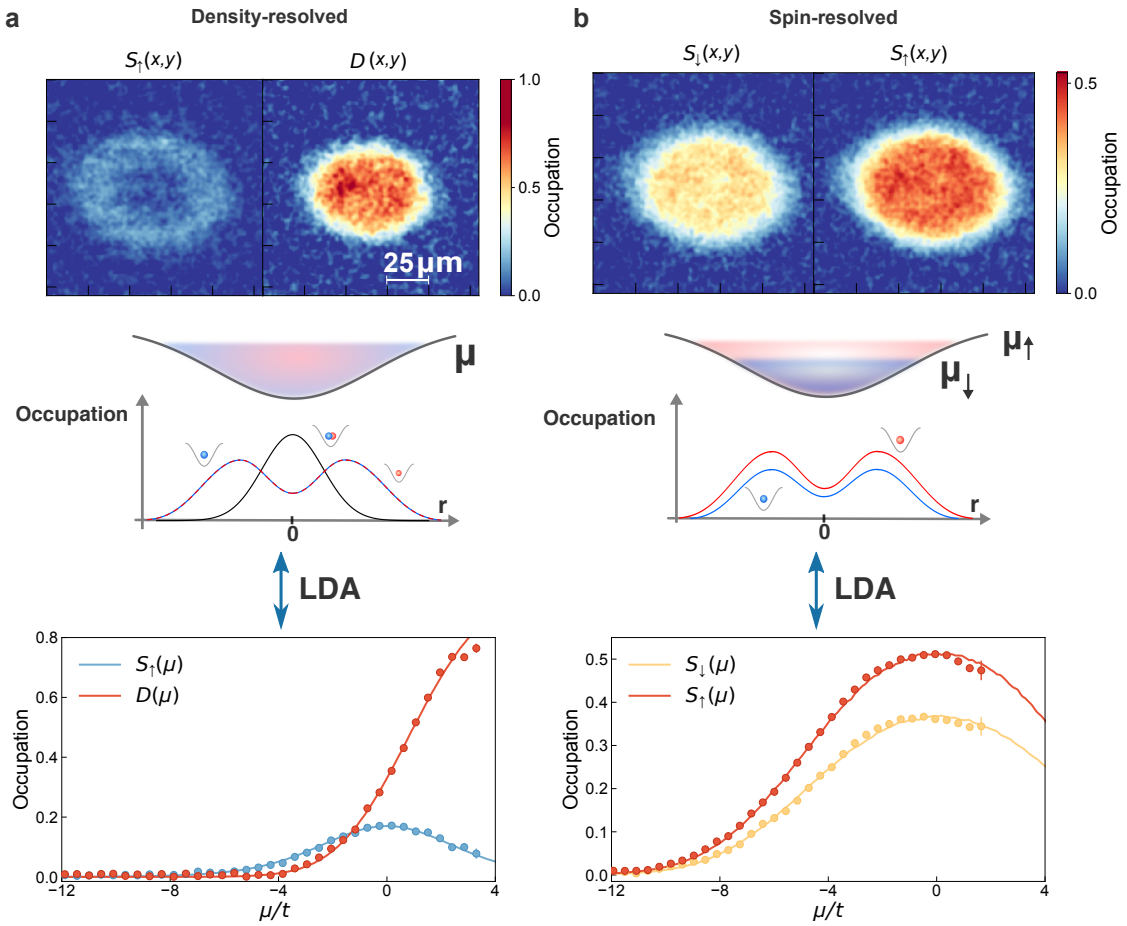

Figure 4.6: **Experimental detection in density and spin sectors.** **a** Density sector measurement. *In-situ* images of singly-occupied $S_\uparrow(x,y)$ and doubly-occupied sites $D(x,y)$, with a Gaussian spatial filter on the order of our imaging resolution to remove noise. By averaging within iso-potential region, we obtain the density profile as a function of chemical potential μ. **b** Spin sector measurement. A spin-resolved measurement opens access to the spatial profile of the magnetisation $m = n_\uparrow - n_\downarrow$. The relative ratio between $S_\uparrow(\mu)$ and $S_\downarrow(\mu)$ allows the extraction of the effective Zeeman field h from a numerical fit with DQMC simulations. The *in-situ* images and data shown are averaged within ~ 40 experimental realisations.

Equations of state In Fig. 4.6, we depict the analysis that converts raw experimental images to the equations of state. For measurements in the density sector, we typically probe the density distribution of $S_\uparrow(x,y)$ and $D(x,y)$. $S_\uparrow(x,y)$ displays a hole near the centre as the filling increases beyond half-filling. And a Mott insulating phase is realised near the peak of $S_\uparrow(x,y)$, forming a ring-like appearance. The doubly-occupied sites $D(x,y)$ rise monotonically with trap depth. We then map the spatial coordinates to chemical potential using Eq. (4.18). To this end, we obtain the density profile as a function of μ, *i.e.* $S_\uparrow(\mu)$ and $D(\mu)$. The sum of two measurements leads to the density equation of state $n(\mu)$,

$$n(\mu) = 2\left[S_\uparrow(\mu) + D(\mu)\right]. \tag{4.19}$$

The equation of state, in general, is a function of temperature T and we implicitly assume in our notation for clarity. As for the spin sector, the main observable is the magnetisation $m = n_\uparrow - n_\downarrow$.

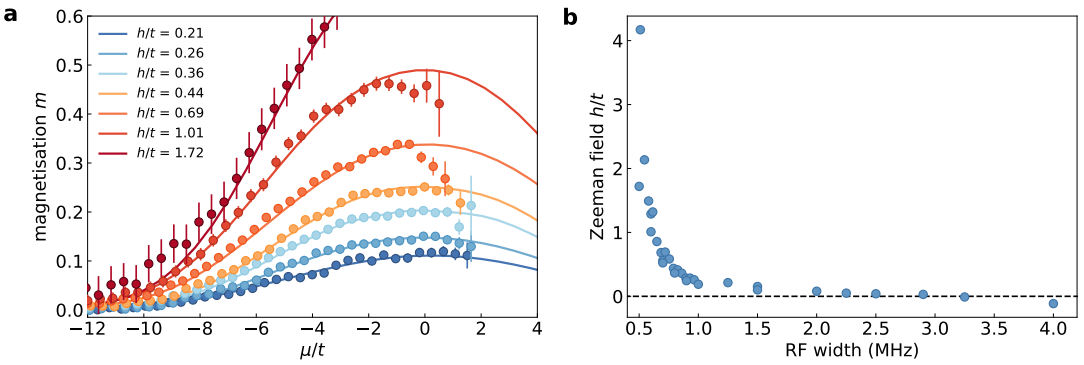

Figure 4.7: **Determination of the effective Zeeman field h.** **a** In addition to temperature extraction, the numerical fit to the magnetisation profile $h(\mu)$ provides a method to calibrate the effective Zeeman field h, which is a global system parameter. Solid lines are results of numerical DQMC simulations. **b** Tuning the spin-mixtures. By varying the frequency width of the spin-mixing pulses, a global population imbalance can be achieved, and thus a finite h. The extracted h versus RF frequency width is plotted. The 50/50 balance point is calibrated at 2.9(4) MHz.

For a spin-balanced system, *i.e.* $h = 0$, we have $\langle m \rangle = 0$. The effective Zeeman field h is varied by imbalancing population of the two spin-states. This can be achieved by varying the sweep width of the RF pulses used for creating a 50/50 mixtures of spin states, see Fig 4.7. Our detection techniques give the spatial profile of $S_\uparrow(\mu)$ and $S_\downarrow(\mu)$ using the same procedures. Again, the magnetisation can be obtained as a function of local chemical potential μ via LDA. To this end, we arrive at the magnetisation, for a given Zeeman field h,

$$m(\mu) = S_\uparrow(\mu) - S_\downarrow(\mu). \tag{4.20}$$

Similarly, the magnetisation equation of state $m(h)$ at fixed chemical potential μ can be extracted from various realisations with different overall spin imbalance, and is given by,

$$m(h) = S_\uparrow(h) - S_\downarrow(h). \tag{4.21}$$

The resulting density and magnetisation equation of state can be found in the next section, at which we derive the corresponding susceptibilities in each sector.

Temperature determination We then compare our experimental data for the equations of state $n(\mu)$ and $m(\mu)$ with numerical DQMC simulations, as discussed in Sec. 2.5. By performing a numerical chi-squared fit to the measured equations of state, we obtain the temperature $k_B T/t$ and global chemical potential μ_0 of the system. As shown in the lower part of Fig. 4.6 **a**, for the density sector, a combined fit is performed for both $S_\uparrow(\mu)$ and $D(\mu)$.

As for the spin sectors, the numerical fit allows us to extract, in addition to the temperature $k_B T/t$ and the chemical potential μ, the effective Zeeman field h. As shown in bottom part of Fig. 4.6 **b**, we perform the numerical fit on $S_\uparrow(\mu)$ and $S_\downarrow(\mu)$ instead. By allowing two spin components to have different global chemical potential ($\mu_\uparrow$ and $\mu_\uparrow$), the effective Zeeman field is obtained as $h = (\mu_\uparrow - \mu_\downarrow)/2$. The global spin imbalance is achieved by varying the frequency width of the RF mixing pulses, and the resulting h/t is shown in Fig. 4.7.

Thermodynamical observables The thermodynamics of the system is fully characterised by the equation of state. Thus, thermodynamical quantities such as pressure, compressibility and entropy can be derived from it. At thermal equilibrium, the temperature throughout the optical lattice is constant, *i.e.* $dT = 0$. Eq. (4.16) can be rewritten as

$$\frac{\partial P}{\partial \mu} = \frac{N}{V} = n. \tag{4.22}$$

Integrating this gives the pressure P,

$$P(\mu) = \int_{-\infty}^{\mu} n(\mu')d\mu' \,. \tag{4.23}$$

Next, from the first law of thermodynamics, the isothermal compressibility κ is the inverse of the bulk modulus, and is define as [52]

$$\kappa = -\frac{1}{V}\left(\frac{\partial V}{\partial P}\right)_T, \tag{4.24}$$

hence κ is the change of volume with respect to a change in pressure, where $dP > 0$ ($dP < 0$) represents a compression (relaxation) applied to the system. The compressibility is sensitive to interaction effect and offers important characterisation of quantum phases. In order to experimentally measure this, we have to rewrite Eq. (4.24) into experimental observables. Using the differential chain rule, we obtain

$$\kappa_T = -\frac{1}{V}\left(\frac{\partial V}{\partial P}\right)_T = -\frac{1}{V}\left(\frac{\partial V}{\partial \mu}\right)_T \left(\frac{\partial \mu}{\partial P}\right)_T = -\frac{1}{nV}\left(\frac{\partial V}{\partial \mu}\right)_T . \tag{4.25}$$

Here, we make use of Eq. (4.22). Furthermore, we can write the differential $dn = d(N/V) = -(N/V^2)dV = -(n/V)dV$, and differentiating with respect to μ, and obtain

$$\left(\frac{\partial V}{\partial \mu}\right)_T = -\frac{V}{n}\left(\frac{\partial n}{\partial \mu}\right)_T . \tag{4.26}$$

Substituting Eq. (4.26) into Eq. (4.25), we finally arrive at the common form of compressibility in quantum gases experiments, which reads

$$\kappa_T = \frac{1}{n^2}\left(\frac{\partial n}{\partial \mu}\right)_T . \tag{4.27}$$

We note that this particular form of κ_T is not symmetric around half-filling $n = 1$, there we focus on a slightly different form of the compressibility, namely by dropping the $1/n^2$ and compute, and define

$$\kappa = \left(\frac{\partial n}{\partial \mu}\right)_T . \tag{4.28}$$

Therefore, the compressibility can be deduced by differentiating the equation of state $n(\mu)$. In a similar fashion, the spin susceptibility χ_s characterises the response of magnetisation to an external field, and is defined as

$$\chi_s = \left(\frac{\partial M}{\partial H}\right)_T \sim \left(\frac{\partial m}{\partial h}\right)_T . \tag{4.29}$$

In later sections, we demonstrate that the spin susceptibility offers equivalent information as the compressibility in the density sector. In other words, the same physics in a metal/Mott-insulator

crossover can be studied using attractive interaction.[4]

4.3 Spin-incompressible phase with attractive interaction

With the equations of state of density $n(\mu)$ and magnetisation $m(h)$, we are in the position to investigate the correspondence between density and spin sectors under a particle-hole transformation as mentioned earlier in this chapter. To illustrate this, we first present local occupation measurement at half-filling ($\mu = 0$) and for the spin-balanced ($h = 0$) scenario. Then we extend to arbitrary μ and h, which leads to the collapse of experimental data points between two sectors. Finally, we show the measurement of the thermodynamic susceptibilities, signalling the observation of a "spin-incompressible" phase using attractive interaction.

4.3.1 Observation of the particle-hole symmetry

At half-filling and spin-balance : $\mu = h = 0$ As explained in Fig. 4.1 **b**, the partial particle-hole transformation maps the site occupations according to

$$\begin{aligned} S_\uparrow(U,\mu,h) &= D(-U,h,\mu), \\ S_\downarrow(U,\mu,h) &= 1 - S_\uparrow(-U,h,\mu) - S_\downarrow(-U,h,\mu) - D(-U,h,\mu). \end{aligned} \tag{4.30}$$

A straightforward starting point to study is at half-filling ($\mu = 0$) and for a spin-balanced cloud ($h = 0$), since the mapping $\mu \leftrightarrow h$ is automatically fulfilled, *i.e.*

$$S_\uparrow(U,0,0) = D(-U,0,0). \tag{4.31}$$

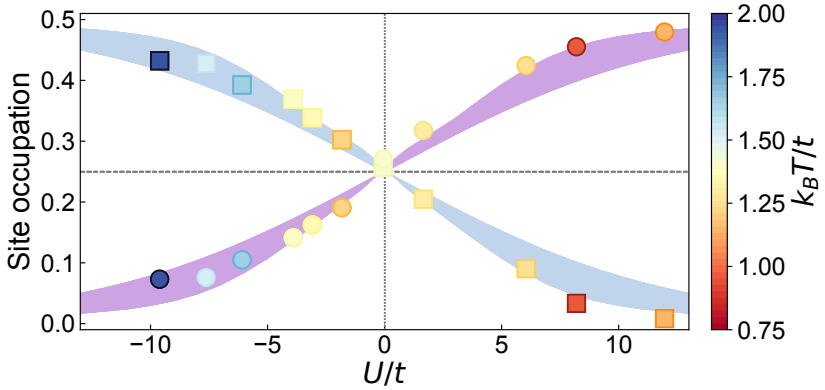

Figure 4.8: **Particle-hole symmetry for various interaction strengths at $\mu = h = 0$.** Doubles (squares) and singles (circles) occupations versus U/t. Colormap represents the extracted temperatures. For each interaction strength, we show the lowest temperature reached in our data sets. The blue (purple) shaded regions show the results of the DQMC numerical calculations for $D(U,0,0)$ ($S_\uparrow(U,0,0)$) over $0.8 \leq k_BT/t \leq 2.0$.

[4]The magnetic susceptibility can also be measured via spin correlation analysis, see more detailed discussion in Chapter 5

In Fig. 4.8, we plot the measured site occupation of singles (spin-up) and doubles over a broad range of interactions at $\mu = h = 0$. Interactions are varied by changing the homogeneous magnetic field around 202 G, realising an interaction range of $-12 \leq U/t \leq 12$. In the non-interacting case at $U = 0$, singly-occupied site and doubly-occupied site are energetically the same. Therefore, at half-filling, all possible states are equally populated, leading to an occupation probability of $1/4$ each. By increasing the repulsive interaction strength ($U > 0$), doubles become energetically less favourable. Therefore, we anticipate a decrease of doubles accompanied by an increase in singles. The opposite case takes place for attractive interactions ($U < 0$), where doubles are favoured and singles suppressed. We observe the nice agreement of the symmetry, as stated in Eq. (4.31), as well as the prediction of DQMC simulations. Such precise mirror symmetry about $U = 0$ is a clear manifestation of the particle-hole symmetry $\mathcal{P}_2$ in our quantum simulator. We note that the suppression of formation of the doubly-occupied sites is related to the energy scale of U. This explains the accuracy of our data despite a change in temperature $k_B T/t$ by a factor of two.

Away from half-filling or spin-balance : $\mu \neq 0$ or $h \neq 0$ We then generalise to arbitrary values of μ and h. Since the role of μ and h interchange according to Eq. (4.30), we need to compare the equations of state $n(\mu)$ to $m(h)$ at opposite interaction strength. As shown in Fig. 4.9 **a**, the attractive interaction ($U/t = -7.6$) in a spin-balanced system ($h = 0$) leads to an accumulation of doubles (black circles) in the center of the trapping potential (highest chemical potential μ). The peak in the

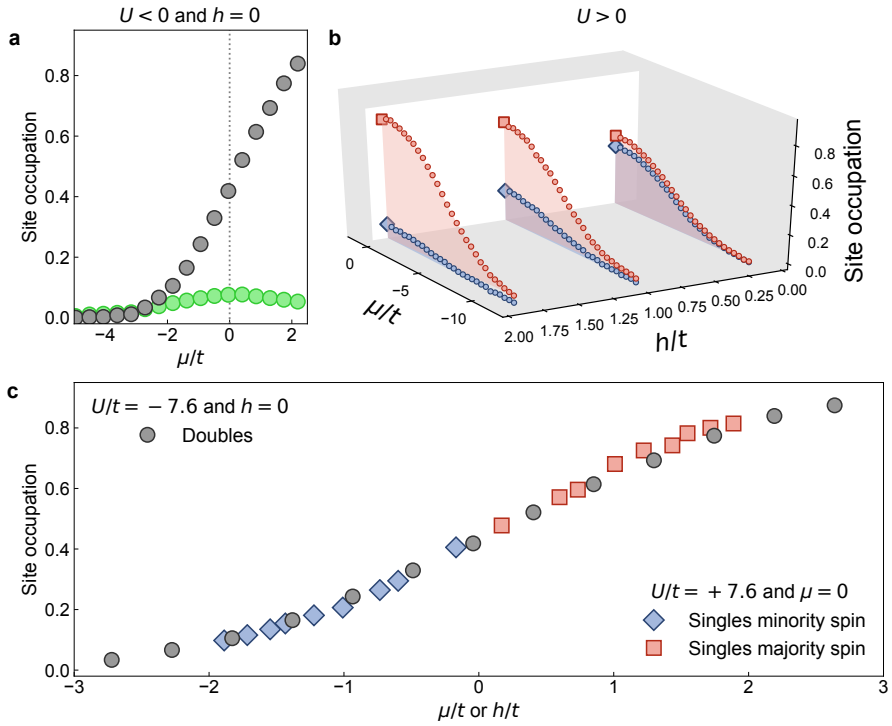

Figure 4.9: **Particle-hole symmetry for arbitrary μ and h.** **a** For the attractive, spin-balanced ($h = 0$) Hubbard model ($U/t = -7.6$), we show the site occupations of singles (green circles) and doubles (black circles) as a function μ. **b** For the repulsive Hubbard model ($U/t = 7.6$) with a finite spin-imbalance ($h \neq 0$) we show the site occupation of the majority/minority spin component (red/blue markers) as a function of both h and μ. The white plane indicates half-filling $\mu = 0$. The data points intersecting this plane are highlighted with squares and diamonds. **c** Combining data sets from **a** and **b** within a similar temperature range ($k_B T/t \approx 1.5$) leads to a collapse of the data onto the same curve.

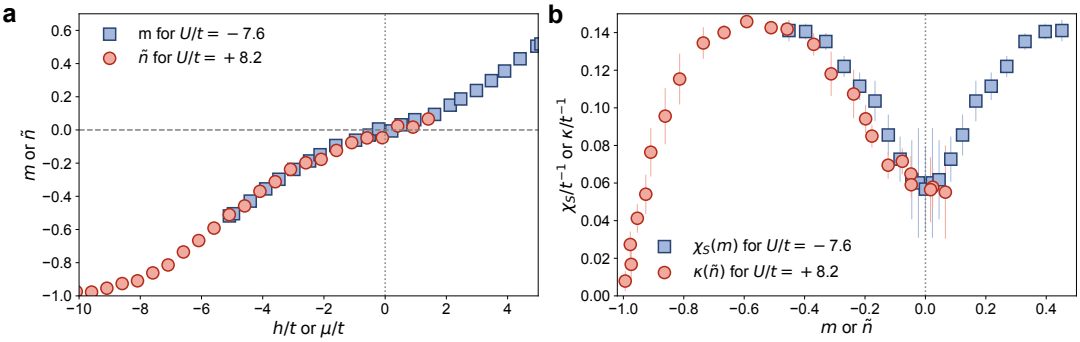

Figure 4.10: **Observing the Mott-like incompressibility with attractive interaction**. **a** The equations of state $n(\mu)$ (red circles) and $m(h)$ (blue squares) for attractive and repulsive interaction, respectively. We observe that near the corresponding symmetry point $\mu = 0$ or $h = 0$, the local magnetisation or density experiences a Mott-like plateau. **b** Spin susceptibility χ_s (blue squares) at half-filling and attractive interactions compared to the compressibility κ (red circles) in a spin-balanced system with repulsive interactions. We measure the magnetisation m at half-filling for a large range of the effective Zeeman field h up to $4.7t$. The spin susceptibility χ_s is obtained by performing the numerical derivative $\partial m/\partial h$. The error bars represent the standard errors in the numerical differentiation.

singles density (green circles) enables the determination of the half-filling point $\mu = 0$ (dashed line). While the chemical potential μ imbalances the populations of doubles and holes when moving away from half-filling, the effective Zeeman field h takes on a similar role if we consider the spin up and down populations instead.

To investigate the effect of spin-imbalance, i.e. $h \neq 0$, we switch our detection routine to the spin sector. In Fig. 4.9 **b**, the site occupation of spin up (red markers) and spin down (blue markers) singles are plotted as a function of μ for different global Zeeman fields h at repulsive interactions ($U/t = +7.6$). We extract corresponding data points at $\mu = 0$, highlighted with squares and diamonds. In Fig. 4.9 **c**, we combine both previous measurements and plot the doubles (black circles) as a function of chemical potential μ for attractive interactions and $h = 0$. Using the same axis scale for the effective Zeeman field h and repulsive interactions, we plot the measured singles spin up (majority) component at half-filling $\mu = 0$ (red squares). Flipping the sign of h interchanges the populations of spin up and down, therefore we can use the minority spin component at half-filling (blue diamonds) when inverting the Zeeman field h. The excellent agreement of our data, when interchanging the role of μ and h, highlights the versatility of the particle-hole symmetry.

4.3.2 Observation of a spin-incompressible phase

Finally, we extend the investigation of the particle-hole correspondence to the phase diagram of the Hubbard model. The Mott insulator on the repulsive side has been studied in detail over the past years [108–112]. At low temperatures, the system favours singly-occupied sites over doubles and holes due to its lower energy profile. Around half-filling the isothermal compressibility $\kappa = \partial\tilde{n}/\partial\mu$ is low, signalling that it is energetically unfavourable to accommodate more particles when raising the chemical potential, which is the hallmark of the insulating nature of this state [113].

The corresponding phase on the attractive side is dominated by preformed pairs, thereby suppressing the local magnetisation m. In contrast to the repulsive side, where the system opposes the formation

of doubles, it is now unfavourable to break them, even when the spin populations get slightly imbalanced. This is observed as a minimum of the static spin susceptibility $\chi_s = \partial m/\partial h$ at $m = 0$. However, even beyond this qualitative argument, the particle-hole transformation provides the exact mapping between the two correlation functions κ and χ, which should precisely equal each other. We display our measurement of $\kappa(\tilde{n})$ and $\chi_s(m)$ in Fig. 4.10 and despite comparing systems with opposite interaction strengths and different observables, we observe a strikingly good agreement. Therefore, we demonstrate that we can use the particle-hole symmetry to simulate the Mott phase with a spin-imbalanced system and attractive interactions.

4.4 Conclusion

With the experimental observation of a Mott-equivalent phase in the attractive Hubbard model, we validate a novel experimental approach in quantum simulations. Not only is the quantum simulation apparatus able to realised model Hamiltonian with specific phenomena, but they could also be used to simulate physics at which the one phase maps to another.

d-wave superconductivity and d-wave anti-ferromagnet For instance, the existence of a d-wave superconducting phase in a density-doped repulsive Hubbard model remains debated in the field of condensed matter physics. By detecting a corresponding d-wave AFM spin correlations on the attractive, spin-doped Hubbard model, the conjecture could be equivalently proved. This might be a more experimentally accessible pathway as spin correlations have been observed with superb spatial detection capabilities in recent years. Discussion and our experimental detection of AFM correlations in the two-dimensional Hubbard model can be found in Chapter 5.

Dynamical symmetry in non-equilibrium state So far, the particle-hole symmetry discussed in this thesis focuses on quantum states in thermal equilibrium. However, a similar idea based on symmetry can be generalised to quantum dynamics or even highly non-equilibrium situation such as sudden, non-adiabatic quenching. For example, under certain conditions, the spin and charge transports in the Hubbard model are proved to be equivalent [114]. This relation is in general termed as the *dynamical* symmetry. Measuring such dynamical symmetry in experiments would allow measuring novel dynamics in a quantum system using this idea, similar to how we measure the charge sectors using a spin measurement.

CHAPTER 5

Coherent manipulation of spin correlations

... one can still say that quantum mechanics is the key to understanding magnetism. When one enters the first room with this key there are unexpected rooms beyond, but it is always the master key that unlocks each door.

JOHN HASBROUCK VAN VLECK

Quantum magnetism emerges in spin-1/2 many-body systems from the interplay of temperature and exchange interaction. In our repulsive Hubbard quantum simulator, we cool down the atomic ensembles to temperatures comparable with the super-exchange energy at which anti-ferromagnetic ordering emerges. In addition to measuring anti-ferromagnetic correlations in real space, we demonstrate a coherent manipulation of the spin correlations in momentum space and observe the time-evolution from an anti-ferromagnetic to a ferromagnetic one. The ability to coherently manipulate spin correlations opens a new pathway to study strongly correlated systems with ultracold atoms.

The main experimental results discussed in this chapter were published in *Phys. Rev.* **A 97**, 051602 (2018) [115].

5.1 Introduction

5.1.1 Types of magnetism

Paramagnetism and Diamagnetism The study of quantum magnetism centres around the ordering of magnetic moments. In real solid materials, the magnetic moment arises from the electronic spin angular momentum [116]. In the presence of an ***external magnetic field***, the alignment of the magnetic moment tends to follow the magnetic field lines, in order to lower the internal energy of the system [1]. This leads to magnetic ordering and the emergence of a finite magnetisation. Depending on whether the electronic spins align ***parallel*** or ***anti-parallel*** to the applied magnetic field, the ordering phenomenon are known as ***paramagnetism*** and ***diamagnetism***, respectively [46].

Exchange interaction Another form of magnetism can arise in the *absence* of an external field. Interaction between magnetic moments, instead of an external field, leads to magnetic ordering. This kind of interaction is called the ***exchange interaction***. The major goal of this section is to outline one of the simplest model Hamiltonian, which describes the effect of exchange interaction in many-body systems. Depending on the sign of the exchange interaction, either ***ferromagnetism*** or ***anti-ferromagnetism*** arises in the low-energy state. The Hubbard model, under specific limiting conditions, possesses a similar exchange-like interaction which arises from the interplay of the Pauli exclusion principle and tunnelling dynamics.

5.1.2 Simplest model for quantum magnetism

Heisenberg model One of the simplest model that captures the essence of exchange interaction is the ***Heisenberg model*** [117]. We consider quantum mechanical spin in a lattice, with nearest neighbour interaction dependent on the relative spin orientation, the explicit form is given by

$$H = -\sum_{<i,j>} J_{ij}\, \boldsymbol{S}_i \cdot \boldsymbol{S}_j\,, \tag{5.1}$$

where $\boldsymbol{S}_i = (S_i^x, S_i^y, S_i^z)$ denotes the local spin operator at site i and J_{ij} represent the strength of the exchange interaction. For simplicity, we consider only the spin-$1/2$ case ($S = 1/2$) and the exchange interaction is isotropic $J_{ij} = J$. For $J < 0$, the ground state corresponds to a state coupled spin prefer to align anti-parallel, *i.e.* $\boldsymbol{S}_i \cdot \boldsymbol{S}_j < 0$, giving rise to an ***anti-ferromagnet*** (AFM). This is analogous to the classical Neel state, in which neighbouring dipoles point exactly in opposite direction. In the AFM state, the lattice is divided into two sublattices A and B, and the ordering manifests as distinct staggered magnetisation between two sublattice. On the other hand, for $J > 0$, the coupled moments align in parallel ($\boldsymbol{S}_i \cdot \boldsymbol{S}_j > 0$), leading to a ***ferromagnet*** (FM). A typical FM exhibits magnetic domains where the quantum mechanical spins tend to align in the same direction within one domain.

A key distinction between AFM and FM is that the former does not have spontaneous magnetisation, whereas the latter does. As shown in Fig. 5.1, the global magnetisation of the AFM state is zero

[1] For classical spin, the magnetic moment aligns parallel/anti-parallel to the magnetic field. In the quantum mechanical picture, however, the spin angular momentum cannot align in parallel/anti-parallel to the magnetic field due to the inherent uncertainty of the spin angular momentum.

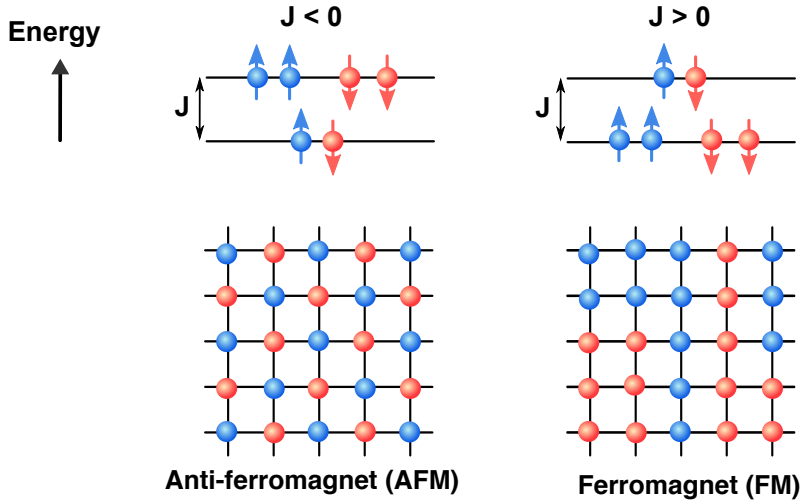

Figure 5.1: **Exchange interactions and magnetically-ordered states.** (Left) The anti-ferromagnetic state where energy is minimal with Anti-parallel spin distributed into two sublattices, forming a classical analogue of a chequerboard board pattern. (Right) The ferromagnetic state with magnetic domains containing only one spin component. For both AFM and FM, the existence of quantum fluctuations leads to an innate uncertainty in the spin orientations even in the ground state.

due to its alternating spin pattern. On the other hand, the FM possess magnetic domains, within which the magnetisation is either entirely up or down. For both antiferromagnetic or ferromagnetic coupling, at high temperatures, thermal fluctuations tend to randomise the many-body spin states. Therefore, there exists a phase transition temperature, or often known as the ***Curie's temperature*** T_C, above which the system becomes paramagnetic.

In addition to temperature effect, it is also important to include the existence of ***quantum fluctuations*** when considering quantum magnetism. These fluctuations essentially entangle the spins, hence forming inherent fluctuation in correlations [116]. To demonstrate this point, we consider the order parameters of the AFM and FM, namely, the *staggered* and *uniform* magnetisation respectively,

$$\begin{aligned} \text{AFM}: M_{\text{AFM}} &= \frac{1}{N}\sum_{i}^{N}(-1)^i\langle S_i^z\rangle \ , \\ \text{FM}: M_{\text{FM}} &= \frac{1}{N}\sum_{i}^{N}\langle S_i^z\rangle \ . \end{aligned} \tag{5.2}$$

A classical spin state in the ground state implies $M = 1/2$ for both AFM and FM, whereas quantum fluctuations brings inherent randomness to the spin states such that $M < 1/2$. This can be brought to analogy with a quantum harmonic oscillator, where the ground state possesses finite energy due to the zero-point motion. The simple patterns shown in Fig. 5.1, nonetheless, capture the essential character of the state. In addition, in two-dimensions, the enhanced quantum fluctuations leads to the absence of finite-temperature phase transition in the thermodynamic limit, *i.e.* $M \neq 0$ only at $T = 0$ when $N \to \infty\, V \to \infty$. In this chapter, we focus on the formation of spin correlations in the short range, which can still emerge at finite temperature.

Magnetism in the Hubbard model From the discussion of the Hubbard model in the double-well limit in Sec 2.2.3, we learn that even with strong repulsion U, the tunnelling of particles to neighbouring sites is possible via virtual hopping, as shown in Fig. 5.2 **a**. This process is known as super-exchange. The term "super" is used with reference to the direct tunnelling process, which is sometimes called kinetic exchange in solid-state physics. We note that in real materials, both kinetic exchange and super-exchange are not limited to nearest neighbour due to their more complex structures. When generalised to the Hubbard model in two-dimension, the super-exchange interaction is vital to the emergence of spin ordering.

We start by considering a strongly repulsive Hubbard system, where the interaction is larger than the bandwidth $U \gg W = 8t$, the energy dispersion is split into two energy bands. The lower energy band contains states with singly-occupied sites, whereas the upper band consists of doublons and holes. At temperature much lower than the interaction $k_B T \ll U$, thermal fluctuations only admix states in the lower band, which does not incur a change in density, but do incur a change in spin magnetisation [2]. An equivalent statement is that density excitations and spin excitations are well separated, and therefore the density degree of freedom can be considered frozen at low temperature. In this scenario, the interplay of the exchange interaction (on the order of J) and kinetic energy (on the order of t) dominates the physical behaviour. Indeed, in the limit $U/t \to \infty$, the Hubbard model around half-filling can be rewritten to a Heisenberg spin Hamiltonian. Using second-order perturbation theory, one can obtain an anti-ferromagnetic coupling $J = -4t^2/U$ between local

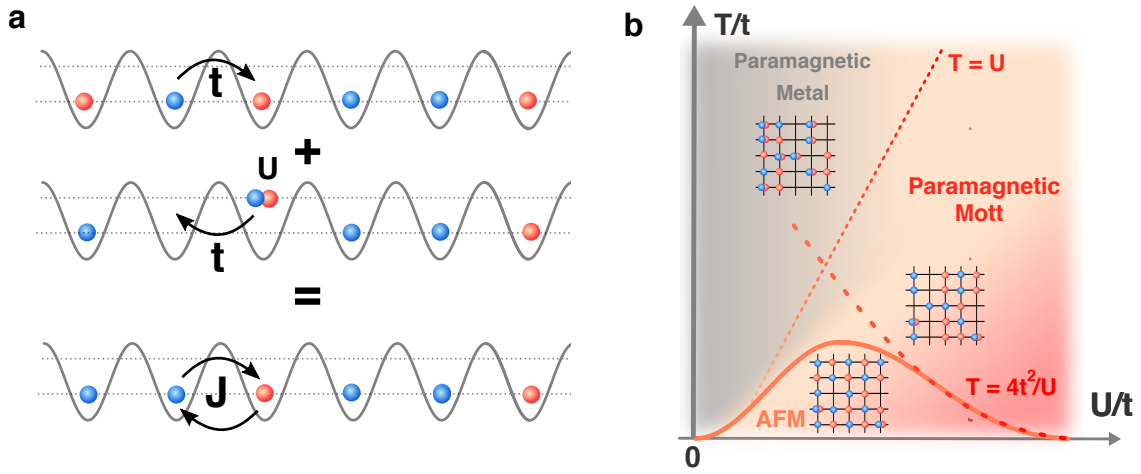

Figure 5.2: **Super-exchange interaction and onset of AFM ordering in the phase diagram at half-filling.** **a**. The virtual hopping is a second-order process where a particle tunnels to a neighbouring site and then hop back via the intermediary state with higher energy. **b**. Phase diagram of the Hubbard model at half-filling. The phase diagram can be understood from two constraining conditions for the emergence of spin ordering. First, there need to be sufficient magnetic moments, which is given by the Mott criteria where repulsive interaction suppresses doubly-occupied sites. The second criterion is met with sufficiently strong exchange interaction $J = 4t^2/U$. Overlapping two criteria give the interaction regime where the onset of anti-ferromagnetic ordering emerges.

[2] This is similar to the case in which spin-singlet and triplet states carry the same average density, but the total spin angular momentum is different.

moments at nearest-neighbouring sites [118], and the Hamiltonian reads

$$H = -J \sum_{<i,j>} \boldsymbol{S}_i \cdot \boldsymbol{S}_j. \tag{5.3}$$

To understand the parameter space at which AFM ordering is favourable, it is advisory to look at two criteria. Firstly, for sufficient exchange interaction between local magnetic moments, the temperature has to be lower than the repulsive interaction U such that the density degree of freedom is suppressed. This goes hand in hand with the accumulation of moments near the dotted line ($k_B T = U$) in Fig. 5.2 **b**. Secondly, the thermal fluctuation, characterised by the energy scale $k_B T$, should be close to or below the super-exchange energy J such that the ordering is preserved. Despite its simplicity and single-particle nature, this simple energy argument gives the correct picture that AFM correlation emerges at the highest temperature around intermediate interaction strengths. More sophisticated calculations reveal that, in two-dimension, the onset of AFM correlations is the most prominent near $U/t \sim 8$ [60], as reflected in the solid line. Throughout this chapter, we, therefore, work at a repulsive interaction strength at $U/t = 7.6(1)$.

5.1.3 Spin-spin correlations of the anti-ferromagnetic state

Real space spin correlations The spatial anti-ferromagnetic ordering is characterised by the correlation between moments at different lattice sites. We define the spin-spin correlations in two-dimension as

$$C^z_{ij} = \langle m^z_i m^z_j \rangle - \langle m^z_i \rangle \langle m^z_j \rangle. \tag{5.4}$$

Here C^z_{ij} is the spin-spin correlation between site i and j. The first term is the correlated expectation value of local moments at two sites and the second term is the offset correlations from the uncorrelated spins. The superscript z refers to the correlation of magnetic moments along the z-axis. The spin correlations in x and y directions $C^{x/y}_{ij}$ are defined in equivalent way. Owing to the spin-SU(2) symmetry introduced in Chapter 4, $C^z_{ij} = C^{x/y}_{ij}$. For $i = j$, the local spin correlator reduces to the on-site fluctuation of the magnetisation, *i.e.*

$$C^z_{ii} = \langle (m^z_i)^2 \rangle - \langle m^z_i \rangle^2 \equiv C^z_{00}, \tag{5.5}$$

which is known as the ***local moment***. For an anti-ferromagnetic state, the spin correlators change signs between every neighbouring site, forming a staggered pattern. In Fig. 5.3 **a**, we depict the spatial spin correlations obtained from the DQMC simulation (details see Sec 2.5). It is straightforward to observe that the spatial spin correlators C^z_{ij} of the spin state depend only on the distance $d = |\boldsymbol{r}_i - \boldsymbol{r}_j|/a$, as shown in Fig. 5.3 **b**. More specifically, the magnitude of the spatial correlators follows an exponential decay,

$$|C_{ij}| \equiv |C_d| \propto e^{-da/\xi}. \tag{5.6}$$

Here, ξ is the spin-spin correlation length. In two-dimensions, the ***Mermin-Wagner theorem*** implies the absence of true long-range order [119]. However, at finite temperature, short-range magnetic correlation is still possible, with the correlation length following an exponential form in temperature $\xi(T) \propto \exp(\frac{J}{T})$ [120].

Static spin structure factor So far, the discussion of correlation focuses on the real space lattice. However, correlations could be equivalently studied in the momentum space. For instance, the

Fourier transform of the real space spin correlation C^z_{ij} results in the static spin structure factor $S(\boldsymbol{q})$,

$$S(\boldsymbol{q}) = \frac{1}{N}\sum_{i,j} e^{-i\boldsymbol{q}\cdot\boldsymbol{r}_{ij}} C^z_{ij} \,. \tag{5.7}$$

The static structure factor is a key quantity describing the many-body system and captures the momentum weight of collective excitations in the system. In the spin sector, $S(\boldsymbol{q})$ entails information about spin excitations in the system. The structure factor in a lattice system is defined within the 1$^{\text{st}}$ Brillouin zone *i.e.* the quasi-momentum $\boldsymbol{q} \in [-\pi/a, \pi/a]$ in a square lattices. At $\boldsymbol{q} = 0$, $S(\boldsymbol{q})$ is the sum of spatial correlators at all distances, and therefore is called the ***uniform*** structure factor. The emergence of magnetic order, on the other hand, is most prominently signaled by a peak in $S(q)$ at the edge of the 1$^{\text{st}}$ Brillouin zone, e.g. at $\boldsymbol{q}_{\text{AFM}} = (\pm\pi/a, \pm\pi/a)$. At $\boldsymbol{q} = \boldsymbol{q}_{\text{AFM}}$, the static structure factor becomes an *alternating* sum of the spatial correlators, and is thus called the ***staggered*** structure factor.

In solid-state systems, the structure factor of a material can be measured using techniques such as nuetron or X-ray scattering [121, 122]. A similar technique was demonstrated in a three-dimensional optical lattices experiment using Bragg scattering of laser light, which gives access to the magnetic structure factor at a fixed wave vector and averaged over regions of different filling [123]. As will be shown later, one of the key results in this chapter is the full momentum-resolved and filling-resolved measurement of the spin structure factor via the coherent evolution of the many-body spin states. This technique not only offers a monotonic probe for thermometry but also opens access to decompose

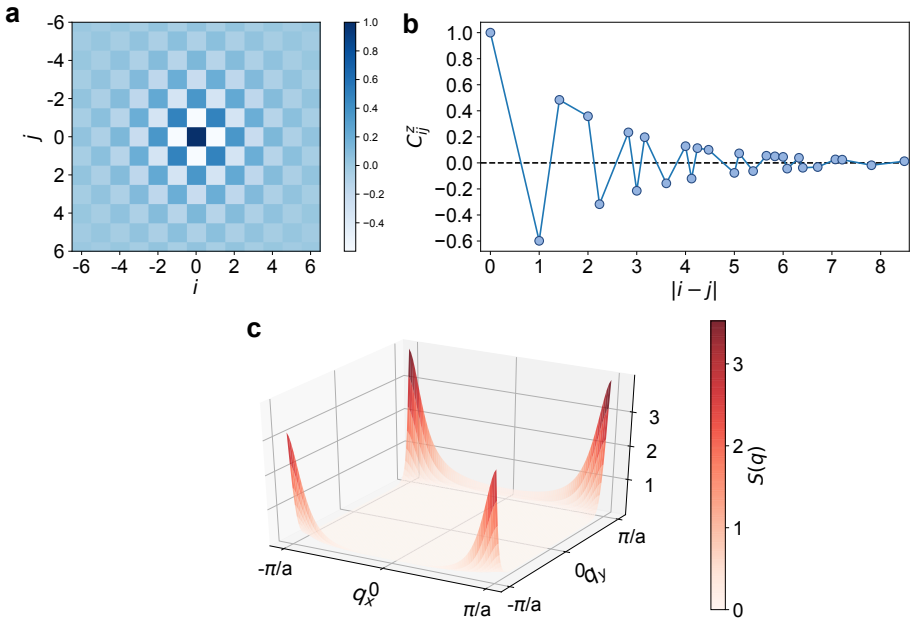

Figure 5.3: **Numerical simulations of spin correlations in position space and momentum space. a**. Spin correlations C^z_{ij}, simulated using the DQMC method at $U/t = 8$ and $k_BT/t = 0.1$ on a 12×12 square lattice, shows a chequerboard pattern, where the sign of the individual correlators flips every site, the hallmark feature of an anti-ferromagnet. **b**. Exponential decay of spin correlations as a function of distance. **c**. The spin correlation in momentum space is characterised by the static spin structure factor $S(\boldsymbol{q})$, which can be computed via the Fourier transform of C^z_{ij}. The alternating spatial correlations, therefore, transform to a peak at the corners of the 1$^{\text{st}}$ Brillouin zone.

individual correlators.

Link to thermodynamic observables It is also worth noting that the structure factor, in essence, encapsulates all fluctuations in $\langle m^z \rangle$ at all length scales, which is apparent from the sum in Eq. (5.7). Therefore, it is related to thermodynamic observables via the fluctuation-dissipation theorem, which connects the response of the system to an external perturbation. In the case of the spin-sector measurement, this corresponds to the spin susceptibility χ_s and fulfils the relation

$$\chi_s = k_B T \cdot S(\boldsymbol{q} = 0)\,. \tag{5.8}$$

This is an alternative approach to measure the magnetic susceptibility, in contrast to measurement presented in Chapter 4. The susceptibility is an important quantity in conventional solid materials as it characterises the response upon external perturbation. In Chapter 6, we utilise a similar relation in the density sector to probe the interacting pair correlation function in the attractive Hubbard model.

5.2 Experimental protocols

In this section, we layout the experimental procedures in measuring spin-spin correlations in real space and show the onset of anti-ferromagnetic correlations in our system. Next, we present a novel technique for coherently manipulating the spin correlations in momentum space, effectively probing the spin structure factor $S(\boldsymbol{q})$ at arbitrary wave vector $\boldsymbol{q}$.

5.2.1 Spatial spin correlations detection

Since we aim to probe the spin correlation, we naturally deploy the spin sector detection sequence, similar to the one disccused in Chapter 4 and shown in Fig. 4.4, to characterise the magnetic correlations in our system. Throughout this chapter, we stay with the repulsive Hubbard model at intermediate interaction ($U/t = 7.6(1)$) and use a spin-balanced (same population of spin-up and spin-down states) atomic sample in the optical lattices, *i.e.* $h = 0$. Under this condition, the averaged magnetisation is zero due to the spin SU(2) symmetry, that is,

$$\langle m^z \rangle = \langle n_\uparrow - n_\downarrow \rangle = 0. \tag{5.9}$$

This makes the spin ordering more difficult to detect since the onset of AFM correlation does not show up in locally-averaged quantity. Instead, we need to study the fluctuation of the magnetisation using Eq. (5.4). In addition, we need to take into account the effect of convolution from the imaging point-spread function (PSF). Therefore, the measured magnetisation in our system is given by

$$\tilde{m}^z(\boldsymbol{r}) = \sum_i p(\boldsymbol{r} - \boldsymbol{r}_i)\left(n_{i,\uparrow} - n_{i,\uparrow}\right) = \sum_i p(\boldsymbol{r} - \boldsymbol{r}_i)\, m_i^z, \tag{5.10}$$

where $\int p(\boldsymbol{r}) d^2 r = 1$ and $n_{i,\sigma}$ is the occupation at site i in a two-dimensional lattice. The tilde sign in $\tilde{m}^z(\boldsymbol{r})$ denotes the convoluted quantity, and the coordinate $\boldsymbol{r}$ is discretised by the pixels of the recorded images. As shown in Eq. (5.10), the magnetisation profile at position $\boldsymbol{r}$ contains contribution

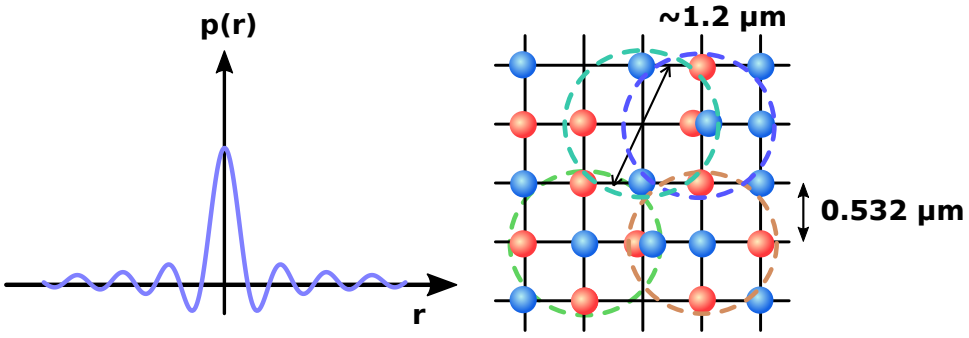

Figure 5.4: **Effect of the imaging point-spread function.** (a) The imaging point-spread function takes the form of an Airy disk [124]. Therefore, the recorded occupation profile is convoluted with $p(r)$. **b** Correlation analysis.

mainly from several lattice sites, that is covered by the main lobe in the imaging PSF.

Next, we compute the correlation between moments at position $\boldsymbol{r}$ and $\boldsymbol{r}+\boldsymbol{d}$, *i.e.*

$$\begin{aligned}\tilde{C}(\boldsymbol{d}) &= \langle \tilde{m}^z(\boldsymbol{r})\tilde{m}^z(\boldsymbol{r}+\boldsymbol{d})\rangle - \langle \tilde{m}^z(\boldsymbol{r})\rangle\langle \tilde{m}^z(\boldsymbol{r}+\boldsymbol{d})\rangle \\ &= \sum_{ij} p(\boldsymbol{r}-\boldsymbol{r}_i)p(\boldsymbol{r}+\boldsymbol{d}-\boldsymbol{r}_j)\left(\langle m_i^z m_j^z\rangle - \langle m_i^z\rangle\langle m_j^z\rangle\right) \\ &= \sum_{ij} p(\boldsymbol{r}-\boldsymbol{r}_i)p(\boldsymbol{r}+\boldsymbol{d}-\boldsymbol{r}_j)\, C_{ij}^z.\end{aligned} \tag{5.11}$$

Here, $\tilde{C}(\boldsymbol{d})$ denotes the correlation signals for a given relative pixel shift $\boldsymbol{d}$, where the expectation values are evaluated over different experimental realisations, as shown in the upper part of Fig. 5.5. We then sum all $\tilde{C}(\boldsymbol{d})$ over a large distance, where $|\boldsymbol{d}_{\max}| \leq 3$ (comparable in absolute size to the width of the PSF), resulting in the integrated signal

$$\begin{aligned}\sum_{\boldsymbol{d}=0}^{\boldsymbol{d}_{\max}} \tilde{C}(\boldsymbol{d}) &= \sum_{ij} p(\boldsymbol{r}-\boldsymbol{r}_i) \underbrace{\sum_{\boldsymbol{d}}^{\boldsymbol{d}_{\max}} \left(p(\boldsymbol{r}+\boldsymbol{d}-\boldsymbol{r}_j)\right)}_{\approx 1} C_{ij}^z = \sum_{ij} p(\boldsymbol{r}-\boldsymbol{r}_i)\, C_{ij}^z \\ &= \sum_{ij} p(\boldsymbol{r}_i)\, C_{0j}^z = \underbrace{\sum_i p(\boldsymbol{r}_i)}_{\approx 1} \sum_j C_{0j}^z = \frac{S(\boldsymbol{q}=0)}{a^2}.\end{aligned} \tag{5.12}$$

Here, we utilise two key approximations. First, we assume that the sum over finite $\boldsymbol{d}$ captures the dominant part of the correlations, which we ensure by empirically setting $|d_{\max}| = 3$, while at the same time minimising the spatial noise from the integration. Second, we assume that the point-spread function does not change significantly over the probed region. Finally, the last equality in Eq. (5.12) is the result of setting $\boldsymbol{q} = 0$ in Eq. (5.7), namely the sum of spatial correlation function overall distance equals the uniform spin structure factor $S(\boldsymbol{q}=0)$.

Non-local correlations At the temperatures reached in our system $k_B T \sim 0.6t$, we expect the emergence of anti-ferromagnetic correlation since $J = 4t^2/U \sim 0.5t$. Yet, the correlation length is

still small comparable to our trap inhomogeneity. Therefore, the use of local density approximation is still valid. By computing the static spin structure factor across our system, using Eq. (5.12), we arrive at the *in-situ* profile of $S(\boldsymbol{q} = 0)$, as shown in Fig. 5.5 **b**. In Fig. 5.5 **c**, we perform the same potential mapping, *i.e.* $(x, y) \rightarrow \mu$, as in Chapter 4 to obtain the structure factor as a function of chemical potential. The static spin structure factor $S(\boldsymbol{q} = 0)$ deviates from the on-site correlation (local moment), indicating an onset of ***non-local*** correlation. In addition, the measured $S(\boldsymbol{q} = 0)$ is always below the local moment, indicating that the remaining non-local correlation is negative in the sum in Eq. (5.12). This gives a clear sign that the dominating non-local correlation is anti-correlated, a hallmark feature of the anti-ferromagnetic phase.

5.2.2 Limitations of the correlation analysis

While our observation of the anti-ferromagnetic correlation offers a clear indication that the temperature regime reached in the optical lattice is comparable with the effective spin interaction (super-exchange J), it also reveals the challenges in detecting even lower temperature phases, such as the conjectured d-wave superconducting state, in the long run. First, since we make use of Eq. (5.12) and probe the integrated correlations, the information of individual correlators is lost. However,

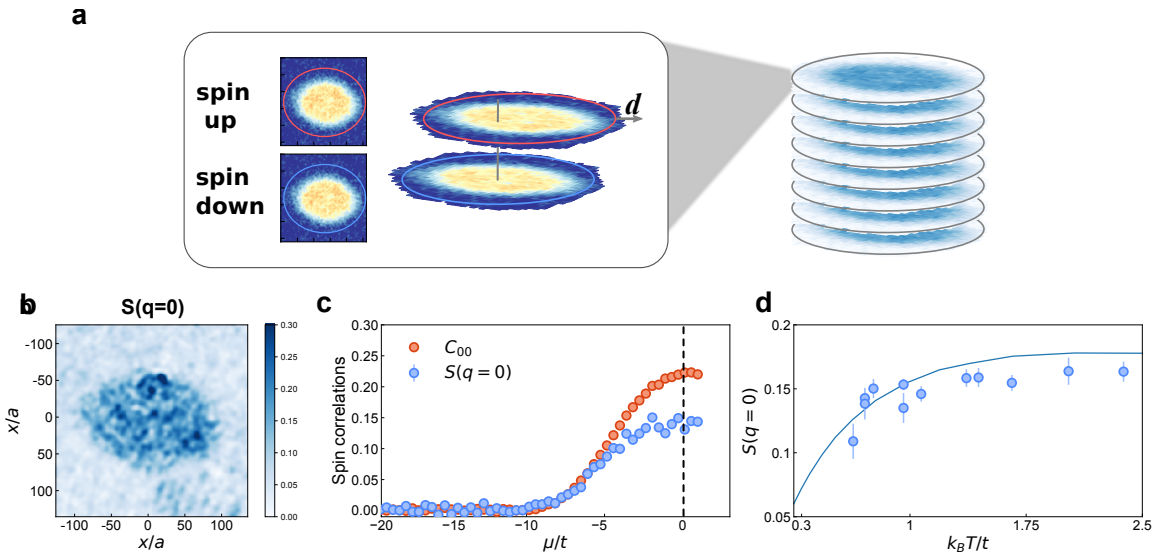

Figure 5.5: **Correlation analysis.** **a** The correlation analysis begins with the evaluation of correlation at a distance $\boldsymbol{d}$. For a given $\boldsymbol{d}$, the product of spin-up and spin-down distribution can be computed. The non-trivial spin-correlations can be obtained upon subtracting the offset correlations. The expectation in Eq. (5.11) are then evaluated across different experimental realisations. Using Eq. (5.12), we integrate the correlations to obtain the spin structure factor. Here, the maximum shift $\boldsymbol{d}_{\text{max}}$ is fixed to 3, up to which our imaging resolution extends. **b** Next, the spatial correlations computed for all shift $\boldsymbol{d}$ are summed over to yield the static spin structure factor $S(\boldsymbol{q} = 0)$. **c** By performing the LDA, we map the spatial profile onto the chemical potential μ axis. Shown in the red data points are the local moment $\langle (m^z)^2 \rangle$ as a function of chemical potential, and the blue data points are the static structure factor. At half-filling $\mu = 0$ (dashed line), we observe a deviation of the integrated correlation from the local moment, indicating a non-local contribution of the spin-spin correlation. **d** Temperature dependence of $S(\boldsymbol{q} = 0)$ at half-filling. Below $k_B T/t \sim 1$, the emergence of anti-ferromagnetic correlations reduces the uniform structure factor.

we note that the full spin structure factor $S(\boldsymbol{q})$ across the entire 1$^{\text{st}}$ Brillouin zone gives equivalent access to the spatial correlators via an inverse Fourier transform, as shown in Eq. (5.7). Therefore, this limitation can be circumvented by probing the spin correlations at finite momenta $\boldsymbol{q}$ as the information of individual correlators can be retrieved.

Secondly, upon lowering temperature, the density degree of freedom is suppressed with respect to thermal fluctuation, *i.e.* $k_B T \ll U$ for repulsive interaction. Empirically, this means that thermometry (determination of temperature) based on fitting the density profile, as shown in Fig. 4.6, becomes insensitive to temperatures as the spin sector dominates over the density one. Therefore, a probe of temperature based on spin correlation measurement is in general preferred. Performing correlation thermometry for the anti-ferromagnetic phase in our system can be difficult due the alternating nature of the correlation and the fact that the static structure factor we probe averages over the staggering correlators. In the $T \to 0$ limit, the static structure factor $S(\boldsymbol{q} = 0) = 0$ as a long-range AFM is established, as reflected in the trend in Fig. 5.5 **d**. Therefore, despite its temperature dependence, using $S(\boldsymbol{q} = 0)$ as a thermometer is not practical due to the low signal-to-noise ratio. Instead, we note that the static structure factor at $\boldsymbol{q} = (\pm\pi/a, \pm\pi/a)$, or equivalently called the ***staggered*** structure factor, given by

$$S(\pm\pi/a, \pm\pi/a) = \frac{1}{N}\sum_{i,j}(-1)^{i+j} C^z_{ij}\,, \tag{5.13}$$

is a sensitive probe for the AFM correlations. As shown in Fig. 5.3 **c**, $S(\boldsymbol{q})$ peaks at the corners of the 1$^{\text{st}}$ Brillouin zone. This sensitivity can be understood as the result of the alternating pre-factor $(-1)^{i+j}$ in the summation in Eq. (5.13). As a result, $S(\pm\pi/a, \pm\pi/a)$ diverges exponentially for $T \to 0$ [125], and thus offers an ideal temperature probe in principle down to the ground state of the system.

5.3 Imprinting spin spiral

Motivated by the need for characterisation of individual correlators and accurate thermometry, we introduce here a novel scheme based on Ramsey interferometry [64, 126, 127], to allow the detection of spin correlations at arbitrary momentum $\boldsymbol{q}$ within the 1$^{\text{st}}$ Brillouin zone. To understand the basic idea of this experimental technique, we first present a quick revision about spin precession in a magnetic field. Then we extend the concept to spatial inhomogeneity, where a magnetic field gradient is applied. Using this idea, we introduce the concept of imprinting a spin spiral to the atomic cloud. The key point here is to expose the atomic cloud to a magnetic field gradient where the local moments precess in the transverse xy-plane at position-dependent rates. As a result, the spin correlations also coherently evolve according to the local magnetic field strengths.

5.3.1 Local spin precession: building blocks of spin spiral

Spin precession In classical physics, when a magnetic moment is subject to external magnetic field $\boldsymbol{B}$, a torque $\boldsymbol{\tau}$ on the magnetic moment is generated, and is given by

$$\boldsymbol{\tau} = \boldsymbol{\mu} \times \boldsymbol{B} = \gamma \boldsymbol{J} \times \boldsymbol{B}\,. \tag{5.14}$$

Here $\boldsymbol{\mu}$ is the magnetic dipole moment, γ is the gyromagnetic ratio and $\boldsymbol{J}$ is the angular momentum

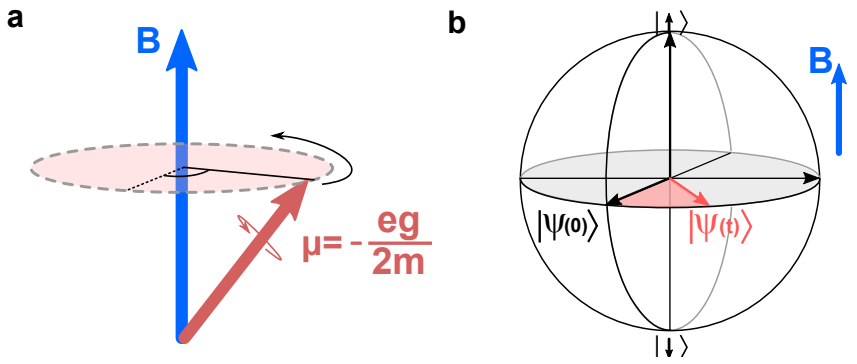

Figure 5.6: **Spin precessions.** **a** Spin precession of a classical magnetic dipole (wire-loop) about applied magnetic field. **b** Spin precession of a quantum mechanical spin state in external magnetic field.

vector. The end result is that the magnetic moment precess about the axis of $\boldsymbol{B}$, as shown in Fig. 5.6 **a**, with the ***Larmor frequency*** $\omega_L = \frac{d\theta}{dt} = \gamma|\boldsymbol{B}|$. Now consider two magnetic moments $\boldsymbol{\mu}_1$ and $\boldsymbol{\mu}_2$ with a different gyromagnetic ratio (γ_1 and γ_2 respectively) subjected to the same magnetic field. They would then precess at a different rate with a frequency difference proportional to the difference $\Delta\gamma = |\gamma_1 - \gamma_2|$. After a certain time Δt, the difference in angle *accumulated* in the process increases linearly with time, according to

$$\Delta\phi = \phi_1 - \phi_2 \propto \Delta\gamma \cdot \Delta t. \tag{5.15}$$

Quantum mechanically, the Hamiltonian of a spin-1/2 particle coupled to an external magnetic field is given by

$$H = -\boldsymbol{\mu} \cdot \boldsymbol{B} = \frac{\hbar\omega}{2}\hat{S}_z. \tag{5.16}$$

Here, we set the magnetic field $\boldsymbol{B}$ such that it is along the quantisation axis (z-direction) and $\hbar\omega$ is the Zeeman splitting between the two spin states in a magnetic field. For simplicity, we consider an initial superposition state $|\psi(t=0)\rangle = \frac{1}{\sqrt{2}}(|\uparrow\rangle + |\downarrow\rangle)$. In the Bloch sphere picture with rotating frame, as shown in Fig. 5.6 **b**, the initial state precesses about the magnetic field axis, according to

$$|\psi(t)\rangle = e^{-\frac{i}{\hbar}\hat{H}t}\,|\psi(0)\rangle \propto \frac{1}{\sqrt{2}}\left(|\uparrow\rangle + e^{i\omega t}\,|\downarrow\rangle\right). \tag{5.17}$$

Therefore, the time-evolution of the spin state can be represented by a *differential rotation* between the spin-up and spin-down state, which introduces a phase lag $\Delta\theta = \omega\Delta t$ between the spin-up and spin-down states.

The Ramsey sequence : Imprinting spin spiral Combining the phase lag $\Delta\theta$ from the differential time-evolution and magnetic field inhomogeneity are of the essence of a Ramsey sequence. To demonstrate, we first consider a spin-polarised cloud of atoms, *i.e.* all atoms in the states $|\uparrow\rangle$ for instance, and the Ramsey sequence, as shown in Fig.5.7 **a**, can be outlined in the following steps,

1. A $\pi/2$-pulse, resonant at the energy difference $\hbar\omega_{\pi/2} = E_\uparrow - E_\downarrow$, is applied to transfer the local spin state to the superposition state $|\psi\rangle = \frac{1}{\sqrt{2}}(|\uparrow\rangle + |\downarrow\rangle)$. The calibration of the $\pi/2$-pulse can be found in Chapter 2.

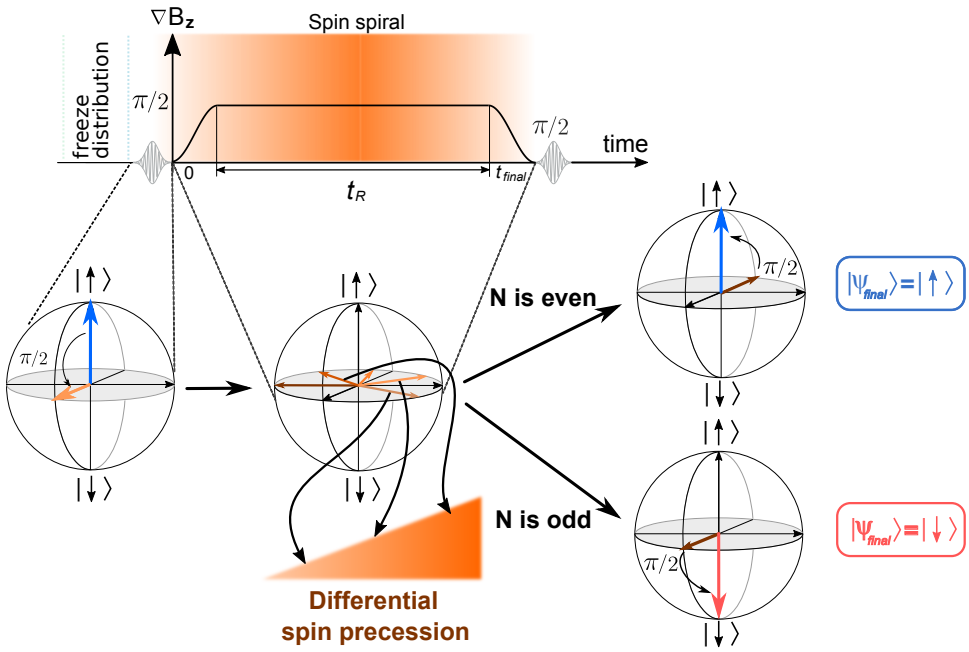

Figure 5.7: **Ramsey sequence.** The Ramsey sequence starts with a $\pi/2$-pulse, which drives the spin-up state to a superposition of spin-up and spin-up. The magnetic field gradient then ramps on, giving a position-dependent magnetic field. Therefore, the local spin states precess at different rates and accumulate a phase difference during the Ramsey evolution time t_R. The end result is in general spin pattern across the lattice.

2. A magnetic field gradient $\nabla \boldsymbol{B}(\boldsymbol{r})$ is turned on for a variable time t_R. Now the atomic ensembles experience a position-dependent magnetic field, thus the atoms acquire a position-dependent phase $\phi(x, y) = \gamma \int_0^{t_{\text{final}}} |\boldsymbol{B}_z(x, y)| dt$.

3. Depending on the phase accumulated during the precession, a second $\pi/2$-pulse drives the spin state back to either the spin-up or spin-down state. For $\phi = N\pi$, where N is odd, the spin state would end up in the spin-down state; whereas if N is even, the spin state would end up in the spin-up state.

Our spin-resolved detection sequence (see Fig. 4.4) detects the occupations of spin-up and spin-down state within a single experimental realisation, therefore allowing us to capture the manipulated spin-wave pattern. Next, we discuss how specific special cases at which the Ramsey sequence serves as a powerful tool in unravelling the anti-ferromagnetic phase.

5.3.2 Mapping anti-ferromagnet to ferromagnet

For the Ramsey sequence, one important special case with optical lattices is when the direction of the magnetic field gradient is aligned to the diagonal of the underlying lattice structure. In this way, when the imprinted $|k_{\text{sp}}| = \sqrt{2}\pi/a$, where $a = 532\,\text{nm}$ is the in-plane lattice spacing, it creates a phase pattern with diagonal iso-phase line of π (see dashed lines in Fig. 5.8 **a**). This can be intuitively understood using the classical picture. In Fig. 5.8, we consider a spin-polarised band insulator, with every site filled with the spin-up state. This initial state, in essence, is a ferromagnetic state, although not induced by spontaneous magnetisation but simply by a population imbalance. After the Ramsey

sequence with the correctly calibrated time t_R, we impose a π phase shift along every diagonal line perpendicular to the imprinted $\boldsymbol{k}_{\rm sp}$. The end result is mapping a chequerboard pattern, which in essence is a classical Neel's AFM state. It is not difficult to see that if one starts with a classical Neel's state, the end result would be a ferromagnetic state as well.

Next, we move onto the effect of imprinting spin spiral onto a *correlated* many-body state. To demonstrate the time-evolution of the correlations, we invoke the Heisenberg picture, where the operators evolve in time instead of the state vector. By imprinting a spin spiral, one can show that equivalently the fermionic operators evolve as follow

$$\begin{aligned}\hat{c}_{i,\uparrow/\downarrow}(t) &= \exp\left[\pm i\frac{\phi(t)}{2}\right]\hat{c}_{i,\uparrow/\downarrow}(0)\\ \hat{c}^{\dagger}_{i,\uparrow/\downarrow}(t) &= \exp\left[\mp i\frac{\phi(t)}{2}\right]\hat{c}^{\dagger}_{i,\uparrow/\downarrow}(0).\end{aligned} \tag{5.18}$$

We consider the spin operators

$$\hat{m}_i^{x/y/z}(t) = \frac{1}{2}\sum_{s,s'=\uparrow,\downarrow}\hat{c}^{\dagger}_{i,\sigma}(t)\left(\sigma_{x/y/z}\right)_{s,s'}\hat{c}_{i,\sigma}(t), \tag{5.19}$$

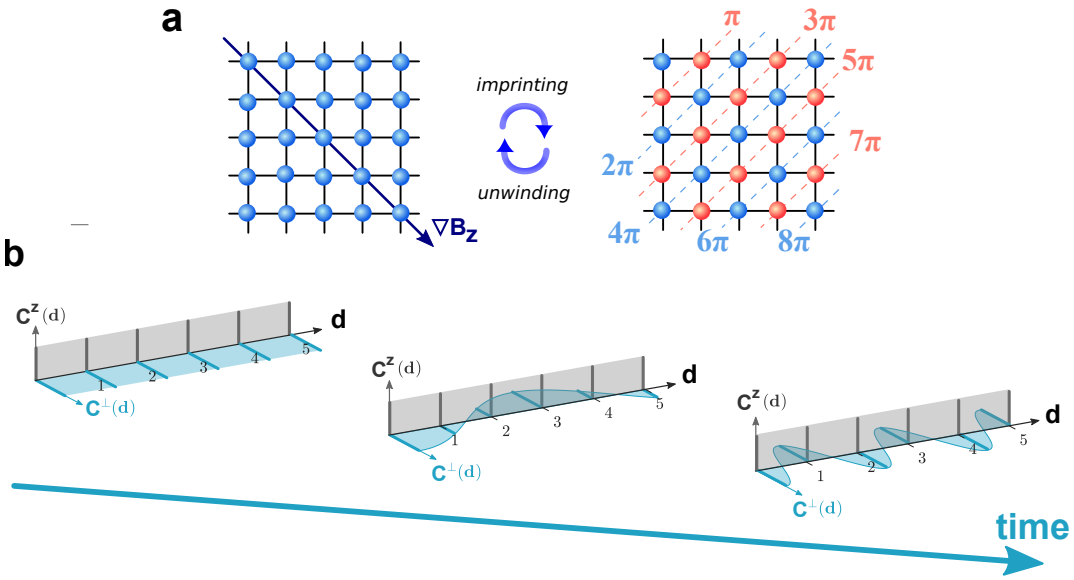

Figure 5.8: **Imprinting spin waves from FM to AFM. a** Starting from a uncorrelated spin-polarised band insulator, the spin spiral can be imprinted such that the wave vector imprinted $\boldsymbol{k}_{sp}$ along the diagonal of a square lattice. Setting the Ramsey evolution time t_R such that phase along neighbouring diagonals (perpendicular to $\mathbf{k}_{sp}$ differs by π. The end result is mapping a ferromagnetic distribution to an anti-ferromagnetic one. **b** Evolution in correlation space. Under the Heisenberg picture, the fermionic operators rotate according to Eq. (5.21), where the vertical (z-direction) correlators is unaffected and the transverse correlators $C^{\perp}(d)$ picks up a rotating phase as a function of distance d. At the special point at which the phase difference is odd multiple of π, the spin correlators obtain a staggering minus sign, *i.e.* $(-1)^d$.

and substituting Eq. (5.18) into it, we then obtain

$$\begin{aligned} \hat{m}_i^z(t) &= \hat{m}_i^z(0)\,, \\ \hat{m}_i^{x/y}(t) &= \cos\phi(t)\,\hat{m}_i^{x/y}(0) \pm \sin\phi(t)\,\hat{m}_i^{y/x}(0)\,. \end{aligned} \tag{5.20}$$

One important consequence from Eq. (5.20) is that the spin operator in the direction of the magnetic field is time-independent, whereas the transverse spin operators precesses. Therefore, the longitudinal spin-spin correlations $C_{ij}^z = \langle m_i^z m_j^z \rangle$ remains unchanged in time, and the transverse one evolves coherently according to

$$C_{ij}^{x,y}(\boldsymbol{k}_{\mathrm{sp}}[t]) = \cos(\boldsymbol{k}_{\mathrm{sp}}[t] \cdot \boldsymbol{r}_{ij})\, C_{ij}\,. \tag{5.21}$$

Eq. (5.21) can be interpreted by imprinting a spatial pattern into the correlators space which changes with the evolution time t_R. Initially, when no spiral is imprinted, the SU(2) symmetry guarantees C_d is isotropic. As time elapses, the transverse correlators pick up a spatially-varying phase structure according to the magnetic field gradient, as shown in the middle plot in Fig. 5.8 **b**. Eventually, by calibrating the magnetic field gradient direction and the evolution time t_R, we can arrive at the condition $\boldsymbol{k}_{\mathrm{sp}}[t_R] \cdot \boldsymbol{r}_{ij} = (\pi/a, \pi/a)$, where alternating correlators flip sign (see right plot of Fig. 5.8 **b**). In this case, Eq. (5.21) reduces to

$$C_{ij}^{x,y}(\boldsymbol{k}_{\mathrm{sp}}[t_R]) = (-1)^{i+j}\, C_{ij}\,, \tag{5.22}$$

thereby allowing us to coherently evolve a state with anti-ferromagnetic correlations to one with ferromagnetic correlations, and *vice versa*. This is in nice agreement with the simple classical picture as shown in Fig. 5.8, where one can imprint an FM to AFM, or unwind the AFM to FM.

Alignment of the spin spiral For the calibration of our technique, we start with a spin-polarized cloud of atoms in $|\uparrow\rangle$ and imprint a spin pattern with wave vector $\boldsymbol{k}_{\mathrm{sp}}$. The observed contrast is given by

$$M(x,y) = \frac{S_\uparrow(x,y) - S_\downarrow(x,y)}{S_\uparrow(x,y) + S_\downarrow(x,y)}. \tag{5.23}$$

Here, $S_{\uparrow/\downarrow}$ is occupations of singly-occupied state. The measured contrasts with different imprinted wave vectors are displayed in Fig. 5.9 **a** and 5.9 **b**. The discretised lattice space implies that the wave vector $\boldsymbol{k}_{\mathrm{sp}}$ that monotonically grows with the spin evolution time t_R is equivalent to a wave vector $\boldsymbol{q}_{\mathrm{sp}}$ within the 1$^{\mathrm{st}}$ BZ. Both the magnitude and the direction of the wave vector $\boldsymbol{q}_{\mathrm{sp}}$ (see Fig. 5.9) can be extracted by Fourier transform of the contrast $M(x,y)$.

Therefore, for evolution times near t_R, at which $k_{sp}[t_R] = (2\pi/a, 2\pi/a)$, we again observe the spin patterns, however, with decreasing wave vector $|\boldsymbol{q}_{\mathrm{sp}}|$ (see Figs. 5.9 **d** and **e**). If the wave vector is aligned with the lattice diagonal as intended, we observe a recurrence of the spin polarized gas at $\boldsymbol{k}_{\mathrm{sp}} = (\frac{2\pi}{a}, \frac{2\pi}{a})$, which we use for fine adjustment of the gradient direction. From a combined fit to the observed evolution of the wave vector of the spin pattern, we extract the evolution time t_{sp}^{π} required for realizing a chequerboard spin pattern with $\boldsymbol{k}_{\mathrm{sp}} = \boldsymbol{q}_{\mathrm{AFM}}$ as illustrated in Fig. 5.9 **e**. The finite wave vector at $t_{\mathrm{sp}} = 0$ is induced by the spin evolution that takes place when the magnetic field gradient is turned on and off, which leads to a finite offset phase.

Due to the effect of extended PSF as depicted in Fig. 5.4, our optical resolution can only resolve spatial spin patterns with wave vectors (spatial frequency) up to $|\boldsymbol{q}_{\mathrm{sp}}| \approx 2\pi/(5a)$. We, however, can resort to momentum space measurement in order to overcome our resolution limit. After applying

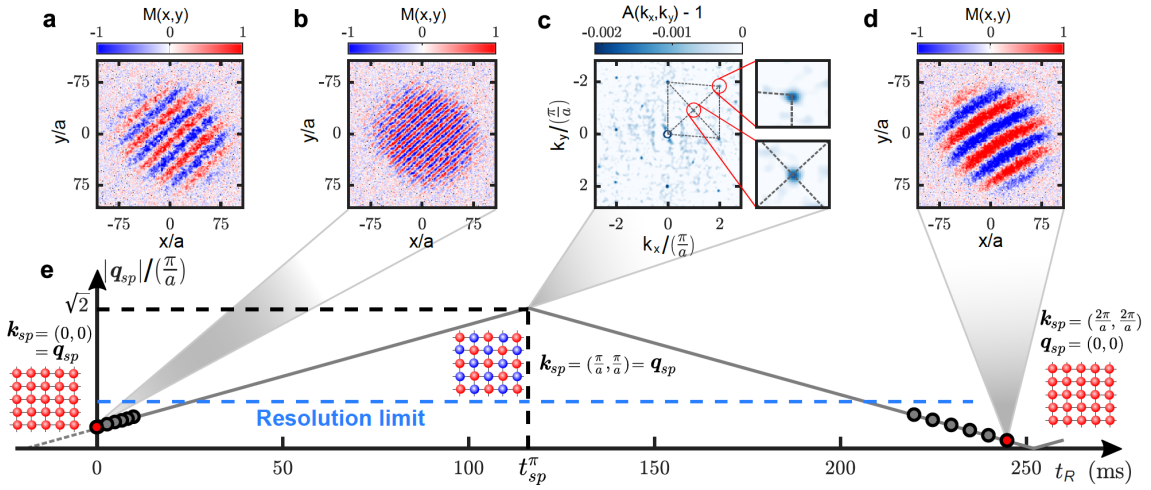

Figure 5.9: **Aligning the spin spiral.** The magnetic field gradient is ramped up to $|\nabla B| = 0.64\,\mathrm{G/cm}$, except for (a), where $|\nabla B| = 0.1\,\mathrm{G/cm}$. **a** and **b** Contrast $M(x, y)$ for spin patterns observed at different gradient strengths, and $t_{\mathrm{sp}} = 0.1\,\mathrm{ms}$. **c** Normalized density-density correlation signal (average of 200 realizations) of a single spin component after trap release and ballistic expansion for 4 ms. The additional correlation dips around $(\pm\pi/a, \pm\pi/a)$ demonstrate the realization of a chequerboard spin pattern with wave vector $\boldsymbol{q}_{\mathrm{AFM}}$. **d** Observed spin pattern with small wave vector after Bragg reflection. At this point, the contrast is still high, suggesting that single-particle coherence is maintained. A small residual magnetic field curvature of around $11\,\mathrm{nG/\mu m^2}$ is deduced from a fit to the fringe pattern. **e** The magnitude of the extracted wave vector $|\boldsymbol{q}_{\mathrm{sp}}|$ versus the duration t_{sp} of the spin evolution in the magnetic field gradient. The dashed red line shows the resolution limit of our imaging set-up. A numerical fit (solid line) provides a precise calibration to imprint spin patterns with arbitrary wave vectors along the diagonal of the 1$^{\mathrm{st}}$ BZ and to extract the turning point $t^{\pi}_{\mathrm{sp}} = 116\,\mathrm{ms}$.

the spin spiral to the extrapolated Ramsey time t_π, where the formation of a chequerboard pattern is expected, we turn off the in-plane lattice and allow a ballistic expansion of the cloud for 4 ms. The atomic cloud profile is recorded afterwards. This so-called time-of-flight (TOF) measurement gives access to the momentum profile of the original spatial pattern. By computing the density-density correlation function, or often referred as ***noise correlations*** [128],

$$A(\boldsymbol{k}) \propto \int d^2\boldsymbol{q} \langle \hat{n}_\downarrow(\boldsymbol{q}) \hat{n}_\downarrow(\boldsymbol{q}+\boldsymbol{k}) \rangle, \tag{5.24}$$

we obtain dips at the reciprocal lattice momentum due to fermionic anti-bunching [129]. Since the imprinted chequerboard spin pattern effectively rotates and shrinks the area of the reciprocal unit cell by a factor of 2, we observe additional anti-bunching dips at $(\pm\pi/a, \pm\pi/a)$ as compared to the case of a spin-polarized 2D lattice (see Fig. 5.9 **c**). This clearly indicates that we successfully imprint the desired spin pattern onto the atomic cloud.

5.4 Observing coherent evolution of spin correlations

The spin spiral technique introduced in previous section allows us to rotate the transverse correlation basis (see Eq. (5.20) and Fig. 5.8 **b**). Our measurement in spin correlations is no longer limited to the special case $\boldsymbol{q} = 0$, as the imprinted spiral permits the measurement of $S(\boldsymbol{q})$ in the momentum

space. In this section, we present the measurement of the spin structure factor in the 2D Hubbard model resulting from the coherent evolution of spin correlations. Using the knowledge of the spin correlation in momentum space, we reconstruct individual spatial correlators and observe excellent agreement with the theoretical predictions. In addition, the access to the staggered structure factor $S(\pm\pi/a, \pm\pi/a)$ allows us to perform local correlation thermometry and compare to thermometry based on fitting the global profile of the atomic distribution.

5.4.1 Decomposition of individual correlators

As shown in Eq. (5.21), spin correlations evolves periodically upon imprinting the spin spiral. This corresponds to measuring the static spin structure factor $S(\boldsymbol{q})$ along the 1$^{\text{st}}$ Brillouin zone. Fig. 5.10 **a** shows the experimental data of the uniform spin structure factor $S(\boldsymbol{q} = 0)$ (recorded without manipulating the spins) and the staggered spin structure factor $S(\boldsymbol{q}_{\text{AFM}})$ as a function of the chemical potential μ, which is inferred in a local density approximation (LDA) from the precisely calibrated trapping potential [112]. Using Eq. (5.5), the measured local moment $C_{ii} \equiv C_{00} = (S_\uparrow + S_\downarrow)/4$ is also plotted in gray, which reaches a maximum at half filling $\mu = 0$.

The uniform spin structure factor is smaller than the local moment C_{00} owing to the presence of negative nearest-neighbour correlations. In contrast, the staggered spin structure factor exceeds the local moment significantly at lowering temperature. This asymmetry with respect to the local moment clearly indicates the presence of beyond nearest-neighbour AFM spin correlations. By direct comparison to numerical linked-cluster expansion (NLCE) calculations for the staggered structure factor at half-filling and $U/t = 8$ [130], we deduce a temperature of $k_B T_s = 0.57(3)t$ in the spin sector at half-filling. In addition, we extract the global density temperature $k_B T_d = 0.63(3)t$, obtained from fitting NLCE results to the singles density profiles.

In Figs. 5.10 **b** and **d**, we plotted the spin structure factor $S(\boldsymbol{q})$ measured along the diagonal of the 1$^{\text{st}}$ BZ for different fillings. At half filling $\mu = 0$, the structure factor exhibits a minimum at $\boldsymbol{q} = 0$ and peaks at $\boldsymbol{q}_{\text{AFM}}$, in nice agreement with the theoretical calculation in Fig. 5.3. We observe a qualitatively similar q-dependence of the structure factor away from half filling, however, the build-up of spin correlations is suppressed. Note, that we can not invert the direction of the in-plane gradient. Hence, the data of the structure factor shown in the interval $q \in \left[-\frac{\pi}{a}, 0\right]$ corresponds to $|\boldsymbol{k}_{\text{sp}}| \in \left[\frac{\pi}{a}, \frac{2\pi}{a}\right]$. The symmetry of the measured structure factor around $q = 0$ therefore indicates that we are not affected by incoherent processes on the time-scale of the spin manipulation t_{sp}.

In addition, recording the spin structure factor as a function of $\boldsymbol{q}$ further provides access to the individual spatial spin correlators C_{ij}. The value of the correlation length deduced at half-filling suggests that spin correlators with $|i - j| \geq \sqrt{8}$ do not contribute significantly to the measured spin structure factor. Rewriting $S(q, q)$ along the diagonal of the BZ as a Fourier series we obtain

$$S(q, q) \approx \sum_{n=0}^{3} f_n \cos(nqa), \tag{5.25}$$

with $f_0 = C_{00} + 2C_{11}$, $f_1 = 4C_{01} + 4C_{12}$, $f_2 = 2C_{11} + 4C_{02}$, and $f_3 = 4C_{12}$. Using the measurement of the local moment C_0 from the density profile alone, we are able to extract all higher spin correlators $C_i j$ up to a distance of $|i - j| = \sqrt{5}$ from the first four Fourier components of the measured structure factor. The first three spin correlators are shown in Fig. 5.10 **c** as a function of μ.

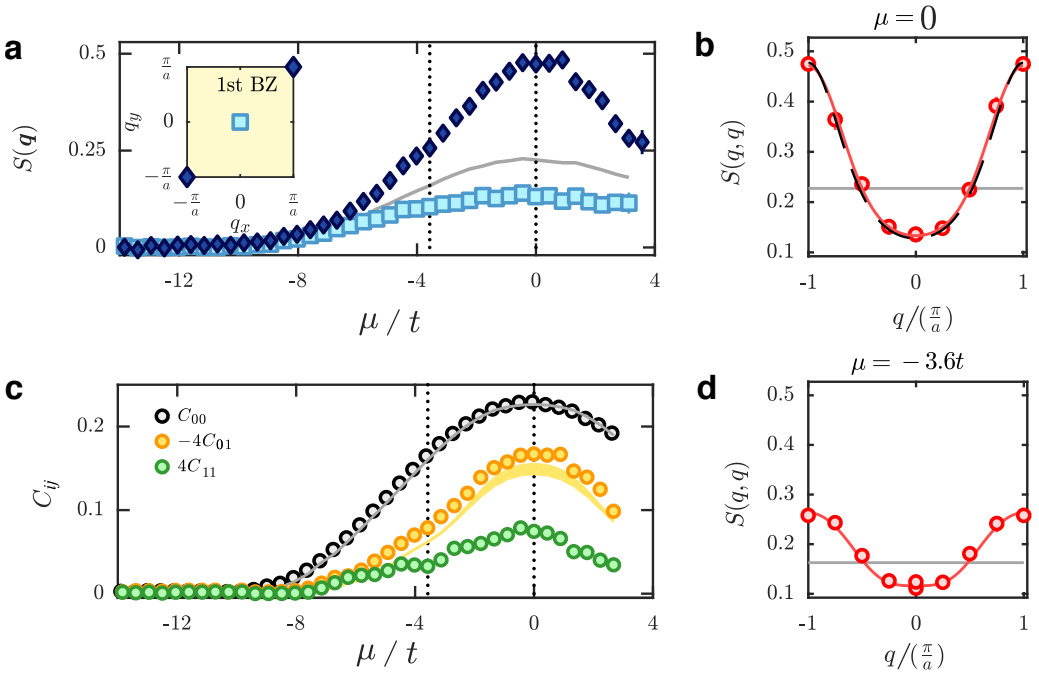

Figure 5.10: **Coherent evolution of spin correlations. a** Uniform (squares) and staggered (diamonds) spin structure factor recorded as a function of chemical potential μ. The solid gray line shows the measured local moment C_0. The two dashed lines highlight the potential bins used for Figs. 3 **b** and 3 **c**. **b**,**d** Spin structure factor (circles) and local moment (solid gray line) recorded along the diagonal of the BZ at half filling $\mu = U/2$ and away from half filling $\mu = U/2 - 3.6\,t$, respectively. We plot the fit using the Fourier series given in Eq. 5.25 (solid red line), and additionally, at half filling, the fit assuming an exponential decay of the magnitude of the spatial correlators according to Eq. 5.6 (black dashed line). **c** Extracted spin correlators C_{ij} (circles) as a function of chemical potential. The gray and yellow shadings show NLCE data for a temperature interval $k_B T = [0.54, 0.6]\,t$ of the local moment and nearest-neighbour correlator, respectively.

We compare the local moment C_{00} and the nearest-neighbour correlator C_{01} to data from NLCE calculations for a temperature interval of $k_B T_s = [0.54, 0.6]t$. The next-to-nearest neighbour correlator C_{11} is observed to contribute significantly to the measured spin structure factor and possesses the correct positive sign. We estimate the length scale over which AFM correlations extend in our system and obtain a spin correlation length of $\xi = 0.43(3)\,a$ at half-filling at the lowest achieved temperature.

5.4.2 Local and global thermometry

As discussed in Sec. 5.2.2, thermometry in strongly interacting fermionic lattice systems is especially difficult at low temperatures, when the density degree of freedom is essentially frozen. The uniform structure factor is not an ideal temperature probe since it reaches zero in the $T \to 0$ limit. In contrast, the staggered spin structure factor is a sensitive measure of the emerging spin order with respect to temperature. We compare the temperature T_s extracted from the measured staggered structure factor at half-filling to the temperature T_d obtained from fitting NLCE data [112, 130] to the singles density profiles. We note that T_s measures the local temperature of the gas around half-filling whereas T_d is a global measure of the temperature since it is extracted from the entire profile of the cloud. Fig. 5.11

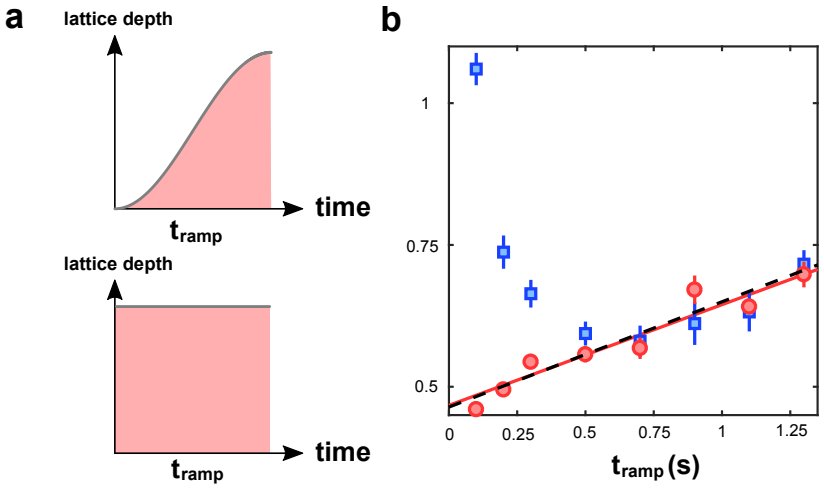

Figure 5.11: **Thermalisation in spin and density sector. a** Two possible lattice ramps. The upper one shows a sine-squared shape ramp, which leads to a thermalisation profile as shown in **b**. The lower one shows the control setup at which the lattice beams are turned on and hold for the same amount of time. **b** Thermalisation profile with sine-squared ramp. Shown are the density temperature T_d (blue) extracted by fitting the global density profile with NLCE calculation, and the spin temperature T_s extracted by comparing AFM correlation at half-filling with NLCE results. We observe that T_d and T_s converges for sufficient ramp time, indicating the local correlation builds up at a rate faster than global thermal equilibrium. The red line is a linear fit to T_s for $t_{\text{ramp}} > 0.5\,\text{s}$, which we compare to an extrapolation using the half the heating rate in lattice holding as shown in lower part in **a**.

shows the measured temperatures T_s and T_d as a function of the duration t_{quench} within which the in-plane lattice depth is increased from $0E_{\text{rec}}$ to $6E_{\text{rec}}$ using a sine-squared ramp shape.

The two independent thermometers agree well for ramp times larger than 0.5 s, where both linearly increase with a slope of $0.18(5)\,t/\text{s}$. We interpret this as genuine heating caused by the lattice beams. To further support this, we compare this slope to the background heating rate $0.37(5)\,t/\text{s}$, obtained by holding the equilibrated cloud at the final lattice depth. Under the assumption that residual heating is proportional to the integrated intensity of the lattice beams seen by the atoms, we expect the heating rate during holding to be twice the heating rate when quenching the lattice depth (sine-squared ramp shape) as shown in the upper half of Fig. 5.11 **a**. The linear increase in the spin temperature T_s over the full range of t_{ramp} suggests that the spins are in ***local equilibrium*** for all our measurement data.

For short ramp times, the density temperature deviates from the linear trend. Since T_d is extracted from the entire density profile, we conclude that the cloud has not reached global equilibrium. This is due to the slight change in the harmonic confinement when quenching the lattice depth. With this equilibration study, we confirm that the spin correlation results presented above are obtained from a thermalised cloud with a reliable temperature estimate for arbitrary filling. More importantly, we observe that the distinct time-scales at which spin-ordering (formation of correlations locally) and density-ordering (density redistribution globally). This measurement thus offers valuable information for future quantum gas experiments in designing novel cooling schemes. A more detailed discussion about potential cooling schemes can be found in Chapter 7.

5.5 Conclusion and outlook

In conclusion, we have measured the spin structure factor of the 2D Hubbard model both *momentum*- and *filling*-resolved using a technique based on the coherent manipulation of spin correlations. We have shown that even with moderate imaging resolution, the staggered structure factor, which is ideally suited for thermometry, can be resolved. The technique of imprinting spin patterns of well-defined wave vector offers novel possibilities and below we list several of possible utilisation of the techniques presented in this chapter.

Spin dynamics As shown in the noise correlation measurement under a time-of-flight, the spin spiral offers the ability to precisely create a classical Neel's state (chequerboard pattern) in the transverse direction. Studying spin diffusion [131, 132] of such initial state would offer new insight into the non-equilibrium dynamics of a Hubbard system. By combining with energy-resolved measurements, such as angle-resolved spectroscopy, the dispersion relation relevant spin-wave excitation can be probed.

Extension to other types of correlations One key feature of the spin-spiral technique is to utilise the coherent evolution time as a tuning knob to removes the need for site-resolved quantum gas microscopes as the same individual correlators can be reconstructed. This is in particular important in probing lower temperature phenomenon typically shows more prominent feature in the momentum space, rather than position space such as the conjectured d-wave pair-pair correlations in doped repulsive Hubbard model.

CHAPTER 6

Formation of preformed pairs in the attractive Hubbard model

I thought, from time to time, that it would be extraordinarily interesting if one could vary the strength of the interaction in order to observe this transition [BCS-BEC crossover]...

LEON N. COOPER [133]

Interaction effects vary drastically from the weak-coupling regime to the strong-coupling one. One important example of this is attractive-interacting fermions, in which weak interaction supports large, overlapping pairs, whereas strong coupling leads to tightly-bound molecules. In this chapter, we experimentally study the formation of local pairs in the attractive Hubbard model. By combining the fluctuation-dissipation theorem and the compressibility equation of state, we extract the interacting pair correlation function integrated over all distances. Finally, we deduce a characteristic length scale of local pairs as a function of interaction, density filling and temperature. At sufficiently low filling and weak on-site interaction, we observe that the pairs extend over approximately one lattice site at temperatures above the superfluid transition temperature.

The experimental results discussed in this chapter was accepted for publication in Phys. Rev. Research. (2020).

6.1 Introduction

The nature of fermionic pairing plays a crucial role in many-body quantum states such as superconductors [134]. For attractive interactions and in the weak-coupling regime, a Bardeen-Cooper-Schrieffer (BCS) description gives rise to large, spatially-overlapping Cooper pairs below the critical temperature T_c [37]. Upon increasing the interaction strength, the BCS ground state crosses over to a Bose-Einstein condensate (BEC) of tightly-bound dimers [135]. Above the transition temperature T_c, the ***crossover*** of a normal state could be characterized by the formation of local pairs, which are linked to the emergence of a pairing pseudogap [136–138]. In this section, we introduce the idea of such BCS-BEC crossover in the attractive Hubbard model. We then compare it with the two other examples of BCS-BEC crossovers, namely in high-T_c superconducting cuprates and Fermi gases (without lattice), that are well-studied [135, 139–141].

6.1.1 Attractive Hubbard model

In Sec. 2.3.1 and 4.1.2, we introduce the attractive Hubbard model and its mapping to the repulsive counterpart. The attractive Hubbard model, in itself, presents an intuitive model to study the pairing in a many-body system. For instance, the attractive Hubbard model shows a ***preformed pair*** phase for temperature $k_B T \ll |U|$ around half-filling. In simple terms, this phase is characterised by the accumulation of pairs (local doublons), due to the attractive interaction, yet without developing long-range coherence (pair-pair correlation).[1] This is analogous to the repulsive case discussed in Chapter 5, where the Mott insulator can be considered as an accumulation of preformed moments before attaining long-range order into the AFM phase. Away from half-filling, the system is said to be ***doped***. Due to the particle-hole symmetry $\mathcal{P}_1$ of the Hubbard model discussed in Eq. (4.6), it suffices to study one side of the doping, *i.e.* either hole doping (removing particle from half-filling) or particle doping (adding particle onto half-filling).

Crossovers from weakly- to strongly-coupled regimes in the ground state In the attractive Hubbard model, the coupling is determined by two parameters: the on-site interaction U and particle filling n, as reflected in the interaction term $U \sum_i n_{i,\uparrow} n_{i,\downarrow}$ in the Hamiltonian. Thus one natural criterion for the weakly coupled regime is the dilute (low-filling), small $|U|$ case. In this limit, at finite temperature, the system behaves similar to weakly interacting Fermi gases without the lattice. This is due to a relatively small occupation of the energy band near the Brillouin zone edges, and thus mainly the bottom band is filled at sufficiently low temperature (see Fig.2.3). The energy dispersion can be recast to a free particle one ($E = \frac{\hbar^2 \boldsymbol{k}^2}{2m^*}$) with effective mass m^* and the underlying physics, therefore, resembles that of Fermi gases without a lattice. Approaching $T \to 0$, an s-wave superconducting phase emerges and can be described by the BCS theory. In the dense (large-filling), large $|U|$ limit, the strong attraction leads to the formation of tightly-bound dimers (pairs). Such dimers are bosons since they are made up of two fermions with opposite spin. At zero temperature, the ground state emerges as the BEC of the composite bosons.

[1] An equivalent interpretation of the term "preformed" refers to the preformed gap in the single-particle density of state before entering a complete superconducting gap. Since it is not superconducting, such gap is often referred to as the pseudogap.

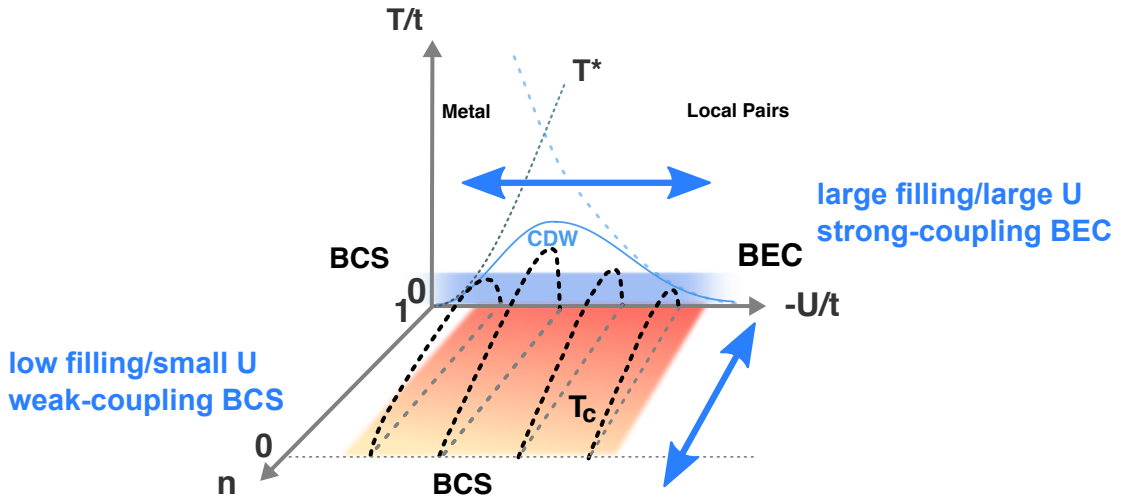

Figure 6.1: **BCS-BEC crossover in the attractive Hubbard model.** At half-filling $n = 1$, the ground state of the two-dimensional attractive Hubbard model exhibits the coexistence of a CDW ordering and superconducting phase. The superconducting behaviour crossovers from a BCS type to BEC one upon increasing interaction strength $|U|$. The narrow blue band indicates the crossover region of the superconducting phase. At high temperatures, both the CDW ordering and superconducting pair-pair correlations fade out as a result of thermal fluctuation. However, below the characteristic pairing temperature $T^* \approx |U|$, local pairing is possible, and it leads to a pseudogap in the single-particle spectral function. Away from half-filling, the critical temperature is no longer zero due to the emergence of a BKT transition. A similar BCS-BEC crossover can be realised via the adjustment on local filling n, as indicated by the broad red gradient band.

Crossover by varying on-site interaction $|U|$ We first look at the scenario with half-filling, $\langle n \rangle = 1$. The ground state exhibits a coexistence of charge-density-wave (CDW) ordering and s-wave superconductivity, where the critical temperature is zero ($T_c = 0$) due to the Mermin-Wagner theorem in two dimensions [119]. When tuning the interaction strength from weak to strong, the pairing nature of the superconducting state crossovers from a BCS type to a BEC one. This is reflected as the blue band around $T = 0$ as shown in Fig. 6.1 **a**. For high temperatures, the weakly-attractive system exhibit normal Fermi liquid behaviour and hence is a metallic phase. With increasing interaction, the metallic phase then crossovers to a phase with local preformed pairs. This crossover is characterised by the pairing temperature $T^* \approx |U|$. Below T^* and above $T_c = 0$, the system enters a phase with a pseudogap, where the single-particle spectral function exhibits a suppression. Such pseudogap in the lattice configuration has been recently measured in a similar quantum gases experiment via photoemission spectroscopy [142].

The crossover realised by tuning the interaction strength bears great similarity with the BCS-BEC crossovers in ultracold Fermi gases *without* lattice, in which the crossover conventionally make uses of the divergence of the scattering length near a Feshbach resonance. The scattering length a can be tuned such that the effective attraction varies from the BCS side ($1/k_F a < -1$), through the unitarity regime (($-1 < 1/k_F a < 1$) to the BEC side ($1/k_F a > 1$). It is worth noting that in Fermi gases without lattice potential, the unitarity emerges as a result of the divergence of the scattering length. The Hubbard system, however, can be realised without the divergence of a. This is due to the effect of the energy band structure, which modifies the interaction term such that the on-site attraction is sufficient to form a molecular bound state. In addition, the existence of a pseudogap phase in Fermi gases remains debated [143, 144]. Studying a similar yet distinct crossover might shed light into the

pairing mechanism of fermions.

Crossover by varying filling n Another "tuning knob" of coupling is the particle filling n. Although $T_c = 0$ at half-filling, it has been shown that away from half-filling in the two-dimensional model, a Berezinskii–Kosterlitz–Thouless (BKT) transition is possible at finite temperature, *i.e.* $T_c \neq 0$ [145] . Away from half-filling, the CDW order becomes short-ranged and suppressed, while the superconducting correlations are enhanced. This enables another possible crossover from BEC to BCS, as n is tuned away from half-filling $n \lesssim 1$ to the dilute limit $n \approx 0$. Similar to the half-filling case, above the critical temperature T_c, the system possesses a pseudogap regime as well.

The gradual crossover when varying filling is not a unique feature of the Hubbard model. In typical cuprate superconductor such as La_2CuO_4, a gradual crossover exist doping [146]. At zero hole doping, these material exhibits an anti-ferromagnetic phase due to the electron-electron Coulombic repulsion. By removing charge carriers by adding impurity atoms, the system can be made superconducting. Similar to what suggested in Fig. 6.1, two distinct regimes can be identified around the optimal doping (where superconducting order is the strongest): the overdoped and underdoped regimes. In the former case, the electron gases become dilute and thus show BCS-type superconducting phase transition, whereas, in the latter, the underdoped cuprates exhibit a BEC phase with the emergence of a pseudogap [139]. The origin of the pseudogap remains highly-debated in the condensed matter community. In particular, the main outstanding question lies on whether the emergence of the pseudogap is related to the superconducting state. Other scenarios such as the formation of electronic stripes or other order parameters competing with the superconducting order were also proposed to explain this peculiar phenomenon. Therefore, investigating the link between the attractive Hubbard model and cuprate materials is one of the key goals in exploring the attractive Hubbard model. In Table 6.1, we summarise our comparison of the BCS-BEC crossovers in different physical systems discussed above.

Physcial systems	**Tuning knobs**	**weak-coupling limit (BCS)**	**strong-coupling limit (BEC)**
Hubbard model ($U > 0$)	U and n	small U / small n	large U / large n
Interacting Fermi gases	$1/k_F a$	$1/k_F a < -1$	$1/k_F a > 1$
High-T_c cuprate superconductors	p/p_{optimal}	underdoped $p/p_{\text{optimal}} > 1$	overdoped $p/p_{\text{optimal}} < 1$

Table 6.1: **Comparing BCS-BEC crossovers in different physical systems.** For interacting Fermi gases, the coupling is determined by the dimensionless parameter $1/k_F a$. For $1/k_F a < -1$, large overlapping Cooper pairs are flavoured, while for $1/k_F a > 1$ tightly-bound molecules forms a BEC. For $-1 < 1/k_F a < 1$, an intermediate regime known as the unitarity limit is realised, where the size of the pairs is comparable to the inter-particle distance. As for cuprate superconductors, the electronic interaction is not independently tunable. However, doping still varies the electrons coupling significantly, resulting in a similar BCS-BEC type crossover.

6.2 Pair correlation function

Quantum mechanically the pairing behaviour between two particles is fully encoded in the second-order pair correlation function $g^{(2)}$. In position space, $g^{(2)}(\boldsymbol{r})$ gives the joint probability of finding a

pair of particles spaced by distance $\boldsymbol{r}$, and is given by

$$\left(\frac{n}{2}\right)^2 g^{(2)}_{\sigma,\sigma'}(\boldsymbol{r}-\boldsymbol{r}') = \langle \hat{\psi}^\dagger_\sigma(\boldsymbol{r})\hat{\psi}^\dagger_{\sigma'}(\boldsymbol{r}')\hat{\psi}_{\sigma'}(\boldsymbol{r}')\hat{\psi}_\sigma(\boldsymbol{r})\rangle. \tag{6.1}$$

Here, $\hat{\psi}_\sigma(\boldsymbol{r})$ is the fermionic field operator with spin σ at position $\boldsymbol{r}$ and the prefactor $(n/2)^2$ is the normalisation constant. The pair correlation is of particular importance as it is related to various thermodynamical observables such as compressibility. In solid materials, $g^{(2)}(\boldsymbol{r})$ is inferred from the Fourier transform of the density structure factor $S(\boldsymbol{q})$, which is experimentally accessible by crystallographic methods such as X-ray diffraction and neutron scattering [147, 148]. For our atomic gases in optical lattices, information about the pair correlation function can be extracted by measuring the density correlations. In this section, we explore the connection between the pair correlation function $g^{(2)}(\boldsymbol{r})$ and the density-density correlations. We then show that a measurement of the isothermal compressibility gives access to the density structure factor at zero momentum. By comparing these measurement with the non-interacting expectation, we can obtain the contribution caused by interaction effects.

6.2.1 Density-density correlation

To begin with, we first derive the core relations to be used in this chapter. We note that a continuous form is assumed here (see Eq. (6.1)) for ease of derivation. The derived results can be put forward in a lattice system without loss of generality. One important role of the $g^{(2)}$ function is its relation to the ***density-density correlation*** function $\nu(\boldsymbol{r},\boldsymbol{r}')$, which is given by

$$\nu(\boldsymbol{r},r) = \frac{1}{\langle n(\boldsymbol{r})\rangle}\left[\langle n(\boldsymbol{r})n(\boldsymbol{r}')\rangle - \langle n(\boldsymbol{r})\rangle\langle n(\boldsymbol{r}')\rangle\right] \tag{6.2}$$

It is not surprising that Eq. (6.2) resembles the form of the spin-spin correlation in Eq. (5.4), in which the first term is the correlated contribution and the second term is the uncorrelated offset. Since the total density operator is given by $n(\boldsymbol{r}) = \hat{\psi}^\dagger_\uparrow(\boldsymbol{r})\hat{\psi}_\uparrow(\boldsymbol{r}) + \hat{\psi}^\dagger_\downarrow(\boldsymbol{r})\hat{\psi}_\downarrow(\boldsymbol{r})$, the correlated contribution $\frac{1}{\langle n(\boldsymbol{r})\rangle}\langle n(\boldsymbol{r})n(\boldsymbol{r}')\rangle$ can be separated into expectation values with the same or opposite spin components, *i.e.*

$$\frac{1}{\langle n(\boldsymbol{r})\rangle}\langle n(\boldsymbol{r})n(\boldsymbol{r}')\rangle = \frac{1}{\langle n(\boldsymbol{r})\rangle}\sum_\sigma\left(\underbrace{\langle \hat{\psi}^\dagger_\sigma(\boldsymbol{r})\hat{\psi}_\sigma(\boldsymbol{r})\hat{\psi}^\dagger_\sigma(\boldsymbol{r}')\hat{\psi}_\sigma(\boldsymbol{r}')\rangle}_{\text{equal-spin}} + \underbrace{\langle \hat{\psi}^\dagger_\sigma(\boldsymbol{r})\hat{\psi}_\sigma(\boldsymbol{r})\hat{\psi}^\dagger_{\sigma'}(\boldsymbol{r}')\hat{\psi}_{\sigma'}(\boldsymbol{r}')\rangle}_{\text{opposite-spin}}\right). \tag{6.3}$$

By using the fermionic anti-commutation relations, $\left\{\hat{\psi}_\sigma(\boldsymbol{r}),\hat{\psi}^\dagger_{\sigma'}(\boldsymbol{r}')\right\} = \delta_{\sigma,\sigma'}\delta(\boldsymbol{r}-\boldsymbol{r}')$, we can express Eq. (6.3) in terms of the pair correlation function,

$$\begin{aligned}\frac{1}{\langle n(\boldsymbol{r})\rangle}\langle n(\boldsymbol{r})n(\boldsymbol{r}')\rangle &= \frac{\langle n(\boldsymbol{r}')\rangle}{4}\sum_{\sigma,\sigma'} g^{(2)}_{\sigma,\sigma'}(\boldsymbol{r}-\boldsymbol{r}') + \delta(\boldsymbol{r}-\boldsymbol{r}') \\ &= \delta(\boldsymbol{r}-\boldsymbol{r}') + \langle n(\boldsymbol{r}')\rangle \underbrace{\left[\frac{g^{(2)}_{\uparrow\uparrow}(\boldsymbol{r}-\boldsymbol{r}') + g^{(2)}_{\uparrow\downarrow}(\boldsymbol{r}-\boldsymbol{r}')}{2}\right]}_{\equiv g^{(2)}(\boldsymbol{r}-\boldsymbol{r}')}.\end{aligned} \tag{6.4}$$

Here, $g^{(2)}(\boldsymbol{r})$ denotes the full pair correlation function $g^{(2)}(\boldsymbol{r}) = \frac{1}{4}\sum_{\sigma=\uparrow,\downarrow}\left(g^{(2)}_{\sigma\sigma}(\boldsymbol{r}) + g^{(2)}_{\sigma\sigma'}(\boldsymbol{r})\right)$ [48], and we assume $g^{(2)}_{\uparrow\uparrow} = g^{(2)}_{\downarrow\downarrow}$ and $g^{(2)}_{\uparrow\downarrow} = g^{(2)}_{\downarrow\uparrow}$ using the spin SU(2) symmetry (see Chapter 4). Substituting Eq. (6.4) into Eq. (6.2), and integrating in $\boldsymbol{r}$, we arrive at the static ***density structure factor*** $S(\boldsymbol{q})$

$$S(\boldsymbol{q}) = \int \nu(\boldsymbol{r}) e^{i\boldsymbol{q}\cdot\boldsymbol{r}}\, d\boldsymbol{r} = 1 + \int n(\boldsymbol{r})\left[g^{(2)}(\boldsymbol{r}) - 1\right] e^{i\boldsymbol{q}\cdot\boldsymbol{r}}\, d\boldsymbol{r}. \tag{6.5}$$

Similar to the static spin structure factor introduced in Chapter 5 and in Eq. (5.8), the density structure factor in Eq. (6.5) at zero momentum is connected to the corresponding susceptibility (isothermal compressibility κ) via the ***fluctuation-dissipation theorem***, *i.e.*

$$\frac{\kappa k_B T}{n} = S(\boldsymbol{q} = \boldsymbol{0}). \tag{6.6}$$

To this end, by combining Eq. (6.5) and Eq. (6.6), we obtain a relation between the pair correlation function and the compressibility,

$$\int \left[g^{(2)}_{\uparrow\uparrow}(\boldsymbol{r}) + g^{(2)}_{\uparrow\downarrow}(\boldsymbol{r}) - 2\right] d^2r = 2\left(\frac{\kappa T}{n^2} - \frac{1}{n}\right). \tag{6.7}$$

We note that the right-hand side can be measured experimentally in our quantum simulator (see Fig. 4.10 **b**). Although theoretically obtaining the full $g^{(2)}$ from Eq. (6.5) requires access to the density structure factor across all momenta, the limiting case at $\boldsymbol{q} = 0$ still encapsulates both the Pauli blocking and interacting contributions of $g^{(2)}(\boldsymbol{r})$.

Eq. (6.7) provides us with two important insights. First, the isothermal compressibility entails the competition of Pauli repulsion and on-site attraction, since an external compression induces pressure between particles with equal and unequal spins within the trap. Second, the experimental determination of the compressibility opens access to the pair correlation function. While previous quantum gas experiments have been focused on measurements of compressibility in relation to transport coefficients such as conductivity [149], its link to pairing has yet to be explored.

6.2.2 Equal-spin and Unequal-spin pair correlations

Before introducing the experimental measurement of density-density correlations, we first discuss the qualitative behaviour of the pair correlation function. As reflected in Eq. (6.3), the full pair correlation function $g^{(2)}(\boldsymbol{r})$ contains contribution from both particles with same and opposite spin, which we referred to as the ***equal-spin*** and ***unequal-spin*** pair correlation functions, respectively.

Equal-spin pair correlation function $g^{(2)}_{\uparrow\uparrow}(\boldsymbol{r})$ Due to the Pauli principle, density correlations exist even for ideal fermions. The equal-spin pair correlation function $g^{(2)}_{\uparrow\uparrow}(\boldsymbol{r})$ exhibits a Pauli correlation hole at short distance, see gray area in Fig. 6.2 **a**. This gives rise to an effective repulsion that solely originates from the anti-symmetric nature of the fermionic state. We note that for non-interacting gases, this Pauli suppression is the only contribution in the full $g^{(2)}(\boldsymbol{r})$.

The pair correlation function in the non-interacting case can be solved numerically. To demonstrate

this, we start by expanding the field operator in plane waves

$$\hat{\psi}_\sigma(r) = \frac{1}{\sqrt{V}} \sum_{\boldsymbol{k}} e^{i\boldsymbol{k}\cdot\boldsymbol{r}} \hat{c}_{\boldsymbol{k},\sigma}. \tag{6.8}$$

Substituting this into Eq. (6.1), we obtain

$$\begin{aligned} \left(\frac{n}{2}\right)^2 g^{(2)}_{\uparrow\uparrow}\left(\mathbf{r}-\mathbf{r}'\right) &= \frac{1}{V^2} \sum_{\mathbf{k},\mathbf{k}'} \sum_{\mathbf{q},\mathbf{q}'} e^{-i(\mathbf{k}-\mathbf{k}')\mathbf{r}} e^{-i(\mathbf{q}-\mathbf{q}')\mathbf{r}'} \langle \hat{c}^\dagger_{\mathbf{k}} \hat{c}^\dagger_{\mathbf{q}} \hat{c}_{\mathbf{q}'} \hat{c}_{\mathbf{k}'} \rangle \\ &= \left(\frac{n}{2}\right)^2 - \left| \frac{1}{V} \sum_{\mathbf{k}} e^{-i\mathbf{k}(\mathbf{r}-\mathbf{r}')} \langle n_{\mathbf{k}} \rangle \right|^2 . \end{aligned} \tag{6.9}$$

Thus, the pair correlation can be obtained by a Fourier transform of the momentum occupation $\langle n_{\boldsymbol{k}} \rangle$, which is determined by the Fermi-Dirac distribution $f(\epsilon) = 1/(e^{\beta(\epsilon-\epsilon_F)} + 1)$ and the underlying two-dimensional energy dispersion $\epsilon(k_x, k_y) = -2t \left[\cos(k_x a) + \cos(k_y a)\right]$ (similar to Eq. (2.15)). We therefore have all the necessary information for computing the $g^{(2)}_{\uparrow\uparrow}(\boldsymbol{r})$ in a square lattice at $U/t = 0$. In Fig. 6.2 **b**, we show the equal-spin pair correlation function, computed using Eq. (6.9) for various filling n at a fixed temperature $k_B T/t = 1$. It is apparent that although the numerical computation is performed on a discrete lattice, it bears the same Pauli correlation hole as shown in Fig. 6.2 **a** for the free Fermi gases. Later in the experimental analysis, we utilise this calculated non-interacting contribution to separate the Pauli and the interacting pair contributions.

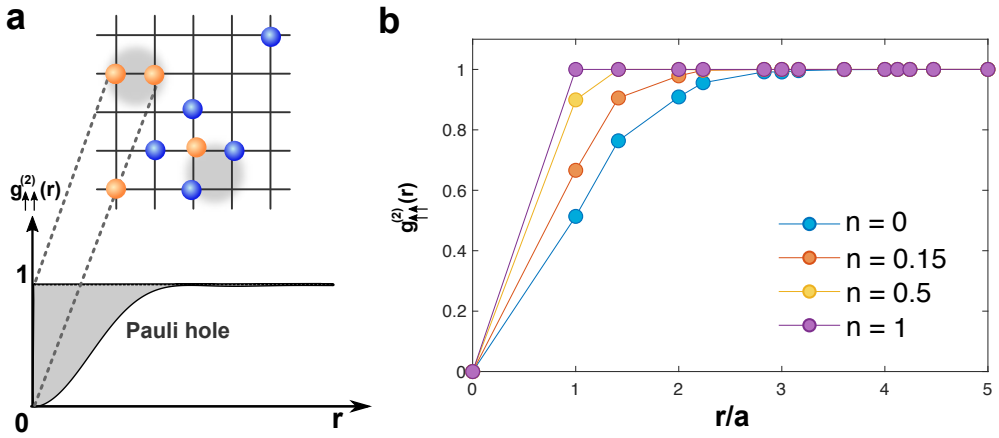

Figure 6.2: **Behaviour of the equal spin pair correlation function.** **a** The equal-spin correlation function $g^{(2)}_{\uparrow\uparrow}(\mathbf{r})$ exhibits a correlation hole, which is a well-known example of anti-bunching. For free gases, the $g^{(2)}_{\uparrow\uparrow}(\mathbf{r})$ oscillates with the frequency of the Fermi wave-vector k_F. We note that the density dependence if embedded in k_F since it is normalised to the total particle number of the system. **b** Equal-spin pair correlation (single spin) in a square lattice at $k_B T/t = 1$ at $U/t = 0$. For fully filled case $n = 1$, the system is a band insulator with all lattice site filled, therefore the probability of finding a particle with same spin is always unity for $\boldsymbol{r} \neq 0$. As filling decreases, the joint probability to find pairs lowers, forming a enlarged Pauli hole near short distance. In the limit of $n \to 0$, the system can be considered as two fermions delocalised in the lattice, and thus forming the largest Pauli hole.

Unequal-spin pair correlation function $g^{(2)}_{\uparrow\downarrow}$ For ultracold fermions, interaction effects are limited to particles with opposite spin since the s-wave scattering is forbidden between particle with same spin. We thus later refer the $g^{(2)}_{\uparrow\downarrow}(\boldsymbol{r})$ as the ***interacting*** pair correlation function. In non-interacting case, particles with opposite spin are uncorrelated and thus their pair correlation is flat, *i.e.* $g^{(2)}_{\uparrow\downarrow}(\boldsymbol{r}) = 1$ for all $\boldsymbol{r}$.

Although the interaction is on-site in the Hubbard model, the pair correlation can extend beyond the local site. This is due to the delocalised nature of the particle's wavefunction, which contributes to non-zero overlap between different sites. For repulsively interacting fermions, the pair correlation between particles with opposite spin is suppressed with respect to the uncorrelated value of one, as shown in Fig. 6.3. This goes hand in hand with the emergence of the Mott insulator when doubly-occupied sites are energetically unfavourable.

On the other hand, attractive interactions lead to an accumulation of local doubly-occupied states, thus the tendency to form pairs is enhanced. In this work, we mainly focus on the attractive side and investigate the extent of such local pairs when traversing from the weak to strong coupling regime. As discussed in Sec. 6.1.1, depending on the strength of the attractive coupling, the Hubbard model support two distinct phases on two sides of the BCS-BEC crossover. Although the lowest temperature reached in our experiment is still above the superfluid critical temperature T_c, we nonetheless observe a significant change in the pair correlation lengths, that is reminiscent to the crossover near the ground state.

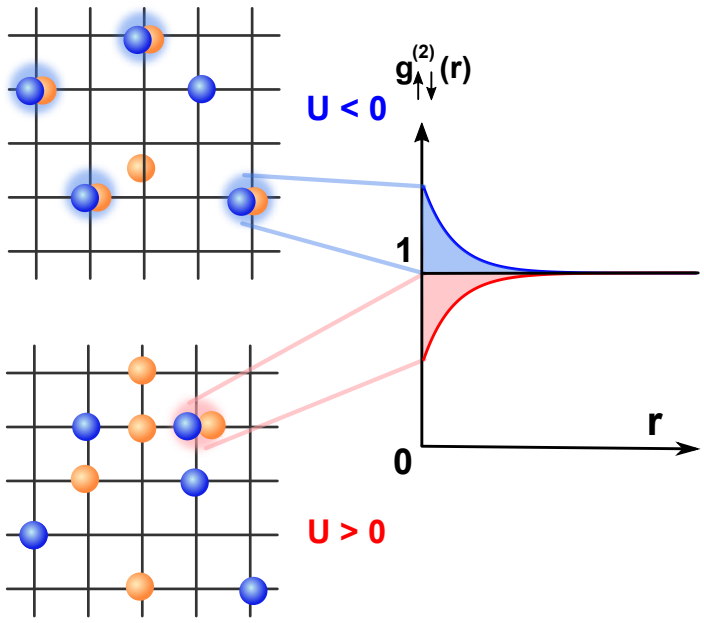

Figure 6.3: **Behaviour of the unequal-spin pair correlation.** $g^{(2)}_{\uparrow\downarrow}(\boldsymbol{r})$ depends strongly on the on-site interaction strength U, where attractive (repulsive) interaction raises (lowers) pair correlation at short distance from the classical value of one. Consider a repulsively interacting system, the doubly-occupied state have a larger separation extent in order to minimise the interaction. On the other hand, the attractive interaction tends bind together the wavefunctions between spin-up and spin-down particles, resulting in a enhanced $g^{(2)}_{\uparrow\downarrow}(\boldsymbol{r})$ at short distance.

6.3 Observation of pair formation

Finally, we are in the position to present our experimental measurement of the pair correlation function in the two-dimensional attractive Hubbard model. In particular, we measure the isothermal compressibility derived from the density of state. We observe an anti-bunching to bunching crossover in the density structure factor $S(\boldsymbol{q} = \boldsymbol{0})$ caused by increasing attractive interaction. By assuming exponential decay of the $g^{(2)}(\boldsymbol{r})$, we extract the pair correlation length of local pairs at various interaction, filling and temperatures. We observe the formation of pairs with increasing attractive interactions even above the superfluid critical temperature. While past experiments have determined the pair size in a trapped Fermi superfluid across the BCS-BEC crossover [150], it has not been measured for lattice gases. Our measurement, therefore, offers novel insight into the pairing behaviour of strongly-correlated quantum matter.

6.3.1 Experimental detection

The main experimental sequence deployed in this chapter is identical to the one depicted in Fig. 4.3, in which we resolve the density equation of state $n(\mu) = S_{\uparrow}(\mu) + D(\mu)$ via the measurement of the *in-situ* occupation of the singly- and doubly-occupied sites $S_{\uparrow}(x, y)$ and $D(x, y)$. Since we perform our measurement with a spin-balanced sample, we can assume $S_{\uparrow} = S_{\downarrow}$ throughout the system. The interaction range explored in this chapter is $-10 < U/t < -1$. Similar to previous chapters, the temperature is extracted via a chi-squared fit to the equation of state $n(\mu)$ with the numerical DQMC results (see Fig. 4.6).

6.3.2 Measurement of the density structure factor

Beginning with the density equation of state $n(\mu)$, we obtain the isothermal compressibility $\kappa = \partial n/\partial \mu$ through numerical differentiation. Unlike the Mott insulating phase with repulsive interaction, the attractive interaction enhances the compressibility near half-filling. In Fig. 6.4 **a**, we depict the density structure factor $S(\boldsymbol{q} = 0)$ derived from the compressibility using Eq. (6.6). We observe that for low filling $S(\boldsymbol{q} = 0)$ exceeds unity. Quantitatively speaking, $S(\boldsymbol{q} = 0) > 1$ indicates particle-bunching, which is typically a boson behaviour. Boson bunching has been observed in various physical systems such as photons in an optical cavity and ultracold bosonic gases in a lattice. We recall that $S(\boldsymbol{q} = 0)$ in Eq. (6.5) composes of both the equal-spin (Pauli) and unequal-spin (interacting) pair correlation functions. At fixed filling n, we observe that the structure factor increases monotonically with interaction strength, suggesting that the interacting pair correlation functions become increasingly dominant.

We then analyse the roles of both the equal- and the unequal-spin contributions by plotting the integral of the full $g^{(2)}(\boldsymbol{r})$ function, computed using Eq. (6.7), as shown in Fig. 6.4 **b**. The horizontal dashed line indicates the point at which the equal- and unequal-spin $g^{(2)}$ exactly compensate each other, *i.e.* $\int \left[g^{(2)}(\boldsymbol{r}) - 1\right] d^2r = 0$. The sign of this integral signals the dominant part in the pair correlation function. Thus, it offers a direct indication that the counter-intuitive "fermion bunching" observed in the density structure factor $S(\boldsymbol{q} = 0)$ is caused by the fact that the attractive on-site interaction

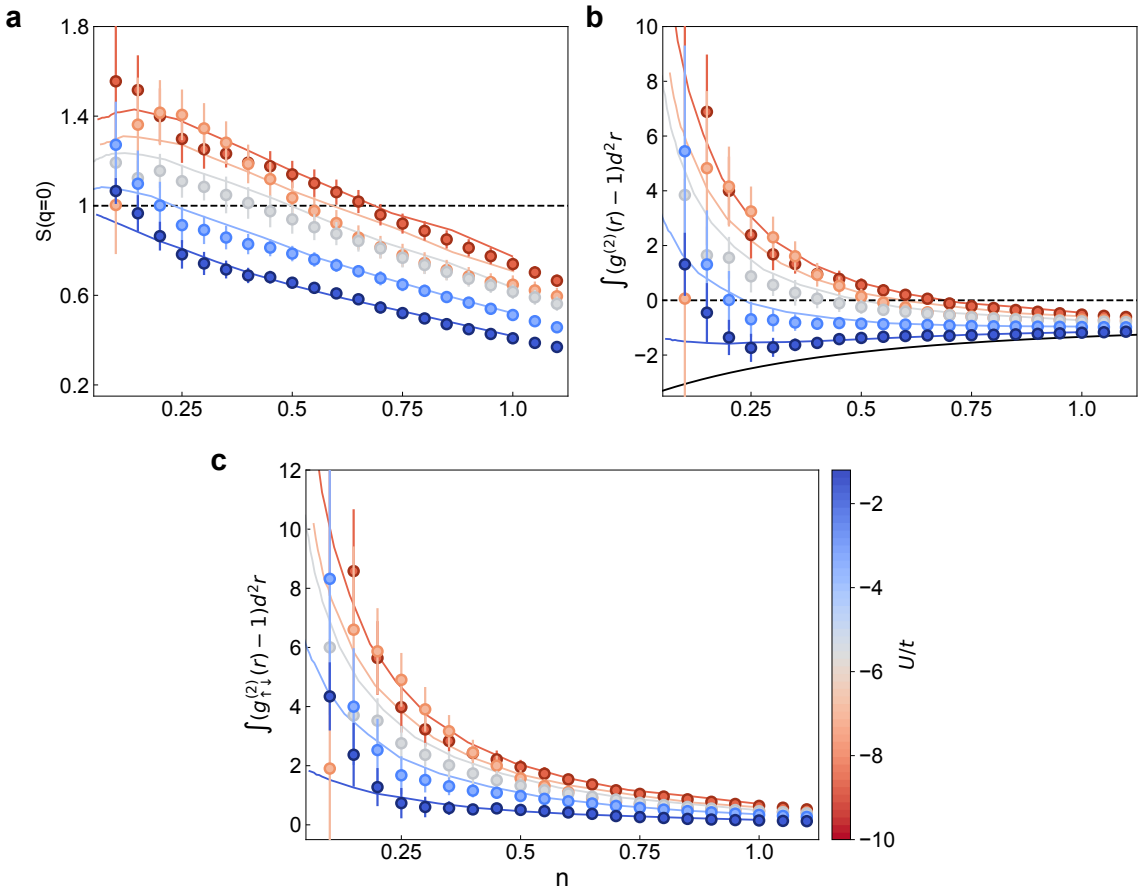

Figure 6.4: **Density correlations. a** Density structure factor at zero momentum $S(\boldsymbol{q}=0)$ for various interaction strengths and filling. **b** $\int (g^{(2)}(\boldsymbol{r})-1)d^2r$ versus interaction strengths U/t. The black solid line shows the non-interacting expectation at the lowest temperature in the data sets. Data points above the horizontal dashed line signal that the unequal-spin $g^{(2)}_{\uparrow\downarrow}(\boldsymbol{r})$ outweighs its equal-spin counterpart, and vice versa. **c** Interacting contribution $\int (g^{(2)}_{\uparrow\downarrow}(\boldsymbol{r})-1)d^2r$ is obtained by subtracting the equal-spin contribution $\int (g^{(2)}_{\uparrow\uparrow}(\boldsymbol{r})-1)d^2r$. Data are for $U/t = -1.83, -3.90, -6.09, -7.62$ and -9.61, and the corresponding temperatures k_BT/t of the data set are 1.26(4), 1.31(5), 1.73(8), 2.05(11) and 2.16(8) respectively.

dominates over the Pauli blocking.[2]

In order to quantitatively compare the contributions from the Pauli principle and the attractive interaction, we note that the equal-spin contribution $\int \left[g^{(2)}_{\uparrow\uparrow}(\boldsymbol{r})-1\right] d^2r$ can be calculated using the tight-binding dispersion relation and temperature, see solid line in Fig. 6.4 **b**. Strictly speaking, this calculation is exact only for the non-interacting case because interactions in principle modify the dispersion from a simple sinusoidal energy band. However, in the low-filling regime, this estimate remains a faithful approximation since most of the occupied part of the energy band remains harmonic. Subtracting the equal-spin contribution from $\int \left[g^{(2)}(\boldsymbol{r})-1\right] d^2r$, we obtain the interacting

[2]While it is true that the tightly-bound local dimers would become composite bosons in the large-U limit, our measurement scheme does not detect the pair-pair correlation. The bunching as reflected in the $g^{(2)}(\boldsymbol{r})$, therefore, is not a sign for the bosonisation of fermions.

$\int \left[g^{(2)}_{\uparrow\downarrow}(\boldsymbol{r}) - 1 \right] d^2r$, as shown in Fig. 6.4 **c**. We observe that the interacting contribution maintains a similar dependence as $S(\boldsymbol{q} = 0)$. For either decreasing filling or increasing interaction strength, the interacting pair correlation increases. This highlights the parameter space at which the interaction effect on $g^2_{\uparrow\downarrow}(\boldsymbol{r})$ is most prominent.

6.3.3 Pair correlation length

To gain further insight into the signature of local pairing, we turn to estimate a length scale up to which the pair correlation extends. We start by noticing that the interacting pair correlation amplitude at $\boldsymbol{r} = 0$ is

$$g^{(2)}_{\uparrow\downarrow}(0) = 4\frac{\langle n_\uparrow n_\downarrow \rangle}{\langle n_\uparrow + n_\downarrow \rangle^2} = \frac{D}{(S_\uparrow + D)^2}. \tag{6.10}$$

This implies that the amplitude can be directly obtained from our local density measurement of singly- and doubly-occupied site occupations. Although the analytical form of the unequal-spin pair correlation function is not known, an exponential decay $e^{-|\boldsymbol{r}|/\xi}$ is expected to be a good approximation, see inset of Fig. 6.5 **a**. Combining the knowledge of the integral $\int \left[g^{(2)}_{\uparrow\downarrow}(\boldsymbol{r}) - 1 \right] d^2r$ and the amplitude at $\boldsymbol{r} = 0$, we then infer the characteristic length scale ξ as

$$2\pi\xi^2 \approx \frac{\int \left[g^{(2)}_{\uparrow\downarrow}(\boldsymbol{r}) - 1 \right] d^2r}{\left[g^{(2)}_{\uparrow\downarrow}(0) - 1 \right]}. \tag{6.11}$$

In Fig. 6.5 **a**, we plot the estimated pair correlation length ξ as a function of filling n. For low filling $n \lesssim 0.5$, we observe a correlation length ξ as large as $0.92(4)\,a$ for the lowest interaction strength at $U/t = -1.83$, where $a = 532\,\mathrm{nm}$ denotes the in-plane lattice spacing. Although the attractive interaction is purely on-site, we observe that its effect extends beyond local site, similar to the Pauli blocking leading to beyond-local density suppression.

Filling dependence The decreasing trend of ξ as filling increases could be attributed to two reasons. First, for dilute filling, particles are described by delocalised wave-packets. With an increasing filling, however, the reduced inter-particle spacing limits the available range for pairing. Second, such localisation of particles means that the continuous integral of Eq. (6.11) starts to deviate from the discretised sum in a lattice. If the interacting contribution is dominated by the local term $g_{\uparrow\downarrow}(0)$, the continuous approximation of Eq. (6.11) would result in $\xi/a \approx \sqrt{1/2\pi} \approx 0.4$, which is in agreement with our observation in Fig. 6.5 **a**.

Interaction dependence Upon changing U/t, we observe that the correlation length ξ shrinks as interaction strength increases, as shown in Fig. 6.5 **b**. This signals the formation of tightly-bound pairs and this pairing behaviour is most prominent below quarter filling ($n \lesssim 0.5$). Above quarter filling, we do not observe a discernible trend of ξ as a function of U/t, as indicated by the lowest data points in Fig. 6.5 **b**. Although we do not expect any macroscopic long-range coherence in our

system, we observe the precursor at which attractive interaction induces the formation of local pairs. And the dependence in density and interaction are in qualitative agreement with the low-temperature phase diagram, as shown in Fig. 6.1.

Temperature dependence Last but not least, we investigate the temperature dependence of the correlation lengths. For temperatures below the critical temperature and low density, the pairing would be described by a BCS-BEC type behaviour. Although the temperatures reached in our experiments remain in the normal phase, we observe a resemblance in the behaviour of the pair correlation length. As shown in Fig. 6.5 **c**, we plot ξ as a function of temperature k_BT/t at $n = 0.2$. The correlation length rises as temperature decreases for the weakly attractive case. In the strongly attractive case, we observe a much less significant trend in temperature dependence. Since the pairing occurs at an energy scale of the interaction U, it is also informative to recast the temperature with respect to $|U|$. In Fig. 6.5(d), we compare the temperature with respect to the interaction energy by plotting the correlation lengths as a function of $k_BT/|U|$. Despite a lower achieved $k_BT/|U|$ for large interaction strengths, the correlation length remains small due to the energetically favourable dimer

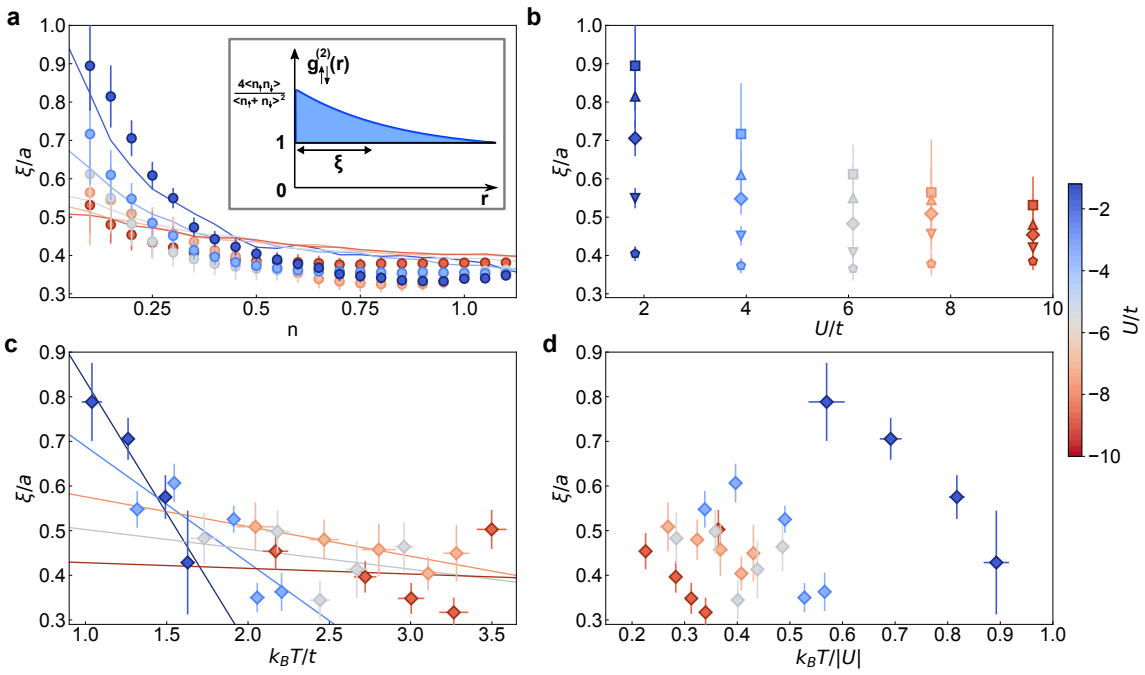

Figure 6.5: **Inferred pair correlation length.** **a** Correlation length ξ versus filling n. As the interaction strength increases, we observe that the correlation length shrinks for low filling $n \lesssim 0.5$. For increasing filling, we observe that ξ settles at approximately the limit of the continuous approximation. The inset exemplifies the estimation of the length scale according to Eq. (6.11), which is effectively dividing the area bound by the $g^{(2)}_{\uparrow\downarrow}(\boldsymbol{r})$ and the uncorrelated value (integral) by height obtained by local pair correlations $g^{(2)}_{\uparrow\downarrow}(\boldsymbol{r})$ (amplitude). **b** Correlation length ξ for specific n versus U/t. $n = 0.1$, 0.15, 0.2, 0.3 and 0.5 correspond to square, up-triangle, diamond, down-triangle and pentagon markers respectively. Temperatures of data points shown in **a** and **b** are same as those in Fig. 6.4. **c** Correlation length ξ versus temperature k_BT/t at $n = 0.2$. For low filling, we observe in general a decreasing trend as temperature rises. While already at $n = 0.5$, no significant temperature dependence is observed. The solid lines are linear fits to the data points. **d** Correlation length ξ versus temperature $k_BT/|U|$ at $n = 0.2$. When rescaled with respect to the interaction strength, the temperatures reached in the weakly-interacting case are higher than the ones in the strongly interacting case.

state. For weak interactions, the pair correlation length rises at much higher $k_B T/|U|$, signalling the tendency to delocalise and form longer-range pairs.

6.4 Conclusion and outlook

In conclusion, we investigate the formation of local pairs across the crossover regime of a normal phase in the attractive Hubbard model. In particular, we observe the competition between Pauli repulsion and on-site attraction. A correlation length scale can be inferred from the data by subtracting the non-interacting contribution in the analysis. We show that for sufficiently low filling and weak interaction, the pair correlation length extends beyond local distance up to one site. This offers a clear signature for the formation of local pairs, a precursor feature in studying the BCS-BEC crossover in a lattice configuration. Our measurement helps to elucidate the outstanding questions regarding the pairing behaviour of a normal state. The approach presented here, in principle, also works beyond simple lattice geometries or on-site interaction, thereby allowing future investigation of long-range correlated systems.

CHAPTER 7

Summary and outlook

7.1 Summary

In conclusion, we present in this thesis the experimental realisation of the two-dimensional Hubbard model with ultracold fermionic ^{40}K atoms in optical lattices. By tuning the dimensionality, kinetic energy and interaction in the optical lattices, a wide range of the phase diagram of the Hubbard model is realised. A pedagogical review of the Hubbard model is presented. Below is a summary of the scientific achievements described in this thesis.

First, we investigate the mapping between the repulsive and the attractive Hubbard model using the particle-hole symmetry. By experimentally probing the density and spin sectors of the Hubbard models with both repulsive and attractive interactions, we demonstrate a direct mapping between relevant observables. In addition, we observe a Mott-like, "spin-incompressible" phase in our realisation of the spin-imbalanced attractive Hubbard model. This demonstrates a novel pathway for quantum simulation to not only solving the system as engineered, but also to provide valuable information on the system that is linked by symmetries.

Second, we explore the emergence of the spin-spin correlations in the repulsive phase diagram. By implementing a highly-controllable manipulation scheme, we demonstrate the first coherent time evolution of the spatial spin correlations in an ultracold atomic lattice gas. This opens access to the *in-situ* correlations in momentum space and allows the extraction of the spatial correlators without the need of a quantum gas microscope. The ability to locally-resolve physical observables in the momentum space provides a powerful tool to study the time-evolution of correlated quantum dynamics in momentum space that is not possible in conventional condensed matter systems.

Finally, we probe the attractive side of the phase diagram with a focus on pairing phenomena, in which we draw a close analogy with BCS-BEC crossovers present in high-temperature superconducting cuprates and trapped ultracold Fermi gases. We extract the second-order pair-correlation functions $g^{(2)}(\boldsymbol{r})$ by combining the fluctuation-dissipation theorem and the compressibility equation of state. This allows us to resolve the competition between the effective Pauli repulsion in fermionic systems and the on-site attraction we implemented. Furthermore, by normalising the pair correlation with respect to the on-site correlation, we infer a pair correlation length ξ in our system, which serves as a precursor of the BCS-BEC crossover in a lattice system.

7.2 Outlook and future works

In this final section, several experimental concepts to extend our understanding of the Hubbard model are presented, some of which are in the works.

7.2.1 The bilayer Hubbard model

Throughout this thesis, we explore the single-band Hubbard model with on-site interaction. However, a vast variety of flavours of the Hubbard model were also proposed to describe real material. The bilayer Hubbard model is one of the natural extensions of the two-dimensional Hubbard model. Due to its intimate link to bilayer high-T_c cuprates such as $Bi_2Sr_2CaCu_2O_{8+\delta}$ [151], it is an ideal model to study various interesting physics such as exotic pairing and magnetism [152, 153], and phase transitions in multi-orbital materials [154, 155]. The bilayer Hubbard model can be written as

$$\begin{aligned}\hat{H} = &- t \sum_{\langle i,j\rangle,m,\sigma} \left(\hat{c}^{\dagger}_{im,\sigma}\hat{c}_{jm,\sigma} + h.c.\right) - t_{\perp} \sum_{i\sigma} \left(\hat{c}^{\dagger}_{i1,\sigma}\hat{c}_{i2,\sigma} + h.c.\right) \\ &+ U \sum_{i,m} \left(\hat{n}_{im,\uparrow} - \frac{1}{2}\right)\left(\hat{n}_{im,\downarrow} - \frac{1}{2}\right) - \sum_{im,\sigma} \mu_{im}\hat{n}_{im,\sigma} \,.\end{aligned} \tag{7.1}$$

Here, we introduce the additional index $m = 1,2$ to denote the two layers, as shown in Fig. 7.1 and $t_{\perp}$ is the interlayer tunnelling amplitude. In the non-interacting limit, $U = 0$, the energy dispersion of the bilayer Hubbard model is given by

$$E^{\pm}(\boldsymbol{k}) = -2t\left[\cos(k_x a) + \cos(k_y a)\right] \pm t_{\perp}. \tag{7.2}$$

The presence of two orbitals in the Hamiltonian results in the so-called ***bonding/anti-bonding*** ($\pm$) bands, which exhibit perfect ***Fermi nesting*** at half-filling for $t_{\perp} < 4$, *i.e.* $E^{\pm}(\boldsymbol{k} + \boldsymbol{Q}) = E^{\mp}(\boldsymbol{k})$, where $\boldsymbol{Q} = (\pi/a, \pi/a)$ is the reciprocal lattice vector. As a result, the ground state for $U > 0$ is predominantly anti-ferromagnetically ordered, as long as a Fermi surface exists. As U increases, the critical $t_{\perp}$ that ensures nesting decreases from the non-interacting value $t_{\perp} = 4$. In the $U \to \infty$ limit,

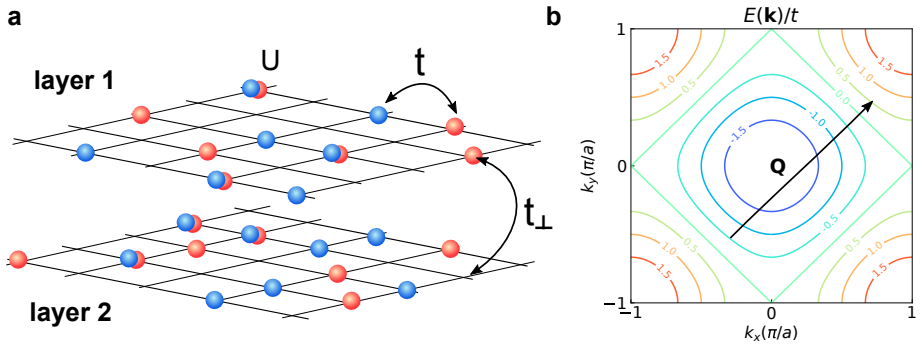

Figure 7.1: **Bilayer Hubbard model. a** Schematic illustration of the bilayer Hubbard model. **b** Fermi nesting. Shown is the energy contour of a simple tight-binding dispersion in a square lattice. With the presence of interlayer tunnelling $t_{\perp}$, the dispersion is split into two bands. The anti-bonding band and the bonding band exhibit perfect nesting at half-filling, as demonstrated by the reciprocal lattice vector $\boldsymbol{Q}$ connecting contours with euqal and opposite energy shift from zero.

the bilayer Hubbard model at half-filling, similar to the single-layer case in Eq. (5.3), reduces to the bilayer Heisenberg model, which is given by

$$\hat{H} = J \sum_{m=1,2} \sum_{\langle ij \rangle} \hat{\mathbf{S}}_{i,m} \cdot \hat{\mathbf{S}}_{j,m} + J_{\perp} \sum_{i} \hat{\mathbf{S}}_{i,1} \cdot \hat{\mathbf{S}}_{i,2} \,. \tag{7.3}$$

Here, $J = 4t^2/U$ and $J_{\perp} = 4t_{\perp}^2/U$ are the intra-plane and inter-plane super-exchange energies, respectively. At $T = 0$, an order-disorder transition is expected to occur at $J_{\perp}/J = 2.552$, which corresponds to $t_{\perp}/t = 1.588$ [156–158]. In Fig. 7.2, we show the results of numerical DQMC simulations on a bilayer Hubbard model. The addition of interlayer tunnelling $t_{\perp}$ in general results in the reduction of the intralayer magnetic correlations, yet increases the interlayer magnetic correlations. As $t_{\perp}$ increases, the AFM would eventually wash out, as expected from the weakening of Fermi nesting mentioned above.

Our implementation of an optical superlattice along the vertical direction opens access to explore the interplay of the Fermi surface topology with interaction effects. Using a symmetric configuration of the superlattice, as shown in Fig. 3.6 **b**, the optical potential along the vertical direction can be treated as a series of isolated double-wells. Recently, we have begun to characterise the tunnelling amplitude between two lattice site in the double-well by measuring coherent tunnelling between them. Combining this with an entropy cooling scheme using a tailored potential landscape (see next subsection), we aim to deterministically prepare a low-entropy sample of a bilayer Hubbard model at half-filling. This would allow us to explore, for the first time in a fermionic quantum gas experiment, the phase diagram of the bilayer Hubbard model. Future work will involve measuring magnetic correlation within a single Hubbard layer in the presence of finite inter-layer tunnelling $t_{\perp}$. The inter-plane magnetic correlations can be measured via singlet-triplet oscillation with the optical superlattice [159]. Information of both the intra-plane and inter-plane magnetic correlations would allow us to reconstruct the magnetic properties of the bilayer Hubbard system.

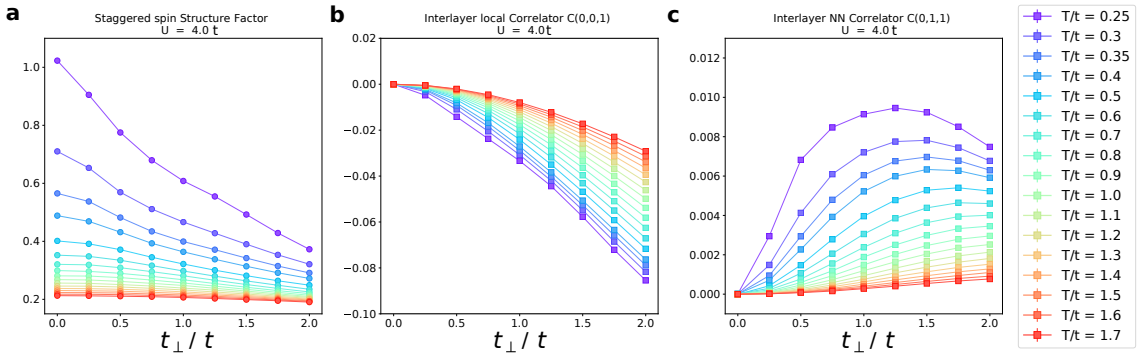

Figure 7.2: **Spin-spin correlations in the bilayer Hubbard model.** DQMC simulation results for the bilayer Hubbard model at $U/t = 4$ and half-filling $n = 0$. Parameters are in the unit of intralayer tunnelling t and the Boltzmann constant is set to unity. **a** Staggered spin structure factor within a single-layer as a function of interlayer tunnelling $t_{\perp}$. As $t_{\perp}$ increases, the anti-ferromagnetic spin correlation reduces. **b** Interlayer spin correlations. At $t_{\perp} = 0$, two layers are uncoupled, resulting in zero correlation. As $t_{\perp}$ increases, so does $J_{\perp}$. This results in anti-ferromagnetic coupling between two layers, *i.e.* $C(i = 0, j = 0, k = 1) < 0$. **c** Nearest-neighbour interlayer spin correlator $C(0, 1, 1)$. In contrast to the case of a single layer, the sign of the nearest-neighbour correlator between two layers is positive, indicating an anti-ferromagnetic coupling across the bilayer system. As $t_{\perp}$ increases, the weakening of Fermi nesting results in a reduction of anti-ferromagnetic correlations.

7.2.2 Novel entropy cooling scheme

Ultracold atoms in optical lattices provide an alternative platform in studying quantum systems, complementary to the conventional condensed matter materials. The high tunability of cold atom experiments allows the dynamical adjustment of system parameters comparable to the intrinsic time-scale of the system, such as the tunnelling time $\tau = h/t$. This offers a powerful tool to manipulate and prepare the many-body quantum state. One common hindrance, however, to probing novel quantum effects such as the conjectured d-wave pairing correlation in the doped Hubbard model, is the low temperature required to access them. Ever since the first generation of cold fermionic gas experiments with optical lattices, the standard for temperature in the community has been refreshed many times: from the original observation of density-ordering at which $k_B T \sim U \gg t$ [32, 33], down to the recent realisation of quasi-long range anti-ferromagnetic order at which $k_B T \approx 0.25t \sim J$ [160].

One proposed route for reaching even lower temperature is by the so-called entropy squeezing approach. This can be achieved by Implementing a tailored potential landscape using a spatial light modulator (SLM). In Fig. 7.3, we show one possible scheme by shining a repulsive optical potential in addition to the optical lattices onto the atoms. Not only does this realise a local, homogeneous potential landscape, it also creates spatially separated regions with a drastic difference in trap depth. Such trap depth difference in two regions leads to an inflow of particles to the deeper region, while the shallower region becomes less dense. At thermal equilibrium, the total entropy of the system is the

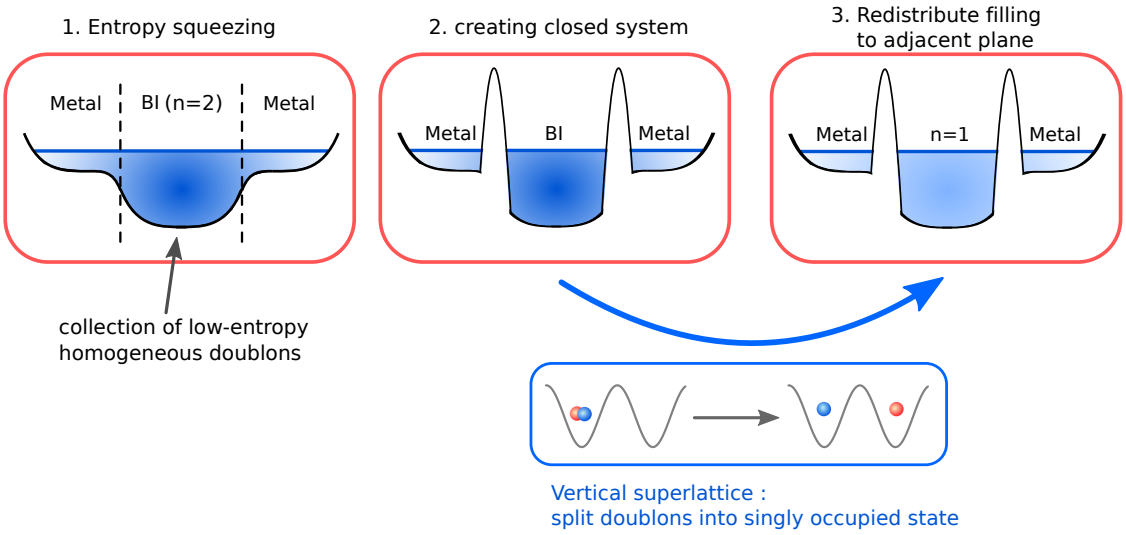

Figure 7.3: **Preparation of low-entropy state.** The scheme begins with shining in tailored optical potential using the SLM, such that the potential landscape consists of two regions. With approximate potential compensation, the deeper, core region forms a homogeneous region with the atoms being in the band insulating phase. The outer region with a shallower potential would contain the metallic phase which acts as an entropy reservoir to carry the majority of the system's total entropy. Subsequently, a sharp potential barrier is turned on, separating the core and outer regions. This results in a closed system with close to unity filling $n = 2$ at ultralow entropy. Finally, to transfer the low entropy state in the core region to another one with targeted filling, for instance, half-filling $n = 1$, we utilise the vertical superlattice and tilt the double-well potential by introducing a relative phase shift between the short- and long-wavelength lattices. The expected net result is an even distribution of particles within a bilayer system at half-filling.

sum of entropy in two regions. Since the Mott insulating (near half-filling $n = 1$) or band insulating (near unity filling $n = 2$) states are ordered state with exceptionally low entropy per particles, realise either Mott insulating or band-insulating phase in the trap centre effectively squeezes entropy out of the core region. The outer region contains atoms at the metallic phase, with lower filling but much higher entropy per particle, and acts as a reservoir which stores the majority of the system's entropy.

This idea resembles the "dimple trick" discussed for the evaporative cooling scheme in Sec. 3.1.3. However, instead of evaporating the atomic cloud carrying high entropy, the SLM allows implementing a potential barrier to create a closed system in the core region, where the total entropy is exceptionally low. Recent experiment utilising such scheme reported to reach a band insulating phase with an estimated entropy per particle of $S/k_B = 0.016(3)$ within a small region of 50 lattice sites [161]. Combining this cooling scheme with our proposed bilayer system (see previous subsection), we aim to prepare a low-entropy state with variable filling by adiabatically adjusting the double-well potential. This would open access to novel quantum phases that only emerge at temperatures significantly lower than that achieved by current generations of fermionic quantum gas apparatus.

7.2.3 Meta-stable η-condensate of fermionic pairs

So far, we had discussed extensively the case of thermal equilibrium, where the low energy states play a dominant role. When driven out of equilibrium, the highly energetic, excited states become relevant. In continuum, the highly excited states typically decay in the presence of interaction due to inelastic scattering. In an interacting lattice system, however, a highly-excited state is gapped by the interaction energy U and exceeds the bandwidth of the lattice dispersion relation. For instance, a doubly-occupied site in the repulsive Hubbard model, cannot easily decay due to conservation of energy. The decay of the highly-excited doublons can only take place via complex many-particle scattering. The on-site interaction in the Hubbard model, on the other hand, does not support such a decay mechanism. As a result, the doublons become meta-stable and possess extended lifetimes.

In particular, a so-called η-pair condensate state can be constructed as a high energy excitations using the creation operator

$$\eta^\dagger = \sum_j e^{i\pi j} c^\dagger_{j,\uparrow} c^\dagger_{j,\downarrow}. \tag{7.4}$$

It has been shown that the η-pair condensate is, in fact, an eigenstate of the Hubbard Hamiltonian [162] and thus does not decay. Despite their proposal nearly three decades ago, experiments have yet to observe a clear signature of such a high-excited condensate. The η-pair state can be understood as a state with an accumulation of coherent doublons with a π phase shift at neighbouring sites, as shown in Fig. 7.4. For sufficiently high phase-space density for the η-pairs, the η-state can condense to a highly-excited Bose-Einstein condensate at the wave-vector $\boldsymbol{q} = (\pi/a, \pi/a)$ (the corner of the 1^{st} Brillouin zone).

Recently, several theoretical proposals have emerged regarding the creation of this high-energy condensates in optical lattices [163–165]. One key step is to deploy experimental scheme in the creation of the η-pairs is to break the so-called η-symmetry since $[\eta^\dagger \eta, H] = 0$ and the number of η-pairs remain unchanged. One way this can be achieved is by introducing a dissipative process which imparts energy into the system in a controllable manner.

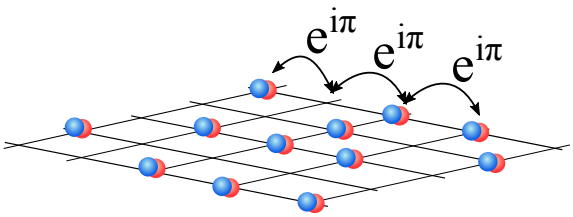

Figure 7.4: **Sketch of the η-pair state.** A macroscopic coherent state with π phase shift at nearest neighbouring sites.

7.2.4 Floquet dynamics : metal-Mott interface

Periodically-driving presents another method to achieve non-equilibrium quantum states. This realises the so-called ***Floquet*** systems.[1] The explicitly time-dependent Hamiltonian generates a new class of novel quantum phases, such as time crystal and driven ferromagnet [167, 168], which are inaccessible within conventional static quantum systems.

In order to realise such Floquet driving in our quantum gas apparatus, we aim to generate a time-periodic potential gradient in our optical lattices using a digital micro-mirror device, which has a refresh rate up to the few kHz range. As shown in Fig. 7.5, we intend to introduce driving in a spatially-dependent fashion. For region with periodic driving, the following time-dependent Hamiltonian is realised,

$$\hat{H} = -t \sum_{\langle i,j\rangle,\sigma} \left(\hat{c}^{\dagger}_{i,\sigma} \hat{c}_{jm\sigma} + h.c. \right) + U \sum_{i} \hat{n}_{i,\uparrow} \hat{n}_{i,\downarrow} + A_0 \sin(\omega t) \sum_{i,\sigma} x_i n_{i,\sigma}. \tag{7.5}$$

A is the amplitude of the potential gradient per lattice site and ω is the driving frequency. In the high frequency limit, the nearest neighbour tunnelling t in Eq. (7.5) is modified to an effective value given by [169]

$$t' = t\mathcal{J}_0(\frac{A}{\hbar\omega}). \tag{7.6}$$

Here, $\mathcal{J}_0$ is the zeroth-order Bessel function of the first kind. As a result, one can engineer, within the region of modulation, a system with drastically different properties compared to the undriven system. It has been demonstrated that for ultracold bosonic atoms trapped in three-dimensional optical lattices, the modulated dynamics induces a superfluid-to-Mott phase transition [170]. In a similar fashion, the spatially dependent driving proposed here allows the realisation of an interface separating different quantum phases, resembling a junction structure in solid-state materials [47]. The simplest kind of such interface is a metal-Mott one, in which the modulated region experiences a modulated effective interaction U/t'. Moreover, unusual transport properties such an Andreev-like reflection is expected to occur in Fermi-liquid and superconducting interface [171]. Measuring dynamics of the strongly-correlated system would also shed light on outstanding questions in non-equilibrium

[1] The name Floquet originates from a theorem for a linear differential equation with discrete symmetry by Gaston Floquet in 1883 [166]. This is in close analogy with the Bloch's theorem with discrete spatial translational symmetry.

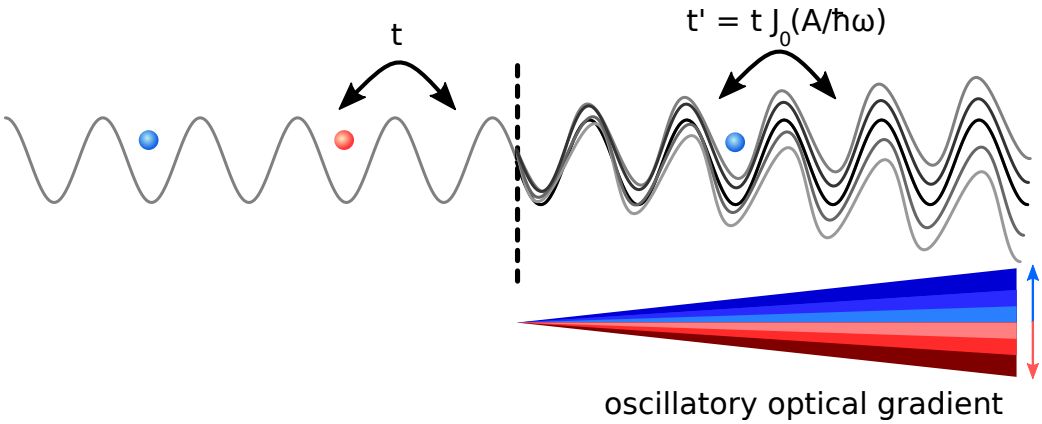

Figure 7.5: **Sketch for Floquet driving in one-dimensional optical lattice.** In the region with periodic driving of potential gradient, the effective tunnelling amplitude is reduced according to the zeroth-order Bessel function of the first kind.

quantum physics such as the Eigenstate Thermalisation Hypothesis (ETH) [172].

APPENDIX A

Determinant Quantum Monte Carlo Simulations

The quantum Monte Carlo (QMC) method has been the powerhouse for simulating many-body systems in two and higher dimensions. In simplest terms, QMC is a stochastic approach to solve the Schrödinger equation. QMC typically comes with many different flavours focusing on various aspect of a quantum system [173]. For instance, the problem at hand is distinct for $T = 0$ physics versus finite temperature $T \neq 0$, fermions versus bosons, continuum versus discrete space, finite particle number versus thermodynamic limit, and the list goes on. In particular, QMC simulations utilise stochastic sampling to map out a small yet representative subspace in the Hilbert space, which offers a tremendous advantage over a brute-force approach. Unlike variational methods, QMC is intrinsically unbiased due to its stochastic nature. In this appendix, we outline the determinant quantum Monte-Carlo (DQMC) method that is used to compare with our experimental data.

Generally speaking, the first step to perform most QMC simulations is casting a n-dimensional quantum system to a $n+1$-dimensional classical system, in which for a set of classical configurations, the partition function can be easily computed. More specifically, the quantum partition function of a quantum many-body Hamiltonian H with inverse temperature $\beta \equiv 1/T$ is given by

$$Z = \mathrm{Tr}\left[e^{-\beta(H_K+H_U)}\right]. \tag{A.1}$$

Here, $H = H_K + H_U$ is written as the sum of kinetic energy term (absorbing the chemical potential term) and the interacting term. And the trace is over the entire Hilbert space, that is, all possible quantum states. For spin-1/2 fermions in a $N \times N$ square lattice, the size of the Hilbert space is 2^{N^2}. In (DQMC) simulation of the Hubbard model, the mapping from quantum system to classical system is achieved via the Trotter decomposition, which discretises the partition function into L imaginary time slices [125], *i.e.* $\beta/L = \Delta\tau$,

$$\begin{aligned} Z &= \mathrm{Tr}\left(e^{-\beta(H_K+H_U)}\right) = \mathrm{Tr}\left(e^{-L\Delta\tau(H_K+H_U)}\right) \\ &= \mathrm{Tr}\left(\prod_{l=1}^{L} e^{-\Delta\tau(H_K+H_U)}\right) = \mathrm{Tr}\left(\prod_{l=1}^{L} e^{-\Delta\tau H_K} e^{-\Delta\tau H_U}\right) + O(\Delta\tau^2). \end{aligned} \tag{A.2}$$

Therefore, the partition function is expressed as a $N \times N \times L$ space-time lattice. However, the problem remains quantum mechanical as the traces in Eq. (A.2) still involves integrating over all possible basis

states. Since the interaction term is quartic, the problem remains computationally costly. To remove this constraint, we invoke the Hubbard-Stratonovich (HS) transformation to the interaction term,

$$e^{-U\Delta\tau(n_\uparrow-\frac{1}{2})(n_\downarrow-\frac{1}{2})} = A\sum_{h_{i,l}=\pm1} e^{\nu\cdot h_{i,l}(n_\uparrow-n_\downarrow)}, \tag{A.3}$$

where this identity is valid for each site in the discrete lattice (i,l), with $A = \frac{1}{2}e^{-U\Delta\tau/4}$ and $\cosh\nu = e^{U\Delta\tau/2}$. Therefore, for a single lattice site (i,l), we can express the contribution of interaction to the partition function by sum over auxiliary parameter $h_{i,l} = \pm1$ known as the Hubbard-Stratonovich (HS) fields. Below, we refer to a set of HS parameters over all lattice sites as ***configuration***. Eq. (A.3) effectively transforms the interaction Hamiltonian from quartic to quadratic as the right-hand side contains only linear term of $n_\uparrow$ and $n_\downarrow$. As a result, the total contribution from interaction to the partition function can be reformulated as, for a given time-slice l,

$$\begin{aligned} e^{-\Delta\tau H_U} &= e^{-U\Delta\tau\sum_i^N(n_{i,l,\uparrow}-\frac{1}{2})(n_{i,l,\downarrow}-\frac{1}{2})} = \prod_i^N\left[e^{-U\Delta\tau(n_{i,l,\uparrow}-\frac{1}{2})(n_{i,l,\downarrow}-\frac{1}{2})}\right] \\ &= A^N\prod_i^N\left[\sum_{h_{i,l}=\pm1} e^{\nu h_{i,l}(n_{i,l,\uparrow}-n_{i,l,\downarrow})}\right] = A^N\,\mathrm{Tr}_h\left(e^{\sum_i^N \nu h_{i,l}n_{i,l,\uparrow}}\cdot e^{-\sum_i^N \nu h_{i,l}n_{i,l,\downarrow}}\right) \end{aligned} \tag{A.4}$$

Here, the trace represents the sum over all possible configurations $h_{i,l} = (h_{1,1},\cdots,h_{N,L})$. Combining Eq. (A.2) and Eq. (A.3), the partition function becomes the sum over HS variables weighted by product of two determinants, one for each spin component, as the following compact, computable form

$$Z = A^{NL}\,\mathrm{Tr}_h\,\det\left[M_\uparrow(h)\right]\cdot\det\left[M_\downarrow(h)\right], \tag{A.5}$$

where $M_\sigma(h)$ is a matrix

$$M_\sigma(h) = I + \left(e^{-\Delta\tau H_K}e^{\sigma\nu h_{i,l=1}\sum_i n_{i,\uparrow}}\right)\cdots\left(e^{-\Delta\tau H_K}e^{\sigma\nu h_{i,L}\sum_i n_{i,\uparrow}}\right). \tag{A.6}$$

The final step is to generate a sample configuration h according to the probability distribution function $P(h)$

$$P(h) = \frac{A^{NL}}{Z}\det\left[M_\uparrow(h)\right]\cdot\det\left[M_\downarrow(h)\right]. \tag{A.7}$$

This is achieved by using stochastic sampling such as the Metropolis-Hasting algorithm [174].

From this point, the DQMC algorithm initialises with a certain configuration and repeatedly flipping one of the HS field parameter (to change the configuration) within a cycle over all lattice sites (referred to as sweep). The physical measurement resulting from this configuration can be computed from the matrix M. For instance, the single-particle measurement can be expressed as the matrix element of the Green's function

$$G_{ij}^\sigma = \langle c_{i,\sigma}c_{j,\sigma}^\dagger\rangle = \left(M_\sigma^{-1}(h)\right)_{ij} \tag{A.8}$$

The Green's function accumulates during the Monte Carlo cycle, and therefore so are the physical measurements. Fig. A.1 shows a typical flowchart of a DQMC algorithm.

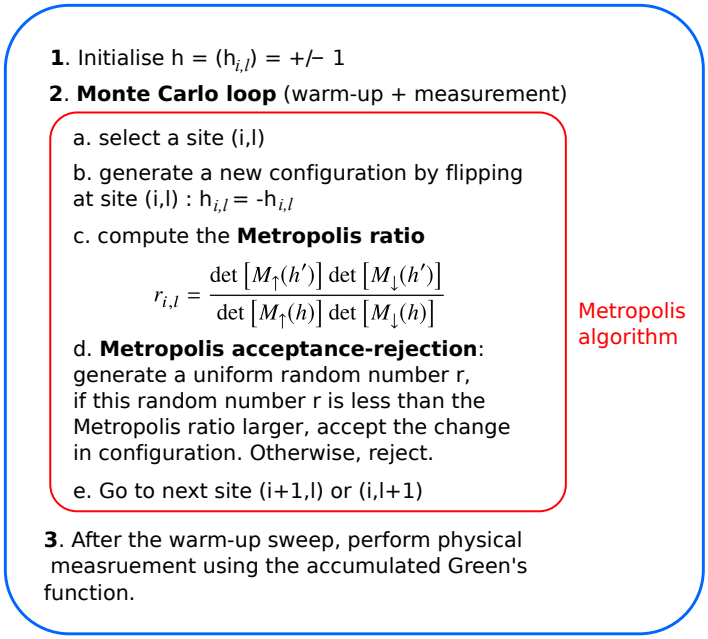

Figure A.1: **Pseudocode for DQMC simulation.** Step 1: Initialize the Hubbard-Stranovich fields, for instance, randomly setting up. Step 2: Monte Carlo loop. Compute, for this set of HS fields, matrices $M_\sigma(h)$ and the Green's function using Eq. (A.8). Next, Generate a new configuration by flipping one site, and then perform the Metropolis algorithm to decide whether or not to accept this change. If yes, compute the new Green's function and accumulate it If not, move on to the next site. Step 3: physical measurement is performed by taking averages over all DQMC measurement loops.

Bibliography

[1] R. P. Feynman, *Simulating physics with computers*, International journal of theoretical physics **21** (1982) 467 (cit. on p. 1).

[2] I. Bloch, J. Dalibard and S. Nascimbene, *Quantum simulations with ultracold quantum gases*, Nature Physics **8** (2012) 267 (cit. on p. 1).

[3] D. Leibfried et al., *Quantum dynamics of single trapped ions*, Reviews of Modern Physics **75** (2003) 281 (cit. on p. 1).

[4] Y. Makhlin, G. Schön and A. Shnirman, *Quantum-state engineering with Josephson-junction devices*, Reviews of modern physics **73** (2001) 357 (cit. on p. 1).

[5] T. Hensgens et al., *Quantum simulation of a Fermi–Hubbard model using a semiconductor quantum dot array*, Nature **548** (2017) 70 (cit. on p. 1).

[6] J. Hubbard, *Electron correlations in narrow energy bands*, Proceedings of the Royal Society of London. Series A. Mathematical and Physical Sciences **276** (1963) 238 (cit. on p. 2).

[7] J. Hubbard, *Electron correlations in narrow energy bands. II. The degenerate band case*, Proceedings of the Royal Society of London. Series A. Mathematical and Physical Sciences **277** (1964) 237 (cit. on p. 2).

[8] J. Hubbard, *Electron correlations in narrow energy bands III. An improved solution*, Proceedings of the Royal Society of London. Series A. Mathematical and Physical Sciences **281** (1964) 401 (cit. on p. 2).

[9] J. Hubbard, *Electron correlations in narrow energy bands-IV. The atomic representation*, Proceedings of the Royal Society of London. Series A. Mathematical and Physical Sciences **285** (1965) 542 (cit. on p. 2).

[10] J. Hubbard, *Electron correlations in narrow energy bands V. A perturbation expansion about the atomic limit*, Proceedings of the Royal Society of London. Series A. Mathematical and Physical Sciences **296** (1967) 82 (cit. on p. 2).

[11] M. H. Anderson et al., *Observation of Bose-Einstein condensation in a dilute atomic vapor*, science (1995) 198 (cit. on p. 2).

[12] K. B. Davis et al., *Bose-Einstein condensation in a gas of sodium atoms*, Physical review letters **75** (1995) 3969 (cit. on p. 2).

[13] C. Regal, M. Greiner and D. S. Jin, *Observation of resonance condensation of fermionic atom pairs*, Physical review letters **92** (2004) 040403 (cit. on pp. 2, 29).

[14] C. Chin et al., *Feshbach resonances in ultracold gases*, Reviews of Modern Physics **82** (2010) 1225 (cit. on pp. 2, 28, 30).

[15] W. S. Bakr et al., *A quantum gas microscope for detecting single atoms in a Hubbard-regime optical lattice*, Nature **462** (2009) 74 (cit. on p. 2).

[16] M. Greiner et al., *Quantum phase transition from a superfluid to a Mott insulator in a gas of ultracold atoms*, nature **415** (2002) 39 (cit. on pp. 2, 15).

[17] M. Greiner, *Ultracold quantum gases in three-dimensional optical lattice potentials*, PhD thesis: Ludwig-Maximilians-Universität München, 2003 (cit. on p. 2).

[18] J. Stewart et al., *Potential Energy of a K 40 Fermi Gas in the BCS-BEC Crossover*, Physical review letters **97** (2006) 220406 (cit. on p. 2).

[19] L. Tarruell et al., *Creating, moving and merging Dirac points with a Fermi gas in a tunable honeycomb lattice*, Nature **483** (2012) 302 (cit. on p. 2).

[20] *The Hubbard model at half a century*, Nature Physics **9** (2013) 523 (cit. on p. 5).

[21] G. D. Mahan, *Many-particle physics*, Springer Science & Business Media, 2013 (cit. on p. 7).

[22] L. Tarruell and L. Sanchez-Palencia, *Quantum simulation of the Hubbard model with ultracold fermions in optical lattices*, Comptes Rendus Physique **19** (2018) 365, Quantum simulation / Simulation quantique, ISSN: 1631-0705 (cit. on p. 9).

[23] T. Esslinger, *Fermi-Hubbard physics with atoms in an optical lattice*, Annu. Rev. Condens. Matter Phys. **1** (2010) 129 (cit. on p. 9).

[24] A. Georges and G. Kotliar, *Hubbard model in infinite dimensions*, Physical Review B **45** (1992) 6479 (cit. on p. 9).

[25] M. Troyer and U.-J. Wiese, *Computational complexity and fundamental limitations to fermionic quantum Monte Carlo simulations*, Physical review letters **94** (2005) 170201 (cit. on p. 9).

[26] M. B. Dahan et al., *Bloch oscillations of atoms in an optical potential*, Physical Review Letters **76** (1996) 4508 (cit. on p. 12).

[27] Z. A. Geiger et al., *Observation and uses of position-space bloch oscillations in an ultracold gas*, Physical review letters **120** (2018) 213201 (cit. on p. 12).

[28] V. Dobrosavljevic, N. Trivedi and J. M. Valles Jr, *Conductor insulator quantum phase transitions*, Oxford University Press, 2012 (cit. on p. 15).

[29] M. P. Fisher et al., *Boson localization and the superfluid-insulator transition*, Physical Review B **40** (1989) 546 (cit. on p. 15).

[30] F. H. Essler et al., *The one-dimensional Hubbard model*, Cambridge University Press, 2005 (cit. on p. 17).

[31] T. Giamarchi, *Quantum Physics in One Dimension*, Oxford University Press, 2004 (cit. on p. 17).

[32] R. Jördens et al., *A Mott insulator of fermionic atoms in an optical lattice*, Nature **455** (2008) 204 (cit. on pp. 18, 110).

[33] U. Schneider et al., *Metallic and insulating phases of repulsively interacting fermions in a 3D optical lattice*, Science **322** (2008) 1520 (cit. on pp. 18, 110).

[34] J. Slater, *Magnetic effects and the Hartree-Fock equation*, Physical Review **82** (1951) 538 (cit. on p. 20).

[35] M. Inui and P. Littlewood, *Hartree-Fock study of the magnetism in the single-band Hubbard model*, Physical Review B **44** (1991) 4415 (cit. on p. 20).

[36] J. Hirsch, *Simulations of the three-dimensional Hubbard model: Half-filled band sector*, Physical Review B **35** (1987) 1851 (cit. on p. 20).

[37] J. M. Singer et al., *From BCS-like superconductivity to condensation of local pairs: A numerical study of the attractive Hubbard model*, Phys. Rev. B **54** (2 1996) 1286 (cit. on pp. 20, 94).

[38] J. M. Singer, T. Schneider and M. Pedersen, *On the phase diagram of the attractive Hubbard model: Crossover and quantum critical phenomena*, The European Physical Journal B-Condensed Matter and Complex Systems **2** (1998) 17 (cit. on p. 20).

[39] E. Zhao and A. Paramekanti, *BCS-BEC crossover on the two-dimensional honeycomb lattice*, Physical review jordens2008mottMzletters **97** (2006) 230404 (cit. on p. 20).

[40] A. Koetsier, D. Dickerscheid and H. Stoof, *BEC-BCS crossover in an optical lattice*, Physical Review A **74** (2006) 033621 (cit. on p. 20).

[41] D. J. Scalapino, *The case for dx2- y2 pairing in the cuprate superconductors*, Physics Reports **250** (1995) 329 (cit. on p. 20).

[42] J. Orenstein and A. Millis, *Advances in the physics of high-temperature superconductivity*, Science **288** (2000) 468 (cit. on p. 20).

[43] R. Grimm, M. Weidemüller and Y. B. Ovchinnikov, *Optical dipole traps for neutral atoms*, arXiv preprint physics/9902072 (1999) (cit. on p. 22).

[44] R. Williams et al., *Dynamic optical lattices: two-dimensional rotating and accordion lattices for ultracold atoms*, Optics Express **16** (2008) 16977 (cit. on p. 23).

[45] F. Bloch, *Über die quantenmechanik der elektronen in kristallgittern*, Zeitschrift für physik **52** (1929) 555 (cit. on p. 25).

[46] N. W. Ashcroft and N. D. Mermin, *Solid state physics (saunders college, philadelphia, 1976)*, Appendix N (2010) (cit. on pp. 25, 74).

[47] C. Kittel, *Quantum Theory of Solids*, John Wiley & Sons, 1987 (cit. on pp. 25, 112).

[48] F. Schwabl, *Advanced quantum mechanics*, Springer, 1999, ISBN: 9783540644781 (cit. on pp. 27, 98).

[49] J. J. Sakurai and E. D. Commins, *Modern quantum mechanics, revised edition*, 1995 (cit. on pp. 27, 45).

[50] H. T. Stoof, K. B. Gubbels and D. Dickerscheid, *Ultracold quantum fields*, Springer, 2009 (cit. on p. 28).

[51] K. Huang and C. N. Yang, *Quantum-mechanical many-body problem with hard-sphere interaction*, Physical review **105** (1957) 767 (cit. on p. 28).

[52] K. Huang, *Introduction to statistical physics*, Chapman and Hall/CRC, 2009 (cit. on pp. 28, 67).

[53] D. Blume and C. H. Greene, *Fermi pseudopotential approximation: Two particles under external confinement*, Physical Review A **65** (2002) 043613 (cit. on p. 28).

[54] Z. Idziaszek and T. Calarco, *Analytical solutions for the dynamics of two trapped interacting ultracold atoms*, Physical Review A **74** (2006) 022712 (cit. on p. 29).

[55] L. A. Miller, *Ultracold Fermions in Two-Dimensional Optical Lattices: Quantum Simulation of the Hubbard Model*, PhD thesis: University of Cambridge, 2016 (cit. on pp. 29, 34, 35, 49).

[56] U. Schneider et al., *Fermionic transport and out-of-equilibrium dynamics in a homogeneous Hubbard model with ultracold atoms*, Nature Physics **8** (2012) 213 (cit. on p. 29).

[57] E. Khatami and M. Rigol, *Thermodynamics of strongly interacting fermions in two-dimensional optical lattices*, Physical Review A **84** (2011) 053611 (cit. on pp. 30, 31).

[58] B. Tang, E. Khatami and M. Rigol, *A short introduction to numerical linked-cluster expansions*, Computer Physics Communications **184** (2013) 557 (cit. on p. 30).

[59] M. Rigol, T. Bryant and R. R. Singh, *Numerical linked-cluster approach to quantum lattice models*, Physical review letters **97** (2006) 187202 (cit. on p. 31).

[60] C. N. Varney et al., *Quantum Monte Carlo study of the two-dimensional fermion Hubbard model*, Phys. Rev. B **80** (7 2009) 075116 (cit. on pp. 32, 77).

[61] B. Fröhlich et al., *Radio-frequency spectroscopy of a strongly interacting two-dimensional Fermi gas*, Physical review letters **106** (2011) 105301 (cit. on p. 34).

[62] M. Feld et al., *Observation of a pairing pseudogap in a two-dimensional Fermi gas*, Nature **480** (2011) 75 (cit. on p. 34).

[63] M. Koschorreck et al., *Attractive and repulsive Fermi polarons in two dimensions*, Nature **485** (2012) 619 (cit. on p. 34).

[64] M. Koschorreck et al., *Universal spin dynamics in two-dimensional Fermi gases*, Nature Physics **9** (2013) 405 (cit. on pp. 34, 82).

[65] E. Cocchi et al., *Equation of state of the two-dimensional Hubbard model*, Physical review letters **116** (2016) 175301 (cit. on p. 34).

[66] E. Cocchi et al.,
Measuring entropy and short-range correlations in the two-dimensional Hubbard model,
Physical Review X **7** (2017) 031025 (cit. on p. 34).

[67] J. Drewes et al.,
Thermodynamics versus local density fluctuations in the metal–mott-insulator crossover,
Physical review letters **117** (2016) 135301 (cit. on p. 34).

[68] J. Drewes et al., *Antiferromagnetic correlations in two-dimensional fermionic Mott-insulating and metallic phases*, Physical review letters **118** (2017) 170401 (cit. on p. 34).

[69] M. Feld, *Ultracold quantum gases in three-dimensional optical lattice potentials*,
PhD thesis: Low temperature phases of interacting fermions in two dimensions, 2011 (cit. on pp. 34–37).

[70] B. Fröhlich, *A Strongly Interacting Two-Dimensional Fermi Gas*,
PhD thesis: Ludwig-Maximilians-Universität München, 2011 (cit. on pp. 34–37).

[71] E. Vogt, *Collective Modes and Polarons in two-dimensional Fermi Gases*,
PhD thesis: University of Cambridge, 2013 (cit. on p. 34).

[72] E. Cocchi, *Analogue Quantum Simulation of the Two-Dimensional Hubbard Model with Ultracold Fermions*, PhD thesis: University of Cambridge, 2016
(cit. on pp. 34, 37, 42, 44, 49).

[73] J. H. Drewes, *Ultracold quantum gases in three-dimensional optical lattice potentials*,
PhD thesis: Rheinischen Friedrich-Wilhelms-Universität Bonn, (to be submitted)
(cit. on pp. 34, 51, 52).

[74] S. Chu et al., *Three-dimensional viscous confinement and cooling of atoms by resonance radiation pressure*, Physical review letters **55** (1985) 48 (cit. on p. 35).

[75] W. D. Phillips, *Nobel Lecture: Laser cooling and trapping of neutral atoms*,
Reviews of Modern Physics **70** (1998) 721 (cit. on p. 35).

[76] W. M. Haynes, *CRC handbook of chemistry and physics*, CRC press, 2014
(cit. on pp. 35, 36).

[77] R. V. Pound, *Electronic frequency stabilization of microwave oscillators*,
Review of Scientific Instruments **17** (1946) 490 (cit. on p. 35).

[78] U. Schünemann et al., *Simple scheme for tunable frequency offset locking of two lasers*,
Review of Scientific Instruments **70** (1999) 242 (cit. on p. 35).

[79] T. Tiecke, *Properties of potassium*,
University of Amsterdam, The Netherlands, Thesis (2010) 12 (cit. on p. 36).

[80] D. E. Pritchard, *Cooling neutral atoms in a magnetic trap for precision spectroscopy*,
Physical Review Letters **51** (1983) 1336 (cit. on p. 36).

[81] C. Henkel, S. Pötting and M. Wilkens,
Loss and heating of particles in small and noisy traps, Applied Physics B **69** (1999) 379
(cit. on p. 36).

[82] D. Harber et al., *Thermally induced losses in ultra-cold atoms magnetically trapped near room-temperature surfaces*, Journal of low temperature physics **133** (2003) 229
(cit. on p. 36).

[83] R. Grimm,
Ultracold Fermi gases in the BEC-BCS crossover: a review from the Innsbruck perspective,
arXiv preprint cond-mat/0703091 (2007) (cit. on p. 38).

[84] P. Pinkse et al., *Adiabatically changing the phase-space density of a trapped Bose gas*,
Physical Review Letters **78** (1997) 990 (cit. on p. 38).

[85] D. Stamper-Kurn et al., *Reversible formation of a Bose-Einstein condensate*,
Physical review letters **81** (1998) 2194 (cit. on p. 38).

[86] D. Rychtarik et al., *Two-dimensional Bose-Einstein condensate in an optical surface trap*,
Physical review letters **92** (2004) 173003 (cit. on p. 38).

[87] M. Gröbner et al., *A new quantum gas apparatus for ultracold mixtures of K and Cs and KCs ground-state molecules*, Journal of Modern Optics **63** (2016) 1829 (cit. on p. 38).

[88] W. Ketterle and M. W. Zwierlein,
Making, probing and understanding ultracold Fermi gases,
arXiv preprint arXiv:0801.2500 (2008) (cit. on p. 39).

[89] D. Swinehart, *The beer-lambert law*, Journal of chemical education **39** (1962) 333
(cit. on p. 51).

[90] G. Reinaudi et al.,
Strong saturation absorption imaging of dense clouds of ultracold atoms,
Optics letters **32** (2007) 3143 (cit. on p. 51).

[91] E. Noether, *Invariante Variationsprobleme*, ger, Nachrichten von der Gesellschaft der Wissenschaften zu Göttingen, Mathematisch-Physikalische Klasse **1918** (1918) 235
(cit. on p. 54).

[92] F. Gebhard, *Metal—Insulator Transitions*, Springer, 1997 (cit. on p. 55).

[93] C. N. Yang and S. Zhang, *SO 4 symmetry in a Hubbard model*,
Modern Physics Letters B **4** (1990) 759 (cit. on pp. 55–57).

[94] M. S. Sozzi, *Discrete Symmetries and CP Violation: From Experiment to Theory*,
Oxford University Press, 2008, ISBN: 978-0-19-929666-8 (cit. on p. 56).

[95] M. E. Peskin and D. V. Schroeder, *An Introduction to quantum field theory*,
Addison-Wesley, 1995, ISBN: 9780201503975, 0201503972 (cit. on p. 56).

[96] C. S. Wu et al., *Experimental Test of Parity Conservation in Beta Decay*,
Phys. Rev. **105** (4 1957) 1413 (cit. on p. 56).

[97] J. H. Christenson et al., *Evidence for the 2π Decay of the K_2^0 Meson*,
Phys. Rev. Lett. **13** (4 1964) 138 (cit. on p. 56).

[98] P. B. Littlewood and C. M. Varma, *Gauge-Invariant Theory of the Dynamical Interaction of Charge Density Waves and Superconductivity*, Phys. Rev. Lett. **47** (11 1981) 811
(cit. on p. 56).

[99] D. Pekker and C. Varma, *Amplitude/Higgs Modes in Condensed Matter Physics*,
Annual Review of Condensed Matter Physics **6** (2015) 269,
eprint: https://doi.org/10.1146/annurev-conmatphys-031214-014350
(cit. on p. 56).

[100] A. Behrle et al., *Higgs mode in a strongly interacting fermionic superfluid*,
Nature Physics **14** (2018) 781 (cit. on p. 56).

[101] Y.-J. Lin, K. Jiménez-García and I. B. Spielman,
Spin–orbit-coupled Bose–Einstein condensates, Nature **471** (2011) 83 (cit. on p. 57).

[102] L. W. Cheuk et al., *Spin-injection spectroscopy of a spin-orbit coupled Fermi gas*,
Physical Review Letters **109** (2012) 095302 (cit. on p. 57).

[103] P. Wang et al., *Spin-orbit coupled degenerate Fermi gases*,
Physical review letters **109** (2012) 095301 (cit. on p. 57).

[104] H. Miyake et al.,
Realizing the Harper Hamiltonian with laser-assisted tunneling in optical lattices,
Physical review letters **111** (2013) 185302 (cit. on p. 57).

[105] M. Aidelsburger et al.,
Experimental realization of strong effective magnetic fields in an optical lattice,
Physical review letters **107** (2011) 255301 (cit. on p. 57).

[106] A. F. Ho, M. A. Cazalilla and T. Giamarchi,
Quantum simulation of the Hubbard model: The attractive route,
Phys. Rev. A **79** (3 2009) 033620 (cit. on p. 57).

[107] C. J. Adkins and C. J. Adkins, *Equilibrium thermodynamics*,
Cambridge University Press, 1983 (cit. on p. 63).

[108] R. Jördens et al., *A Mott insulator of Fermionic atoms in an optical lattice*,
Nature **455** (2008) 204 (cit. on p. 70).

[109] U. Schneider et al., *Metallic and Insulating Phases of Repulsively Interacting Fermions in a 3D Optical Lattice*, Science **322** (2008) 1520,
eprint: http://www.sciencemag.org/content/322/5907/1520.full.pdf
(cit. on p. 70).

[110] D. Greif et al., *Site-resolved imaging of a Fermionic Mott insulator*,
Science **351** (2016) 953 (cit. on p. 70).

[111] L. W. Cheuk et al.,
Observation of 2D Fermionic Mott Insulators of ^{40}K with Single-Site Resolution,
Phys. Rev. Lett. **116** (23 2016) 235301 (cit. on p. 70).

[112] E. Cocchi et al., *Equation of State of the Two-Dimensional Hubbard Model*,
Phys. Rev. Lett. **116** (17 2016) 175301 (cit. on pp. 70, 88, 89).

[113] P. M. Duarte et al., *Compressibility of a Fermionic Mott Insulator of Ultracold Atoms*,
Phys. Rev. Lett. **114** (7 2015) 070403 (cit. on p. 70).

[114] J. Yu, N. Sun and H. Zhai,
Symmetry protected dynamical symmetry in the generalized Hubbard models,
Physical review letters **119** (2017) 225302 (cit. on p. 71).

[115] N. Wurz et al., *Coherent manipulation of spin correlations in the Hubbard model*,
Phys. Rev. A **97** (5 2018) 051602 (cit. on p. 73).

[116] S. Sachdev, *Quantum magnetism and criticality*, Nature Physics **4** (2008) 173
(cit. on pp. 74, 75).

[117] W. Greiner, L. Neise and H. Stöcker, "The Models of Ising and Heisenberg",
Thermodynamics and Statistical Mechanics, Springer, 1995 436 (cit. on p. 74).

[118] C. L. Cleveland and R. Medina A,
Obtaining a Heisenberg Hamiltonian from the Hubbard model,
American Journal of Physics **44** (1976) 44 (cit. on p. 77).

[119] N. D. Mermin and H. Wagner, *Absence of Ferromagnetism or Antiferromagnetism in One- or Two-Dimensional Isotropic Heisenberg Models*, Phys. Rev. Lett. **17** (22 1966) 1133 (cit. on pp. 77, 95).

[120] E. Manousakis, *The spin-½ Heisenberg antiferromagnet on a square lattice and its application to the cuprous oxides*, Rev. Mod. Phys. **63** (1 1991) 1 (cit. on p. 77).

[121] J. B. Smathers, *Introduction to the Theory of Thermal Neutron Scattering, by G. L. Squires*, Medical Physics **7** (1980) 264, ISSN: 2473-4209 (cit. on p. 78).

[122] P. M. Platzman and N. Tzoar,
Magnetic scattering of X rays from electrons in molecules and solids,
Physical Review B **2** (1970) 3556 (cit. on p. 78).

[123] R. A. H. and Pedro M. Duarte et al.,
Observation of antiferromagnetic correlations in the Hubbard model with ultracold atoms,
Nature **519** (2015) 211 (cit. on p. 78).

[124] J. W. Goodman, *Introduction to Fourier optics*, Roberts and Company Publishers, 2005 (cit. on p. 80).

[125] S. R. White et al., *Numerical study of the two-dimensional Hubbard model*,
Physical Review B **40** (1989) 506 (cit. on pp. 82, 115).

[126] N. F. Ramsey, *A molecular beam resonance method with separated oscillating fields*,
Physical Review **78** (1950) 695 (cit. on p. 82).

[127] R. Grimm, "Ultrafast many-body interferometry of impurities coupled to a Fermi sea",
APS Meeting Abstracts, 2017 (cit. on p. 82).

[128] T. Rom et al., *Free fermion antibunching in a degenerate atomic Fermi gas released from an optical lattice*, Nature **444** (2006) 733 (cit. on p. 87).

[129] E. Altman, E. Demler and M. D. Lukin,
Probing many-body states of ultracold atoms via noise correlations,
Physical Review A **70** (2004) 013603 (cit. on p. 87).

[130] E. Khatami and M. Rigol,
Thermodynamics of strongly interacting fermions in two-dimensional optical lattices,
Physical Review A **84** (2011) 053611 (cit. on pp. 88, 89).

[131] A. Sommer et al., *Universal Spin Transport in a Strongly Interacting Fermi Gas*,
Nature **472** (2011) 201 (cit. on p. 91).

[132] M. Koschorreck et al., *Universal spin dynamics in two-dimensional Fermi gases*,
Nature Physics **9** (2013) 405 (cit. on p. 91).

[133] L. N. Cooper et al., *BCS: 50 years*, World scientific, 2011 (cit. on p. 93).

[134] P. A. Lee, N. Nagaosa and X.-G. Wen,
Doping a Mott insulator: Physics of high-temperature superconductivity,
Rev. Mod. Phys. **78** (1 2006) 17 (cit. on p. 94).

[135] W. Zwerger, *The BCS-BEC Crossover and the Unitary Fermi Gas*,
Lecture Notes in Physics, Springer Berlin Heidelberg, 2011, ISBN: 9783642219771
(cit. on p. 94).

[136] M. Randeria et al.,
Pairing and spin gap in the normal state of short coherence length superconductors,
Phys. Rev. Lett. **69** (13 1992) 2001 (cit. on p. 94).

[137] H. Ding et al., *Spectroscopic evidence for a pseudogap in the normal state of underdoped high-Tc superconductors*, Nature **382** (1996) 51 (cit. on p. 94).

[138] T. Esslinger, *Fermi-Hubbard Physics with Atoms in an Optical Lattice*,
Annual Review of Condensed Matter Physics **1** (2010) 129,
eprint: https://doi.org/10.1146/annurev-conmatphys-070909-104059
(cit. on p. 94).

[139] A. V. Chubukov, D. Pines and B. P. Stojkovic, *Temperature crossovers in cuprates*,
Journal of Physics: Condensed Matter **8** (1996) 10017 (cit. on pp. 94, 96).

[140] Q. Chen et al.,
BCS–BEC crossover: From high temperature superconductors to ultracold superfluids,
Physics Reports **412** (2005) 1 (cit. on p. 94).

[141] Q. Chen, K. Levin and J. Stajic, *Applying BCS–BEC crossover theory to high-temperature superconductors and ultracold atomic Fermi gases*,
Low Temperature Physics **32** (2006) 406 (cit. on p. 94).

[142] P. T. Brown et al., *Angle-resolved photoemission spectroscopy of a Fermi-Hubbard system*,
arXiv preprint arXiv:1903.05678 (2019) (cit. on p. 95).

[143] I. Bloch, J. Dalibard and W. Zwerger, *Many-body physics with ultracold gases*,
Reviews of modern physics **80** (2008) 885 (cit. on p. 95).

[144] S. Giorgini, L. P. Pitaevskii and S. Stringari, *Theory of ultracold atomic Fermi gases*,
Reviews of Modern Physics **80** (2008) 1215 (cit. on p. 95).

[145] R. Scalettar et al., *Phase diagram of the two-dimensional negative-U Hubbard model*,
Physical review letters **62** (1989) 1407 (cit. on p. 96).

[146] B. Batlogg and V. Emery, *Crossovers in cuprates*, Nature **382** (1996) 20 (cit. on p. 96).

[147] J. C. Brooks-Bartlett and E. F. Garman,
The Nobel Science: One Hundred Years of Crystallography,
Interdisciplinary Science Reviews **40** (2015) 244,
eprint: https://doi.org/10.1179/0308018815Z.000000000116 (cit. on p. 97).

[148] M. Bée, *Quasielastic Neutron Scattering*, Adam Hilger, 1988, ISBN: 9780852743713
(cit. on p. 97).

[149] P. T. Brown et al., *Bad metallic transport in a cold atom Fermi-Hubbard system*,
Science **363** (2019) 379 (cit. on p. 98).

[150] C. H. Schunck et al.,
Determination of the fermion pair size in a resonantly interacting superfluid,
Nature **454** (2008) 739 (cit. on p. 101).

[151] A. Damascelli, Z. Hussain and Z.-X. Shen,
Angle-resolved photoemission studies of the cuprate superconductors,
Reviews of modern physics **75** (2003) 473 (cit. on p. 108).

[152] R. T. Scalettar et al., *Magnetic and pairing correlations in coupled Hubbard planes*,
Physical Review B **50** (1994) 13419 (cit. on p. 108).

[153] T. A. Maier and D. Scalapino, *Pair structure and the pairing interaction in a bilayer Hubbard model for unconventional superconductivity*, Physical Review B **84** (2011) 180513 (cit. on p. 108).

[154] R. R. Dos Santos, *Magnetism and pairing in Hubbard bilayers*, Physical Review B **51** (1995) 15540 (cit. on p. 108).

[155] S. Florens et al., *Mott transition at large orbital degeneracy: Dynamical mean-field theory*, Physical Review B **66** (2002) 205102 (cit. on p. 108).

[156] A. Sandvik and D. Scalapino, *Order-disorder transition in a two-layer quantum antiferromagnet*, Physical review letters **72** (1994) 2777 (cit. on p. 109).

[157] C. Gros, W. Wenzel and J. Richter, *The transition from an ordered antiferromagnet to a quantum disordered spin liquid in a solvable bilayer model*, EPL (Europhysics Letters) **32** (1995) 747 (cit. on p. 109).

[158] L. Wang, K. Beach and A. W. Sandvik, *High-precision finite-size scaling analysis of the quantum-critical point of S= 1/ 2 Heisenberg antiferromagnetic bilayers*, Physical Review B **73** (2006) 014431 (cit. on p. 109).

[159] D. Greif et al., *Short-range quantum magnetism of ultracold fermions in an optical lattice*, Science **340** (2013) 1307 (cit. on p. 109).

[160] A. Mazurenko et al., *A cold-atom Fermi-Hubbard antiferromagnet*, Nature **545** (2017) 462, ISSN: 0028-0836 (cit. on p. 110).

[161] C. S. Chiu et al., *Quantum state engineering of a Hubbard system with ultracold fermions*, Physical review letters **120** (2018) 243201 (cit. on p. 111).

[162] C. N. Yang, *η pairing and off-diagonal long-range order in a Hubbard model*, Physical review letters **63** (1989) 2144 (cit. on p. 111).

[163] A. Rosch et al., *Metastable superfluidity of repulsive fermionic atoms in optical lattices*, Physical review letters **101** (2008) 265301 (cit. on p. 111).

[164] A. Kantian, A. Daley and P. Zoller, *η condensate of fermionic atom pairs via adiabatic state preparation*, Physical review letters **104** (2010) 240406 (cit. on p. 111).

[165] J.-S. Bernier et al., *Emergence of spatially extended pair coherence through incoherent local environmental coupling*, Physical Review A **87** (2013) 063608 (cit. on p. 111).

[166] G. Floquet, "Sur les équations différentielles linéaires à coefficients périodiques", *Annales scientifiques de l'École normale supérieure*, vol. 12, 1883 47 (cit. on p. 112).

[167] J. Smits et al., *Observation of a space-time crystal in a superfluid quantum gas*, Physical review letters **121** (2018) 185301 (cit. on p. 112).

[168] C. V. Parker, L.-C. Ha and C. Chin, *Direct observation of effective ferromagnetic domains of cold atoms in a shaken optical lattice*, Nature Physics **9** (2013) 769 (cit. on p. 112).

[169] A. Eckardt, C. Weiss and M. Holthaus, *Superfluid-insulator transition in a periodically driven optical lattice*, Physical review letters **95** (2005) 260404 (cit. on p. 112).

[170] A. Zenesini et al., *Coherent control of dressed matter waves*, Physical review letters **102** (2009) 100403 (cit. on p. 112).

[171] R. Matsunaga et al., *Higgs amplitude mode in the BCS superconductors Nb 1- x Ti x N induced by terahertz pulse excitation*, Physical review letters **111** (2013) 057002 (cit. on p. 112).

[172] J. M. Deutsch, *Quantum statistical mechanics in a closed system*, Physical Review A **43** (1991) 2046 (cit. on p. 113).

[173] K. A. Benedict, *Quantum Monte Carlo methods: algorithms for lattice models*, 2019 (cit. on p. 115).

[174] W. K. Hastings, *Monte Carlo sampling methods using Markov chains and their applications*, (1970) (cit. on p. 116).

List of Figures

List of Tables